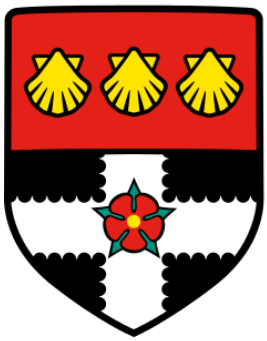

University of Reading

Department of Meteorology

Decadal Variability of Tropical Cyclones in the Northern Hemisphere:

Natural Variability or Anthropogenic Influence?

PINELOPI LOIZOU

A thesis submitted for the degree of Doctor of Philosophy

October 2021

Declaration

I confirm that this is my own work and the use of all material from other sources has been properly and fully acknowledged.

Publications

Chapter 6 of this thesis, titled "*Development of a simple, open-source hurricane wind risk model for Bermuda with a sensitivity test on decadal variability*", has been peer-reviewed and accepted for Open Access publication in the book "*Hurricane Risk in a Changing Climate, Vol. 2*" which will be published by Springer in 2022. All work undertaken in this publication was carried out by Pinelopi Loizou with co-authors providing guidance and review.

Acknowledgments

I would first like to thank my supervisors: Prof. Pier Luigi Vidale, for giving me the opportunity and for trusting me to undertake such an interesting and demanding PhD project, as well as for the countless of times he provided me with explanations that have broaden my scientific knowledge; Dr. Kevin Hodges, for the numerous times he reviewed any written documents and for the infinite amount of technical help, without which this PhD would have not been completed; Dr. Silke Dierer for her guidance and contributions in the industrial aspect of the PhD project.

Additional thanks to Dr. Mark Guishard for being an incredible mentor during the 12-week internship at BIOS, during which I was able to explore the work of insurance companies and catastrophe modeling. I would also like to acknowledge Malcolm Roberts from the UK Met Office for being a star and always answering my questions about model simulations and for providing me with the model data used in the study. Special thanks to Dr. Nicholas Klingaman and Dr. Armenia Franco Diaz for assisting and providing me with the code for EOTs. Additionally, I would like to thank my monitoring committee, Prof. Nigel Arnell and Dr. Pete Inness, for their guidance and comments throughout this PhD. Last but not least, I would like to thank SCENARIO NERC and the UK Associates of BIOS for their financial support during the PhD and the internship.

This academic endeavour would not have started without a special group of people. First, my MSc tutor, Dr. Michaela Hegglin, and my MSC dissertation project supervisor, Dr. Helen Dacre, for encouraging me to pursue a PhD project and for always being happy to chat with me. Second, I would like to thank my family for their unconditional love and care and for always supporting my dreams and goals. Third, it is important to acknowledge by name the friends who have been by my side during this journey (especially during the pandemic), who were always there whenever I needed a chat, a walk, help or proof reading of my writing: Nefeli, Pedro, Marianna, Evdokia, George, Zak, Shannon, Gabriel, Elli, Mary, Stef, Chrystalla and Irene. Sincerely, thank you. Finally, I want to thank technology and my optometrist for allowing me to produce and examine almost 22000 figures.

Dedication

This thesis is dedicated to my family, my home, friends and teachers, particularly to those who are no longer here, for their unconditional love and support.

Abstract

Understanding which environmental processes are responsible for driving the interannual and decadal variability of tropical cyclones (TCs) is important for providing TC impact-related mitigation and planning information to the responsible agencies and business. TC activity in the northern hemisphere is examined in IBTrACS, seven recent reanalyses and coupled and atmosphere-only simulations at various resolutions from HadGEM3-GC3.1. Drivers of TC activity are examined for the current climate, on decadal time scales and in scenarios of a warming climate. Different tools, including the standard power spectrum method, the wavelets, and the Empirical Teleconnections method are utilized. TC activity in the North Atlantic (NATL), characterized by high variability, is primarily influenced on interannual and decadal time scales by the Atlantic Multi-decadal Oscillation (AMO) via warm local Sea Surface Temperatures (SSTs). The primary driver for TC activity in the Eastern Pacific (EPAC) and Central Pacific (CPAC) regions under current climate conditions is the El-Niño Southern Oscillation (ENSO) with associated warm SSTs and weak Vertical Wind Shear (VWS) in the Pacific, whereas decadal variability is driven by both ENSO and AMO. Typhoon activity in the Western Pacific (WPAC) is found to be driven by more than one main driver in observations and the model. Variability of TC activity in the North Indian Ocean (NIND) is not linked significantly to the climate modes (ENSO, AMO, PDO) examined in the study. With a warming climate, ACE increases in NATL, EPAC, CPAC and WPAC and decreases for NIND. For EPAC there is a westward shift, while for WPAC there is a poleward shift in TC activity. Finally, a simple, open-source hurricane-catastrophe model is developed for assessing risk associated with hurricane winds for Bermuda and it is used to test the sensitivity of hurricane wind risk to variability of the frequency of events, particularly related to the AMO.

Contents

Acronyms

ACE Accumulated Cyclone Energy.

AEP Aggregate Exceedance Probability.

AEW African Easterly Wave.

AMM Atlantic Meridional Mode.

AMO Atlantic Multi-decadal Oscillation.

AMOC Atlantic Meridional Overturning Circulation.

ARV Annual Rental Value.

CDF Cumulative Distribution Function.

CMIP3 Coupled Model Intercomparison Project phase 3.

CMIP5 Coupled Model Intercomparison Project phase 5.

COI Cone of Influence.

CPAC Central Pacific.

CVDP Climate Variability Diagnostics Package.

ECMWF European Centre for Medium-Range Weather Forecasts.

El-Niño warm phase of ENSO.

EMD Empirical Mode of Decomposition.

ENSO El-Niño Southern Oscillation.

EPAC Eastern Pacific.

ESM Earth System Model.

GCM General Circulation Model.

HighResMIP High Resolution Model Intercomparison Project.

IBTrACS International Best-Track Archive for Climate Stewardship.

IPO Interdecadal Pacific Oscillation.

ITCZ Inter-tropical Convergence Zone.

JRA25 Japanese 25-yr Reanalysis.

JRA55 Japanese 55-yr Reanalysis.

KDE Kernel Density Estimation.

La-Niña cold phase of ENSO.

MDR Main Development Region.

MERRA Modern-Era Retrospective Analysis for Research and Applications.

MERRA2 Modern-Era Retrospective Analysis for Research and Applications version 2.

MJO Madden-Julian Oscillation.

NAO North Atlantic Oscillation.

NATL North Atlantic Region.

NIND North Indian Ocean.

OEP Occurrence Exceedance Probability.

PDO Pacific Decadal Oscillation.

QBO Quasi-Biennial Oscillation.

RCM Regional Climate Model.

SP Stochastic Physics.

SPHINX Stochastic Physics High Resolution Experiments.

SST Sea Surface Temperature.

TC Tropical Cyclone.

VWS Vertical Wind Shear.

WPAC Western Pacific.

Chapter 1

Introduction

1.1 Motivation and Research Questions

Tropical Cyclones (TCs) belong to the category of weather systems which bring severe damage and destruction across many regions of the planet. It is therefore crucial to understand which environmental processes and phenomena drive their inter-annual and longer term variability so that impact related mitigation and planning information can be provided to decision makers and to those strongly affected by TCs such as insurance companies.

McCarthy et al. (2015) and Goldenberg et al. (2001) have shown that TC activity around the globe undergoes important variability through the decades. It is believed that dynamic and thermodynamic environmental conditions are the source of this variability. This Ph.D. study aims to:

1. Understand what drives the natural variability of TCs and to detect evidence of anthropogenic influence.

2. Separate and attribute the impact of natural variability and anthropogenic influence on the variability of TCs.

3. Understand the nature of natural variability under various forcing scenarios and compare this with a scenario of changing forcing.

4. Explore how decadal variability is related to known modes of variability.

The thesis is structured as follows: Chapter one provides the theoretical background on TC formation as well as a literature review. The aim of the literature review is to understand what other studies have shown regarding the decadal variability of TCs, and to also identify the gaps in current knowledge of TC variability. The chapter includes definitions and examples of climate variability as well as how these modes of variability have been found to influence the different TC basins in previous studies. Furthermore, a summary of representation of TCs in various datasets (paleo-climate studies, reanalyses, model simulations) as well as a summary of future TC projections is given. Lastly, potential drivers of TC variability are introduced.

Chapter two provides the methodology of the study. This includes the various datasets along with the tools used in order to answer the research questions.

Chapters three, four and five cover the results obtained by the analyses in terms of the drivers of TC variability under the current climate, under decadal time scales and under climate change and in future projections, respectively.

As part of this Ph.D. study, a 12-week internship was undertaken on the industrial aspects of the project. The objective was to develop a hurricane catastrophe model for assessing the risk associated with hurricane winds for Bermuda. The sensitivity of the hurricane wind risk to decadal variability of TC events was tested. Results are presented in chapter six.

Finally, results from the previous chapters as well as future work recommendations are presented in seventh and final chapter.

1.2 Conditions for TC formation - Drivers

The term tropical cyclone is used to describe a rotating low-pressure weather system originating in the tropical or sometimes sub-tropical oceanic regions of the planet. Depending on the region of origin, a TC can be called a hurricane (North Atlantic and Eastern Pacific) or a typhoon (Western Pacific and Indian Ocean) or a cyclone (Indian Ocean).

In contrast to the mid-latitude cyclone, the structure of a TCs is nearly symmetric without fronts. They have a warm centre and their typical path is from east to west. Based on their intensity, TCs can be categorised into three main classes: a tropical depression, a tropical storm and a TC. TCs in the North Atlantic, Eastern and Central Pacific Oceans

are classified using the Saffir-Simpson Wind Scale. The scale ranges from category 1 (least intense) to category 5 (most intense) and the categories are defined in table 1.1. Hurricanes of category 3 and above are occasionally referred to as major hurricanes. A tropical depression is a tropical storm with 1-minute sustained or 10-minute sustained low-level wind speeds below $17ms^{-1}$. A tropical storm has sustained wind speeds of 17-33 ms^{-1}. Hurricanes have sustained wind speeds larger than $33ms^{-1}$.

In the Western Pacific different agencies, including the China Meteorological Administration (CMA), the Hong Kong Observatory (HKO), the Japan Meteorological Agency (JMA, RSMC Tokyo) and the United States' Joint Typhoon Warning Center (U.S. JTWC), monitor systems occurring in the Western North Pacific, specifically between $100°E$ and the 180^{th} meridian. The systems are classified by the Typhoon Committee (TyC) as, shown on Table 1.2, into tropical depressions, tropical storms, severe tropical storms and typhoons. A tropical depression in the basin is a non-frontal synoptic scale system which has sustained wind speeds of less than $17ms^{-1}$. If the system intensifies and it has wind speeds between 17 and $24ms^{-1}$, it is classified as a tropical storm, whereas if the wind speeds are between 25 and $32ms^{-1}$, the system is classified as a severe tropical storm. Should a system have sustained wind speeds higher than $33ms^{-1}$, it is classified as a typhoon. This classification, however, can be split into additional categories, depending on which agency monitors the system. The classifications for each agency are summed up on Table 1.2 (WMO, 2015).

In the North Indian Ocean, the India Meteorological Department (IMD, RSMC New Delhi) monitors systems developing between $100°E$ and $45°E$. Table 1.3 shows the classification for this basin. Using an averaging period of 3-minute sustained wind speeds, a system is classified as a depression (17-27 kn), as a deep depression (28-33 kn), as a cyclonic storm (34-47 kn), as a severe cyclonic storm (48-63 kn), as a very severe cyclonic storm (64-89 kn), as an extremely severe cyclonic storm (90-119 kn) or as a super cyclonic storm (winds stronger than 120 kn).

A set of six necessary, but not sufficient, conditions for tropical-cyclone formation have been defined by numerous studies as:

1. Warm ocean waters of at least 26°C throughout sufficient depth (at least $50m$) (Briegel and Frank, 1997; Palmen, 1948).

2. Weak vertical wind shear between the surface and the upper troposphere.

Table 1.1: Saffir-Simpson Wind Scale

Category	**Central Pressure (hPa)**	**1-min Sustained Wind Speed (ms^{-1})**	**Damage**
1	≥ 980	33-42	Minimal
2	965-979	43-49	Moderate
3	945-964	50-58	Extensive
4	920-944	59-69	Extreme
5	< 920	> 69	Catastrophic

3. A warm core initial disturbance: a pre-existing near-surface disturbance with sufficient vorticity (low-level relative vorticity).

4. Relatively moist layers near the mid-troposphere ($5km$).

5. Minimum 5°N or 5°S of the equator.

6. An atmosphere which cools fast enough with height such that it is potentially unstable for moist convection (conditional instability).

As outlined in the conditions, large-scale environmental factors, such as Sea Surface Temperatures (SSTs), Vertical Wind Shear (VWS) and others, are important for TC formation as well as intensification in regions known as Main Development Regions (MDRs). These regions are conductive to TC formation, such as the conditions on SSTs and VWS. Understanding which processes dominate TC activity in the MDRs have been under investigation ever since the global climatology of TCs was studied by Gray (1968). Warm SSTs of at least 26°C act as a source of energy for TCs. The warm water, via the process of evaporation, leads to warm moist air above the surface which, by latent heat, gives energy to the system. For intensification, the air temperature at 10m above the surface must be less than the SST, otherwise the enthalpy flux is cut off, prohibiting intensification (Cione, 2012).

One of the main dynamical components of whether a TC will form or dissipate is the VWS, which is defined as the magnitude of the difference between winds at two pressure levels (usually 850hPa and 250hPa). According to Gray (1968), with the presence of

Table 1.2: TC Intensity Scale for Western North Pacific

	Sustained winds (ms^{-1})	**17-24**	**25-32**	≥ 33		
TyC	10-min	TS	STS	TY		
CMA	2-min	TS	STS	TY (33-41)	STY (44-54)	Super TY (≥ 51)
HKO	10-min	TS	STS	TY (33-41)	STY (44-54)	Super TY (≥ 51)
JRA	10-min	TS	STS	TY (33-43)	Very Strong TY (44-54)	Violent TY (≥ 54)
U.S.	1-min	TS		TY (33-66)		Super TY (≥ 67)

strong VWS, the heat and moisture are ventilated away from the core by the upper level flow. This leads to convective asymmetries (tilting), therefore preventing the development of the TC (DeMaria, 1996; Frank and Ritchie, 2001). Conversely, weak VWS has been found to be beneficial for the development and intensification of TCs.

As mentioned in the conditions for cyclone formation, an initial disturbance is required in order to organise convection. For the Atlantic basin this is often an African Easterly Wave (AEW) (Hopsch et al., 2010), while for the Indian and Pacific Oceans, it can be superclusters in the Madden-Julian Oscillation (MJO) and high-frequency equatorial waves such as an eastward mixed Rossby/gravity wave. Lastly, for the Bay of Bengal this is often a depression in the monsoon trough.

A humid environment in conjunction with the warm SSTs can benefit convection over tropical regions and TCs require a humid environment in order to form and intensify. The absence of moisture near the mid-troposphere can prohibit TC development. In addition, according to Emanuel (2008), the presence of moisture is crucial for determining the amount of time required for the formation of an initial disturbance.

In order for a TC to form and to preserve its cyclonic motion, the presence of enough planetary vorticity (i.e. the spin due to Earth's rotation) is necessary. The planetary

Table 1.3: India Meteorological Department TC Intensity Scale

Category	**3-min Sustained Winds in knots (ms^{-1})**
Depression	17-27 (~ 8-13)
Deep Depression	28-33 (~ 14-16)
Cyclonic Storm	33-47 (~ 17-24)
Severe Cyclonic Storm	48-63 (~ 24-32)
Very Severe Cyclonic Storm	64-89 (~ 33-45)
Extremely Severe Cyclonic Storm	90-119 (~ 46-60)
Super Cyclonic Storm	≥ 120 (~ 61)

vorticity (or Coriolis parameter) is given by:

$$f = 2\Omega \sin\phi \tag{1.1}$$

where Ω is the rate of Earth's rotation ($7.292 \times 10^{-5} s^{-1}$) and ϕ is the latitude. At the equator ($\phi = 0$) f becomes equal to 0, hence it is physically impossible for a TC to form on the equator. A minimum of 5°N or 5°S of the equator (corresponding to around 550km) can provide the necessary amount of vorticity for the development of a TC.

1.3 Definitions and Examples of Natural Climate Variability

Before examining the decadal variability of TCs and before assessing which factors influence this variability, it is important to define known modes of climate variability. According to the Intergovernmental Panel on Climate Change (IPCC) climate variability is defined as "variations in the mean state and other statistics (such as standard deviations, the occurrence of extremes etc.) of the climate on all spatial and temporal scales beyond that of individual weather events" (IPCC, 2018, p. 546). Natural (or internal) variability can be attributed to natural innate processes within the climate system, while anthropogenic (or external) variability is caused by changes in natural or anthropogenic forcing (IPCC, 2018).

Table 1.4: Details (data extent and source) about indices

Index	Extent	Source
QBO	1948-present	https://psl.noaa.gov/data/correlation/qbo.data
ENSO	1870-2021	https://psl.noaa.gov/gcos_wgsp/Timeseries/Nino34/
AMM	1948-present	https://psl.noaa.gov/data/timeseries/monthly/AMM/
AMO	1870 - 2021	https://climatedataguide.ucar.edu/climate-data/atlantic-multi-decadal-oscillation-amo
PDO	1900-2018	http://research.jisao.washington.edu/pdo/PDO.latest

There are several examples of internal climate variability and they are usually referred to as modes of natural variability. Some of the modes considered in this study are the MJO, the Quasi-Biennial Oscillation (QBO), the El-Niño Southern Oscillation (ENSO), the Atlantic Multi-decadal Oscillation (AMO), the Atlantic Meridional Mode (AMM) and the Pacific Decadal Oscillation (PDO). Details about the extent of index reconstructions for the different modes of variability are given on table 1.4.

The QBO is a quasi-periodic variation of the zonal wind between easterlies and westerlies in the tropical stratosphere above the equator. Strong winds in the stratosphere travel around the planet, and every approximately 14 months, these winds reverse direction. A full cycle of the QBO lasts for around 28 months, therefore making this oscillation the 2^{nd} most regular slow atmospheric variation after the seasonal cycle. A review on QBO can be found in Baldwin et al. (2001).

The MJO (Madden and Julian, 1971; Zhang, 2005) is the strongest mode of intraseasonal tropical variability with a period of 30-90 days. The MJO is characterised by large-scale coupled patterns of deep convection and atmospheric circulation and it propagates towards the east across the tropics. Klotzbach et al. (2019) found that the MJO is favoured during the boreal winter when the easterly phase of the QBO takes place, whereas when the westerly phase QBO phase occurs the MJO gets weaker. They stated that this

relationship has appeared since the beginning of the 1980s and it was suggested that the appearance of this relationship was the result of climate change.

ENSO is one of the major coupled global modes of variability. It is an interaction between the ocean and the atmosphere over the tropical Pacific, which occurs roughly every 4-5 years and generally lasts for 1-2 years (Burgers and Stephenson, 1999). It is associated with the Southern Oscillation Index (which is defined as the pressure difference between Tahiti and Darwin) (Walker, 1924) and tropical Pacific SSTs (Bjerknes, 1966). During neutral conditions, trade winds near the equator from east to west bring warm moist air and warm SSTs towards the western Pacific while keeping the eastern and central Pacific relatively cool. The warm SSTs drive deep convection releasing heat and moisture in the atmosphere, and if the atmosphere contains enough moisture, it can lead to the formation of cumulonimbus clouds and thunderstorms. Then, the air, which is no-longer moist, travels to the east where it descends over the cool eastern tropical Pacific. This process of rising air in the west and descending air in the east, along with easterly moving air at the surface and westerly air high in the atmosphere, is referred to as the Walker Circulation. During a warm phase of ENSO (El-Niño), the trade winds relax, causing the warm water to move back into the central and eastern tropical Pacific. Therefore, the thermocline gradient across the basin reduces, since the thermocline deepens in the central and eastern part of the basin. SSTs near north Australia fall below normal and the convection is moved towards the central tropical Pacific. On the other hand, a La Niña event is considered to be an extension of neutral conditions. During a cold phase of ENSO (La-Niña), the trade winds become stronger than normal since the Walker Circulation intensifies. This results in the pool of warm waters to move further into the western tropical Pacific, near Australia. SSTs in the central and eastern Pacific fall below usual temperatures leading to the thermocline moving closer to the surface, while in the west convection deepens and the Walker Circulation intensifies. The index, along with its associated SST and VWS patterns and power spectral density are shown on figure 1.1.

The AMO is a mode of multi-decadal variability in the North Atlantic Region (NATL), which manifests as variations of SSTs on decedal time scales in the basin between the Equator and Greenland (Schlesinger and Ramankutty, 1994). The oscillation is described by cold and warm phases that can last for periods of 20-40 years. McCarthy et al. (2015) stated that a noticeable characteristic of the Atlantic Ocean and the climate of influenced

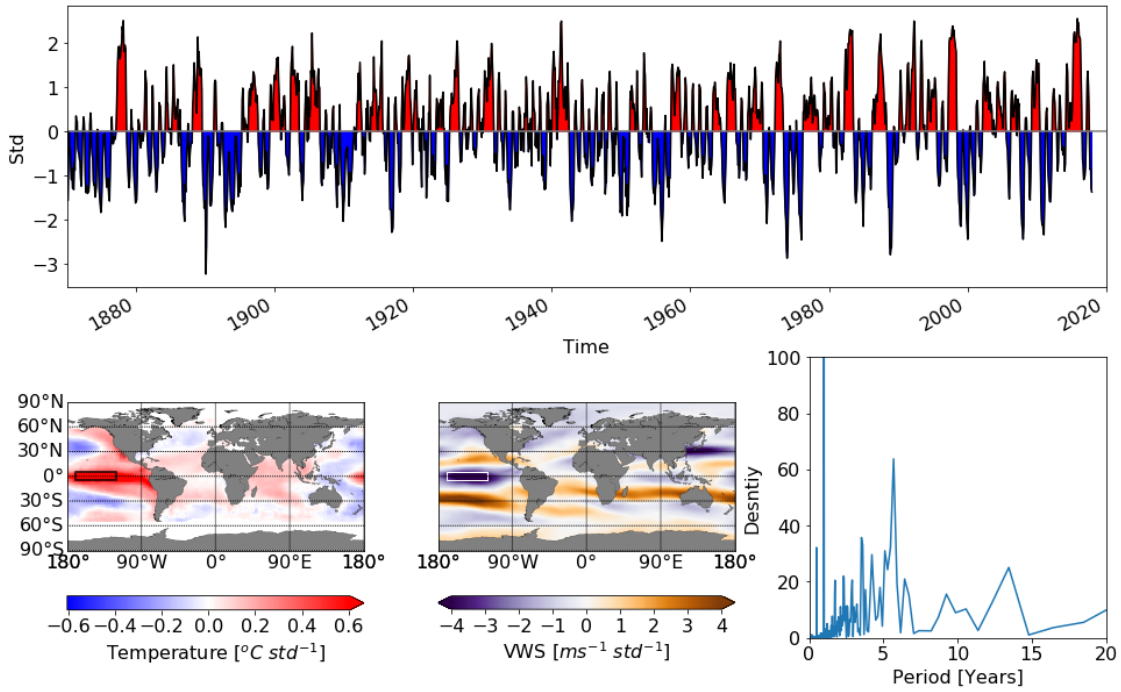

Figure 1.1: Upper: ENSO index for the 1870-2017 period; Lower left: Associated SST pattern, obtained by regressing SST anomalies onto the index. The SST anomalies were computed by subtracting the monthly climatology using the HadISST dataset (Rayner et al., 2003); Lower centre: Associated VWS pattern, obtained by regressing the 1980-2013 ERA5 VWS field onto the corresponding period of the index; Lower right: Power Spectral Density of the ENSO index.

areas is its decadal variability, which is evident in SSTs in the AMO. The index, along with its associated SST and VWS patterns and power spectral density are shown on figure 1.2. The AMO is connected to the Atlantic Meridional Overturning Circulation (AMOC) in the following sense: A further northward transport of warm SSTs in the equatorial NATL occurs when the AMOC is stronger, while the opposite happens when the AMOC is weaker. Ting et al. (2011) used Coupled Model Intercomparison Project phase 3 (CMIP3) simulations for the 20^{th}, 21^{th} and pre-industrial periods with 23 IPCC models to confirm the strong relationship between the Sahel rainfall and the Atlantic multi-decadal variability. Studies such as Mann and Emanuel (2006) have questioned whether the observed multi-decadal variability of Atlantic SSTs is due to natural causes. Instead, they argued that the variability can perhaps be attributed to anthropogenic and volcanic aerosol forcing. Terray (2012) suggested that anthropogenic forcing mainly drives the resent quick temperature increase in the tropical and subtropical Atlantic basin.

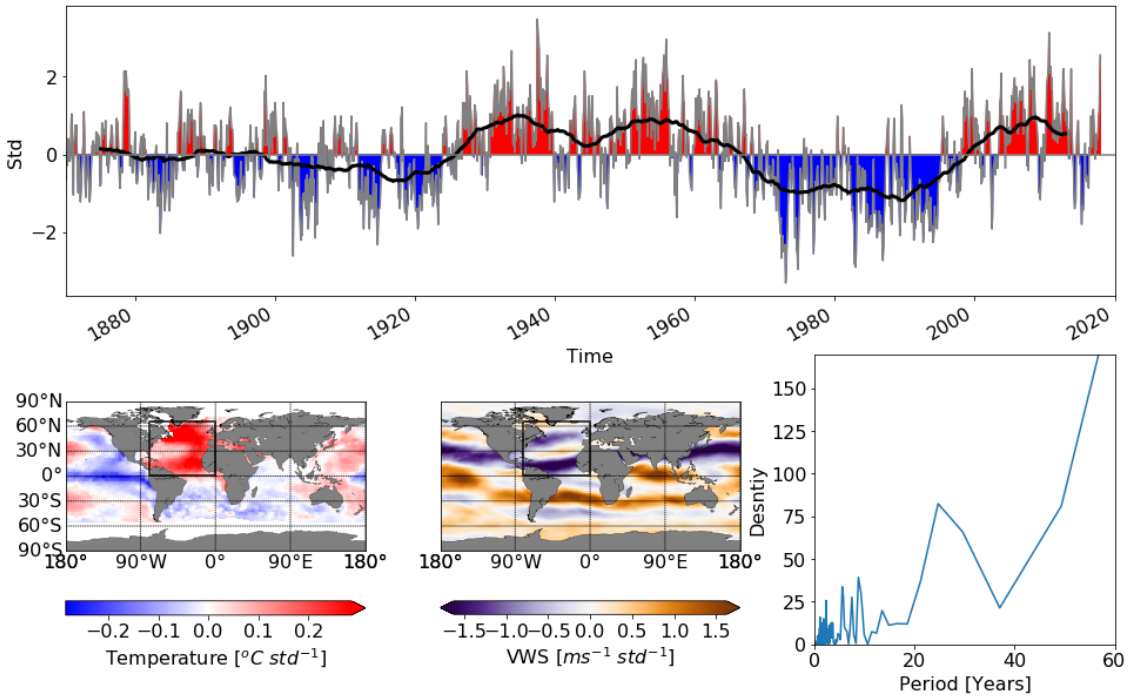

Figure 1.2: Upper: AMO index for the 1870-2017 period; Lower left: Associated SST pattern, obtained by regressing SST anomalies onto the index. The SST anomalies were computed by subtracting the monthly climatology using the HadISST dataset (Rayner et al., 2003); Lower centre: Associated VWS pattern, obtained by regressing the 1980-2013 ERA5 VWS field onto the corresponding period of the index; Lower right: Power Spectral Density of the AMO index.

The leading mode of the ocean-atmosphere variability in the tropical region of the Atlantic is called the Atlantic dipole mode or AMM. The index, along with its associated SST and VWS patterns and power spectral density are shown on figure 1.3. According to Chiang and Vimont (2004) it is associated with meridional shifts of the Inter-tropical Convergence Zone (ITCZ), SSTs and winds. On decadal time scales the AMM has a periodicity of around 11-13 years (Veiga et al., 2020). Even though their studies are focused on SST patterns rather than the AMM, Chiang et al. (2002) and Czaja et al. (2002) have shown that changes in the North Atlantic Oscillation (NAO) and ENSO can excite the AMM. Contributing to this, Vimont and Kossin (2007) found that on decadal time scales the AMM can be excited by the AMO.

According to Mantua and Hare (2002) the PDO is a pattern of Pacific climate variability on decadal time scales and it is considered to be the dominant mode of decadal variability in the Pacific region. It is connected to SSTs north of 20°N, and impacts the North Pacific

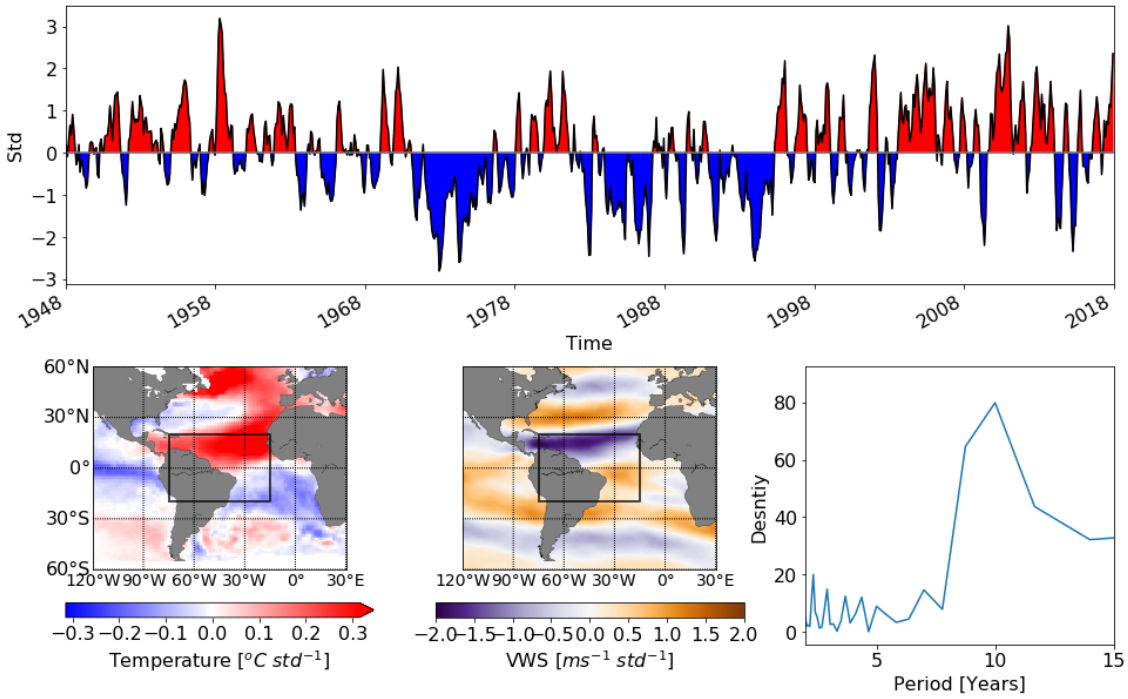

Figure 1.3: Upper: AMM index for the 1948-2017 period; Lower left: Associated SST pattern, obtained by regressing SST anomalies onto the index. The SST anomalies were computed by subtracting the monthly climatology using the HadISST dataset (Rayner et al., 2003); Lower centre: Associated VWS pattern, obtained by regressing the 1980-2013 ERA5 VWS field onto the corresponding period of the index; Lower right: Power Spectral Density of the AMM index.

and North America with a period of approximately 20-30 years. The index, along with its associated SST and VWS patterns and power spectral density are shown on figure 1.4. According to Mantua et al. (1997) the phases of PDO influence ENSO and affect the SSTs in the Pacific region. Henley (2017) used observations and paleo-climate reconstructions in order to review the Pacific decadal climate variability. They stated that the Pacific decadal variability is a result of the constant interactions between tropics and extra-tropics throughout the decades.

1.4 Modes of Variability Affecting TCs

A number of studies have been conducted in an effort to assess what affects the variability of TCs. A study by Knutson et al. (2010) highlighted the uncertainty on whether changes in past TC activity can be attributed only on natural causes or whether they have been

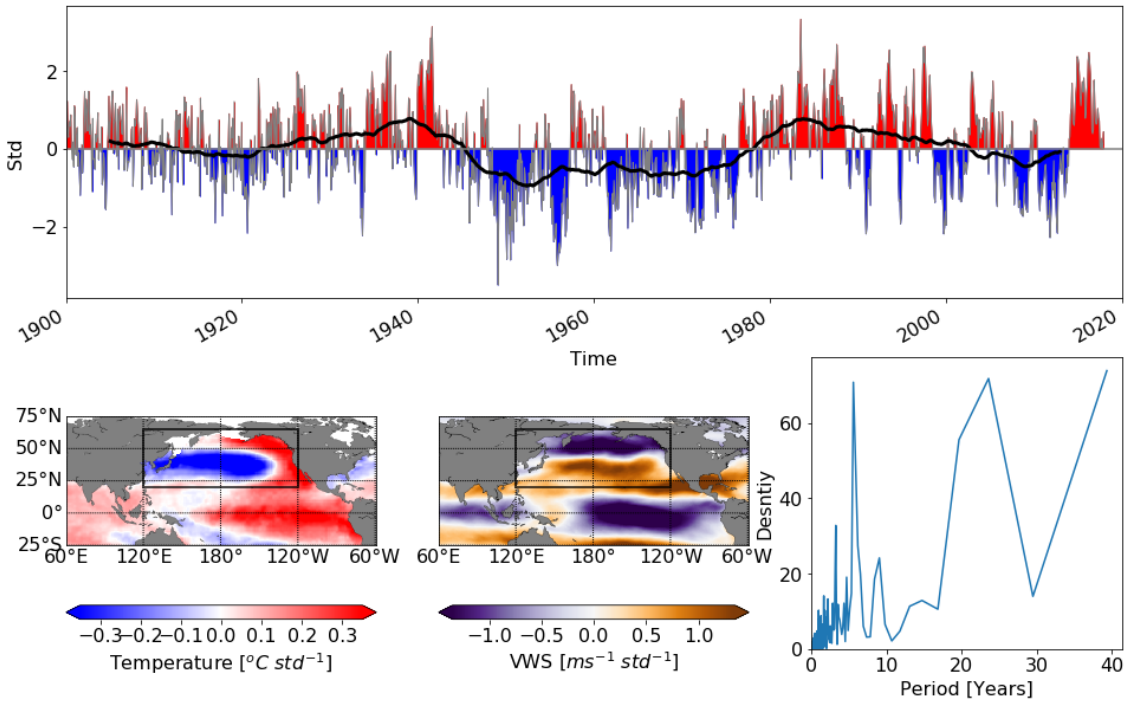

Figure 1.4: Upper: PDO index for the 1900-2017 period; Lower left: Associated SST pattern, obtained by regressing SST anomalies onto the index. The SST anomalies were computed by subtracting the monthly climatology using the HadISST dataset (Rayner et al., 2003); Lower centre: Associated VWS pattern, obtained by regressing the 1980-2013 ERA5 VWS field onto the corresponding period of the index; Lower right: Power Spectral Density of the PDO index.

anthropogenically influenced.

According to IPCC (2019), since the 5^{th} IPCC Assessment Report and Knutson et al. (2010), more evidence of historical variability on TC activity over the past millennia is provided by paleoclimatic surveys that have been conducted. Studies by Toomey et al. (2013), Denommee et al. (2014) and Denniston et al. (2015) showed variations in patterns of TC activity across different basins. These variations seem to be connected to modes of climate variability such as ENSO and NAO as well as to variations in atmospheric dynamics due to changes in sun precession.

While achieving understanding of each one of these modes of variability and their individual influence on TC activity is important, one should also take into account the possible interactions between the modes. ENSO has been perhaps the only mode of variability whose interactions with each of the remaining modes have been researched to a sufficient degree. Only a few studies have been conducted that fully examine and ascertain

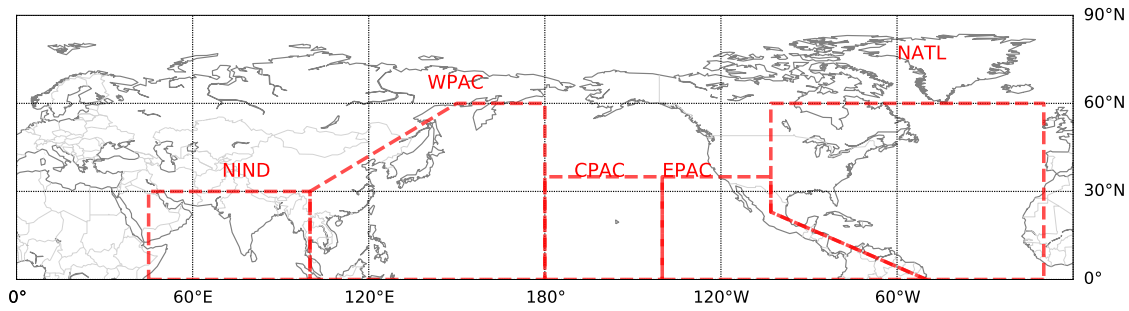

Figure 1.5: Tropical cyclone basins used in this study.

the dynamics behind the interactions between different modes of variability. Even fewer studies have taken these interactions into consideration when examining influences on TC activity either regionally or globally. These interactions must be taken into account when investigating possible influences on TC activity. And even though the exact dynamics behind the possible interactions are outside the scope of this study, an attempt will be made to take them into consideration for the physical interpretation of results. The present sub-chapter serves as a summary of the studies whose aims have been to examine how TCs are influenced by modes of variability. The review of the literature will be separated according to each TC basin. The basins are shown on figure 1.5.

1.4.1 Global Activity

The global interannual variability of TCs for the period 1985-2003 was examined by Frank and Young (2007). Their belief of global TC counts being less variable than TC counts in each individual basin was proven wrong. Variability in global number of TCs was not distinguishable from the variability that was expected in each individual basin. They also found that large-scale modes of interannual variability like ENSO and NAO significantly affected global TC variability and particularly major TCs rather than weaker storms.

1.4.2 North Atlantic

The North Atlantic basin is considered to be the best-documented basin when it comes to TC activity. Maloney (2000) found that during the active phase of the MJO the number of TCs that form in the Gulf of Mexico and the western Caribbean Sea is four times the number of storms that form during the suppressed phase. In addition, during the active phase of the MJO over the Eastern Pacific (EPAC), the location of cyclogenesis in the

NATL is mitigated towards the north of the Gulf of Mexico.

A few studies have found a relationship between the Sahel rainfall and TCs in the NATL. The Sahel rainfall has been found to be strongly connected to both long-term changes in the Saharan Air Layer (SAL) and the VWS in the MDR. A dry SAL at lower latitudes and an increase of the VWS in the MDR are produced due to a shift of the African Easterly Jet and the African Eastern Waves towards the east caused by a drying of the Sahel region (Wu and Tao, 2011). Goldenberg et al. (2001) discovered that when there is increased rainfall in the Sahel, there is a reduction of up to $7ms^{-1}$ in the VWS. Furthermore, Vecchi and Soden (2007) found that TC activity in the NATL region can be influenced by the drying of the Sahel through an increase in temperature anomalies in the upper atmosphere.

Gray (1984) was the first to discover a relationship between the QBO and TC activity in the Atlantic. They found an increase in TC activity when the QBO was either in or towards its westerly phase. A statistically significant relationship between Atlantic TC activity and the QBO for the period between the 1950s and the 1980s was discovered by Shapiro (1989). Camargo and Sobel (2010) attempted to explore this relationship more recently and they detected that it has not been present during later years, however, they were unable to explain why this was the case.

It is well known amongst the scientific community that ENSO influences TC activity in the NATL region. ENSO events cause changes in the Walker Circulation therefore reducing or enhancing wind shear in the MDR and Caribbean Sea which can then influence TCs (Goldenberg and Shapiro, 1996; Knaff, 1997; Madl, 2000). Lander and Guard (1998) stated that more TCs are produced during La-Niña than El-Niño years, while at the same time they are more intense during prolonged La-Niña events.

When it comes to local modes of variability, Camargo et al. (2010) found an increase in TC activity and east- and equator-ward shift in TC genesis during the positive phase of the AMM. Furthermore, Klotzbach and Gray (2008) have shown that during the warm phase of the AMO more tropical storms can become strong hurricanes compared to the respective proportion during the cold phase of the AMO.

Dunstone et al. (2013) and Booth et al. (2012) studied the variations in TC activity over the North Atlantic basin through the 20th century and they attributed the variability partially to variations in atmospheric aerosol forcings. On the other hand, various studies

(Vecchi and Delworth, 2017; Weinkle et al., 2012; Yan et al., 2017; Zhang et al., 2013) have highlighted the uncertainty of attributing the relative importance of natural and external variability to TC variability.

1.4.3 Eastern Pacific

Zhao and Chu (2006) found that the periods from 1972 to 1981 and 1999 to 2003 were inactive in regards to TC activity for the EPAC. The period 1982 to 1998 however was active. A strong relationship was detected by Frank and Young (2007) between ENSO and TC counts. Camargo et al. (2008) found a migrarion towards the west in locations of cyclogenesis that resulted in an increased number of TCs spreading into the region.

1.4.4 Central Pacific

Inactive periods for the region Central Pacific (CPAC) were during 1966-1981 and 1995-2000, whereas there was one active period (1982-1994) as found by Chu and Zhao (2004). During the active period favourable conditions for TC development included amongst others warmer SSTs, lower mean sea level pressure and reduced wind shear. A few studies (Camargo et al., 2007; Chu and Wang, 1997; Clark and Chu, 2002) determined that due to reduced wind shear and low-level vorticity, more TCs formed during El-Niño years.

1.4.5 Western Pacific

Due to the vast area covered by the Pacific ocean, it is expected that regions in the Pacific are more directly influenced by local modes of variability. Indeed, there have been various studies regarding the relationship between ENSO and TCs in the Western Pacific (WPAC). A reduction of TCs during the summer after an El-Niño event was found by Chan (2000), while Wang and Chan (2002) discovered a southeast mitigation of cyclogenesis locations during El-Niño years, in contrast to a northwest mitigation during La-Niña years. Chan (2007) found that during El-Niño years typhoons have a longer lifetime and are more intense due to the southeast displacement of warm waters. In a subsequent study, Chan (2008) showed that the counts of strong typhoons exhibit a multi-decadal variability, which they have attributed to both ENSO and the PDO.

According to Camargo et al. (2007) TCs in the WPAC region are controlled by the

MJO and favourable conditions for TC development occur during its active phase. The conditions include increased mid-level humidity and low-level vorticity. They also found that the MJO affects the track densities in the region. Furthermore, the influence of the QBO on TC tracks in the region was examined by Ho et al. (2009). Their study concluded that the total number of TCs in the region remained unaffected by the two changing phases of the QBO. However, during the westerly phase the amount of TCs moving close to the East China Sea is larger, while the amount of TCs close to Japan is larger during the easterly phase. The authors associated the reasoning behind this change with the background flow variations related to QBO.

The summary by IPCC (2019) on TC detection and attribution stated that there is *low to medium confidence* that the unusual observed shift of the latitude of maximum TC intensity towards the pole in the western North Pacific shows an evident change in climate. However, there is *low confidence* that the detected migration has a distinguishable contribution from external forcing, which is thought to be causing a poleward spread of the tropical circulation with a warmer climate. Even though there is *low confidence* due to limited evidence, some studies on observed long-term changes in TC activity suggest developing anthropogenic signals.

1.4.6 North Indian Ocean

During monsoon seasons, TCs in the North Indian Ocean (NIND) region tend to form. Singh et al. (2000) stated that TCs are favoured by the monsoon trough over the ocean, even though the increased wind shear can suppress the TC activity. They also found that fewer TCs develop between May and November in the Bay of Bengal during El-Niño years. Lastly, according to Frank and Young (2007) during the positive phase of the NAO there are fewer TCs in this region. Recent studies (Evan and Camargo, 2011; Evan et al., 2011; Muni Krishna, 2009; Rajeevan et al., 2013) have highlighted that TC activity in the Arabian Sea is separated mainly in pre-monsoon and post-monsoon seasons. However, there are less TCs in the Arabian Sea compared to the Bay of Bengal (Rajeevan et al., 2013). Evan et al. (2011) reported that during the 1979-2010 period increases in anthropogenic black carbon and sulfate emissions resulted in more intense TCs in the Arabian Sea during pre-monsoon seasons (May-June). They proposed that the anthropogenic aerosols resulted in a reduction of VWS in the basin via anomalous anthropogenic circulation over South

Asia, condition favourable for TC intensification.

1.5 TCs in Palaeoclimate Studies, Observations and Reanalyses

Long-term records are important for assessing how TCs have changed over multiple decades. Scientists have tried to find other means apart from direct observations of TCs (discussed below) for creating long records in order to assess this variability (Oliva et al., 2018). Therefore, the field of paleotempestology, meaning the study of past TC activity by using geological proxies and other historical records, was born. Different studies have used different proxies which include extreme precipitation events (Frappier et al., 2007), tree rings (Miller et al., 2006), sediment grain size (Liu and Fearn, 1993), coral (Lough, 2007; Nyberg et al., 2007) and using evidence of intense terrestrial floods (Besonen et al., 2008; Noren et al., 2002). For the Western North Atlantic region in particular Oliva et al. (2018) created a new database of paleotempestology records which is publicly available by NOAA. The database was created using 61 studies published during the 1993 to 2018 period. A paleotempestology study by Haig et al. (2014), for the Australian region, has shown that TC occurrence in north-east Queensland was higher during the past 1500 years compared to the present. For the Atlantic basin, Brandon et al. (2013) (another paleotempestology study) found that between ~1700 and ~600 year before present (B.P.) there was increased strong TC frequency, while from ~2500 to ~1700 and from ~600 years BP to the present there was decreased frequency of intense TCs. However, as Walsh et al. (2016) concluded, there is a need for paleotempestology records to be extended in time and to other basins in order to be used in combination with proxy-based and modelling studies of past climates for determining the reasons for TC variability on centennial and millennial time-scales. Doing so, could perhaps help in developing a more robust climate theory of TC formation.

Observations of TCs act as the primary source of knowledge of the variability of TCs. They come from ship reports, aircraft reconnaissance, weather station data and satellites. The classification of TCs, according to Velden et al. (2006), is mainly based on interpreting satellite observations, since aircraft reconnaissance are limited to certain basins, for example the North Atlantic. Walsh et al. (2016) highlighted the need for aircraft

reconnaissance to be extended to other basins. Various agencies around the world such as the Regional Specialized Meteorological Centers (RSMCs), the TC Warning Centers (TCWCs) as well as other agencies like the Hong Kong Observatory contribute information regarding the location and intensity of TCs as their postseason analyses of TC tracks which are collected into the International Best-Track Archive for Climate Stewardship (IBTrACS) (Knapp et al., 2010).

The use of satellites since the early 1970s has lead to better observations (Chan and Holland, 1989). A notable example is in the case of the North Indian Ocean, where before the satellite era, monsoons were reported in the TC observations. Webster et al. (2005) examined the observed global TC activity for the period of 1970-2004. They found a big increase in the ratio of hurricanes that achieved intensities of categories 4 and 5 (according to the Saffir-Simpson Hurricane Wind Scale). The biggest increase was found in the North Pacific, Indian and South-west Pacific, while the smallest increase was detected in the North Atlantic region.

However, this difference in the increases in the ratio of hurricanes that reached major hurricane intensities is probably due to observational biases arising from the fact that the North Atlantic has been the best-documented basin. In addition to being biased, the observational records are relatively short and have undergone significant changes in operational procedures since the early 1900s, something that introduces uncertainties in the records as well as in the variability of TCs in terms of counts and the Accumulated Cyclone Energy (ACE) (Landsea, 2007; Landsea et al., 1999, 2010). Even though the record for the North Atlantic is considered the longest and most comprehensive record, it suffers from homogeneity issues (Landsea, 2007). For the Western Pacific, the record is even more problematic since different agencies keep different records (Ren et al., 2011). Hodges et al. (2017) emphasize that due to these large uncertainties, there should be caution in using observations when studying TCs and climate. Therefore, they quoted Gyakum (2011) in recommending a universal methodology for TC classification.

In an effort to reduce uncertainties and biases in the observations, reanalysis can be used for identification and tracking of TCs. Reanalysis are based on a combination of observations with a short forecast from a General Circulation Model (GCM). Gridded datasets, constrained by the observations, are produced.

A few studies have looked into how well TCs are represented in reanalysis datasets.

Bengtsson et al. (2007) used the European Centre for Medium-Range Weather Forecasts (European Centre for Medium-Range Weather Forecasts (ECMWF)) 40-yr Reanalysis (ERA40) (Uppala et al., 2005) and the Japanese 25-yr Reanalysis (Japanese 25-yr Reanalysis (JRA25)) (Onogi et al., 2007). They found that the intensities of the strongest storms were underestimated when it came to maximum winds.

Hodges et al. (2017) used an objective, feature-tracking algorithm (similar to Bengtsson et al. (2007) and Strachan et al. (2013)) to identify and track TCs in six different, recent atmospheric reanaysis datasets: ECMWF ERA-Interim (ERAI; Dee et al. (2011)); JRA25 (Onogi et al., 2007) and Japanese 55-yr Reanalysis (JRA55) Kobayashi et al. (2015); the National Aeronautics and Space Administration (NASA) Modern-Era Retrospective Analysis for Research and Applications (Modern-Era Retrospective Analysis for Research and Applications (MERRA); Rienecker et al. (2011)) and the following version Modern-Era Retrospective Analysis for Research and Applications version 2 (MERRA2) (Bosilovich et al., 2015; Molod et al., 2015); and the National Centers for Environmental Prediction Climate Forecast System Reanalysis (NCEP; Saha et al. (2010)). When they compared their results to the TCs in IBTrACS, they found that almost all systems in IBTrACS for the 1979-2012 period can be found in all the reanalysis datasets they examined. However, as in the case of Bengtsson et al. (2007), there was a clear under-representation of TC intensities in the reanalyses compared to the observations. In addition, it was shown that the identification of weaker storms (e.g. tropical depressions, subtropical cyclones and monsoon depressions) had the largest uncertainties. This is due to the aforementioned uncertainties in the observations since not all agencies include weak storms in the best-track data. Hodges et al. (2017) also commented on the improvement of TC representation in recent, higher-resolution reanalysis datasets by mentioning that MERRA2 performed better than MERRA and that it is comparable to NCEP and JRA55.

Murakami (2014) also conducted a study on TC representation in six of the above-mentioned reanalysis datasets. Their key finding was that the reanalysis with the highest resolution was not always the best in simulating TC climatology. From their work it was concluded that simulating TCs in reanalyses strongly depends on model configuration (Schenkel and Hart, 2012).

When it comes to the contrast between the northern and southern hemispheres (NH, SH) and how TCs are represented in observations and reanalyses, what is particularly

obvious are the differences between how well reanalysis datasets represented TCs in the two hemispheres. Most modern reanalyses manage to represent the counts of TCs in the NH reasonably well. However, compared to IBTrACS, all of them overestimate the counts in the SH. Hodges et al. (2017) stated that this can be attributed to possible biases in the observations and to how identification is carried out in the study since no re-tuning is performed specific to the SH as is the case in other methods. TC basins like the South Pacific and South Atlantic are not densely inhabited, therefore according to Kucas et al. (2014), it is possible that less attention is given in detecting TCs in those basins, unless severe systems are likely to make landfall. Furthermore, tropical depressions and sub-tropical storms are not included in the best-track data in these SH basins (Hodges et al., 2017).

Even though reanalyses are very useful, one should keep in mind that they can vary in how well TCs are represented. These problems can occur due to changes in the observational system which can result in artificial trends as well as due to the use of different GCMs with different configurations. Lastly, even though the reanalyses offer some benefits over direct observations, they cover periods that are generally shorter than observational data, therefore, they are not ideal for examining decadal variability.

1.6 TCs in General Circulation Models (GCMs)

As mentioned before, observational and reanalysis records are quite short and fairly inconsistent for the study of TC variability. One of the most important aims of this study is to use climate simulations for examining decadal variability of TC activity since they can provide longer, more consistent records. Here the types of models are discussed with some of their most important components, that have been used to explore TC activity including the skill in simulating TCs as well as the relationship between TCs and climate change.

1.6.1 Types of GCMs

General Circulation Models (GCMs) are extremely useful for studying the interaction of the different processes that govern our atmosphere and oceans. The climate system in its entirety involves interactions between processes on various temporal and spatial scales.

These processes are typically formulated in models using non-linear differential equations which are solved on a 3-D grid by temporal and spatial discretisation. Some of these processes, however, occur on finer spatial scales than GCMs are able to model. In order to represent these processes as accurately as possible, their properties in a grid-box must be parameterized and is one of the main sources of uncertainty in climate model simulations.

Various types and configurations of GCMs have been used for simulating TC activity. Atmosphere - only GCMs (AGCMs) use SSTs and sea ice distributions obtained from observations or from low-resolution coupled Atmosphere-Ocean GCMs (AOGCMs) as boundary conditions. An ocean-only GCM is designed to realistically simulate the state of the ocean and is run by having surface winds, surface air temperatures and other processes prescribed. The coupling of an atmosphere model and an ocean model results in an AOGCM, allowing the components of each model to interact with one another. The use of the coupling means that some of the observational constraints that the AGCMs have, are removed. A notable example is that SSTs are no longer prescribed and they are instead determined by how the atmospheric and oceanic GCMs adjust to the insolation and other parts of the model.

Another type of a GCM are the Earth System Models (ESMs) which, compared to AGCMs and AOGCMs, also include physical, chemical and biological processes. ESMs have the atmospheric and oceanic components of GCMs with added modeled carbon cycle and other aspects of atmospheric chemistry. These models, even though they can increase biases and uncertainties, they can provide important understanding into the variability of the climate and the impact of human activities.

Lastly, Regional Climate Models (RCMs) cover only a specific geographic area, as their name indicates. Therefore, they can be run at much higher resolutions compared to GCMs and can model finer-scale-processes, such as those that control TC intensity and structure. RCMs are useful since their domain can be a whole tropical region or the whole tropics. Nevertheless, RCMs have a number of handicaps. One is the fact that they require boundary forcing data to drive the RCM, often taken from reanalyses or low resolution GCMs. Being dependent on biases in the driving data restricts the use of the model. But most importantly, RCMs are unable to model effectively any interaction outside the domain, such as the ENSO-teleconnection relationship with TC activity in the Atlantic.

1.6.2 Skill in Simulating TCs

The use of GCMs is constrained by computational limitations. Apart from the type of model (AGCM or AOGCM), these include horizontal resolution, type of domain, length of experiment, the existence and number of ensemble members and the complexity of the simulation (i.e. forcing, inclusion of greenhouse gas emissions).

Perhaps the most important aspect of a GCM regarding simulated TC activity is the horizontal resolution. A range of studies, using both AGCMs and AOGCMs, have highlighted the impact of horizontal resolution on effectively simulating TC activity around the globe. With an hierarchy of Hadley Center AGCMs of various resolutions, Strachan et al. (2013) showed that capturing the location of TCs was achieved at resolutions of 135km or higher. They, along with Roberts et al. (2015) (who used an ensemble of AGCM simulations), concluded that a resolution of 60km is sufficient for the simulation of TC variability on interannual time-scales, but inadequate for realistic intensity representation. Studies like Manganello et al. (2012) and Manganello et al. (2014) (using the ECMWF Integrated Forecast System), Camargo (2013) (using 14 Coupled Model Intercomparison Project phase 5 (CMIP5) models), Roberts et al. (2015) (using the Met Office Unified Model Global Atmosphere 3 configuration), Yamada et al. (2017) (using a High-Resolution Global Non-hydrostatic Model), Roberts et al. (2020a) (using the High Resolution Model Intercomparison Project (HighResMIP)-PRIMAVERA multimodel ensemble; Haarsma et al. (2016)) and Vidale et al. (2021) (using EC-Earth Climate Stochastic Physics High Resolution Experimentss (SPHINXs) and HadGEM3-GC3.1) highlighted the need for GCMs to simulate TC activity using 10km grid-spacing, since significant improvement in the intensity and structure of the most intense TCs has been found to be associated with simulations of such resolution. These models, however, still have limitations due to parameterized processes.

Another key aspect of a GCM shown to influence the simulation of TCs are the dynamics - the equations that describe the state of atmospheric and oceanic decomposition - as well as the physics package. According to Vidale et al. (2021), long-established schemes have depended upon the theory that the equations of the unresolved processes are independent from the dynamics of the flow. Stochastic Physics (SP) parameterization schemes aim to account for the uncertainty in parameterized processes. This can have the effect of giving an apparent increase in resolution at lower computational cost. The use of

such schemes is becoming very common in operational weather and seasonal forecasts as stated by various studies (Leutbecher et al., 2017; MacLachlan et al., 2015; Palmer et al., 2009; Stockdale et al., 2018; Walters et al., 2019). With regard to TCs, approaching the unresolved processes using SP schemes can potentially complement advances in enhanced resolution in better TC representation in climate studies. Indeed, some of the models used by Roberts et al. (2020a) (namely HadGEM3-GC3.1 and ECMWF-IFS) contained such schemes, but the impact of SP on TC activity was outside the scope of the study. Vidale et al. (2021) assessed the impact of SP schemes on simulated TC activity using EC - Earth simulations from the Climate - SPHINXs project and compared results to simulations by HadGEM3-GC3.1. Apart from confirming the impact of mimicking an increase in resolution, they concluded that SP leads to further enhancement of TC frequency. Nevertheless, the impact of such schemes on the decadal variability of TCs has yet to be explored.

1.6.3 TCs and Climate Change

Various studies have investigated the relationship between TCs and climate change using AGCMs or AOGCMs. Dunstone et al. (2013) used HadGEM2-ES, a coupled ESM, to examine the relationship between hurricanes and anthropogenic forcing. Their results showed that the multi-decadal variability of hurricanes was mainly driven by anthropogenic aerosols throughout the 20^{th} century.

Holland and Bruyère (2014) concluded that an increase has been observed since 1975 in the percentage of storms reaching category 4 and 5 intensities of around $25-30\%$ per 1 degree Celsius of anthropogenic global warming on regional and global scales. However, a decrease in weaker TCs has also been observed. It is worth mentioning the abovementioned increase appears to be in response to warming oceans.

Bhatia et al. (2018) used HiFLOR to assess the projected response of TC intensity and intensification from climate change. They found that HiFLOR is one of the first global coupled models to also predict major hurricanes as well as to simulate intensification distributions. They also found that throughout the 21^{th} century the values for counts, intensity and intensification rates are increasing, even though caution is needed since their projection have important uncertainties.

A source of uncertainty in regards to TCs in climate models arises from the fact that if different methods for TC detection are used in climate models, then different results

can be gathered from model sensitivity tests (Walsh et al., 2016). Therefore, Walsh et al. (2016) proposed that the scientific community perhaps converges on a universal method for detecting TCs in climate models as well as on using coupled models that are capable of simulating more realistic TCs.

1.7 TCs in the Future

Several studies (Knutson et al., 2015; Manganello et al., 2014; Murakami et al., 2015; Roberts et al., 2015; Wehner et al., 2015; Yamada et al., 2017) support the 5^{th} IPCC Assessment Report that the most intense TCs get more intense while the overall frequency of TCs decreases. Studies by Emanuel (2013), using a dynamical downscaling technique with particular assumptions, and Bhatia et al. (2018) differed from other TC studies since they predict an increase in the global TC frequency. Christensen et al. (2013) projected that the frequency of TC activity globally will probably decrease or remain stable. At the same time, the average global TC maximum wind-speed and precipitation amount is expected to increase, even though there is not much confidence in the prediction of frequency and intensity for particular regions. Studies by Kim et al. (2014) and Bhatia et al. (2018) found that coupled atmosphere models continue to strongly predict increasing TC intensities in a warmer climate.

Even though various studies (Kim and Cai, 2014; Knutson et al., 2015; Li et al., 2010; Manganello et al., 2014; Murakami et al., 2015; Nakamura et al., 2017; Park et al., 2017; Roberts et al., 2015; Sugi et al., 2017; Wehner et al., 2015; Yamada et al., 2017; Yoshida et al., 2017; Zhang et al., 2017) have examined how TC tracks might change under future climate warming scenarios, there is no clear agreement on projected changes. However, either an eastward or a poleward spread of TC development over the North Pacific basin has been found in several of the aforementioned studies.

Studies by Kim et al. (2014), Knutson et al. (2015) and Yamada et al. (2017) found that in future climate warming scenarios, the size of TC storms is projected to change up to ± 10% between different basins.

According to IPCC (2019) in the majority of the literature, conclusions about TC event attribution are generally not supported from a confident detection of a long-term trend in TC activity that is attributed to climate change. Therefore, confidence in projection

as well as event attributions is limited due to the lack of confidence in detecting climate change in most TC metrics. It is stated that:

1. There is *medium confidence* in the increase of the percentage of TCs that achieve cat 4 and cat 5 intensities.

2. With an assumption of a 2-degree-rise in global temperatures, there is *medium confidence* in 1-10% increase of the average TC intensity.

3. There is *medium confidence* that the mean amount of TC precipitation per storm will see an increase by at least 7% per 1-degree Celsius warming on SSTs due to increased water vapour in the atmosphere.

4. There is *low agreement and medium evidence* in global TC frequency changes even though the majority of modelling studies predict a decrease in global TC frequency.

5. There is *very high confidence* that higher storm surge levels from TCs that occur will be caused by a rise in sea levels, with the assumption that all other factors remain stable.

When it comes to modes of variability influencing future TC activity, Bell et al. (2014) concluded that ENSO and other modes of natural variability will dominate variability of TC activity in the future, therefore understanding the global ENSO-TC teleconnection using GCMs is important. The authors stated that the role of ocean coupling on the simulation of the ENSO-TC connection needs to be further researched.

Chapter 2

Data and Methods

2.1 Datasets

For the purposes of this study three different kinds of datasets are used; best-track data, data from seven recent global reanalyses, and multiple model simulations.

2.1.1 Best-track Dataset (Observations)

The tropical warning centres produce the best-track data as a post-season analysis of the tropical cyclone tracks from all available data. That includes observations from ships, in-situ, satellites and air-craft reconnaissance. Air-crafts are fitted with multiple instruments and fly above and through systems, weather radars are used for locating systems within $320km$ from the station and satellites are used for TC tracking. The most valuable (based on availability) tool for operational measurement of a TC's maximum intensity is the Dvorak technique (Dvorak, 1973, 1975, 1984, 1995). The technique includes locating the centre of the system, determining a pattern and making a measurement from satellites (visible or infrared), assigning an intensity number and then estimating the current intensity (CI) according to specific rules by the technique, which is then translated into a maximum wind speed (Dvorak, 1984). The technique has been developed further in recent years in order to take advantage of the improved satellite measurements (Olander and Velden, 2007; Velden et al., 2006). Similar CIs have been developed, used and modified by national agencies in order to account for the use of various wind-averaging periods and relationships between pressure and wind. Zehr et al. (2010) showed that the technique has been rather stable regarding changes to satellite sensor resolution, while it can also be reproducible. A few

studies (see Knaff et al., 2010) have detected biases and intensity errors, which have been used for calibrating intensity estimates from the technique for TC forecasts and post-season best-track analysis.

The best-track data are combined into the International Best Track Archive for Climate Stewardship (IBTrACS) dataset (Knapp et al., 2010). The data are taken from different agencies such as the Regional Specialized Meteorological Centers (RSMCs), the Tropical Cyclone Warning Centers (TCWCs) as well as other national agencies. The IBTrACS version 4 dataset, which includes data taken from all agencies, is used for this study. Full details can be found in Knapp et al. (2018). Data are available since the 1840s until the present. The agencies provide information about the best estimated position of each storm in terms of longitude and latitude in addition to reporting wind speed and mean sea level pressure (MSLP) values. The IBTrACS data are provided at 6-hour intervals. The different agencies use different wind-averaging periods and the values are reported in knots. However, the data used in this study have the wind speed values converted in 1-min sustained winds at 10-m height in meters per second. Details about the conversions can be found in Harper et al. (2010). Such conversions include different factors, depending on whether a TC is considered to be above sea, off-land or in-land, therefore introducing uncertainties about their accuracy.

Even though the development of IBTrACS has been a crucial step towards a more homogeneous dataset for the whole globe, the dataset suffers from limitations. Ironically the key limitation is global inhomogeneity (Landsea, 2007) and changes or differences in global observational techniques (Landsea, 2006). The inhomogeneity issue rises from the fact that the national agencies monitor TC activity in their region of interest and as a result regions in the CPAC or large southern-hemisphere areas remain completely or largely unobserved, unless there is development of an intense system that can potentially make landfall (Kucas et al., 2014). Furthermore, the IBTrACS dataset is formed by data gathered by the agencies using different procedures (e.g. different averaging periods) or by changing observational techniques throughout the record (Schreck et al., 2014). Lastly, for the Pacific basin, different agencies keep different records for the same systems developing in the basin, which introduces further uncertainties in the IBTrACS record with the regards to that particular basin (Barcikowska et al., 2012; Ren et al., 2011).

Table 2.1: Details for the reanalysis datasets used in this study. Abbreviations: 4D-Var, 4D variational data assimilation; 3D-Var, 3D variational data assimilation; TL255L60, triangular truncation 255, with linear grid, 60 vertical levels (approximate horizontal grid spacing in parentheses); GSI, Grid-point Statistical Interpolation; IAU, Incremental Analysis Update.

Dataset	Assimilation	Model Resolution	Data Grid
ERAI	4D-Var	TL255L60 (80 km)	480×241
ERA5	4D-Var	TL1279L137 (31 km)	1440×750
MERRA	3D-Var GSI+IAU	$1/2^\circ \times 2/3^\circ$ L72 (55 km)	540×361
MERRA-2	GSI+IAU	Cubed sphere (50 km)	576×361
NCEP	3D-Var GSI	T382L64 (38 km)	720×361
JRA-25	3D-Var	T106L40 (120 km)	288×145
JRA-55	4D-Var	TL319L60 (55 km)	288×145

2.1.2 Reanalysis Datasets

Reanalysis is a combination of observations with a short-range forecast from a GCM. They provide gridded datasets, constrained by the observations and they act as a bridge between the observations and the model simulations using data assimilation. For this study, seven recent global atmospheric reanalysis datasets are used; the ECMWF Interim Re-Analyses (ERAI) (Dee et al., 2011); the ERA5 (Hoffmann et al., 2019); The National Aeronautics and Space Administration (NASA) Modern-Era Retrospective Analysis for Research and Applications (MERRA) (Rienecker et al., 2011); the next version 2 (MERRA-2) (Bosilovich et al., 2015; Molod et al., 2015); the National Centers for Environmental Prediction (NCEP) Climate Forecast System Reanalysis (CFS) (Saha et al., 2010); the Japanese 25-year Reanalysis (JRA-25) (Onogi et al., 2007); and the Japanese 55-year Reanalysis (JRA-55) (Kobayashi et al., 2015). Details for all datasets are summarised in Table 2.1. The 2nd column indicates the data assimilation method, the 3rd indicates the resolution of the datasets, with the approximate horizontal grid spacing in parenthesis, and the 4th column indicates the grid of the data. The model resolution and data grid information for all the reanalyses except ERA5 are the same as in Hodges et al. (2017) and Roberts et al. (2020a).

Among the reanalyses used in the present study, NCEP is the only coupled atmosphere-ocean-land surface-sea ice reanalysis dataset, and it underwent an upgrade to CFS2 in March 2011. NCEP, MERRA and MERRA2 use the Grid-point Statistical Interpolation (GSI) scheme for 3D variational data assimilation (3D-Var) (Shao et al., 2016). The Incremental Analysis Update (IAU; (Bloom et al., 1996; Rienecker et al., 2011)) system is also used as part of the data assimilation process for the two MERRA reanalyses. The two reanalysis products from the Japan Meteorology Agency (JMA) differ from the rest in terms of how the tropical wind retrievals (TWR) are assimilated. According to Hatsushika et al. (2006), data for wind profiles over and around TC centres are taken from historical data and they are processed and assimilated in the same way as dropsonde observations. This has been found to improve the intensity of systems in the Japanese reanalysis products. On the other hand ERAI, ERA5 and JRA55 use 4D-Var data assimilation. Lastly, for MERRA2 and NCEP, adjustments of the position of the TC to its observed position before the process of assimilation is used for improved representation of TCs.

2.1.3 High Resolution Climate Model Simulations

Even though IBTrACS and reanalyses are extremely useful for the development and validation of the techniques used in this Ph.D. study, their records are short and inconsistent for the purposes of the study. High resolution GCMs provide longer and more consistent records to work with. Results for TCs from both atmosphere-only and coupled simulations from the Hadley Centre Global Environment Model 3 - Global Coupled vn 3.1 (HadGEM-GC3.1) model are used and analysed. A full description of the resolution hierarchy for the model as it was used in the Coupled Model Intercomparison Project phase 6 (CMIP6) HighResMIP experiments is given by Roberts et al. (2019). A schematic for the HighResMIP experimental design is shown in Roberts et al. (2019) (see fig. 1), whilst Tables 2.2, 2.3 and 2.4 summarise the resolutions, simulations and Unified Model (UM) suite names analysed in this study.

The HighresMIP forcing protocol for CMIP6 was used to force the experiments used in this study. Even though a full description is given by Haarsma et al. (2016) a short outline is presented here. The project uses a multi-model approach in order to investigate the effect of horizontal resolution. According to Haarsma et al. (2016), these experiments are categorised into three tiers covering a 100-year period (1950-2050).

Table 2.2: Details about oceanic and atmospheric resolutions with naming conventions for HadGEM3-GC3.1 simulations.

Model Name	**Atmospheric resolution** CMIP6 nominal	**Ocean resolution** CMIP6 nominal
LL	168.4 km (N96)	100km (ORCA1)
LM	168.4 km (N96)	25km (ORCA025)
MM	74.8 km (N216)	25km (ORCA025)
MH	74.8 km (N216)	8km (ORCA12)
HM	31.6 km (N512)	25km (ORCA025)
HH	31.6 km (N512)	8km (ORCA12)

Table 2.3: Details about Atmosphere-only model simulations from HadGEM3-GC3.1 with UM suite names

Model Resolution	**highresSST-present (1950-2014)**	**highresSST-future (2015-2050)**
HadGEM3-GC31-LM	u-ai674, u-ak681, u-ak687, u-bd058, u-bd423	u-bf004, u-bf553, u-bf831, u-bg139
HadGEM3-GC31-MM	u-ai718, u-aj530, u-ak185	u-bf082, u-bf773, u-bg565
HadGEM3-GC31-HM	u-ai685, u-aj558, u-aq581	u-bf101, u-bg091, u-bi512

2.1.3.1 Tier 1: HighresSST-present (1950-2014)

The period for these experiments is 1950-2014, and they have been forced by daily $1/4°$ SSTs and sea-ice from the HadISST2 dataset (Titchner and Rayner, 2014). Initial conditions come from the ERA-20C reanaalysis from January 1950, while for anthropogenic aerosol forcing the recommendation was to use a common, simplified aerosol optical property scheme (MACv2-SP; (Stevens et al., 2017)).

Table 2.4: Information about Coupled model simulations with UM suite names

Model Resolution **Atmos/Ocean**	**ORCA1** **(100km)**	**ORCA025** **(25km)**	**ORCA12** **(8km)**
N96 – 130km (250km) (HadGEM3-GC31-LL)	**Control-1950**: u-ak306 (1950-2550) **Hist-1950**: u-ak356, u-ak731, u-ak743, u-ak938 (1950-2014) **Highres-future**: u-bd064, u-bd244, ubd410, u-be500 (2015-2050)	NA	NA
N216 – 60km (100km) (HadGEM3-GC31-MM, MH)	NA	**Control-1950**: u-aj368 (1950-2500) **Hist-1950**: u-aj354, u-ak141, u-ak144, u-ar599 (1950-2014) **Highres-future**: u-bd066, u-bd414, u-bd656, u-be499 (2015-2050)	**Control-1950**: u-aj393 (1950-2150) **Hist-1950**: u-bk610 (1950-2014) **Highres-future**: u-bq218 (2015-2050)
N512 – 25km (50km) (HadGEM3-GC31-HM, HadGEM3-GC31-HH)	NA	**Control-1950**: u-ay355 (1950-2013) **Hist-1950**: u-ay585, u-az094, u-bb527 (1950-2014) **Highres-future**: u-bd174, u-bg726, bj612 (2015-2050)	**Control-1950**: u-ay490 (1950-2092) **Hist-1950**: u-ay652 (NOC, 1950-2014) **Highres-future**: u-bj590 (2015-2050)

2.1.3.2 Tier 2: Control runs

Couple runs are useful because by systematically comparing couple runs with uncoupled runs, different biased affecting climate models can be identified and explored (Haarsma et al., 2016). The HighresMIP control runs (hereafter referred as Control-1950) correspond to the pre-industrial control runs. For this study they are 1950s control runs forced with fixed 1950s forcing. Greenhouse gases for the forcing include a 10-year mean of 1950s aerosol climatology. Initial ocean conditions are provided by the Met Office Hadley Centre EN4 dataset (Good et al., 2013). Differences between historic (hereafter referred as Hist-1950) and control runs can be used as an estimation of how changing forcing can impact the state of the climate. The period for Hist-1950 experiments is also 1950-2014. For each type of resolution there are at least 3 ensemble members and each member is initialised from a different year at the corresponding control run. The external forcings are the same as in Tier 1. Lastly the highres-future runs are essentially continuations of the Hist-1950 runs from 2015-2050. They are taken as the coupled scenario experiments. The forcing for the future experiments is based on high-end emission scenario of the CMIP6 Shared Socioeconomic Pathways (SSPx). In order to use a simpler terminology when distinguishing the control experiments from the scenario experiments, the combination of hist-1950 (e.g. u-ay652) and highres-future (e.g. u-bj590) will be referred to as historic experiment/run/simulation even when referring to the future (2020-2050) period.

2.1.3.3 Tier 3: HighresSST-future (2015-2050)

Extensions of the atmosphere-only tier 1 experiments to 2050 form the tier 3 runs. The same forcing scenario as for tier 2 (SSPx) is used. An ensemble mean of the CMIP5 RCP8.5 runs provides the future warming rate.

2.1.4 The HadISST Dataset

The Met Office Hadley Centre Sea Ice and Sea Surface Temperature dataset (HadISST, Rayner et al. (2003)) consists of monthly global fields of SSTs and sea ice concentrations since 1871. The SST data are a blend of SSTs from the Marine Data Bank (MDB, mainly ship observations), the International Comprehensive Ocean-Atmosphere Data Set (ICOADS, through 1981), in-situ and satellite-derived SST estimates. Sea ice data are

taken from historical ship and airborne observations and satellite estimates. Reduced-space optimal interpolation, followed by super-positioning gridded observations improved in quality, has been used to reconstruct the HadISST1 dataset in order to restore local detail (Rayner et al., 2003). For this study, apart from being regressed onto the EOT time series, the HadISST1 temperatures are used for the computation of various indices.

2.1.5 Climate Indices

Different climate indices are investigated as the source of natural variability of TCs. As mentioned in section 1.3, these include QBO, ENSO, AMM, AMO and PDO. Due to the complexity and often ambiguity surrounding the calculation of the various indices, for the investigation in IBTrACS and reanalyses, data for the indices were taken from sources outlined in table 1.4. For the model simulations, only the ENSO, AMO and PDO are computed from the model data. For each model simulation they were derived from surface temperatures using the methodology presented below.

For ENSO, the Niño3.4 index is computed as followed:

1. Compute the monthly climatology for the period examined (1980-2013 for observed SSTs; 1950-2050 for models) for the Niño3.4 region ($5°S-5°N, 170°W-120°W$)
2. Compute area averaged total SST from the Niño3.4 region
3. Subtract the monthly climatology from the area averaged total SST time series to obtain anomalies
4. Repeat steps 1-3 for he whole globe ($55°S-70°N$) to obtain global SST anomalies
5. Detrend by subtracting global SST anomalies from Niño3.4 anomalies
6. Remove the mean of the detrended time series and divide by the standard deviation to derive a standardised Niño3.4 index.

For the AMO index, the same process is followed for the Atlantic region ($0-65°N, 80°W-0$). For the computation of the PDO index the Climate Variability Diagnostics Package (CVDP) is used (Phillips et al., 2014).

2.2 Methodology

Every method used in this Ph.D. study is first applied to IBTrACS and reanalysis data in order to test the method by obtaining results and drawing conclusions which can be verified by the literature. Therefore, confidence in the physical interpretation of results before using the methods on model simulation results can be gained.

2.2.1 Tracking Algorithm

An objective, feature-tracking algorithm described in Strachan et al. (2013) and Bengtsson et al. (2007), is applied to the reanalysis data to identify and track tropical cyclone-like features. Firstly, all tropical disturbances are tracked before applying the identification method according to the tracking methodology outlined in (Hodges, 1994, 1995, 1999). The domain covered is from 60°S to 60°N and vertically averaged. Relative vorticity data at 6-hourly intervals at 850, 700 and 600 hPa are used for tracking. Triangular truncation is used for spectral filtering of the data, which removes the noise caused by the finest spatial scales in the vorticity. This beneficially contributes to the reliability of tracked data and to eliminate the large-scale background. A maximization scheme (Hodges, 1995) is used to identify if the off-grid vorticity maxima exceeds the value of $0.5 \times 10^{-5} s^{-1}$ in each time step, initially using a nearest-neighbour approach to link the maxima. Then for track smoothness, they are refined by minimization of a cost function, depending on constraints on track smoothness and distance of displacement. An important advantage of using vertically averaged vorticity is the improvement of the temporal coherence when a vorticity maximum changes levels (Fine et al., 2016; Serra et al., 2010) and the detection of more stages of a system's life-cycle.

In order for vorticity centre tracks to be kept for further analysis, they need to have a lifetime of over two days. In order to do that, additional fields must be added to the tracks. These include T63 vorticity at the 850 and 700-200 hPa levels for the provision of intensity and warm core criteria. For the addition of the vorticity fields a steepest ascent maximization method was applied with the B-spline interpolation and a 5° radius search centred on the location of the previous level. Furthermore, fields for minimum MSLP and maximum winds at 10m and at 925 hPa are added, as surrogate measures of intensity. For adding the wind field, the maximum winds at up to 6° radius from the tracked centre were

searched directly, while for the MSLP field a steepest descent method was applied to the B-spline interpolated field along with a 5° geodesic radius search centred on the tracked vortex centre for finding the nearest pressure minimum.

For this study, TCs have been objectively identified based on a set of identification criteria on intensity and structure. The tracks are considered tropical cyclone-like features if the following criteria, as outlined by Strachan et al. (2013), are attained:

1. T63 relative vorticity at 850 hPa must attain an intensity threshold of $6 \times 10^{-5} s^{-1}$;
2. to establish a coherent vertical structure, a positive T63 vorticity center must exist at all levels between 850 and 200 hPa;
3. For evidence of a warm core, a reduction in vorticity from 850 to 200 hPa (at T63 resolution) of $6 \times 10^{-5} s^{-1}$ is required;
4. criteria 1 to 3 must be attained for a minimum of one day over the oceans.

The methodology used for identification and tracking of TCs is applied at all reanalyses using common resolution, ensuring that the identification and tracking are as resolution independent as possible. The tracking was performed to each full year, January - December for the 1980-2013 period for the NH. Results from the algorithm for each year are extracted in files that contained the number of storms for the year in question, the longitude and latitude of each track point of each storm as well as the intensity of the storm at each point in terms of T63 vorticity, and full resolution MSLP, 10m winds and 925hPa winds. For IBTrACS only wind speeds at 10m are available.

2.2.2 Defining the tropical cyclone regions

The first step of the process is to define the tropical cyclone regions that will be analysed. The regions that were chosen are a combination of the regions by the World Meteorological Organisation (WMO) Tropical Cyclone Programme with the regions by Strachan et al. (2013). They are shown on figure 1.5.

2.2.3 Time series of annual TC counts and ACE

For each year, for each storm the point of maximum intensity is found. If the intensity is in terms of vorticity or wind speed, then the maximum intensity is where the maximum of

the desired quantity is. If the intensity is in terms of mean sea level pressure (MSLP), then the maximum intensity is where the minimum MSLP is. In case the storm has missing values (for the windspeed or MSLP) for all the track points, then the maximum intensity is taken at the middle of the TC track. In case the storm has some missing values (for windspeed or pressure cases, a problem only for IBTrACS) along the track but there are also reported values, then the point of maximum intensity is taken as the location of the minimum or maximum of the reported data. By counting how many storms achieved their maximum intensity in each of the defined regions, time series of annual TC counts are created.

To obtain a time series of storms stronger than a tropical depression or storms which achieved hurricane/typhoon intensity, criteria on wind speeds (or MSLP) values must be applied. For appropriate threshold values one can refer to the Saffir–Simpson hurricane wind scale (SSHWS). For example, for storms stronger than a tropical depression a criterion of the wind speed value being larger than $17ms^{-1}$ is applied.

Time series of annual ACE are also computed, since ACE is used as a measure of a TC-season's activity. It is computed by:

$$ACE_{season} = 10^{-4} \sum v_{max}^2 \tag{2.1}$$

where v_{max} is a storm's estimated sustained wind speed in knots in 6-hourly intervals. For the reanalysis and models, wind speeds at the 925 hPa levels are used.

2.2.4 Power Spectral Density of a time series

Once TC counts have been obtained a spectral analysis is performed in order to examine any periodicities within the time series. The distribution of power into frequency components of a time series $x(t)$ is described by the power spectral density (or simply power spectrum) $S_{xx}(f)$ of the time series. One estimate of the spectral density of a signal is the periodogram. The method of averaged periodograms, which is called the Bertlett method, reduces the variance of the periodogram at the expense of resolution reduction. The original time series is split up into non-overlapping segments and for each segment the periodogram is computed with the use of the discrete Fourier Transform and by squaring the magnitude of the result and dividing it by the length of the segment. Lastly, by averaging the periodograms, the power spectrum is estimated. The 95% confidence level

based on a white noise spectrum is calculated as well.

Subsequently, in an effort to simplify the results for each basin, the seven individual reanalysis power spectra are combined into one by firstly calculating the power spectrum of each individual reanalysis time series and subsequently averaging the seven spectra. The same process is followed for the two 95% confidence levels.

2.2.5 Wavelet analysis

Wavelet analysis allows the detection of periodicities in localised periods of time. The analysis performed in this study was based on Torrence and Compo (1998), which is a guide on how to perform a wavelet analysis. Compared to the well-known Fourier Transforms, the Continuous Wavelet Transform (CWT, discussed below) compares the time series to scaled and shifted versions of a wavelet, whereas the Fourier transforms decompose a time series into sines and cosines of infinite length. This means that the CWT, which is used for this study, has an advantage over Fourier in time-frequency representation of a time series with adequate localisation in both domains.

2.2.5.1 Continuous Wavelet Transform

A wavelet is a function with zero average, localised in both time and frequency and its characterization is based on the localization in time (Δt) and frequency ($\Delta\omega$). Two classes of wavelet transforms exist; The Continuous Wavelet Transform (CWT) and the Discrete Wavelet Transform (DWT). The important difference between the two transforms depends on the scaling parameter. The CWT discretization is finer than the DWT one, making the CWT more appropriate for time-frequency analysis (MathWorks, n.d.). For the calculation of CWT the Morlet wavelet function was chosen and it is defined as:

$$\psi_0(\eta) = \pi^{-1/4} e^{i\omega_0\eta} e^{-\eta^2/2} \tag{2.2}$$

were ω_0 and η are the non-dimensional frequency and time respectively. Even though a few studies have used the wavelet method to investigate TC variability, there has not been a sensitivity analysis regarding which wavelet function is more appropriate. The Morlet wavelet function is used in this study because, according to Grinsted et al. (2004), with the Morlet wavelet function (with $\omega_0 = 6$) there is a good balance between time and frequency.

Therefore, it was deemed an appropriate choice when the purpose of using wavelets is to extract features.

Along with the wavelet function a set of scales s must be chosen. The scales, just as in Torrence and Compo (1998), are written as fractional powers of two:

$$s_j = s_0 2^{j\delta j}, j = 0, 1, ...J \tag{2.3}$$

$$J = \delta j^{-1} log_2(N\delta t/s_0), \tag{2.4}$$

where s_0 is the smallest resolvable scale, while J gives the largest scale. According to Torrence and Compo (1998) 0.5 is the largest value which can also provide adequate sampling in scale for the Morlet wavelet. For the wavelet analysis in this study δj was set to 0.125. By varying the scale (s) of the wavelet in order for $\eta = s \cdot t$ and by normalizing it, the wavelet is stretched in time. The CWT of a given time series x_n of length N whose time steps (δt) are uniform, is defined as:

$$W_n^X(s) = \sqrt{\frac{\delta t}{s}} \sum_{n'=1}^{N} x_{n'} \psi_0[(n'-n)\frac{\delta t}{s}] \tag{2.5}$$

essentially the convolution of the time series with the scaled and normalized wavelets. The function $\psi(\eta)$ is in general a complex function, therefore $W_n^X(s)$ is complex as well (Torrence and Compo, 1998). Then the wavelet power spectrum is defined as $|W_n^X(s)|^2$.

2.2.5.2 Cone of Influence

The localization of a wavelet is not complete in time. Consequently, the CWT has edge effects. The Cone of Influence (COI) is defined as the region of the wavelet power spectrum in which the edge artefacts can not be ignored. The COI is chosen as the area in which the wavelet power for a discontinuity at the edges reduces by a factor e^{-2} (Torrence and Compo, 1998), ensuring the negligibility of the edge effects beyond that point.

2.2.5.3 Significance Levels

In order to determine significance levels for wavelet spectra, it is stated in Torrence and Compo (1998) that choosing a suitable background spectrum is needed. For many geophysical phenomena, a white noise (which has a flat Fourier spectrum) or a red noise

(which shows increasing power with decreasing frequency) can be suitable background spectra. For red noise, a simple model is the first order autoregressive (AR1) process given by:

$$x_n = ax_{n-1} + z_n \tag{2.6}$$

with a the assumed lag-1 autocorrelation, $x_0 = 0$ and z_n taken from a Gaussian white noise. Then, after normalization, the discrete Fourier power spectrum of equation (3) according to Gilman et al. (1963) is:

$$P_k = \frac{1 - a^2}{1 + a^2 - 2a\cos(2\pi k/N)} \tag{2.7}$$

with $k = 0, ..., N/2$ being the frequency index. Therefore, with a suitable α, equation (2.7) can be used to model a red noise spectrum. However, for this Ph.D. study, in order to analyse TC variability on interannual and decadal time scales in conjunction with a range of climate indices, annual time series of TC counts and ACE are used, leading to choosing a value of $a = 0$, which gives a white noise spectrum.

According to Torrence and Compo (1998) the null hypothesis for the wavelet power spectrum is that the time series is assumed to have a mean power spectrum, possibly given by equation (2.7); A peak is assumed to be a true feature with a certain percent of confidence if a peak in the wavelet power spectrum is significantly above the background spectrum. For this Ph.D. study the 95% confidence level (CL) was chosen.

2.2.5.4 Global Wavelet Spectrum and Averaging In Scale

The global wavelet spectrum and the scale-average wavelet power are calculated as well. The local spectrum is a vertical slice through the wavelet domain. Therefore, the global wavelet spectrum is an average over all the local wavelet spectra and it is given by:

$$\overline{W}^2(s) = \frac{1}{N}\sum_{n=0}^{N-1} |W_n(s)|^2 \tag{2.8}$$

The time series of the average variance in a specific band is the scale-averaged wavelet power. For the analysis of IBTrACS and the reanalysis datasets for the common period (1980-2013) the band was chosen between five and ten years. Full details for the global

wavelet spectrum and the scale-averaged wavelet power can be found in Torrence and Compo (1998).

2.2.5.5 Cross Wavelet Transform

The cross wavelet transform (XWT) is used to find regions in the time-frequency space where two time series show high common power. The XWT of two given time series x_n and y_n, with wavelet transforms $W_n^X(s)$ and $W_n^Y(s)$ respectively, is defined as $W_n^{XY}(s) = W_n^X(s)W_n^{Y*}(s)$ where $W_n^{Y*}(s)$ is the complex conjugate of $W_n^Y(s)$. Therefore, the cross-wavelet spectrum is complex and the cross-wavelet power can be defined as $|W_n^{XY}(s)|$ (Torrence and Compo, 1998). The local relative phase between the two time series in time-frequency space is given by the complex argument $\arg(W_n^{XY}(s))$ (Grinsted et al., 2004). Assuming that the two time series have background power spectra P_k^X and P_k^Y (equation 2.7), the theoretical distribution of the cross wavelet power of the two time series is given in Torrence and Compo (1998) by:

$$D\left(\frac{|W_n^X(s)W_n^{Y*}(s)|}{\sigma_X\sigma_Y} < p\right) = \frac{Z_\nu(p)}{\nu}\sqrt{P_k^X P_k^Y} \tag{2.9}$$

with ν the degrees of freedom and $Z_\nu(p)$ the CL associated with the probability p for a probability density function which is defined by the square root of the product of two χ^2 distributions. According to Torrence and Compo (1998), the inverse of the cumulative distribution function (percent point function - PPF) of a χ^2 distribution at the 95% confidence and two degrees of freedom is $Z_2(95\%)$=3.999. However, calculating the PPF using χ^2 ppf gives $Z_2(95\%)$=5.991. To ensure similar significance intervals as in Grinsted et al. (2004), one has to use confidence of 86.46%.

2.2.5.6 Wavelet Coherence and Coherence Phase

The wavelet coherence is a measure of the cross-correlation between two time series as a function of frequency. The coherence finds regions in time-frequency space where the two time series co-vary, but do not necessarily have high power. It is defined in Torrence and Compo (1998) as the square of the cross-spectrum normalised by the individual power spectra and it provides a quantity between zero and one. Grinsted et al. (2004) defined the coherence of two time series as

$$R_n^2(s) = \frac{|S(s^{-1}W_n^{XY}(s))|^2}{S(s^{-1}|W_n^X(s)|^2) \cdot S(s^{-1}|W_n^Y(s)|^2)} \tag{2.10}$$

where S is a smoothing operator. Grinsted et al. (2004) also highlighted that their definition is very similar to the definition of the traditional correlation coefficient and can be thought of as a localised correlation coefficient in the time-frequency space. The smoothing operator is defined as

$$S(W) = S_{scale}(S_{time}(W_n(s))). \tag{2.11}$$

where S_{scale} is the smoothing along the axis of the wavelet scale, while S_{time} is the smoothing in time. Grinsted et al. (2004) mentioned that for the Morlet Wavelet an appropriate smoothing operator is presented in Torrence and Compo (1998) and given by:

$$S_{time}(W)|_s = \left(W_n(s) * c_1^{\frac{-t^2}{2s^2}} \right) \Bigg|_s, \tag{2.12}$$

$$S_{time}(W)|_s = (W_n(s) * c_2 \Pi(0.6s)) \big|_n \tag{2.13}$$

using the normalisation constants c_1 and c_2, the rectangle function Π and the scale decorrelation length factor of 0.6 for the Morlet wavelet, which is determined empirically (Torrence and Compo, 1998). The normalisation constants are computed numerically due to the fact that the convolutions are performed discretely (Grinsted et al., 2004). Lastly, the coherence phase is defined in Torrence and Compo (1998) as

$$\tan^{-1}\left[\frac{\Im(W_n^{XY}(s))}{\Re(W_n^{XY}(s))}\right] \tag{2.14}$$

Full details can be found in Grinsted et al. (2004).

2.2.5.7 Kernel Density Estimation

In an effort to combine and compare the wavelet spectra for each basin from the multiple datasets, the distribution of the power within certain bands in investigated. The wavelet power spectrum of a time series is calculated as described in section 2.2.5.1 and a Kernel Density Estimation (KDE) is performed on the power within a specific band (for example the 2-8 year band). The KDE provides a non-parametric way to estimate the probability density function of a random variable. With the use of this technique, it is possible to

directly, quantitatively compare wavelet spectra from different datasets and/or different period bands.

2.2.6 Empirical Mode of Decomposition and Hilbert Analysis

The way the wavelet analysis is performed is characterised by uncertainties. Two notable sources of uncertainties are the choice of the wavelet function and the padding of the time series with zeroes. Depending on which wavelet function is chosen and whether the time series will be padded with zeroes, results can differ.

In order to validate the results of wavelet analysis and to trust that decisions were appropriate, another method with less arbitrary decisions was used; The Empirical Mode of Decomposition (EMD) along with the Hilbert spectrum. The EMD method decomposes a data set into a finite number of "intrinsic mode functions" (IMFs). The decomposition is based on the local and innate characteristics of the data in respect of time. With the use of the Hilbert transform, instantaneous frequencies are produced from the IMFs as functions of time, distinctly identifying embedded features. Finally, the power within the signal in the time-frequency domain, known as the Hilbert spectrum, is computed. Full details can be found in Huang et al. (1998).

2.2.7 Empirical Orthogonal Teleconnections

Even though the spectral methods can provide indications of modes of variability influencing TC activity, they alone cannot explain what mainly drives TC variability. Despite the fact that one of the standard techniques for analysing the spacial and temporal variability of data is the Empirical Orthogonal Function (EOF) method, for this Ph.D. study the Empirical Orthogonal Teleconnections (EOTs) method is used. The EOTs method is an alternative method used for the empirical and orthogonal calculation of functions from space-time datasets. One of the advantages of EOTs over EOFs is that the former are orthogonal in only one direction (time or space) instead of two (space and time) as is the case for the latter, making the computation less expensive (Smith, 2004; van den Dool et al., 2000). The EOTs can be thought of as the rotated EOFs (van den Dool et al., 2000).

The EOTs method tries to find the point in space (or time) - base point - which, by using linear regression, can explain the majority of variance at all other points. The first spatial pattern is the slope (regression coefficient) between the base point and every other

point. The first time series (mode) is the time series of the raw data at the base point. The original data are reduced by subtracting what is explained by the first mode. The process can be repeated exactly as before for the remaining modes. Full details for the method can be found in van den Dool et al. (2000).

By using this method the main drivers of the decadal variability of TCs, are investigated. We have chosen to search for the base point in space which explains most of the variance in TC track densities. The method is applied on track densities computed using the seasonal (May to November) statistics methodology based on spherical nonparametric Kernel estimators as outlined in Hodges (1996). The track densities are computed for all datasets, but only the track densities at locations were the mean track density over the period analysed is equal or greater than two TCs per season per unit area are used.

In order to identify which phenomena may be responsible for TC variability, fields of different drivers such as SSTs and VWS, are regressed onto the EOT time series. By linearly regressing the driver field onto the EOT time series we aim to find patterns that resemble and are significantly correlated (at the 90% CL) to known canonical patterns of climate indices such as ENSO, AMO and others. The term canonical refers to patterns which are well known in the literature and are results of either Principal Component Analysis (PCA) or composite analysis. For examining the SSTs as a driver the SST field obtained from the $1^\circ \times 1^\circ$ Hadley Centre Sea Ice and SST data set (Had-ISST; Rayner et al. (2003)) was regressed onto EOT time series from IBTrACS and reanalyses. For the model simulations, for each model simulation shown in tables 2.3 and 2.4 the corresponding SST field was used. It is important to note here that for the investigation of decadal variability (under the 1950-2050 period) the trend in SSTs is removed, but for the analysis of climate change, it is not. Lastly, for examining the VWS as a driver, from the reanalysis datasets only the ERA5 VWS field was regressed onto the ERA5 and IBTrACS EOT time series following the same process as for the SSTs. For ERA5 and for the model simulations the VWS was computed as the magnitude of the difference between the zonal and meridional winds at the 850 and 250 hPa.

For the linear regression, the EOT time series are standardised and then at each grid point, the linear regression coefficient (slope) is calculated. The resulting patterns (regression maps) are compared against the canonical patterns for the different climate indices. The first regression pattern indicates the phenomenon or phenomena responsible

for the majority of variance in TC activity at the base point. When the influence of the first phenomenon is removed, the second pattern indicates the phenomenon which is responsible for the majority of variance at the second EOT point, and so on.

2.2.8 Pearson Correlation Coefficients

Throughout the thesis, the time series of TC counts, of ACE and the EOTs are correlated using simple Pearson correlation coefficients with the climate indices. The correlations are considered to be significant at the 90% CL if the corresponding two-tailed p-value is less than 0.1. Lastly, they are characterised based on Table 2.5.

Table 2.5: Characterising correlations

Absolute value	**Category**
0 - 0.24	Weak
0.25 - 0.49	Moderate
0.5 - 0.74	Strong
0.75 - 1	Very strong

Chapter 3

Drivers of TC Variability in the Current Climate, 1980-2013

3.1 Introduction

The drivers of TC variability in the different regions of the northern hemisphere for the current climate, specifically the 1980-2013 period, are examined in this chapter. For each region, as well as for the total NH activity, results from the analysis on observations (IBTrACS) and reanalyses are presented first. In addition, in order to assess the skill of HadGEM3-GC3.1 in simulating TC activity in the present day and gain confidence before examining the drivers of decadal TC variability and the impact of climate change, results from the different model simulations, specified on table 2.3 and 2.4, are compared against IBTrACS and reanalyses. Results discussed will be mainly focused on the analysis from spectral methods on time series of TC activity (annual counts and ACE), the EOTs method on TC track densities as well Pearson correlations between different time series and climate indices, defined in chapter 1.3. In terms of TC counts, for each basin, figures of time series as well as results from the spectral methods and from Pearson correlation coefficients will be presented. In terms of ACE, for each basin, the figures/tables presented in this chapter will be focused only on Pearson correlation coefficients between the annual ACE time series and the May-November averaged climate indices. Results from spectral analysis on EOTs will be discussed, but no figures will be shown. The spectral methods are used for detecting periodicities within time series of TC counts and ACE, whereas the EOTs method is used for examining the influence of two main drivers, SSTs and VWS,

on TC variability. For observations, the QBO, ENSO, AMM, AMO and PDO climate indices are used, whereas for the models, only the ENSO, AMO and PDO indices are taken into consideration. Even though the period analysed in this chapter is very short in order to fully assess the decadal variability of TCs, it is important to examine, both in observations and in models, whether the decadal modes of climate variability (AMO and PDO) have had any influence on TC variability. It is true that their respective periodicities are not expected to be captured by the spectral methods and that examining the influence by the two decadal modes in this short period is complicated due to biases and artificial trends in the observations. However, despite the fact that this investigation is not ideal, it is crucial to examine whether there is any decadal variability associated with the two decadal modes for completeness and comparison purposes with chapter 4. The present chapter is structured by the different regions examined: total NH, North Atlantic, Eastern Pacific, Central Pacific, Western Pacific and North Indian Ocean.

3.2 Total NH Activity

The mean track densities in the NH (0-60°N) for the 1980-2013 period for IBTrACS, ERA5 and a range of model simulations by HadGEM3 are presented on figure 3.1. Using the track density statistics allows the assessment of the ability of a GCM to simulate the spatial distribution of TCs (Strachan et al., 2013). It can be seen that in all different NH regions there are higher mean track densities in ERA5 (fig. 3.1b) and the rest of the reanalyses (not shown) compared to IBTrACS. This can be particularly observed for the central Pacific region (180 - 140°W) since very few TCs in that particular region are included in the IBTrACS. In addition, TC tracks are longer in ERA5 and the rest of reanalyses compared to IBTrACS, since storms in the reanalyses are tracked even if they transition into extra-tropical systems. This can influence the EOT analysis resulting in EOTs located outside the respective MDRs and in high latitudes. More discussion on how the track densities can influence EOT analysis follows in the next chapters.

Results for the atm-only runs are based on observed SSTs, therefore it is possible to compare track densities for the atm-only runs (fig. 3.1c, 3.1d) with the ones for IBTrACS and reanalyses. The comparison, however, will extent to the track densities from the coupled runs (fig. 3.1e - 3.1j), in order to assess the spatial distribution of TCs in all

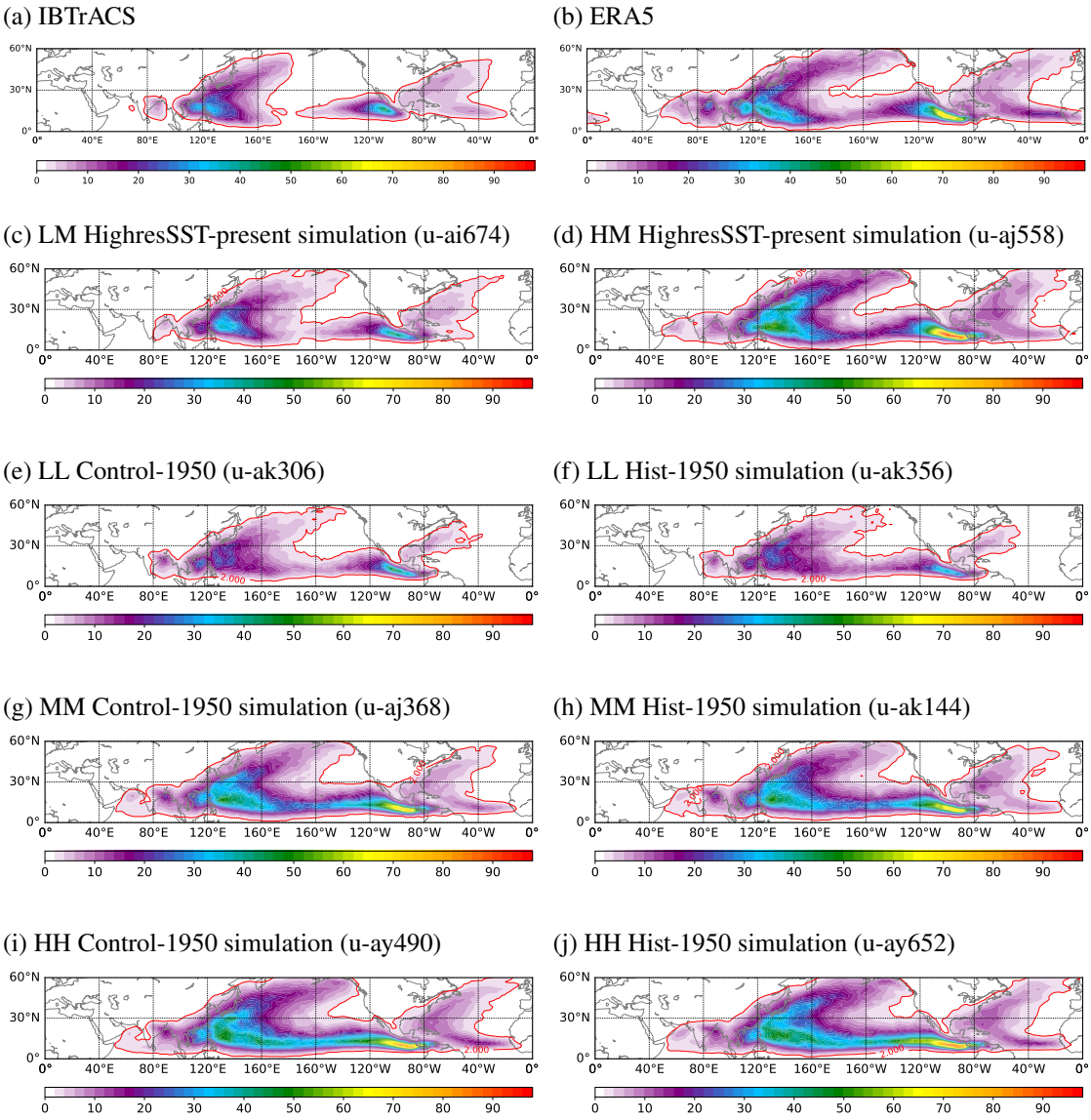

Figure 3.1: Mean track density during in the NH (0-60°N) for the 1980-2013 period for: (a) IBTrACS, (b) ERA5, (c) - (d) atm-only runs of low (LM) and high (HM) resolution, (e) - (j) a coupled control-1950 and one corresponding coupled hist-1950 run of LL, MM and HH resolution. Red contour indicates where the mean track density is greater that 2 TCs per season, per unit area.

the datasets examined in the study. Similarly to the reanalysis datasets, the tracks in the model runs are longer compared to the IBTrACS, and in general, it can be seen that with increasing horizontal resolution there are increases in the mean track densities in the different regions. Furthermore, the N96-resolution (LM atm-only and LL coupled) runs show less TCs than observations, particularly in the NATL region, whereas results for the N216 and N512 runs simulate similar or higher spatial distributions of TCs compared to the ones in reanalyses.

Summary statistics by basin for the NH TC activity of the 1980-2013 period are presented on figure 3.2. The upper two rows represent the statistics in terms of TC counts, while the statistics for ACE are displayed in the lower two rows. The average number of storms and ACE per year are shown in the centre.

As already found by Hodges et al. (2017), for the TC counts in the NH using the objective identification there is generally good agreement between the reanalysis datasets and IBTrACS, except for MERRA. According to the summary statistics for IBTrACS, on average around 77 TCs occur per year. In the reanalyses the highest annual average is found for JRA55 with 84 TCs per year, while the lowest is found for MERRA with approximately 50 TCs. NCEP, ERA5 and MERRA2 show more than 79 TCs per year, whereas ERAI and JRA25 have less than 69 TCs per year. In terms of annual average ACE, the same picture is found, with NCEP, ERA5, MERRA2 and JRA55 overestimating it compared to IBTrACS' value, while the remaining reanalyses underestimate ACE. It is possible that these differences in the ACE statistics are due to a combination of different TC counts, representation of wind speeds in reanalyses, missing wind speed data in IBTrACS and the longer TC tracks in reanalyses.

Studies have shown that in order to correctly simulate the TC variability in models, it is important to have both a number of ensemble members at a given resolution (Mei et al., 2019; Yoshida et al., 2017) as well as an ensemble of runs at different resolutions (Roberts et al., 2015; Zhao et al., 2009). For the former, having a number of ensemble members at a given horizontal resolution improves the signal-to-noise ratio. For the latter, even though running a GCM at high resolution provides better representation of TCs, it can be expensive. Therefore, it is crucial to also have runs at different resolutions. For this study, at each run presented on tables 2.3 and 2.4, TC activity under the same period is examined individually.

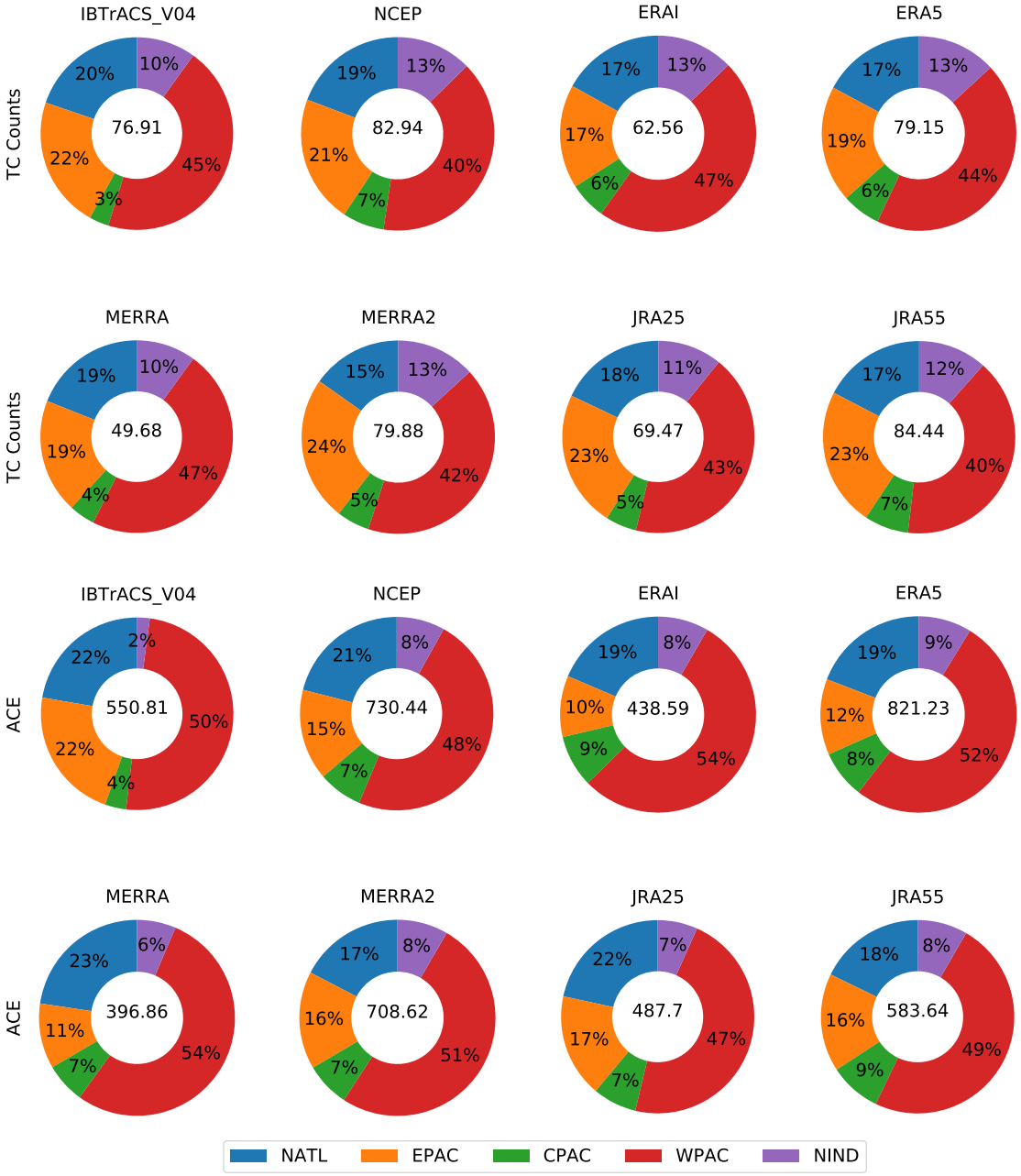

Figure 3.2: Northern hemisphere TC activity summary statistics for IBTrACS and reanalysis products for the 1980-2013 period in terms of TC counts (upper two rows) and ACE (lower two rows). The different colours indicate the basins with the proportion of each basin's activity to the total northern hemisphere activity, while mean number of storms and mean ACE per year are shown in the centre.

Table 3.1: Pearson correlations between the time series of total NH annual (a) TC counts and (b) ACE of IBTrACS and reanalyses with the seasonal climate indices for the 1980-2013 period. Correlations which are significant at the 90% CL are in bold.

	QBO	AMM	ENSO	AMO	PDO
IBTrACS	-0.00	-0.15	-0.08	**-0.29**	0.05
ERAI	-0.16	0.27	-0.08	**0.39**	**-0.57**
MERRA	-0.17	0.15	0.02	0.23	-0.13
MERRA2	0.09	0.10	0.28	0.04	-0.16
NCEP	-0.04	**-0.49**	0.20	**-0.69**	**0.32**
JRA25	-0.12	0.26	0.11	0.21	**-0.29**
JRA55	-0.01	-0.08	0.03	-0.17	0.01
ERA5	-0.13	0.25	-0.07	0.36	**-0.44**

(a) TC counts

	QBO	AMM	ENSO	AMO	PDO
IBTrACS	0.03	-0.13	**0.52**	**-0.39**	**0.32**
ERAI	-0.18	0.18	**0.37**	0.10	-0.11
MERRA	-0.16	0.22	0.23	0.23	-0.06
MERRA2	-0.06	0.18	**0.55**	0.09	-0.12
NCEP	-0.03	-0.19	**0.43**	**-0.48**	0.22
JRA25	-0.11	0.28	**0.36**	0.16	-0.16
JRA55	-0.00	**-0.39**	**0.46**	**-0.62**	**0.53**
ERA5	-0.02	0.12	**0.45**	0.06	-0.05

(b) ACE

In general, the atm-only runs are significantly positively correlated with the time series from IBTrACS compared to the coupled runs. Furthermore, for all the individual basins and time periods analysed, annual TC counts and ACE are underestimated for the N96 model experiments, compared to the N216 and N512 experiments. This result is in agreement with numerous studies such as Roberts et al. (2020a) which highlight that skill in simulating TC-like features depends on resolution. As is evident from TC track densities and time series of TC activity, the low-resolution model simulations significantly underestimate the number of TCs in all basins in addition to the intensities. Even though they might not appear ideal for adequate TC representation, they are less computationally expensive compared to the higher resolution experiments. Hence, they allow the scientific community to conduct a greater number of experiments much faster than the higher resolution runs.

For total TC activity in the NH, almost all the atm-only runs showed significant positive correlations with the IBTrACS time series of total ACE. As indicated on figure 3.3 the May-November averaged ENSO index has a significant moderate-to-very strong positive influence on global ACE, particularly for the atm-only experiments. This is similar to the results seen from IBTrACS and the reanalyses (tab. 3.1). On the other hand, AMO has a significant negative moderate-to-strong influence on both ACE and counts, particularly for

the atm-only and the LL or MM coupled experiments. Furthermore, there are significant moderate correlations between the May-November averaged PDO index and the time series of global counts for 4 (1 LL, 2 MM and 1 HM) of the atm-only experiments, and significant moderate anticorrelations for 5 (1 LL hist, the MM control, 1 MM hist, one HM hist and the HH control) of the coupled simulations examined. For the PDO's influence of ACE, similar conclusions can be drawn, since 4 of the atm-only time series displayed significant moderate positive interaction with the seasonal index, and 3 of the coupled runs showed a significant moderate anticorrelation with the climate mode.

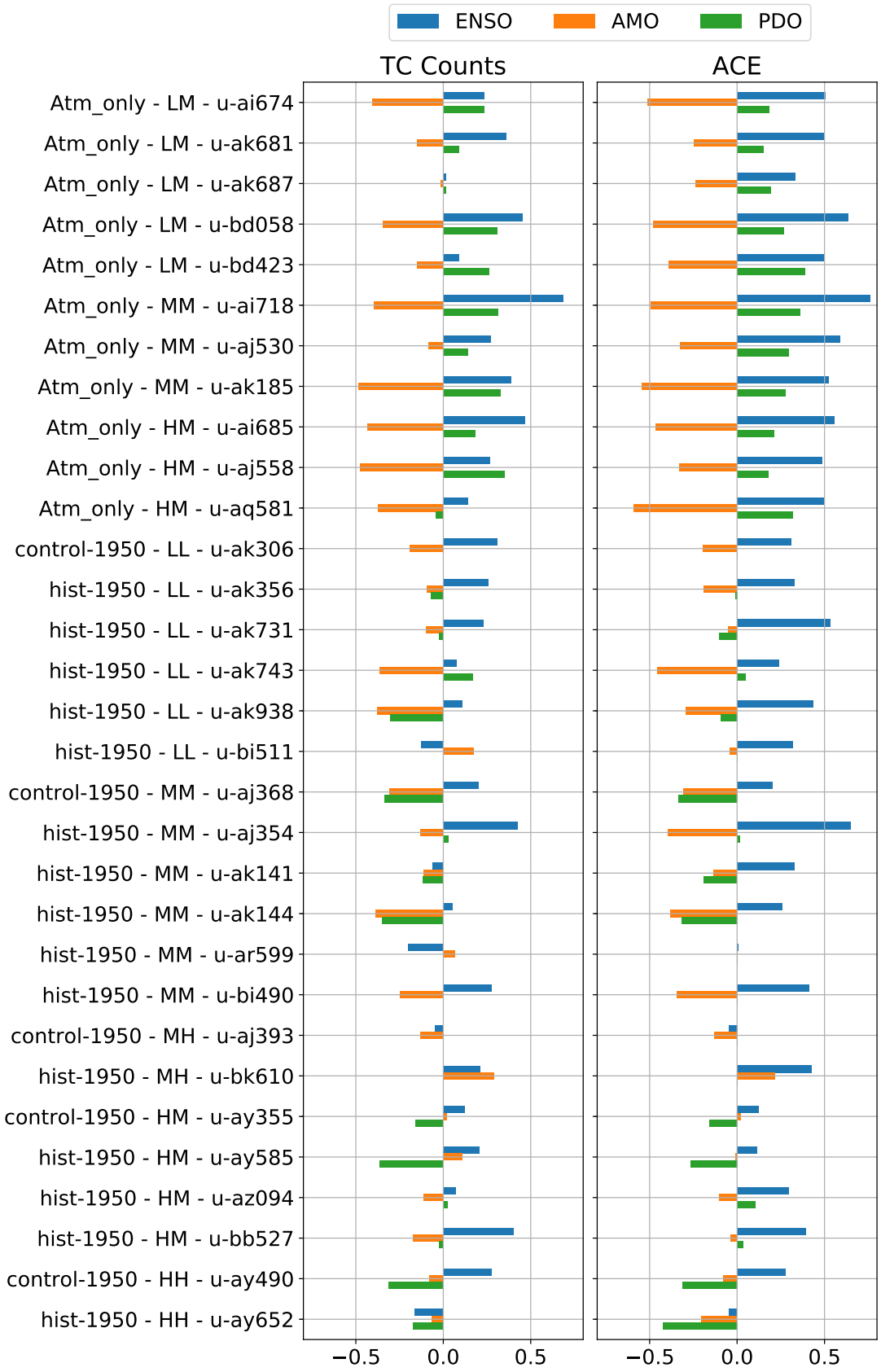

Figure 3.3: Pearson correlations between the time series of total NH annual TC counts and ACE of models with the seasonal climate indices for the 1980-2013 period. Hatched bars indicate the correlations that are significant at the 90% CL.

3.3 North Atlantic

3.3.1 Observations - Current Climate

For the 1980-2013 period the NATL region has 20% (fig. 3.2) of the NH's TC activity according to IBTrACS. The reanalyses have shown a reasonably good agreement representing around 15-19% (fig. 3.2) of the hemisphere's activity, something that is also indicated by Pearson correlation coefficients (not shown) between the IBTrACS and the reanalysis time series. In terms of TC counts, the NATL is the only basin for which the correlations between IBTrACS and reanalysis time series are significant (at the 90% CL) and higher than 0.5. In terms of ACE, correlations between IBTrACS and reanalysis time series are consistently higher than 0.6, highlighting once again how well reanalyses can simulate TC activity in the basin.

The time series of TC counts and ACE are analysed using the spectral methods outlined in sections 2.2.4 - 2.2.6. Figures 3.4a and 3.5a present the 1980-2013 time series of TC counts and ACE for IBTrACS and reanalyses. Results from the standard power spectrum and wavelet analysis of the time series are presented on figures 3.4b, 3.4c, 3.5b and 3.5c. The different reanalysis spectra, which are combined into one spectrum (blue line), are compared against the corresponding IBTrACS spectrum (green line). For the wavelets, the mean of the wavelet reanalysis spectra is computed (shown with colours) and it is compared against the IBTrACS wavelet spectrum (black contour lines). The shaded area indicates the COI.

Significant peaks within the 2-8-year power band are detected from the standard power spectrum method, a power band typically associated with ENSO, hinting at ENSO influence on hurricane activity for the 1980-2013 period. Given the short records of TC counts and ACE that are analysed, there is considerable difficulty in resolving peaks in power on decadal time scales. Providing the ability to detect peridiocities in localised time-frequency domain, in terms of the frequency of Atlantic systems, wavelet analysis results show significant regions within the 2-3 and 5-7 year bands for the 2004-2008 and 1994-2005 periods, respectively (fig. 3.4c). In terms of ACE, there is a consistent significant signal around the 3-yr-period band, positioned in the mid-1990s, marking the shift towards more frequent above-normal hurricane seasons (fig. 3.5c).

Tables 3.2a and 3.2b display Pearson correlation coefficients between the time series of

(a) Time series

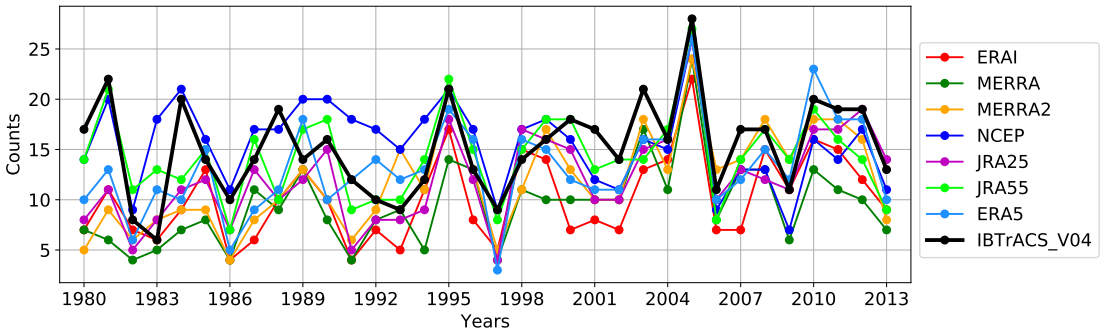

(b) Standard power spectrum

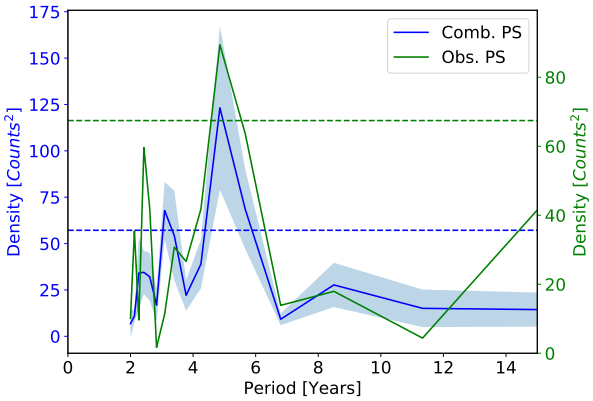

(c) Wavelet spectrum

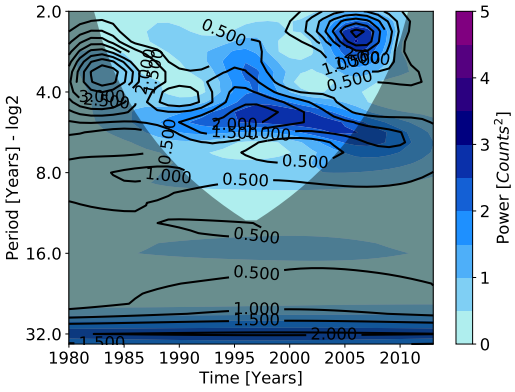

Figure 3.4: (a) Time series of counts for NATL; b) Standard power spectrum analysis for the time series. The individual reanalysis spectra are combined into one (blue line) and they are compared against the IBTrACS power spectrum (green line). The dashed lines indicate the 95% confidence level. The shaded area indicates the 95% confidence intervals for the combined spectrum; c) Mean of the seven reanalysis wavelet spectra (colours) and IBTrACS wavelet spectrum (black contours) of TC counts time series. The shaded area indicates the COI.

(a) Time series

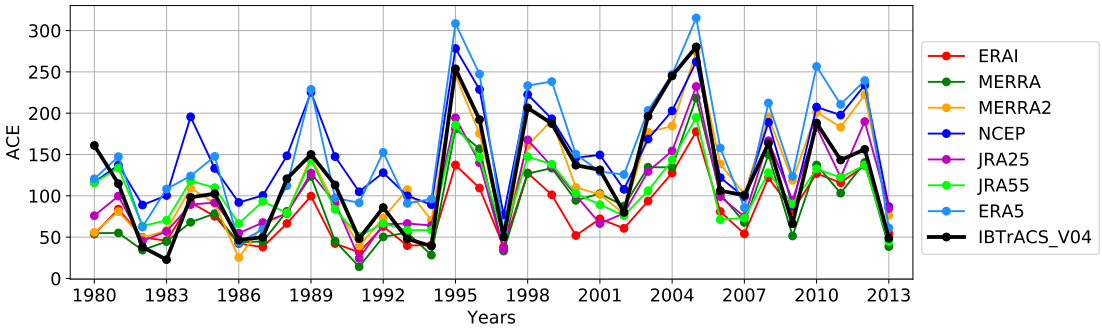

(b) Standard power spectrum

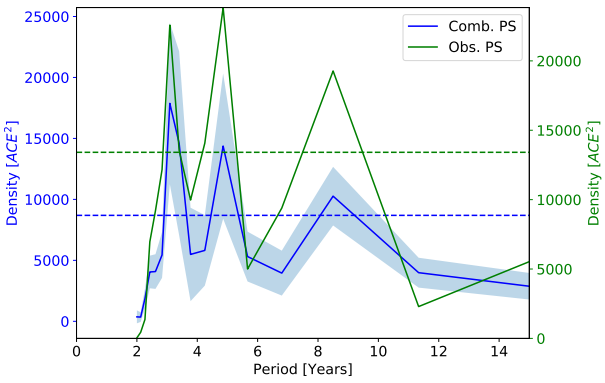

(c) Wavelet spectrum

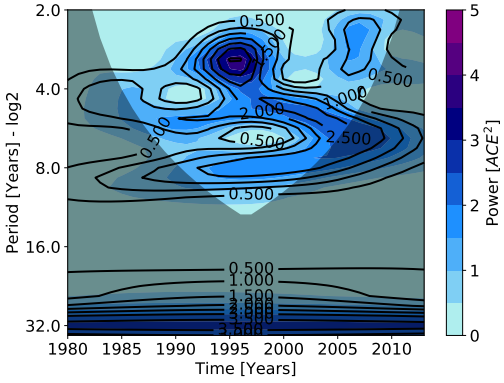

Figure 3.5: (a) Time series of ACE for NATL; b) Standard power spectrum analysis for the time series. The individual reanalysis spectra are combined into one (blue line) and they are compared against the IBTrACS power spectrum (green line). The dashed lines indicate the 95% confidence level. The shaded area indicates the 95% confidence intervals for the combined spectrum; c) Mean of the seven reanalysis wavelet spectra (colours) and IBTrACS wavelet spectrum (black contours) of TC counts time series. The shaded area indicates the COI.

Table 3.2: Pearson correlations between the time series of NATL annual (a) TC counts and (b) ACE of IBTrACS and reanalyses with the seasonal climate indices for the 1980-2013 period. Correlations which are significant at the 90% CL are in bold.

	QBO	AMM	ENSO	AMO	PDO
IBTrACS	-0.26	**0.54**	**-0.49**	**0.58**	**-0.37**
ERAI	-0.09	**0.64**	**-0.44**	**0.62**	**-0.45**
MERRA	**-0.31**	**0.58**	**-0.35**	**0.63**	-0.20
MERRA2	-0.19	**0.52**	**-0.37**	**0.66**	**-0.40**
NCEP	**-0.32**	0.18	**-0.40**	0.07	0.06
JRA25	-0.22	**0.69**	**-0.42**	**0.72**	**-0.43**
JRA55	-0.13	**0.53**	**-0.31**	**0.47**	-0.25
ERA5	**-0.30**	**0.59**	**-0.48**	**0.57**	**-0.38**

(a) TC counts

	QBO	AMM	ENSO	AMO	PDO
IBTrACS	-0.13	**0.68**	**-0.44**	**0.66**	**-0.32**
ERAI	-0.22	**0.65**	**-0.39**	**0.65**	**-0.40**
MERRA	-0.19	**0.61**	**-0.41**	**0.68**	**-0.35**
MERRA2	-0.19	**0.64**	**-0.36**	**0.72**	**-0.42**
NCEP	-0.26	**0.54**	**-0.49**	**0.53**	**-0.34**
JRA25	-0.18	**0.69**	**-0.40**	**0.72**	**-0.40**
JRA55	-0.21	**0.56**	**-0.41**	**0.53**	-0.25
ERA5	-0.17	**0.62**	**-0.43**	**0.62**	**-0.35**

(b) ACE

TC counts and ACE, respectively, from IBTrACS and reanalyses with the May-November averaged climate indices (QBO, AMM, ENSO, AMO and PDO) for the 1980-2013 period. It can be seen that both counts and ACE are significantly anticorrelated with ENSO for all datasets. In addition, for the majority of the datasets, the time series are significantly correlated with the AMM and the AMO indices, and anticorrelated with the PDO index. Lastly, for only three of the datasets the time series of counts are significantly anticorrelated with QBO.

According to the literature, since 1995 there has been an increase in Atlantic TC activity. This increase has been attributed to a combination of the AMO (through SSTs and VWS) along with increasing SSTs (due to climate change) influencing TC activity (Goldenberg et al., 2001). According to Bell and Chelliah (2006), TC activity in the basin can be influenced by both ENSO and multi-decadal signals. For example, during a high-activity era such as the one since 1995 (which has been associated with the warm phase of AMO; Goldenberg et al. (2001)) an El-Niño (like the 1997 event) is likely to result in a near-normal TC season, while a La-Niña (like the 1998-1999, 2020 events) is likely to result in an above-normal season. It is, therefore, possible that, even though the frequency of the AMO may not be detectable, the multi-decadal mode of variability may still influence Atlantic TC activity through ENSO, whose frequency is detectable in most

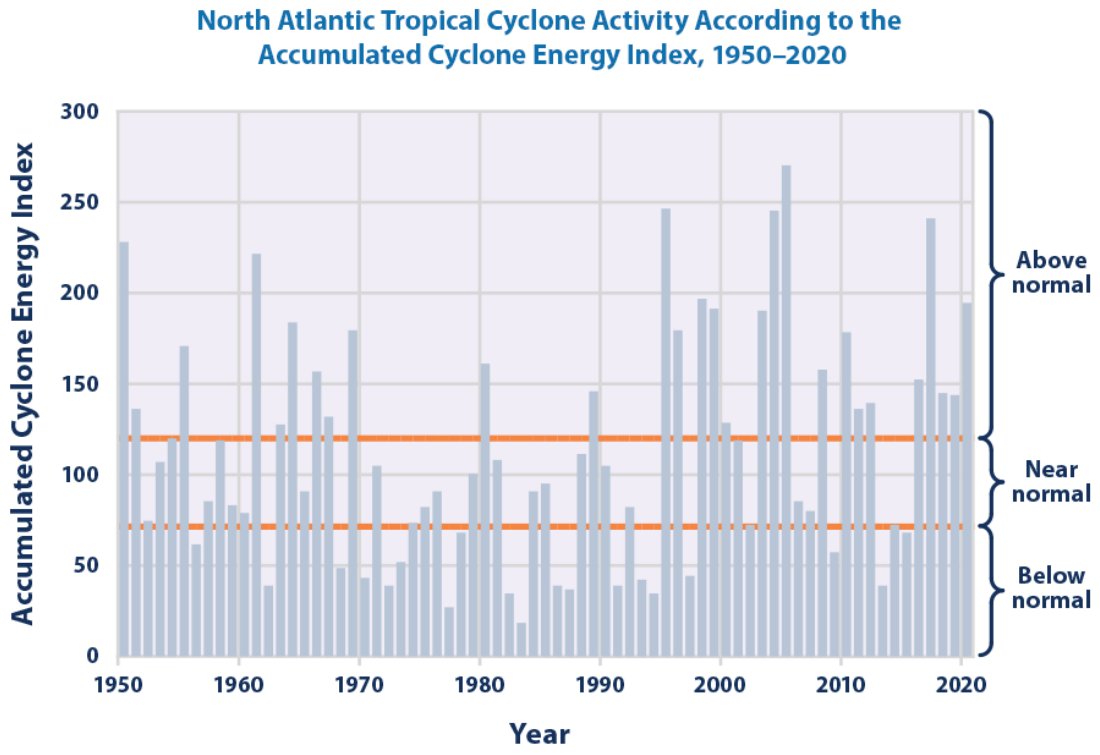

Figure 3.6: NATL ACE index for the 1950-2020 period. Source: U.S. (2021)

reanalysis wavelet spectra during the 1995-2005 period. Various studies (Klotzbach and Gray, 2008; Knight, 2005; Zhang and Delworth, 2006) have also suggested that fluctuations in the strength of the AMO likely drive the Atlantic TC variability since the mid-1990s, whereas Mann and Emanuel (2006) have argued that the increase in TC activity during this period is more likely to be associated with anthropogenic factors. According to the ACE index for 1950-2020 (obtained from the Atlantic Hurricane Database Re-analysis Project; U.S. (2021)), shown on figure 3.6, almost two thirds of the 26 hurricane seasons since 1995 were categorized as above normal. Given that, since 1995, there has been an increase in not only ACE (as shown on fig. 3.5a) but in TC counts as well, it is very difficult to attribute the increasing ACE trend to either only an increase of counts or to an increase in both counts and intensity.

Upon examining the drivers of TC activity under the current climate using the EOTs method, results showed that for each dataset the point explaining the majority of variance in the basin is positioned in the MDR. As shown on figure 3.7a, the EOT1 points are

(a) Locations for IBTrACS and reanalyses EOTs

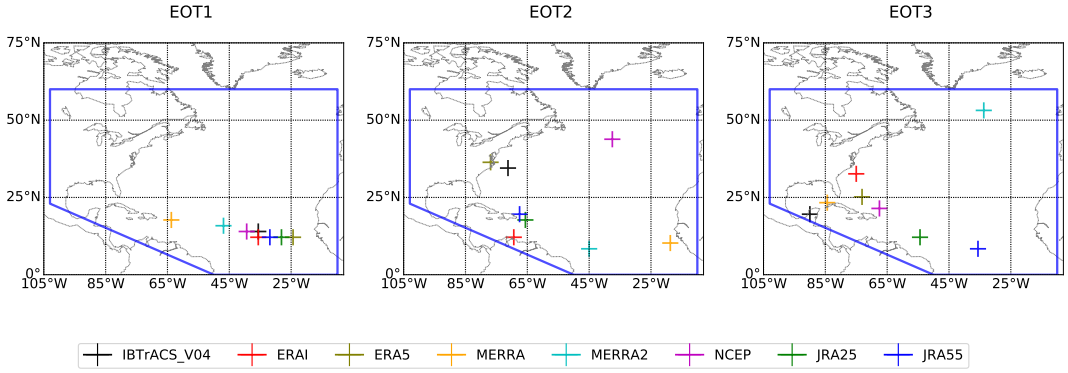

(b) SST regression patterns for IBTrACS. The HadISST SST field is regressed onto the IBTrACS EOTs

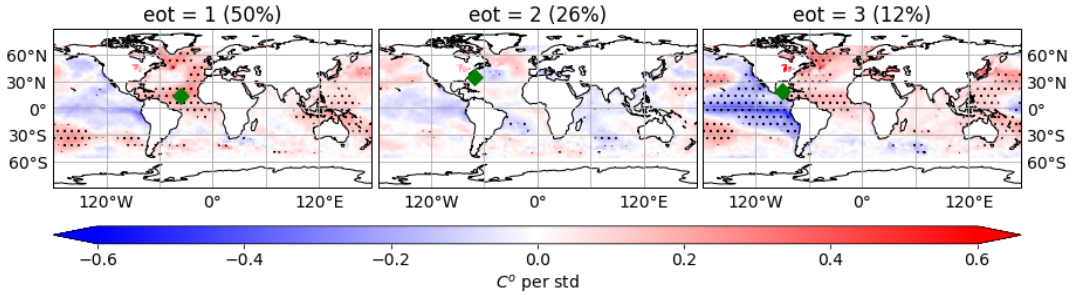

(c) VWS regression patterns for IBTrACS. The ERA5 VWS field is regressed onto the IBTrACS EOTs

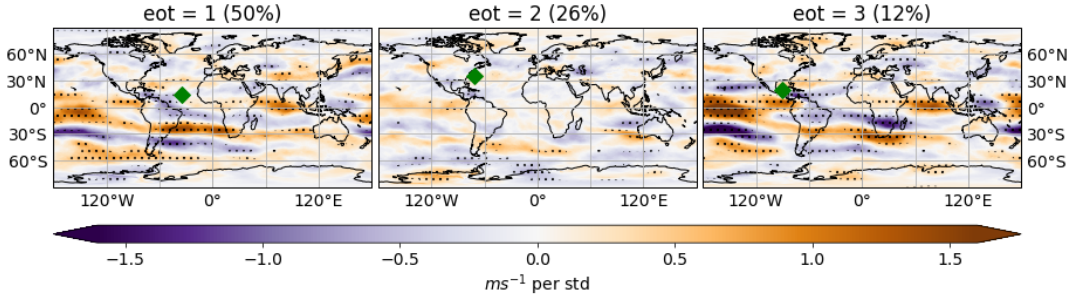

(d) Correlations between EOTs and May-November average climate indices

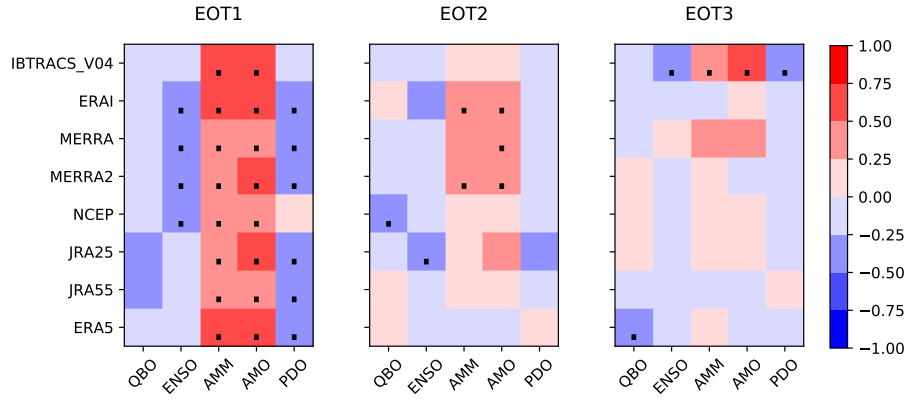

Figure 3.7: Results of EOT analysis for NATL under the current climate for IBTrACS and reanalyses. On b and c, locations of EOTs are indicated with a green marker and the amount of variance explained is in parenthesis. Significance at the 90% CL is indicated with dots on b, c and d.

closely located, with the exception of MERRA which is positioned near the Caribbean Islands, and each one of them explains more than 50% of the variability in the basin (fig. 3.8). It is possible that the agreement in the position of EOT1 in the MDR is attributed to the high-level of predictability of TCs in the basin. Lastly, it was found that three EOTs were sufficient in order to explain at least 75% of the variance in the basin.

Spectral analysis of the EOT1 time series shows periodicities on interannual time scales at frequencies similar to ENSO, but not on decadal time scales. Figures 3.7b and 3.7c, respectively, present results of the HadISST SST and ERA5 VWS fields being regressed onto the first three IBTrACS EOT time series. Even though results for the reanalyses are not shown, they indicate that TC activity in the basin for six of the datasets is influenced by cold SSTs in the Eastern and Central Pacific, typically associated with La-Niña events (inverse SST pattern of fig 1.1) and warm SSTs in the western and north western parts of the basin, conditions typically associated with the cold phase of PDO (inverse SST pattern of fig. 1.4). Simultaneously, TC activity in the MDR in all datasets is influenced by local warm SSTs, usually representative of the AMM (SST pattern on fig. 1.3), as well as warm SSTs in the Northern part of the Atlantic basin (near Greenland) which are associated with the warm phase of the AMO (SST pattern on fig. 1.2). Lastly, the ERA5 VWS regression pattern shown on figure 3.7c indicates that increases in TC activity are linked to strong VWS in Central Pacific and North Indian Ocean and weak VWS in the Atlantic, pattern usually associated with how the Walker Circulation is modified during a La-Niña event.

In order to back up the qualitative interpretation of the regression patterns, the EOT time series are correlated with the May-November averages of the climate indices. The Pearson correlation coefficients are presented on figure 3.7d with the dot indicating which coefficients are significant at the 90% CL. It can be seen that AMM and AMO have a robust moderate to strong positive relationship with the TC activity in the MDR for the first EOT, while ENSO and PDO have a moderate negative influence in more than half of the datasets. Once the influence of the EOT1 is removed, the base points for the second mode are no longer clustered and the percentage of variance explained by EOT2 drops to below 25%. The EOTs that remain in the MDR are moderately positively influenced by only AMM and AMO via warm SSTs. For IBTrACS the cold phases of ENSO and PDO and the warm phases of AMM and AMO appear to influence TC activity in the western tropical part of the region (inside the Gulf of Mexico) for EOT3, which explains around

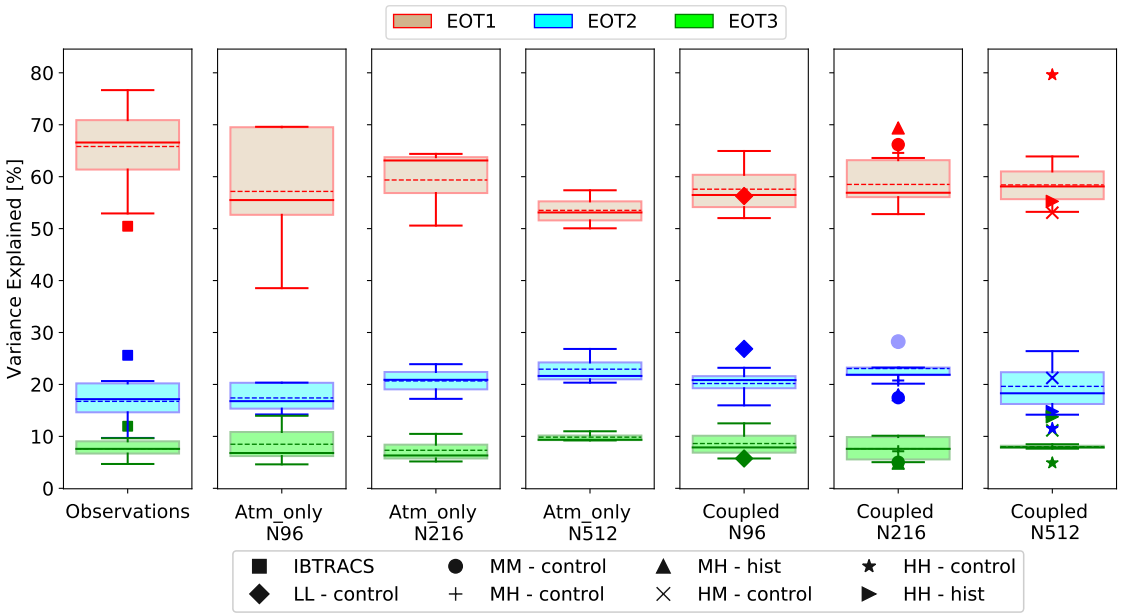

Figure 3.8: Percentage of variance explained by the EOTs for NATL. Column 1: Reanalyses (as an ensemble) against IBTrACS (■); Columns 2-4: ensemble of atm-only runs split by atmospheric resolution; Column 5: ensemble of LL historic runs against the control run (♦); Column 6: ensemble of MM historic runs against the MM control (●), MH control run (+) and MH historic run (▲); Column 7: ensemble of HM historic runs against HM control run (×), HH control run (★) and HH historic run (►). Faded circles (●) show outliers. Dotted lines show the ensemble means.

12% of variance. However, this result was deemed unreliable since the location of EOT3 is very close to the border with EPAC.

Even though the present study investigates the connections to only a few specific climate modes through only two main drivers, in the future it is important to broaden the investigation. By examining the relationship between Atlantic TC activity and the Sahel rainfall, it has been found that the Sahel precipitation as well as the NAO, strongly influence TC activity in the Atlantic during unfavourable conditions such as the ones during a negative AMO phase (Fink et al., 2010). Furthermore, during favourable conditions induced by a warm AMO phase, Caron et al. (2015) determined that Atlantic TC activity is linked with the variability associated to the solar cycle as well as dust concentrations over the basin. Li et al. (2015) found that the Interdecadal Pacific Oscillation (IPO), a Pacific decadal mode which covers a larger portion of the basin compared to PDO, can suppress TC activity in the Atlantic during its positive phase, likely by shifting the location

of increased VWS in the Atlantic.

3.3.2 Models - Current Climate

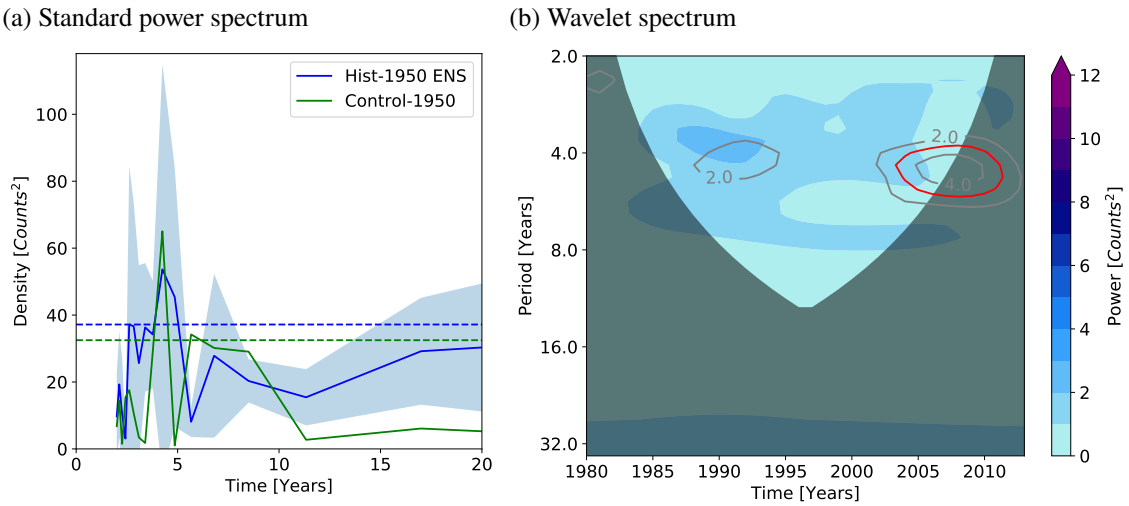

Figure 3.9: Spectral analysis on NATL TC counts for the coupled HM runs: (a) Power spectrum: The spectra of the HM hist-1950 ensemble runs are combined into one (blue line) and are compared against control-1950. The dashed lines indicate the 95% confidence level. The shaded area indicates the 95% confidence intervals for the mean power spectrum; (b) Wavelets: The grey contour lines indicate the spectrum for the control run. Colors indicate the mean spectrum for the ensemble of HM hist-1950 runs. The shaded area indicates the COI, while the 95% CL for the control run is shown with red contours.

The time series for both frequency and ACE for the atm-only experiments for the 1980-2013 are significantly positively correlated with the corresponding time series from IBTrACS, in contrast to the coupled runs. Standard spectral and wavelet analysis of the time series for both counts and ACE, resulted in significant peaks at periodicities similar to the ones found in the observations. An example of this is presented on figure 3.9 which shows results from the spectral analysis on time series of TC counts for the coupled HM runs.

Pearson correlations between the metrics (time series of annual TC counts and ACE) and the May-November averaged climate indices, presented on figure 3.10, show that almost all the atm-only experiments have significant moderate-to-strong anticorrelations with ENSO for both frequency and ACE. However, such relationships are not present for

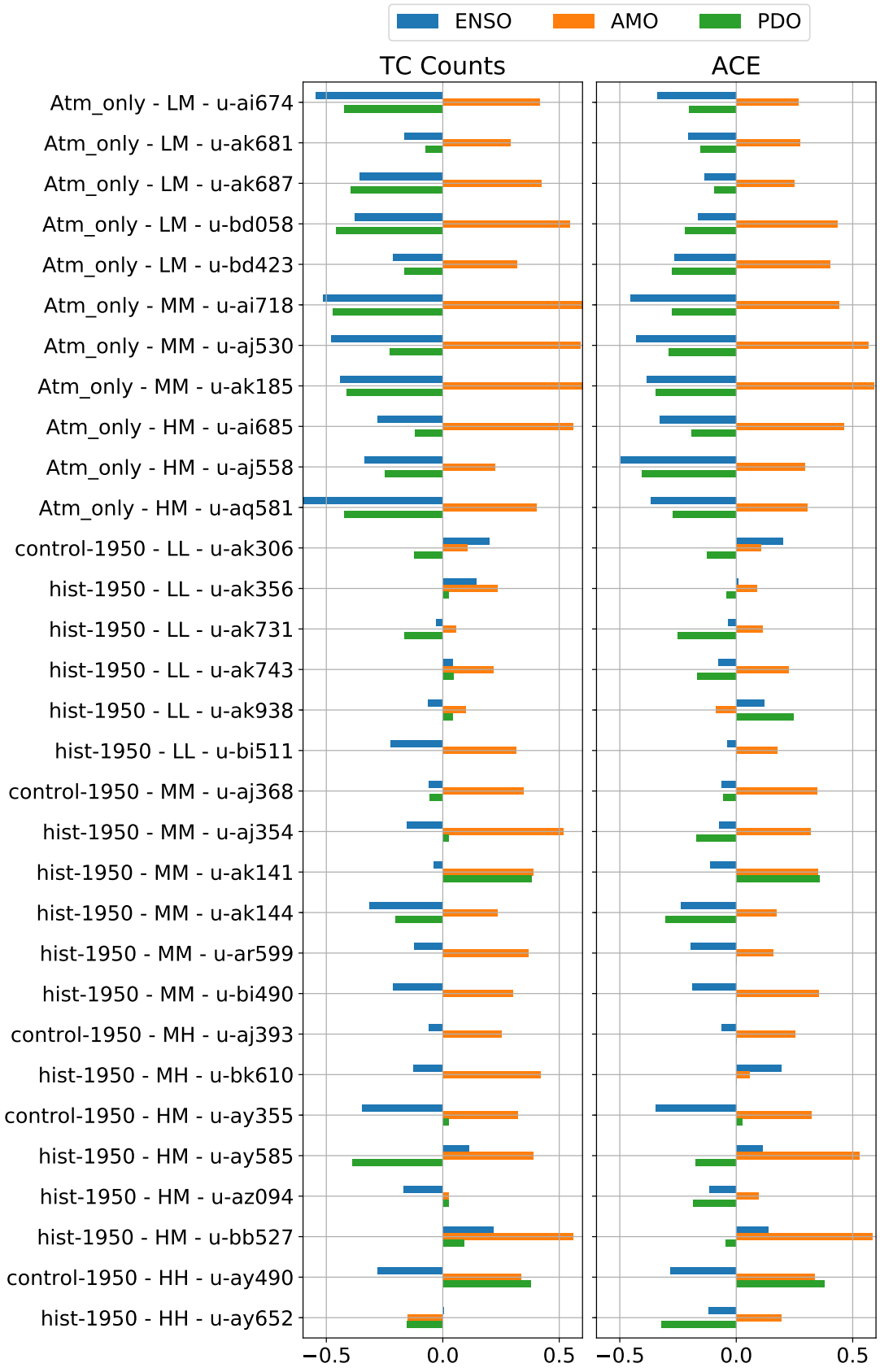

Figure 3.10: Pearson correlations between the time series of NATL annual TC counts and ACE of models with the seasonal climate indices for the 1980-2013 period. Hatched bars indicate the correlations that are significant at the 90% CL.

the coupled runs, irrespective of resolution. As it will be seen further on in the study, for the rest of the basins there is a lack of significant correlations with the ENSO index (except over Central Pacific) for most coupled runs. It is important to note here that this difference is only seen for the coupled runs, since they are not forced by the same observed SSTs as is the case for the atm-only runs. One possible explanation is that this is related to the teleconnections and to the strength of ENSO events in the coupled runs. It might, also, be due to the fact that only the May-November averaged climate index is examined across all basins. Therefore, it is important to additionally examine lagged correlations for the rest of the basins.

Almost all the atm-only simulations have significant moderate-to strong positive correlations with AMO in terms of counts, whilst only eight of them have significant moderate or strong positive correlations with the time series of ACE, indicating that the climate mode has a greater impact on the frequency of TCs rather than on intensity. Additionally, the majority of MM, MH, HM and HH coupled runs show significant moderate or strong positive correlations with the AMO index for the two metrics, in contrast to the LL runs which have weak and not significant correlations with the AMO index. The TC frequency in 6 of the atm-only and in 1 coupled HM hist-1950 runs appears to be anticorrelated with the May-November averaged PDO index, while 2 of the coupled runs (1 MM hist and the HH control) display significant moderate positive correlations with the index. The climate mode (PDO) appears to have a greater influence on the frequency of TCs for this particular basin, since more significant correlations are observed between the index TC counts compared to ACE.

The SST and VWS are also examined as drivers in the model simulations in order to first examine and understand the current climate in the model before formally assessing the impact of climate change and longer periods.

Before concentrating on the interpretation of the results for the NA region, it is worth noting the consistency between results from the hist-1950 runs and the results from the reanalysis and IBTrACS in terms of the drop in the percentage of variance explained by EOT1 and EOT2 for the NATL region (fig. 3.8). The respective points explaining the majority of variance for the LL (control and ensemble of historic) runs are located in the western part of the basin, near Florida, the Gulf of Mexico and along the TC re-curving path (fig. 3.11a). This result was expected since TCs in the low-resolution simulations are

more concentrated in that part of the region instead of the MDR, as was observed from the mean track density in the basin (fig. 3.1). From the regression plots (not shown) none of the EOT1 patterns display a robust known canonical pattern. It is possible that this might be due to the fact that there are less TCs (than observed) found in the low-resolution simulations as is evident from track densities on figure 3.1 (e and f)), since the skill in simulating TC-like features depends on resolution (Roberts et al., 2020a).

For the higher resolution simulations (MM and HM), EOT1 for the MM control run is positioned on Florida (frequently impacted by TCs) as shown on figure 3.11a, while the respective base point for the HM run is located out of the main region for TC activity for reasons unknown at this stage, and it is therefore excluded from the analysis. In contrast, for seven out of eight historic runs the base point explaining the majority of variability is positioned in the MDR. Results from the linear regression of SSTs and VWS on the EOT time series are displayed on figures 3.11b and 3.11c, respectively. They show an AMO or AMM-resembling SST pattern in at least one of the first three EOT regression patterns for six of the hist-1950 runs, where the base point was positioned in the MDR, such as the SST pattern shown for EOT2. For the same EOT, the VWS pattern appears to be a combination of the local pattern associated with the warm phase of the AMM with the La-Niña VWS pattern over the Atlantic basin.

Compared to the robust La-Niña feature found in the observations, it might be surprising that the AMM or the AMO appear to have more influence on TC activity in the MDR than ENSO. This difference can perhaps be attributed to the difference in tele-connections between GCMs and reanalyses. Reanalyses are constrained by observations, whereas GCMs are not. Previous versions of this model have been found to not be able to capture the ENSO-TC teleconnection in the region (Bell et al., 2014). It is, therefore, possible that for these model simulations the Atlantic modes (AMM and AMO) have a greater influence on the NATL TC activity compared to the ENSO-TC teleconnection, or that the SST pattern resembles the AMO's canonical pattern. In addition, on interannual time scales the AMM is driven by ENSO (Amaya et al., 2017; García-Serrano et al., 2017; Oettli et al., 2016), while on decadal time scales it can also be excited via the AMO (Vimont and Kossin, 2007). The AMM's frequency is similar to ENSO's and it would be difficult to distinguish it from its frequency on a power spectrum. On the other hand, on decadal time scales, the AMM's periodicity is around 11-13 years (Veiga et al., 2020).

(a) Locations of EOTs for all the model runs

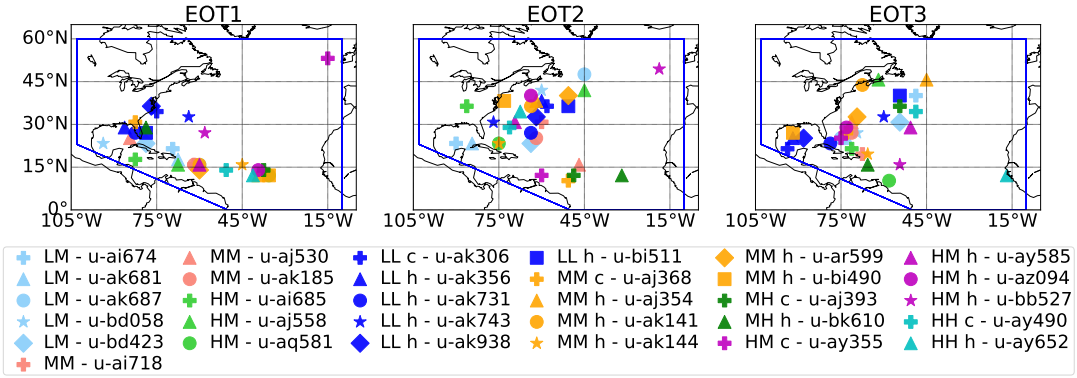

(b) SST regression patterns for the u-aj368 run.

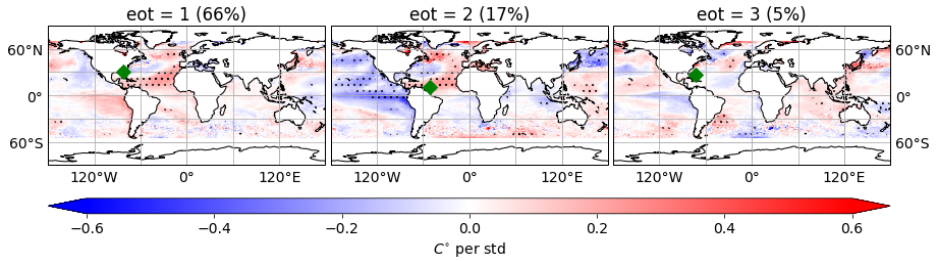

(c) VWS regression patterns for the u-aj368 run

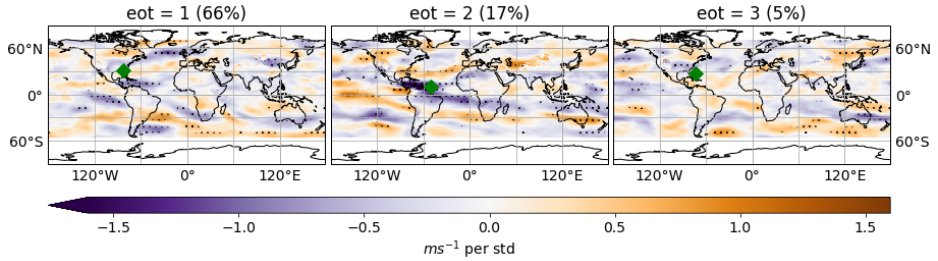

(d) Summary statistics of the Pearson correlation coefficients between the NATL EOT time series for the different model simulations and the May-November averaged ENSO, AMO and PDO indices.

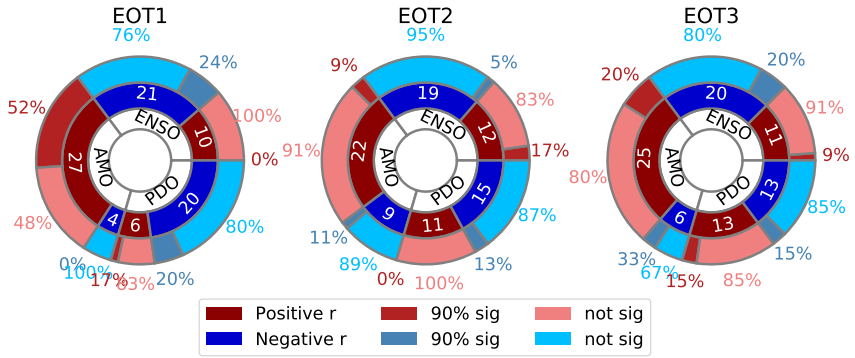

Figure 3.11: EOT results for TC variability in NATL for the model simulations. Location of EOT is shown with green marker and significance at the 90% CL is indicated with dots on b and c. Period examined is 1980-2013. For the correlations dark red (blue) colors indicate how many of the 31 models have positive (negative) correlations with each index, medium red (blue) indicate how many of the dark red (blue) correlations are significant at the 90% CL, while light red (blue) indicate how many are not significant.

Both frequencies have been found in the power spectra of the EOT time series. Therefore, it is possible that the presence of the AMM is due to modulation by the other modes of variability.

Lastly, EOT1 base points for the HH-control run and the respective historic run are located in the MDR (fig. 3.11a). The amount of variance explained is 80% and 55% for the control and the historic run, respectively. A weak AMM pattern is found on the regression map for the control run, but no known canonical pattern is displayed for the historic run. Even though both EOT2 base points are closely located along the recurving track and the amount of variance explained by each of them is similar, there is no agreement or conclusion arising from the equivalent regression maps. Since only one HH control and one historic run are examined in the study, it is not possible to arrive to a conclusion. In the future, having more ensemble members of this or higher resolution to analyse might provide useful insight on the drivers of TC variability in high resolution climate models.

Figure 3.11d presents the Pearson correlation coefficients between the first three EOT time series for all the model runs and the seasonally averaged climate indices. The figure is a summary plot of how many EOTs of the model experiments are positively or negatively correlated with ENSO, AMO and PDO. For example, for 27 of the simulations, EOT1 has positive correlations with the AMO index (dark red), 52% of which are significant (semi dark red). In addition, negative correlations, indicated by dark blue, are observed between EOT1 and ENSO (PDO) for 21 (20) of the runs, 24% (20%) of which are significant (semi dark blue). These results, further support the conclusion that the Atlantic modes (AMM and AMO) have a greater, more significant, impact on TC activity compared to the Pacific modes (ENSO and PDO). A caveat of this analysis is that only three climate indices are taken into consideration for the analysis of model simulations. It is very important that future work includes investigation of this climate mode in order to provide further understanding of the drivers of TC variability in the Atlantic.

3.3.3 Summary

In summary, the observed TC activity in the Atlantic MDR under the current climate (1980-2013) which exhibits high variability is mainly driven by local warm SSTs associated with the warm phases of the AMM and the AMO, cold SSTs in the tropical eastern and central parts of the Pacific ocean linked to La-Niña events and SSTs describing the cold phase

of PDO. Lastly, VWS conditions associated with the Walker Circulation during La-Niña events (strong VWS in central Pacific and North Indian Ocean and low VWS in the Atlantic) also aid increases in TC activity in the Atlantic MDR. The primary driver of TC variability for the model simulations appears to be the AMO via SSTs in the MDR, which leads to enhanced convection aiding the formation and development of TCs during its warm phase and inhibiting it during its cold phase. ENSO influence on TC variability in the basin under the current climate, albeit not as a robust as the influence by the AMO, is present in all datasets and tools utilised in the study. It is true that previous versions of the model have had adequate ENSO representation and that HadGEM3-GC3.1 has improved both the simulation of ENSO as well as TC-representation (Kuhlbrodt et al., 2018; Menary et al., 2018; Roberts et al., 2019; Williams et al., 2018). Previous studies on other models such as Bell et al. (2014) have highlighted the importance of improving the ENSO-teleconnections relationship. It is possible that further work on HadGEM3, focusing on this area of research, in conjunction with running the model on finer resolution can improve the influence ENSO has on TCs in the basin.

3.4 Eastern Pacific

3.4.1 Observations - Current Climate

According to IBTrACS, TC activity in terms of frequency and ACE for the EPAC accounts for 22% of the NH's activity (fig. 3.2). For the reanalyses the percentage is within 17-24% and 10-17% for frequency and ACE, respectively (fig. 3.2). The time series of TC counts (fig. 3.12a) do not display any trends, however, there is a noticeable decrease in the number of TCs and ACE after 1995. There is a larger spread between the different reanalysis datasets before 1995 compared to after 1995, however the different reanalyses, with the exception of ERAI and ERA5, display significant (at the 90% CL) moderate to very strong positive correlations between their time series and those from IBTrACS. In terms of ACE, the same is true with the exception of ERAI. The rest of the reanalyses (not MERRA) show strong to very strong positive correlations with the IBTrACS ACE time series. The reason MERRA does not display such strong correlation with IBTrACS in terms of ACE is attributed to the fact that MERRA has the weakest maximum wind speeds (Hodges et al., 2017).

Significant peaks in the 2-5-year-band, hinting at ENSO influence on TC activity in the basin, are displayed in some the individual reanalysis power spectra, even though none are seen in the combined reanalysis spectrum, both for ACE and counts (fig, 3.12b). No robust conclusion is drawn from the wavelet analysis since, in terms of frequency, four of the reanalysis wavelet spectra displayed significant regions within the 2-5-year-band (fig. 3.12c), hinting once again on ENSO influence, but not in a common time period. Just like in the standard power spectrum, for IBTrACS the wavelet spectrum revealed one significant region in the 7-8-year-band (fig. 3.12c), localised around the early to mid 90's, roughly around the time period during which the AMO and PDO changed phases. In terms of ACE, IBTrACS and JRA25 show exactly the same significant region that was found for IBTrACS in terms of counts. The rest of the reanalyses (with the exception of NCEP and JRA55) showed significant peaks mostly within ENSO's periodicity around 1995.

Moderate significant positive correlations with the May-November average of ENSO and PDO indices and moderate to strong significant anticorrelations with the AMO index (in terms of counts) are found for three and four of the reanalysis datasets, respectively, as shown on table 3.3. Results for ERAI stand out since, instead of an anticorrelation,

(a) Time series

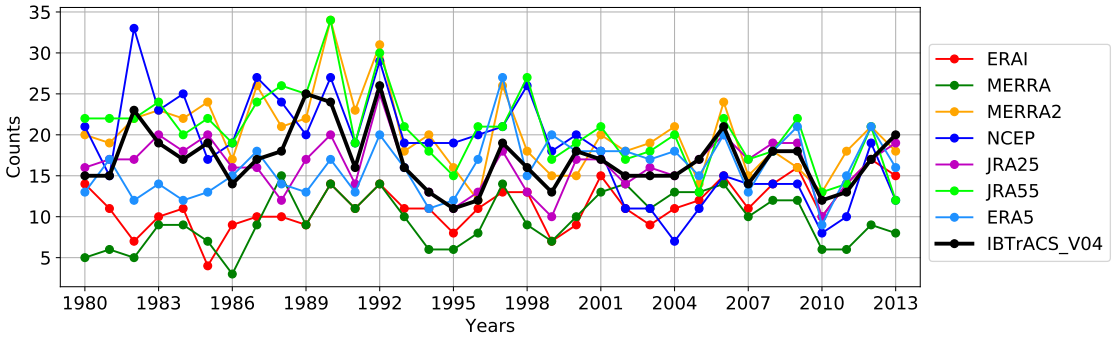

(b) Standard power spectrum

(c) Wavelet spectrum

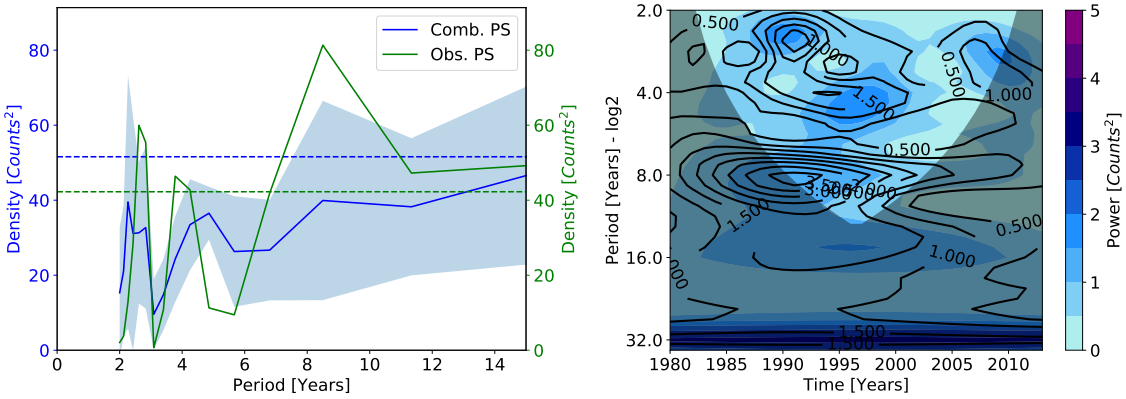

Figure 3.12: (a) Time series of TC counts for EPAC; b) Standard power spectrum analysis for the time series. The individual reanalysis spectra are combined into one (blue line) and they are compared against the IBTrACS power spectrum (green line). The dashed lines indicate the 95% confidence level. The shaded area indicates the 95% confidence intervals for the combined spectrum; c) Mean of the seven reanalysis wavelet spectra (colours) and IBTrACS wavelet spectrum (black contours) of TC counts time series. The shaded area indicates the COI.

Table 3.3: Pearson correlations between the time series of EPAC annual (a) TC counts and (b) ACE of IBTrACS and reanalyses with the seasonal climate indices for the 1980-2013 period. Correlations which are significant at the 90% CL are in bold.

	QBO	AMM	ENSO	AMO	PDO
IBTrACS	0.14	-0.12	0.22	-0.24	0.15
ERAI	-0.08	**0.30**	0.20	**0.29**	-0.25
MERRA	0.06	0.09	0.16	0.13	0.08
MERRA2	**0.29**	-0.18	**0.38**	**-0.39**	**0.34**
NCEP	-0.08	**-0.40**	0.18	**-0.53**	**0.34**
JRA25	0.07	-0.16	**0.30**	-0.27	0.24
JRA55	0.03	-0.21	0.13	**-0.37**	**0.34**
ERA5	0.20	0.04	**0.45**	0.12	0.11

(a) TC counts

	QBO	AMM	ENSO	AMO	PDO
IBTrACS	0.20	**-0.34**	0.26	**-0.53**	**0.37**
ERAI	-0.16	0.18	**0.32**	0.24	-0.16
MERRA	0.05	0.03	**0.29**	0.10	0.17
MERRA2	0.23	-0.24	**0.54**	**-0.38**	0.27
NCEP	0.01	**-0.32**	**0.36**	**-0.54**	**0.41**
JRA25	0.12	-0.09	0.19	-0.18	-0.06
JRA55	0.08	**-0.42**	0.05	**-0.55**	**0.41**
ERA5	0.16	0.00	**0.44**	-0.00	0.10

(b) ACE

moderate positive significant correlations are found between the time series of counts and the two Atlantic modes (AMM and AMO indices). In terms of ACE, for six of the datasets, moderate to strong positive correlations (five of which are significant) are found with the May-November average with ENSO and for four of the datasets, moderate positive (three of which are significant) correlations are detected with the May-November averaged PDO index. For the Atlantic modes, moderate to strong significant anticorrelations with the May-November AMO index and moderate significant anticorrelations with the AMM index are found for four and three of the datasets, respectively (tab. 3.3). NCEP is the only dataset for which the relationships are significant at the 90% CL .

The EOT analysis shows that the points explaining the majority of variance in the basin for the reanalysis products are clustered in the eastern part of the tropical EPAC as displayed on figure 3.13a, while for IBTrACS EOT1 is located in the middle of the region. More than 57% of the basin is explained by EOT1 for each dataset (fig. 3.14). The percentage of variance explained by EOT2 drops to a range of 9-25% (fig. 3.14), while the majority of them relocate towards the centre if the basin (fig. 3.13a). For this region's TC activity, two EOTs are sufficient for explaining 75% of the variability.

Spectral analysis of the EOT time series with both the standard power and the wavelet spectrum have detected periodicities similar to ENSO's frequency in all datasets for the

(a) Locations for IBTrACS and reanalyses EOTs

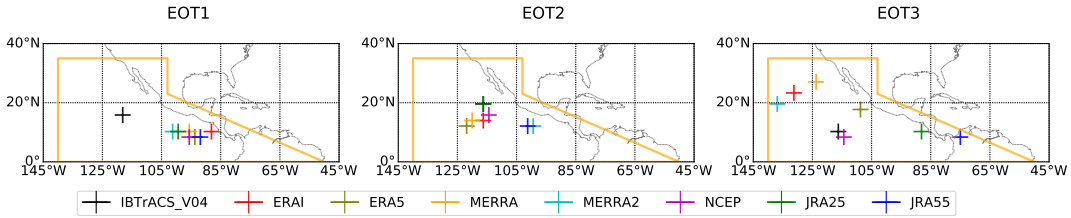

(b) SST regression patterns for IBTrACS. The HadISST SST field is regressed onto the IBTrACS EOTs

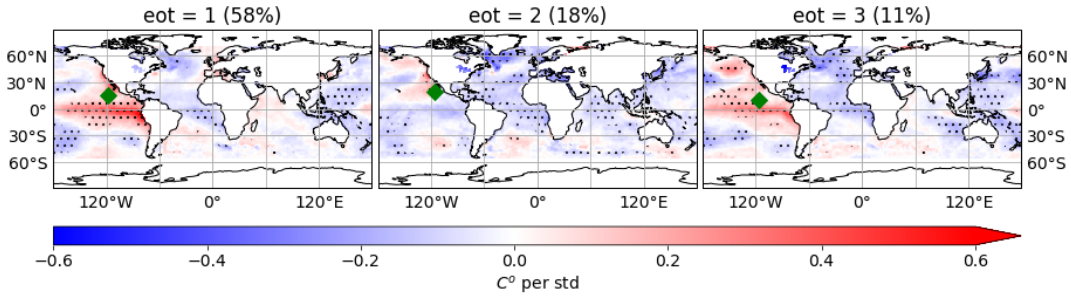

(c) VWS regression patterns for IBTrACS. The ERA5 VSW field is regressed onto the IBTrACS EOTs

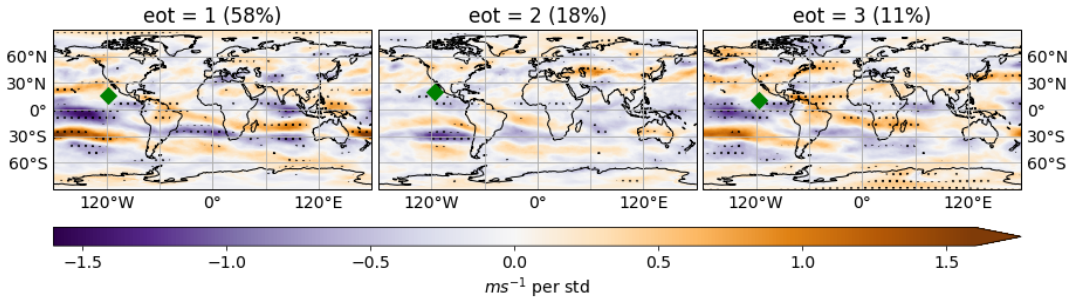

(d) Correlations between EOTs and May-November average climate indices

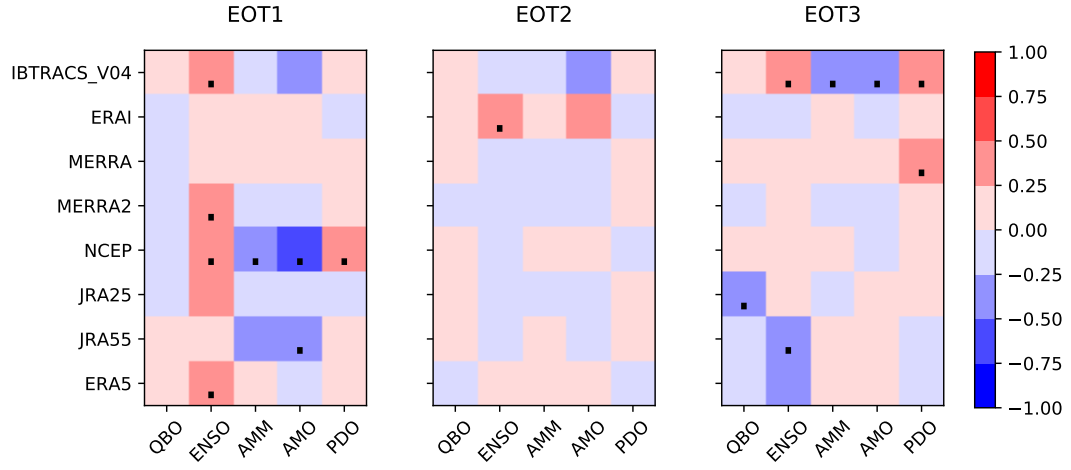

Figure 3.13: Results of EOT analysis for EPAC under the current climate for IBTrACS and reanalyses. Locations of EOTs are indicated with a green marker on b and c. Significance at the 90% CL is indicated with dots on b, c and d.

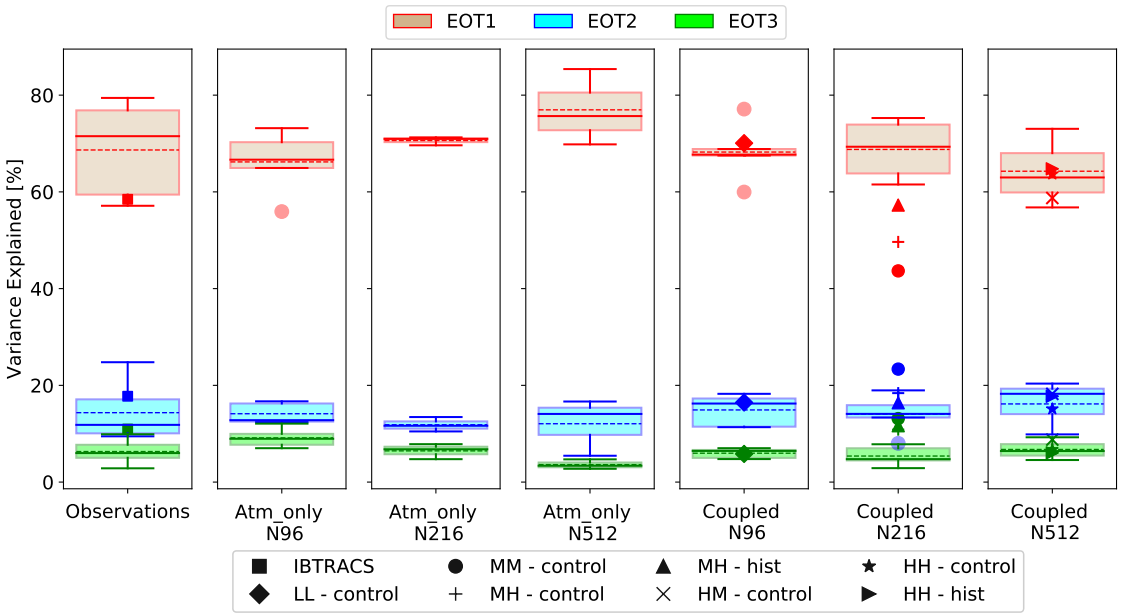

Figure 3.14: Percentage of variance explained by the EOTs for EPAC. Column 1: Reanalyses (as an ensemble) against IBTrACS (■); Columns 2-4: ensemble of atm-only runs split by atmospheric resolution; Column 5: ensemble of LL historic runs against the control run (♦); Column 6: ensemble of MM historic runs against the MM control (●), MH control run (+) and MH historic run (▲); Column 7: ensemble of HM historic runs against HM control run (×), HH control run (★) and HH historic run (►). Faded circles (●) show outliers. Dotted lines show the ensemble means.

first two EOTs. For five of the datasets the May-November averaged ENSO index shows a positive moderate (significant at the 90% CL in four datasets) relationship with the EOT1 time series (fig. 3.13d). NCEP is the only dataset for which TC activity at EOT1 is significantly moderately correlated with ENSO and PDO, significantly moderately anticorrelated with AMM and significantly strongly anticorrelated with the AMO.

From the SST and VWS regression maps for the IBTrACS EOTs presented on figures 3.13b and 3.13c, respectively, it is concluded that increases in TC activity in the eastern part of the region are associated with the warm phase of ENSO via warm SSTs in the eastern and central Pacific and low VWS in central Pacific, both of which are conditions favourable for TC formation and development. Regression maps of reanalysis EOTs (not shown) for which significant correlations ($r \geq 0.25$ or $r \leq -0.25$) with the climate indices are computed such as the one for IBTrACS, are characterised by patterns similar to the ones seen on the regression maps on figure 3.13. For NCEP, TC activity at EOT1 is additionally

driven by cold SSTs in the North Atlantic region, associated with the cold phases of the AMM and AMO. Finally, IBTrACS is the only dataset for which EOT1 and EOT2 are in the same location and EOT1 is influenced by both ENSO and the AMO, while EOT2 is driven only by AMO. EOT3 for IBTrACS, which explains around 11% of the variability in the basin, shows that variations in TC activity deep in the tropics are attributed to all modes except the QBO, a connection that can be also seen from the Pearson correlation coefficients on figure 3.13d.

Different studies have investigated the mechanisms responsible for TC activity in the EPAC, the majority of them focusing on Pacific climate modes (ENSO and PDO). Boucharel et al. (2016) discovered that an El-Niño event, characterised with warm SSTs concentrated in the eastern part of the Pacific, via redistributing the warm SSTs meridionally, acts as the main driver of TC activity. Moreover, Li et al. (2015) studied the influence of IPO, a possible manifestation of the PDO in a wider area of the Pacific ocean (Salinger et al., 2001), on TC activity in EPAC for a longer period than the one examined in this study. They found that during the warm phase of this inter-decadal Pacific mode, weaker VWS shear in the Pacific, leads to more TCs in EPAC, while the reverse occurs during the negative phase.

Not many studies, however, have been able to link the AMO to TC activity in the EPAC. It is worth exploring whether AMO has an indirect impact on TC activity in the basin. For example, Dong et al. (2006) has investigated how the AMO, through its warm phase, can modulate ENSO. By using a coupled model they showed that warm SSTs in the Atlantic during the warm AMO phase can generate latent heat anomalies. These anomalies will suppress convection and will lead to anomalous easterlies over the central and western part of the equatorial Pacific. As a result the thermocline will deepen in the west Pacific and it will propagate towards the central and eastern Pacific during the winter and spring, causing a weakening in coupled instability which is essential for an El-Niño. The study, however, did not investigate how a cold AMO phase might modulate ENSO. Is it possible that the inverse mechanism can lead to an enhanced El-Niño in a way that can influence the EPAC TC activity in coupled models such as NCEP? More investigation is essential in order to examine this theory.

3.4.2 Models - Current Climate

For this basin, there is better agreement between the atm-only models and IBTrACS in terms of frequency, rather than for ACE, as indicated by Pearson correlation coefficients. Power spectral analysis reveals once again significant peaks on inter-annual time scales, the majority of them not exceeding a periodicity of around 7 years. An example of standard power spectrum and wavelet spectrum results is shown on figure 3.15 for the time series of TC counts for the HM coupled runs.

ENSO influences TCs in terms of frequency and ACE, particularly for the atm-only experiments, as well as for a few of the higher (MM, MH, HM and HH) resolution coupled experiments, since moderate or strong significant correlations are found between the time series and the ENSO index as shown on figure 3.16. For all the MM and HM atm-only runs, there are significant moderate-to-strong anticorrelations with the May-November averaged AMO index, for both metrics (TC counts and ACE). Moreover, AMO appears to have a greater influence on ACE than on counts for the coupled simulations, since more significant anticorrelations are found for ACE compared to frequency. The PDO significantly influences TC activity in the EPAC basin in only two atm-only runs in terms of frequency and in four atm-only and one coupled hist-1950 runs in terms of ACE. The correlations between the time series and the seasonally averaged index are moderately positive.

The vast majority of EOT1s from the model simulations, irrespective of resolution and configuration, are located in the tropical part of the basin below $20^{\circ}N$ and within $115 - 85^{\circ}W$, as shown on figure 3.17a. As found by Roberts et al. (2020a), with higher resolution TC activity shifts slightly towards the south, something that is observed for the locations of EOT1s when comparing different resolutions. The distribution of variance explained by the EOTs in the model simulations is similar to the one seen for the observations (fig. 3.14), varying only in the fact that, the EOT1s for the different ensemble members explain similar amounts of variance. The vast majority of EOT1s, explain more than 55% of the variance in the basin indicating that there is one primary driver of TC variability, whilst the percentage of variance explained by EOT2s and EOT3s is very small.

Pearson correlations between the EOTs and the seasonally averaged climate indices, the summary of which is presented on figure 3.17d, show that, for five atm-only runs and 1 coupled run, significant positive (negative) correlations are found between EOT1s

(a) Standard power spectrum

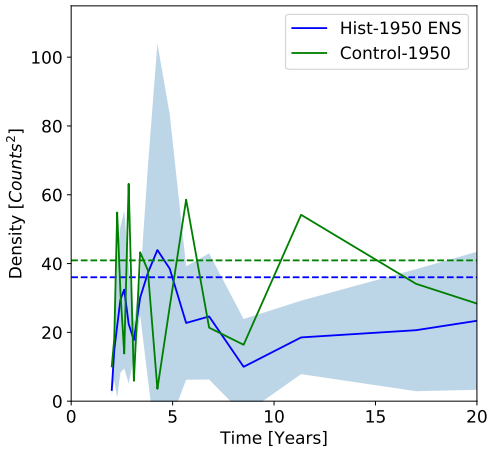

(b) Wavelet spectrum

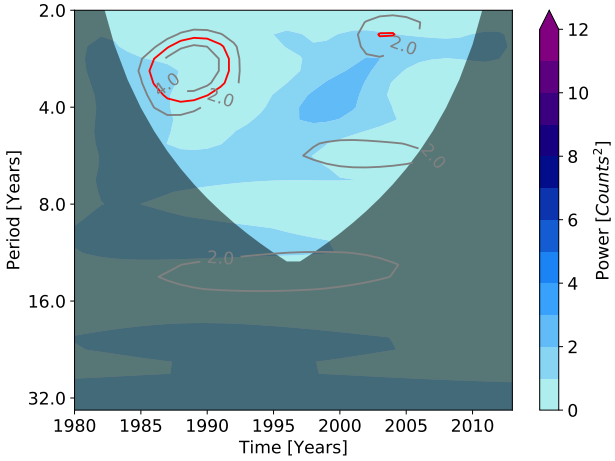

Figure 3.15: Spectral analysis on EPAC TC counts for the coupled HM runs: (a) Power spectrum: The spectra of the HM hist-1950 ensemble runs are combined into one (blue line) and are compared against control-1950. The dashed lines indicate the 95% confidence level. The shaded area indicates the 95% confidence intervals for the mean power spectrum; (b) Wavelets: The grey contour lines indicate the spectra for the control run. Colors indicate the mean spectrum for the ensemble of HM hist-1950 runs. The shaded area indicates the COI while the 95% CL for the control run is shown with red contours

and ENSO (AMO). In general, for 25 of the models anticorrelations with the AMO are found, whereas positive correlations are observed for with ENSO and PDO for more than half of the runs. The only coupled run for which significant relationships are found with both ENSO and AMO is the coupled control-1950 MM run (u-aj368), for which SST and VWS regression maps are displayed on figures 3.17b and 3.17c. For this run, as well as for 5 atm-only runs, TC activity at EOT1 is influenced by warm El-Niño-like SSTs in the Pacific region, as well as cold SSTs in the Atlantic, in a cold-AMO-phase-resembling pattern. Furthermore, the VWS distribution throughout the globe points again to El-Niño-like conditions since increases in TC activity at the EOTs location are linked to weak VWS in the central Pacific and increased VWS in the Atlantic, locations associated with the ascending and descending branches of the Walker Circulation during such conditions. Activity at EOT3, which is located further north, near the edge of the tropics, appears to me more prone to La-Niña conditions as a cold SST tongue is observed in the Pacific and weak VWS in the Atlantic (fig. 3.17c).

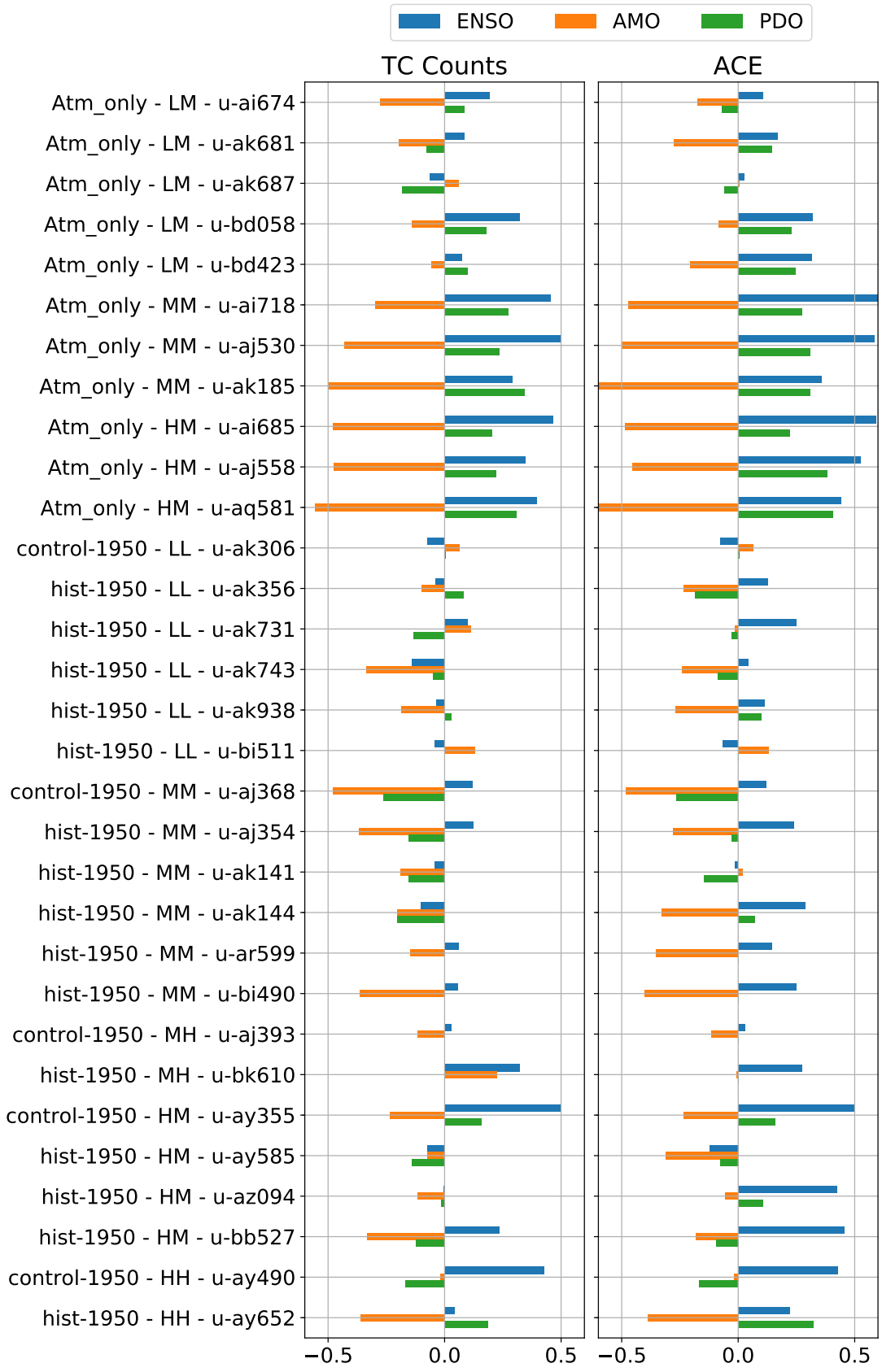

Figure 3.16: Pearson correlations between the time series of EPAC annual TC counts and ACE of models with the seasonal climate indices for the 1980-2013 period. Hatched bars indicate the correlations that are significant at the 90% CL.

(a) Locations of EOTs for all the model runs

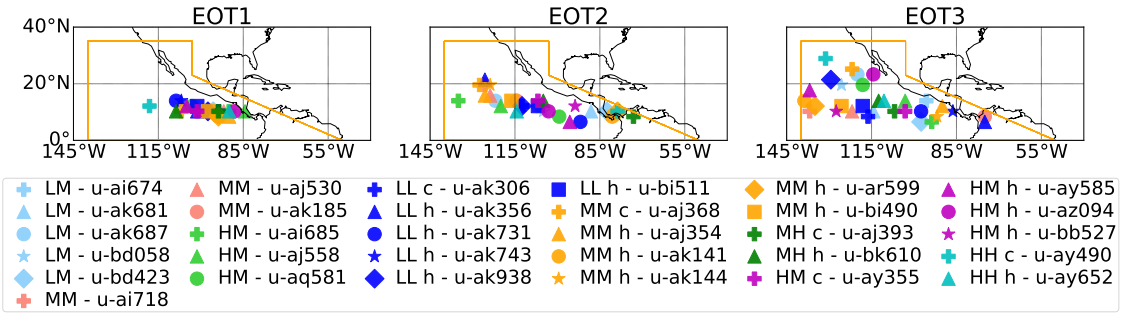

(b) SST regression patterns for the u-aj368 run

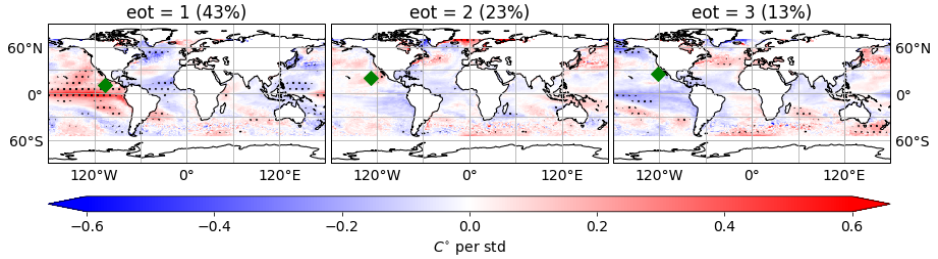

(c) VWS regression patterns for the u-aj368 run

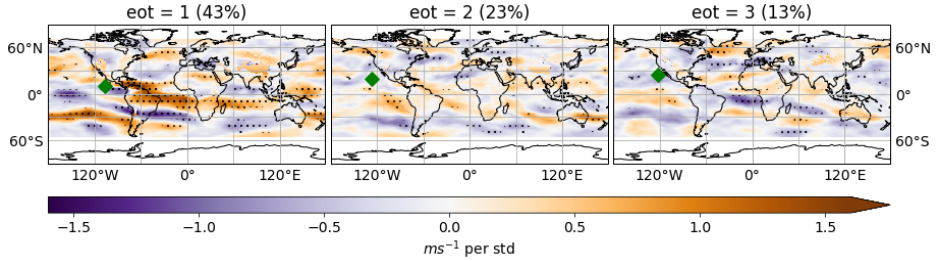

(d) Summary statistics about the Pearson correlation coefficients between the EPAC EOT time series for the different model simulations and the May-November averaged ENSO, AMO and PDO indices.

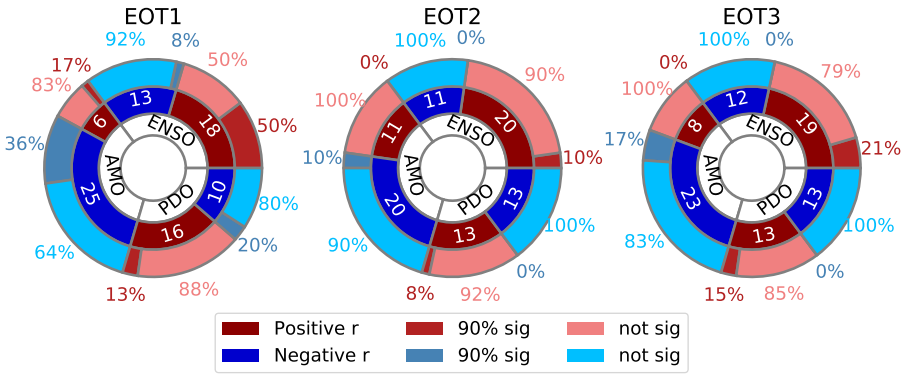

Figure 3.17: EOT results for TC variability in EPAC for the model simulations. Location of EOT is shown with green marker and significance at the 90% CL is indicated with dots on b and c. Period examined is 1980-2013. For the correlations dark red (blue) colors indicate how many of the 31 models have positive (negative) correlations with each index, medium red (blue) indicate how many of the dark red (blue) correlations are significant at the 90% CL, while light red (blue) indicate how many are not significant.

3.4.3 Summary

Analysis from IBTrACS and reanalysis shows that TC activity under the present climate in the EPAC region off the coast of Mexico is primarily positively influenced by the warm phase of ENSO, while it is anticorrelated with the AMM and AMO. Warm SSTs in the eastern and central Pacific region, accompanied by low VWS over the central Pacific, are associated with increases in TC activity in the basin. Correlating the time series of frequency and ACE with the climate indices examined in the study shows that ENSO has a greater influence on ACE than on frequency.

ENSO is found to influence TC activity in the range of model simulations from HadGEM3-GC3.1 for both counts and ACE, especially in the atm-only experiments, whereas the AMO has a greater influence on ACE than on counts. EOT analysis of track densities under the present climate in the model shows that ENSO and AMO are associated with TC activity off the west coast of Mexico. A large number of experiments have negative correlations with the AMO, however, only a few of them are significant, whereas 18 out of the 31 runs show positive correlations with ENSO, only 9 of which are significant. In order to assess which climate mode is more responsible for influencing TC activity in the basin, it is important to examine how the cold phase of the AMO can modulate El-Niño events.

3.5 Central Pacific

3.5.1 Observations - Current Climate

The amount of tracked TC systems in the CPAC region is rather small compared to the other basins in the NH. Only 3% of the hemisphere's activity has had its maximum intensity in this region according to the IBTrACS summary statistics (fig 3.2) in terms of frequency and 4% in terms of ACE. The different reanalyses consistently overestimate these amounts with 4-7% for frequency and 7-9% for ACE.

In terms of time series of TC counts, no trends nor big discrepancies are found for the different datasets (fig. 3.18a). However, in terms of ACE there is a large spread between the datasets, with ERA5 giving the highest ACE amounts on a nearly yearly basis since 1995. This is potentially due to a combination of ERA5 overestimating how many storms form in the basin as well as representing wind speeds better than the other reanalyses, considering that it is the most recent reanalysis dataset used in the study and the one with the highest resolution. Lastly, it is worth noting that TC activity in some of the datasets shows a decrease after 1995.

The spectral analysis of the ACE time series resulted in multiple significant peaks within the 2-6 year band in all datasets except MERRA2, whereas in terms of counts the IBTrACS power spectrum (green line on fig. 3.18b) showed significant signals in the 2-3 year band with only three of the reanalysis spectra displaying similar results. This indication of ENSO influence on TC activity in the basin is observed in the wavelet results (fig. 3.18c) as well, since analysis of the time series of frequency from IBTrACS, ERAI and ERA5 revealed significant regions in the 2-6 year band, localised around the mid-90's, during the period when the AMO shifted towards a warm phase. Furthermore, MERRA and JRA25 displayed similar regions with respect to periodicity, localised in the mid-to-late 2000's. In terms of ACE, seven of the datasets (not JRA25) display similar results, signifying that the shift of the AMO, via modulation of ENSO, has influenced TC activity in the basin.

Pearson correlation coefficients (shown in table 3.4) between the time series of counts and ACE with the May-November average of the climate indices reveal that TC activity for more than three datasets is affected by the warm phase of ENSO and the cold phases of the two Atlantic modes (AMM and AMO). This is particularly representative for ACE

(a) Time series

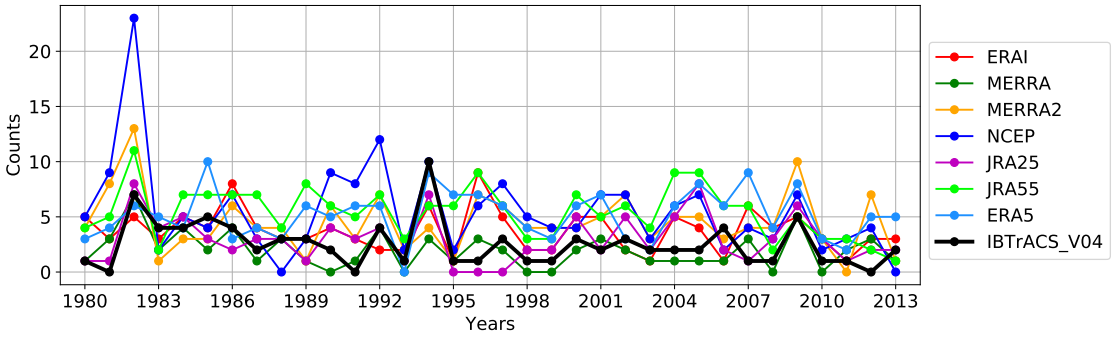

(b) Standard power spectrum

(c) Wavelet spectrum

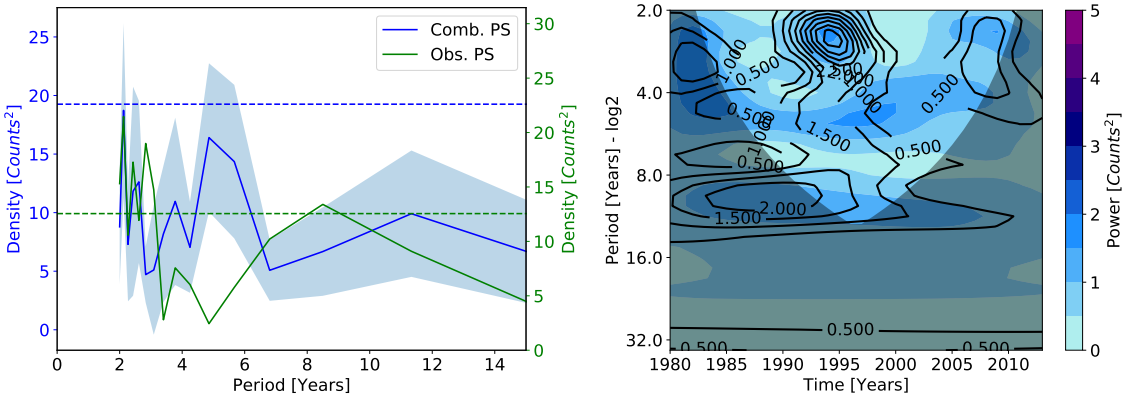

Figure 3.18: (a) Time series of TC counts for CPAC; b) Standard power spectrum analysis for the time series. The individual reanalysis spectra are combined into one (blue line) and they are compared against the IBTrACS power spectrum (green line). The dashed lines indicate the 95% confidence level. The shaded area indicates the 95% confidence intervals for the combined spectrum; c) Mean of the seven reanalysis wavelet spectra (colours) and IBTrACS wavelet spectrum (black contours) of TC counts time series. The shaded area indicates the COI.

Table 3.4: Pearson correlations between the time series of CPAC annual (a) TC counts and (b) ACE of IBTrACS and reanalyses with the seasonal climate indices for the 1980-2013 period. Correlations which are significant at the 90% CL are in bold.

	QBO	AMM	ENSO	AMO	PDO
IBTrACS	-0.03	**-0.47**	0.28	**-0.50**	0.11
ERAI	-0.29	**-0.32**	0.15	**-0.35**	0.06
MERRA	**-0.33**	**-0.44**	0.23	**-0.51**	0.09
MERRA2	-0.12	-0.19	**0.46**	-0.28	0.03
NCEP	-0.11	**-0.33**	**0.51**	**-0.51**	0.07
JRA25	-0.16	-0.18	0.22	-0.21	-0.14
JRA55	-0.18	-0.24	**0.32**	**-0.40**	0.28
ERA5	-0.22	0.00	0.09	-0.08	-0.10

(a) TC counts

	QBO	AMM	ENSO	AMO	PDO
IBTrACS	0.00	**-0.45**	0.21	**-0.42**	0.10
ERAI	-0.22	**-0.39**	**0.54**	**-0.42**	0.27
MERRA	-0.11	**-0.45**	**0.55**	**-0.43**	0.27
MERRA2	-0.09	**-0.31**	**0.59**	**-0.36**	0.09
NCEP	-0.03	**-0.42**	**0.49**	**-0.60**	0.20
JRA25	-0.10	**-0.36**	**0.52**	**-0.39**	0.15
JRA55	-0.06	**-0.47**	**0.50**	**-0.64**	**0.52**
ERA5	-0.06	**-0.34**	**0.47**	**-0.38**	0.28

(b) ACE

since moderate-to-strong correlations and anticorrelations with the AMM, ENSO and AMO indices are found for almost all datasets. NCEP is the only dataset for which the relationships between TC frequency and ACE with the May-November averaged AMM, ENSO and AMO indices are significant.

All the EOT1 base points are located below 20°N, covering almost the whole longitudinal length of the basin (around 30°) as shown on figure 3.19a. EOT1 for IBTrACS explains 90% of the variance in the basin, MERRA explains 60%, while the rest of the reanalysis EOTs explain between 70-76% (fig. 3.20). Just like the EPAC, power spectrum and wavelet analysis of EOT time series detected significant signals within ENSO's periodicity, between 2-7 years.

ENSO's dominant influence on TC activity in the basin can be further established by the moderate-to-strong positive Pearson correlation coefficients between the EOT1 time series of seven datasets (six of them being significant) and the May-November averaged ENSO index as shown on figure 3.19d. Indeed, the SST and VWS patterns highlight the association of increases in TC activity to El-Niño's warm SSTs and to weak VWS shear in the central part of the region. Additionally, for five of the datasets, moderate anticorrelations with the AMM (three of them being significant) and the AMO (four of them being significant) show how the cold phases of the Atlantic modes, probably via

(a) Locations for IBTrACS and reanalyses EOTs

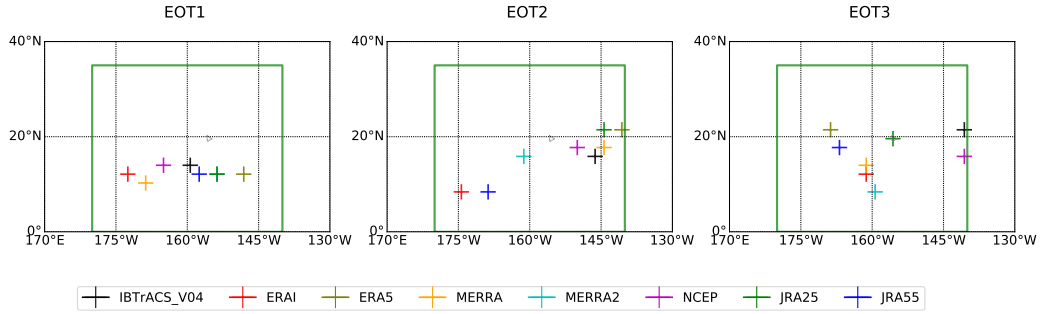

(b) SST regression maps for IBTrACS. The HadISST SST field is regressed onto IBTrACS EOTs

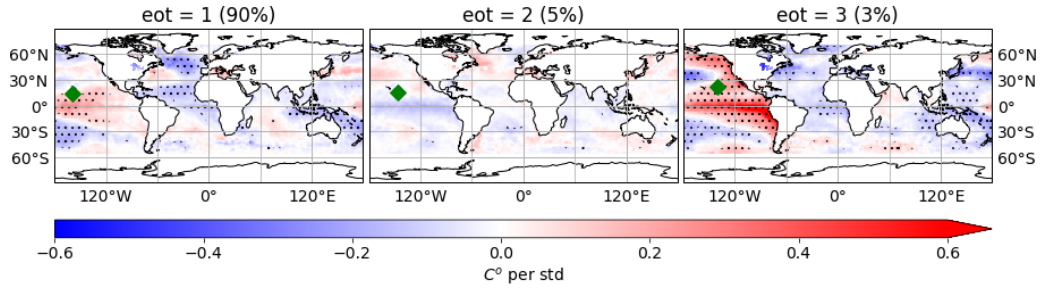

(c) VWS regression maps for IBTrACS. The ERA5 VWS field is regressed onto IBTrACS EOTs

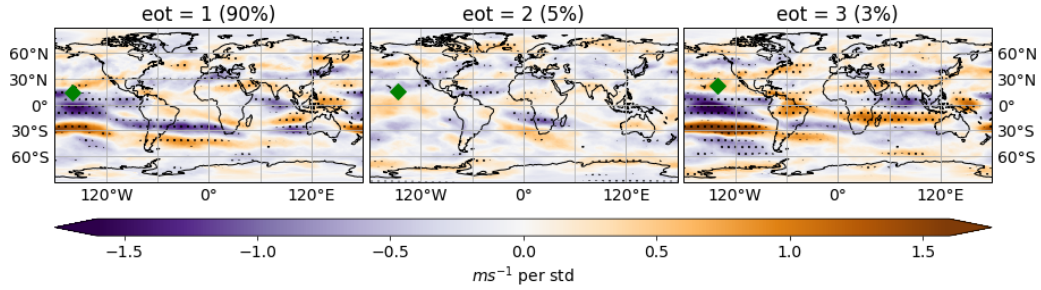

(d) Correlations between EOTs and May-November average climate indices

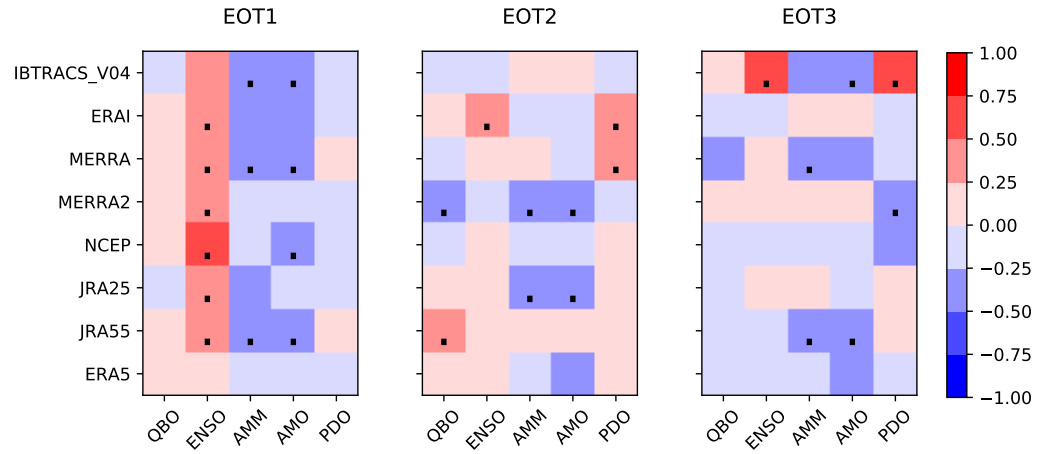

Figure 3.19: Results of EOT analysis for CPAC under the current climate for IBTrACS and reanalyses. Locations of EOTs are indicated with a green marker on b and c. Significance at the 90% CL is indicated with dots on b, c and d.

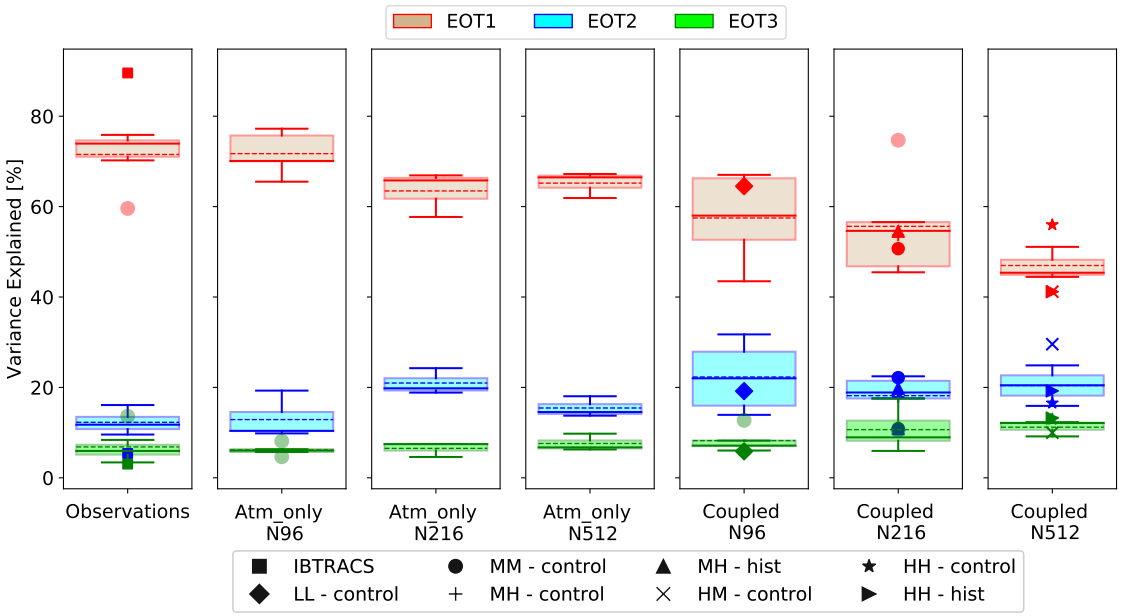

Figure 3.20: Percentage of variance explained by the EOTs for CPAC. Column 1: Re-analyses (as an ensemble) against IBTrACS (■); Columns 2-4: ensemble of atm-only runs split by atmospheric resolution; Column 5: ensemble of LL historic runs against the control run (♦); Column 6: ensemble of MM historic runs against the MM control (●), MH control run (+) and MH historic run (▲); Column 7: ensemble of HM historic runs against HM control run (×), HH control run (★) and HH historic run (►). Faded circles (●) show outliers. Dotted lines show the ensemble means.

modulating ENSO can also drive activity in the basin.

3.5.2 Models - Current Climate

The different atm-only simulations appear to have similar TC representation in both frequency and ACE with the observations. The power spectra of the time series of TC counts and ACE for the atm-only runs detect significant periodicities within the 2-6 year band, whereas for some of the coupled runs this range goes up 9 years (not shown). For this particular basin, the wavelet spectra of the individual time series have shown similarities between frequency and ACE, both in terms of interannual periodicities, but also in terms of localisation in time as shown on figure 3.22. The wavelet spectra for the time series of TC counts for the N216 coupled runs are shown on figure 3.22a, while the corresponding wavelet spectra for ACE are shown on figure 3.22b. The colors indicate the mean wavelet spectrum of the ensemble of MM hist-1950 runs on the left and of the MH hist-1950 run

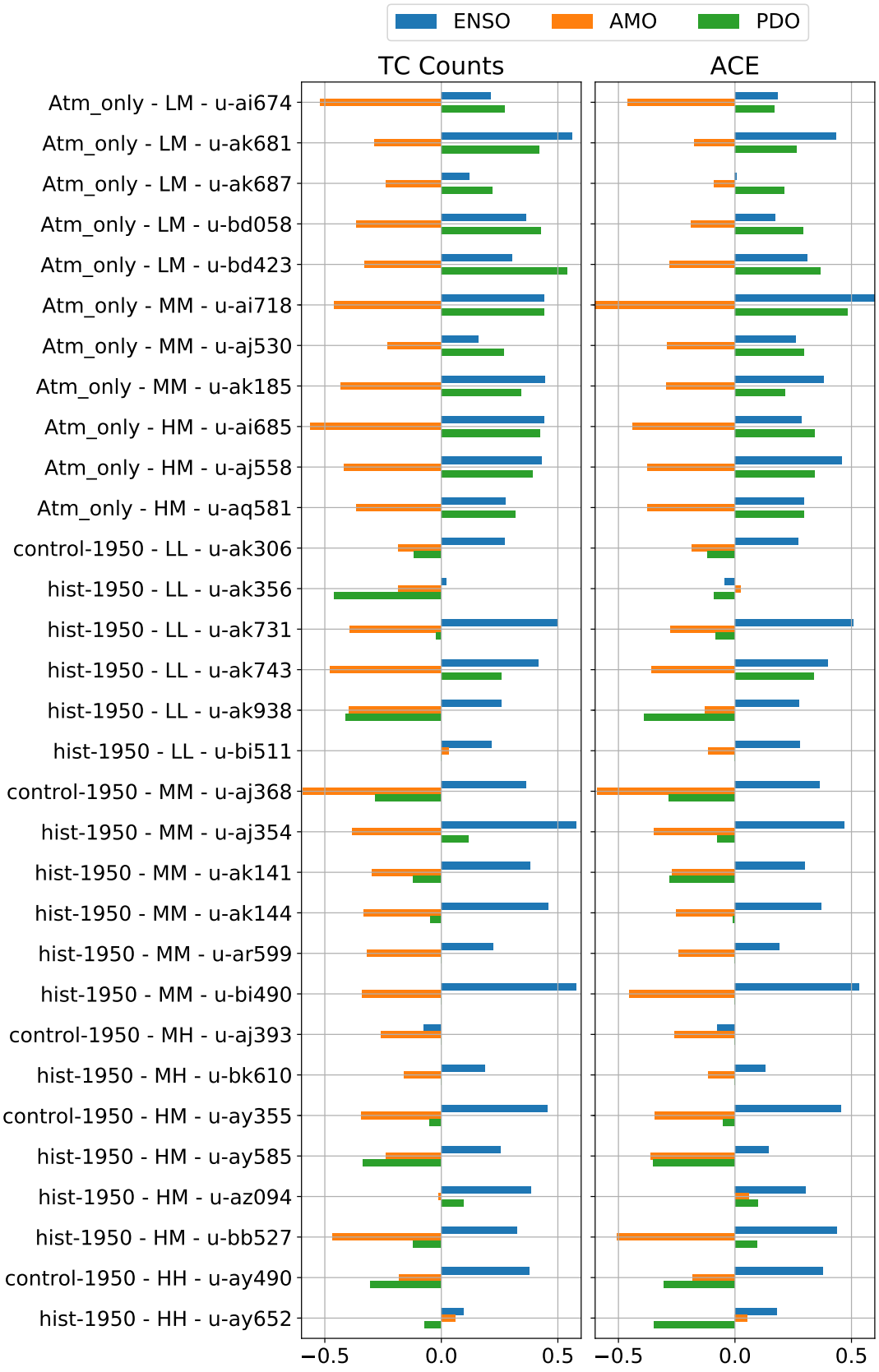

Figure 3.21: Pearson correlations between the time series of CPAC annual TC counts and ACE of models with the seasonal climate indices for the 1980-2013 period. Hatched bars indicate the correlations that are significant at the 90% CL.

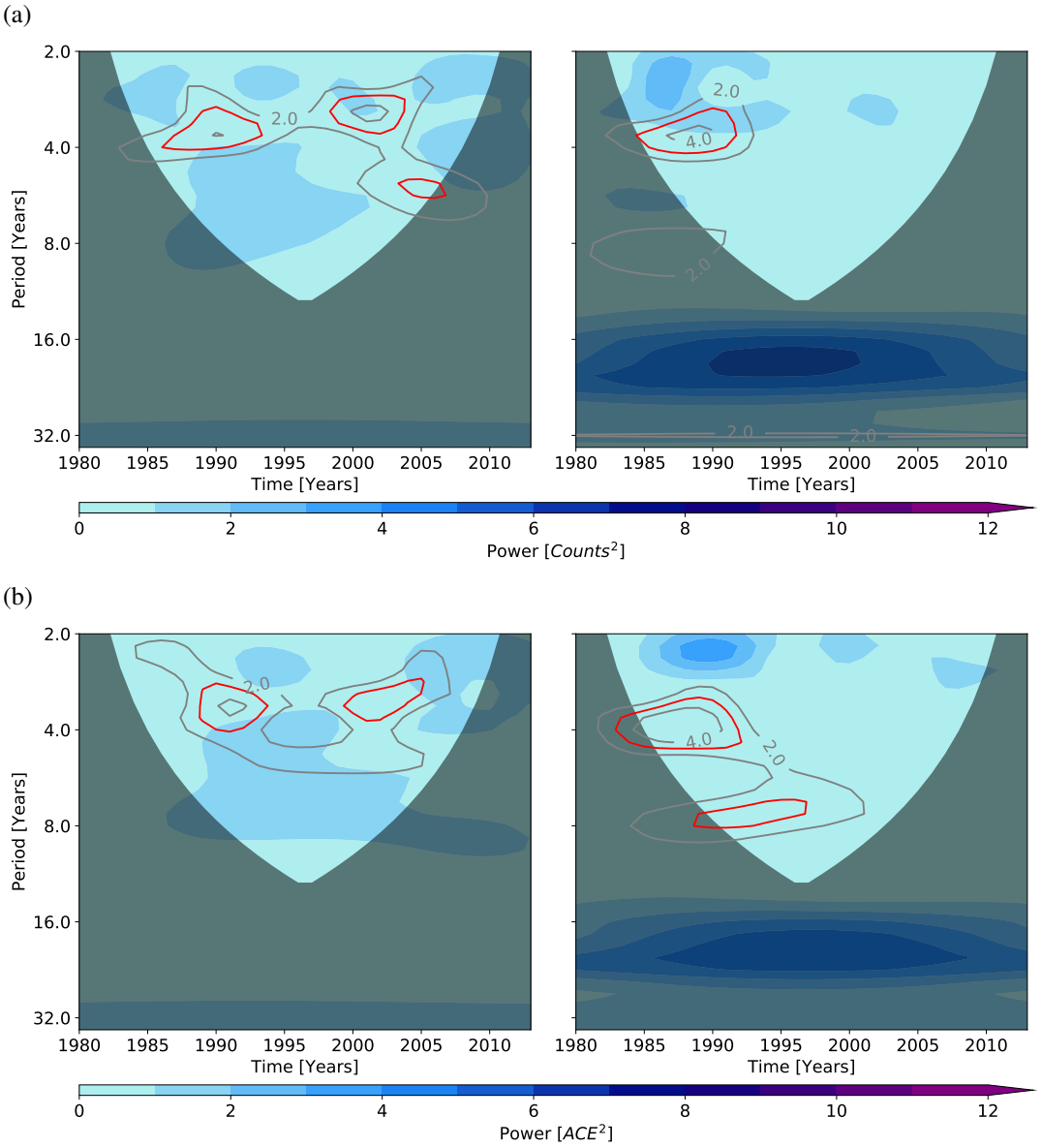

Figure 3.22: Wavelet results for TC variability in CPAC for the N216 coupled model simulations in terms of TC counts (a) and in terms of ACE (b). Left: Mean wavelet spectrum the ensemble of MM coupled hist-1950 runs (colours), and wavelet spectrum of the MM coupled control run (gray contours); Right: Wavelet spectrum of the MH coupled hist-1950 run (colours) and wavelet spectrum of the MH coupled control run (gray contours). The 95% significance level of each control run's wavelet spectrum is shown with red contours.

on the right. The corresponding wavelet spectra for the control runs are presented with gray contours. The red lines indicate where the wavelet spectrum of each control run is significant at the 95% CL. The region of maximum power for the wavelet of the MH hist-1950 run which has a periodicity within the 16-32 year band for both ACE and counts, is not in the COI (shaded area), and it is therefore not taken into account.

The May-November averaged ENSO index has a significant moderate or strong positive relationship with both frequency and ACE in the basin for at least 17 of the 31 model experiments examined as shown from Pearson correlations on figure 3.21. Furthermore, nearly all atm-only simulations show a significant moderate or strong anticorrelation between the seasonally averaged AMO index and the time series of TC counts. For ACE in the atm-only experiments, all of the MM and HM runs, as well as two of the LM experiments, show a significant moderate anticorrelation with AMO. Three of the LL hist runs, all the N216 runs and two of the high resolution coupled runs also show significant moderate or strong inverse relationship with the AMO in terms of frequency. The AMO appears to have a greater impact on the frequency compared to ACE in this basin since, even though the same relationship is detected in terms of ACE, it is detected in fewer runs. The May-November averaged PDO index appears to be significantly, moderately to strongly correlated with the frequency of TCs in 8 of the atm-only runs, and moderately anticorrelated with 4 of the coupled runs. ACE has the same connection to the seasonally averaged PDO index by being positively correlated with 7 atm-only and 1 LL hist-1950 runs and negatively correlated with 4 coupled experiments.

The percentage of variance explained by the EOTs is characterised by a big difference between EOT1 and EOT2 particularly for the atm-only experiments, in distributions similar to the ones seen for the observations (fig. 3.20). For the coupled experiments, with increasing resolution the difference between the EOT1 and EOT2 reduces. For the coupled runs, EOT1s start by being spread out in the basin below $20°N$, and with increasing resolution, they cluster into the western tropical part of the region (fig. 3.23a). This is related to the track densities, since higher track densities are observed as resolution increases (fig. 3.1). For the atm-only experiments, no similar observation is made, since there is a low density of TCs in the CPAC region. After the influence by the first mode is removed, the different EOT2 points spread in the region examined with no apparent connection. The locations of EOTs for all the model runs are shown on figure 3.23a.

(a) Locations of EOTs for all the model runs

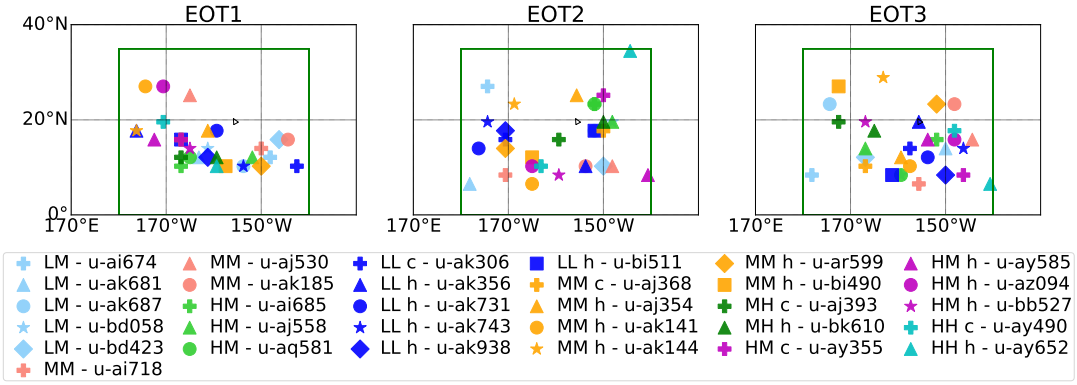

(b) SST regression patterns for the u-ai685 run

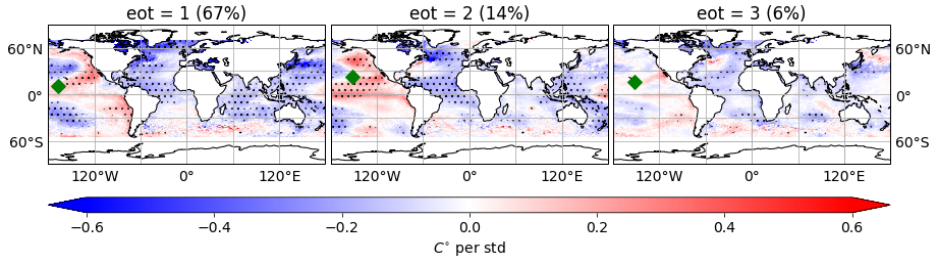

(c) VWS regression patterns for the u-ai685 run

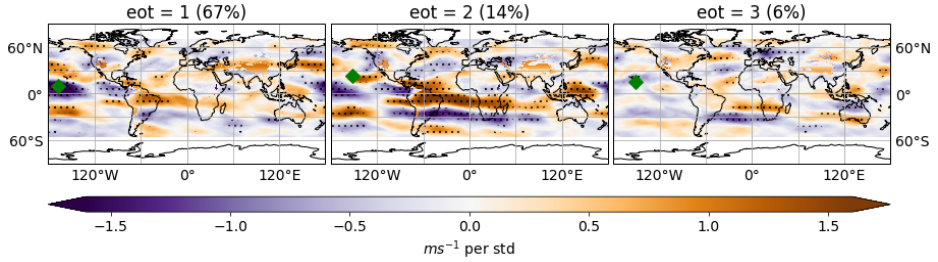

(d) Summary statistics about the Pearson correlation coefficients between the CPAC EOT time series for the different model simulations and the May-November averaged ENSO, AMO and PDO indices.

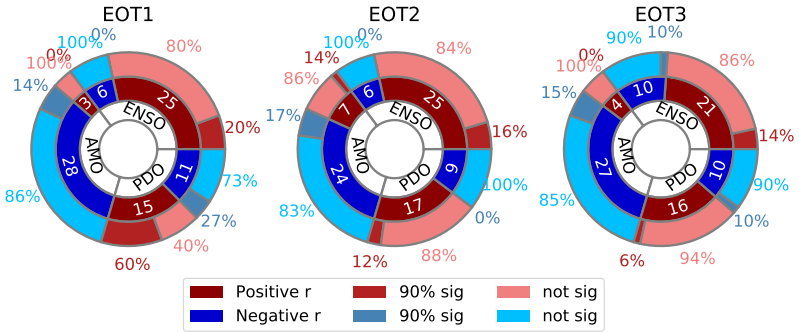

Figure 3.23: EOT results for TC variability in CPAC for the model simulations. Location of EOT is shown with green marker and significance at the 90% CL is indicated with dots on b and c. Period examined is 1980-2013. For the correlations dark red (blue) colors indicate how many of the 31 models have positive (negative) correlations with each index, medium red (blue) indicate how many are not significant.

Interestingly, robust significant connections between EOTs and the climate indices, particularly the AMO and PDO, as observed from Pearson correlations on figure 3.23d, are seen only for 5 MM and HM atm-only experiments. In general, however, activity at EOT1 base points in the basin is positively correlated with ENSO for 25 experiments and with PDO for 15 experiments, while it is anticorrelated with the AMO for 28 experiments. Similar relationships are found for the remaining two EOTs, as seen on figure 3.23d. One of the atm-only runs for which relationships with ENSO and PDO was observed is the u-ai685 (HM). The SST and VWS regression maps for this particular experiment, shown on figures 3.23b and 3.23c, respectively, show that for the first two EOTs, TC activity is mainly affected by warm Pacific SSTs and low VWS in the central Pacific, in El-Niño- and PDO-resembling patterns. Additionally, the cold phase of the AMO, possibly by strengthening the descending branch of the Walker Circulation over the NATL region due to colder SSTs (less moisture available) and therefore aiding convection over the central Pacific, provides additional influence on TCs over the CPAC region.

3.5.3 Summary

ENSO is found to be the dominant climate mode influencing TC activity in IBTrACS and the reanalysis products, with possible modulation by the AMM and AMO in almost half of the datasets examined. Similar mechanisms as the ones described for TC activity in the EPAC can be assumed, with El-Niño creating favourable conditions with warm SSTs and low VWS in the Pacific region.

The model simulations, particularly the atm-only experiments, yield similar results for both frequency and ACE in the CPAC region, with ENSO showing once again to be the main climate mode influencing TC activity in more than half of the model runs. The AMO appears to influence TC activity in terms of frequency, particularly in the atm-only experiments, possibly by modulating the Walker Circulation. TC activity in this basin is not so systematically studied using model simulations, compared to the other basins. It is important that more studies using both observations and GCMs are conducted in order to further understand the driving modes of TC activity in this basin.

3.6 Western Pacific

3.6.1 Observations - Current Climate

For the period examined (1980-2013), the WPAC region has 45% of the hemisphere's TC activity in terms of frequency and around 50% in terms of ACE, according to the summary statistics by IBTrACS (fig. 3.2). For the reanalyses the corresponding percentages of TC activity range from 40-47% and 47-54%, respectively. A drop in both TC counts (fig. 3.24a) and ACE after 1996 can be observed for IBTrACS and the majority of reanalyses. Significant moderate-to-strong correlations (except for JRA25) for the time series of counts, and significant strong-to-very strong correlations for the time series for ACE indicate good agreement between IBTrACS and reanalyses on TC representation for this basin.

Spectral analysis shows significant peaks in the 2-4 year band for the combined reanalysis and the IBTrACS spectrum, for both TC counts (fig. 3.24b) and ACE. In contrast to the Atlantic, the location of the highest power in the wavelet analysis of the time series of counts, as seen on figure 3.24c, is around 1985, in the 4-5-year band, which is within ENSO's power band.

Pearson correlation coefficients between the May-November averaged climate indices and the time series of frequency and ACE are presented on table 3.5. It can be seen that the time series for ACE for all datasets are significantly, positively correlated with the May-November averaged ENSO index. In contrast, for only three of the datasets the time series of counts have a similar relationship with the ENSO index. Furthermore, for at least half of the datasets, both the time series of counts and the time series of ACE, are significantly anticorrelated with the AMM and AMO. Lastly, the PDO index is significantly correlated with only the IBTrACS time series of counts as well as the time series of ACE for IBTrACS and JRA55.

During the 1995-2011 period, there has been a significant decrease in TC activity in the basin (Hsu et al., 2014) compared to the active era before 1995. A possible important factor for this change is the distribution of SSTs (Choi et al., 2015). A shift of the AMO to a positive phase during the 1990s may have caused a reduction of ENSO activity (Lübbecke and McPhaden, 2014), which resulted in the decrease of TC activity. It is possible that the negative phase of the AMO before the mid-1990s, in combination with the positive phase

(a) Time series

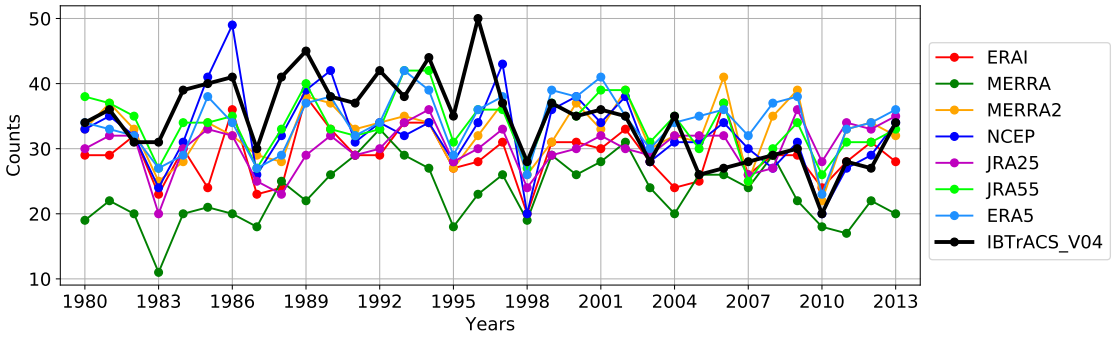

(b) Standard power spectrum

(c) Wavelet spectrum

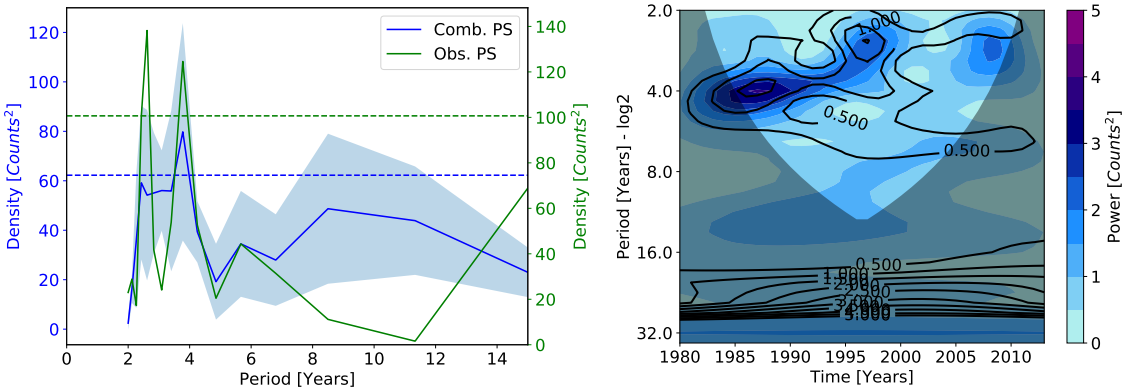

Figure 3.24: (a) Time series of TC counts for WPAC; b) Standard power spectrum analysis for the time series. The individual reanalysis spectra are combined into one (blue line) and they are compared against the IBTrACS power spectrum (green line). The dashed lines indicate the 95% confidence level. The shaded area indicates the 95% confidence intervals for the combined spectrum; c) Mean of the seven reanalysis wavelet spectra (colours) and IBTrACS wavelet spectrum (black contours) of TC counts time series. The shaded area indicates the COI.

Table 3.5: Pearson correlations between the time series of WPAC annual (a) TC counts and (b) ACE of IBTrACS and reanalyses with the seasonal climate indices for the 1980-2013 period. Correlations which are significant at the 90% CL are in bold.

	QBO	AMM	ENSO	AMO	PDO
IBTrACS	0.03	**-0.58**	0.00	**-0.66**	**0.29**
ERAI	0.09	**-0.46**	**0.30**	**-0.30**	-0.05
MERRA	0.04	-0.29	0.14	-0.11	-0.14
MERRA2	0.28	**-0.31**	**0.46**	-0.22	-0.04
NCEP	0.27	**-0.47**	0.24	**-0.48**	0.17
JRA25	0.09	-0.14	**0.37**	-0.16	-0.19
JRA55	0.19	**-0.46**	0.24	**-0.41**	0.08
ERA5	0.19	**-0.31**	0.23	-0.19	-0.16

(a) TC counts

	QBO	AMM	ENSO	AMO	PDO
IBTrACS	0.01	**-0.40**	**0.76**	**-0.59**	**0.42**
ERAI	0.09	-0.27	**0.66**	**-0.40**	0.22
MERRA	-0.02	-0.27	**0.60**	**-0.33**	0.13
MERRA2	0.08	-0.18	**0.76**	-0.29	0.10
NCEP	0.11	**-0.34**	**0.64**	**-0.55**	0.25
JRA25	0.08	-0.23	**0.72**	**-0.38**	0.17
JRA55	0.11	**-0.51**	**0.69**	**-0.68**	**0.51**
ERA5	0.07	**-0.33**	**0.77**	**-0.43**	0.20

(b) ACE

of the PDO (Deser et al., 2010), by modulating ENSO (Verdon and Franks, 2006), may have resulted in a high-frequency TC activity era in the basin.

For the WPAC region, EOT1 base points are not as clustered as in NATL (fig. 3.25a), and there is not an analogously big difference between the amount of variance explained by EOT1 and EOT2 (fig. 3.26). This is an indication that TC activity in the region is influenced by more than one driver. For EOT1, there is a moderate-to-strong significant positive correlation with the May-November averaged ENSO index for six of the datasets examined and a similar relationship with the PDO for four of the datasets (fig. 3.25d). Furthermore, for some of the EOT1s, moderate-to-strong negative correlations with the AMM and AMO indices are found. For NCEP, these relationships with the climate indices appear to influence activity at EOT2 instead of EOT1. For this dataset, the first base point sits closer to the edge of the tropics, whereas EOT2 is located south-east of EOT1, in the middle of the tropics. This might serve as an explanation of the difference between the datasets, excluding the fact that NCEP is the only coupled reanalysis product.

Figures 3.25b and 3.25c present the SST and VWS regression maps, respectively, when the HadISST SST and ERA5 VWS fields are regressed onto the first three EOTs for IBTrACS. In general, from the regression maps from all the datasets, it is found that for at least one of the first three EOTs the main mode of influence is ENSO, and more

(a) Locations for IBTrACS and reanalyses EOTs

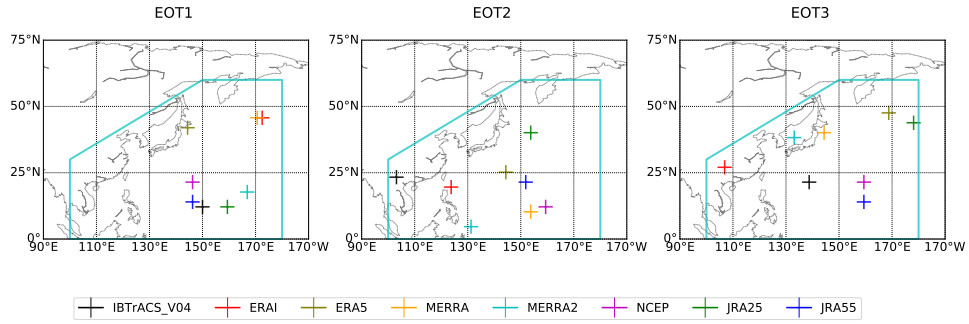

(b) SST regression patterns for IBTrACS. The HadISST SST field is regressed onto the IBTrACS EOTs

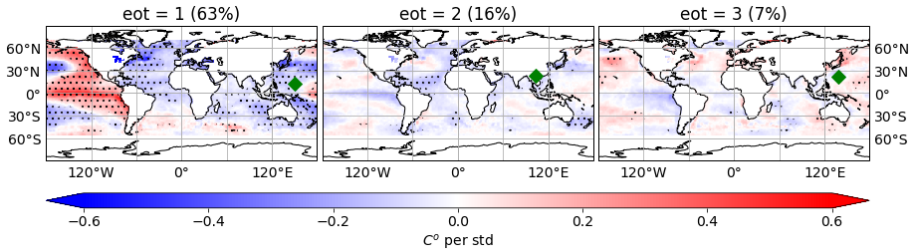

(c) VWS regression patterns for IBTrACS. The ERA5 VSW field is regressed onto the IBTrACS EOTs

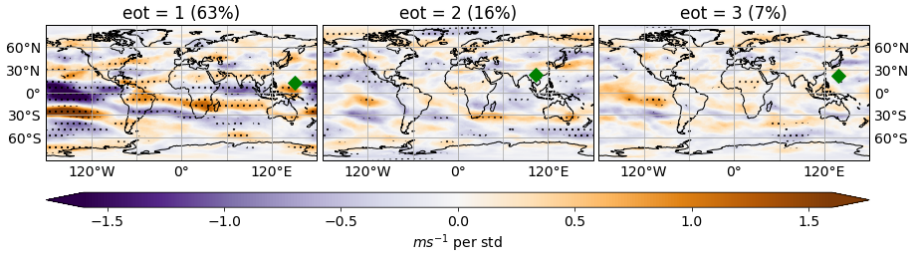

(d) Correlations between EOTs and May-November average climate indices

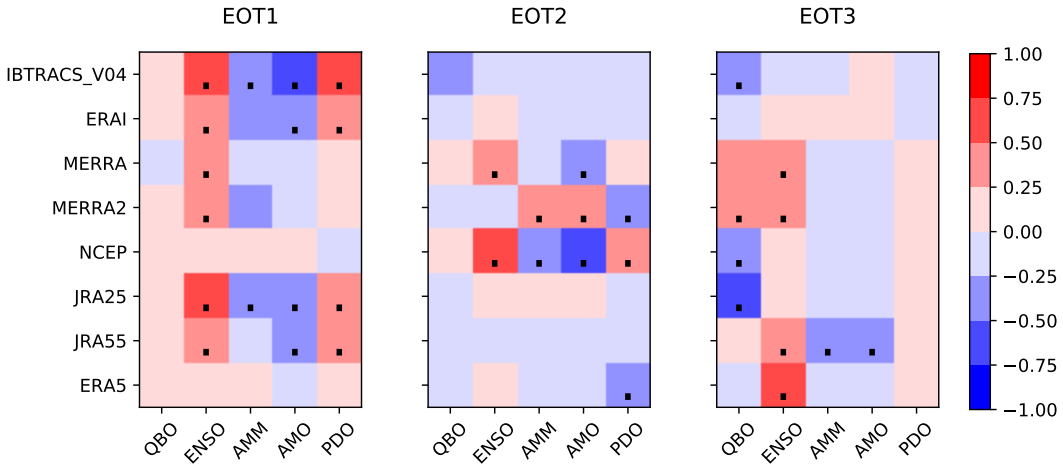

Figure 3.25: Results of EOT analysis for WPAC under the current climate for IBTrACS and reanalyses. Locations of EOTs are indicated with a green marker on b and c. Significance at the 90% CL is indicated with dots on b, c and d.

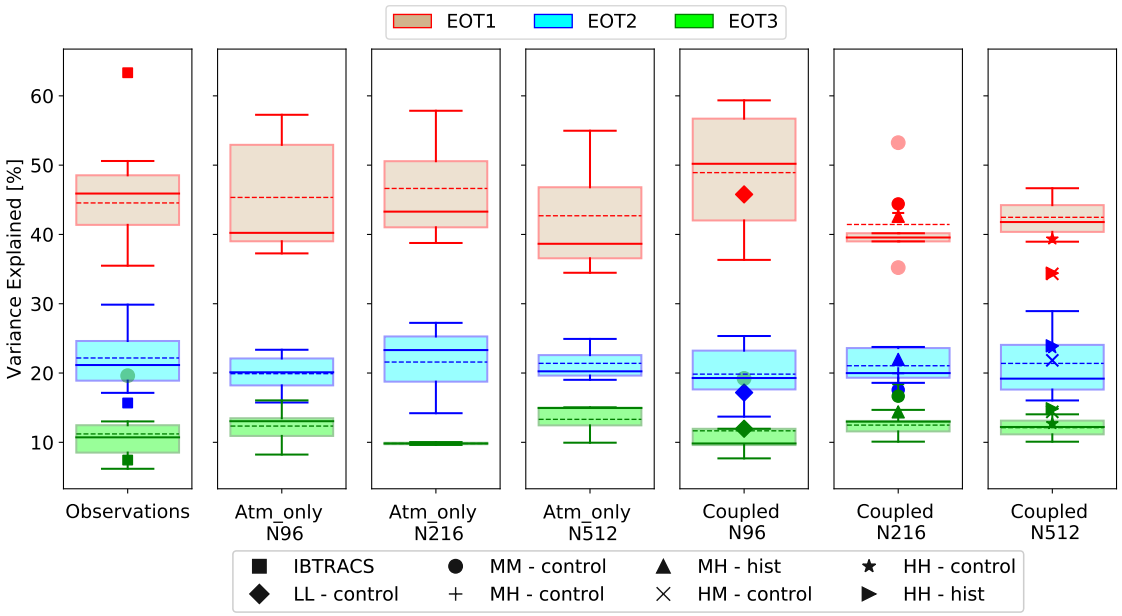

Figure 3.26: Percentage of variance explained by the EOTs under current climate for WPAC. Column 1: Reanalyses (as an ensemble) against IBTrACS (■); Columns 2-4: ensemble of atm-only runs split by atmospheric resolution; Column 5: ensemble of LL historic runs against the control run (♦); Column 6: ensemble of MM historic runs against the MM control (●), MH control run (+) and MH historic run (▲); Column 7: ensemble of HM historic runs against HM control run (×), HH control run (★) and HH historic run (►). Faded circles (●) show outliers. Dotted lines show the ensemble means.

specifically the El-Niño, or the warm phase of the PDO, since significant warm SSTs and weak VWS in the eastern and central parts of the Pacific ocean are displayed. It seems more probable, however, for the patterns to resemble ENSO rather PDO, simply because the spectral signals are on interannual time scales.

3.6.2 Models - Current Climate

When comparing the time series of frequency and ACE with the ones in IBTrACS for the WPAC region, a significant agreement in terms of ACE is found in all the atm-only experiments, but not in terms of frequency. The power spectra of those time series resulted in significant signals on interannual periodicities within the 2-7-year band such as the ones shown on figure 3.27a, something that is also observed for the power spectra of the time series of TC counts. For the coupled simulations, such signals are present. However, for some of the higher resolution runs, signals at greater (up to 10 years) periodicities are

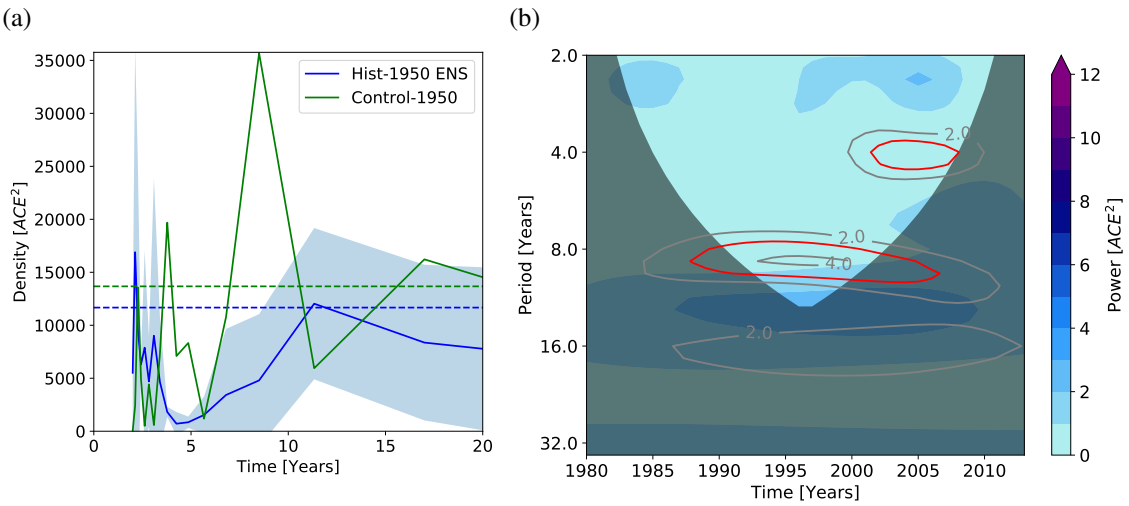

Figure 3.27: Spectral analysis on WPAC ACE for the coupled HM runs: (a) Power spectrum: The spectra of the HM hist-1950 ensemble runs are combined into one (blue line) and are compared against control-1950. The dashed lines indicate the 95% confidence level. The shaded area indicates the 95% confidence intervals for the mean power spectrum; (b) Wavelets: The grey contour lines indicate the spectra for the control run. Colors indicate the mean spectrum for the ensemble of HM hist-1950 runs. The shaded area indicates the COI while the 95% CL for the control run is shown with red contours

also observed such as the ones shown on figure 3.27a which presents the standard power spectrum for the time series of ACE of the coupled HM runs. Similar periodicities can be observed on the wavelet spectrum (fig. 3.27b).

The Pearson correlation coefficients between the time series of counts and ACE and the seasonally averaged climate indices presented on figure 3.28, reveal that for the period examined ENSO has a greater influence on ACE than on frequency. Significant moderate-to-strong positive relationships between the ENSO index and ACE are found for all the atm-only experiments, for 5 out of 6 coupled LL runs, 3 of the MM coupled experiments and only the HH control run, while for counts none of the higher resolution (MM, MH, HM and HH) experiments show a significant connection to ENSO. Similarly, AMO has a greater influence on ACE in the basin than on the frequency, particularly for the atm-only simulations. Only one of the coupled runs in terms of counts and three of the coupled runs in terms of ACE show a moderate connection to AMO, whilst the rest show weak relationships. For the period examined there is no robust conclusion for the influence of the PDO on TC activity in the region. The May-November averaged PDO index has significant

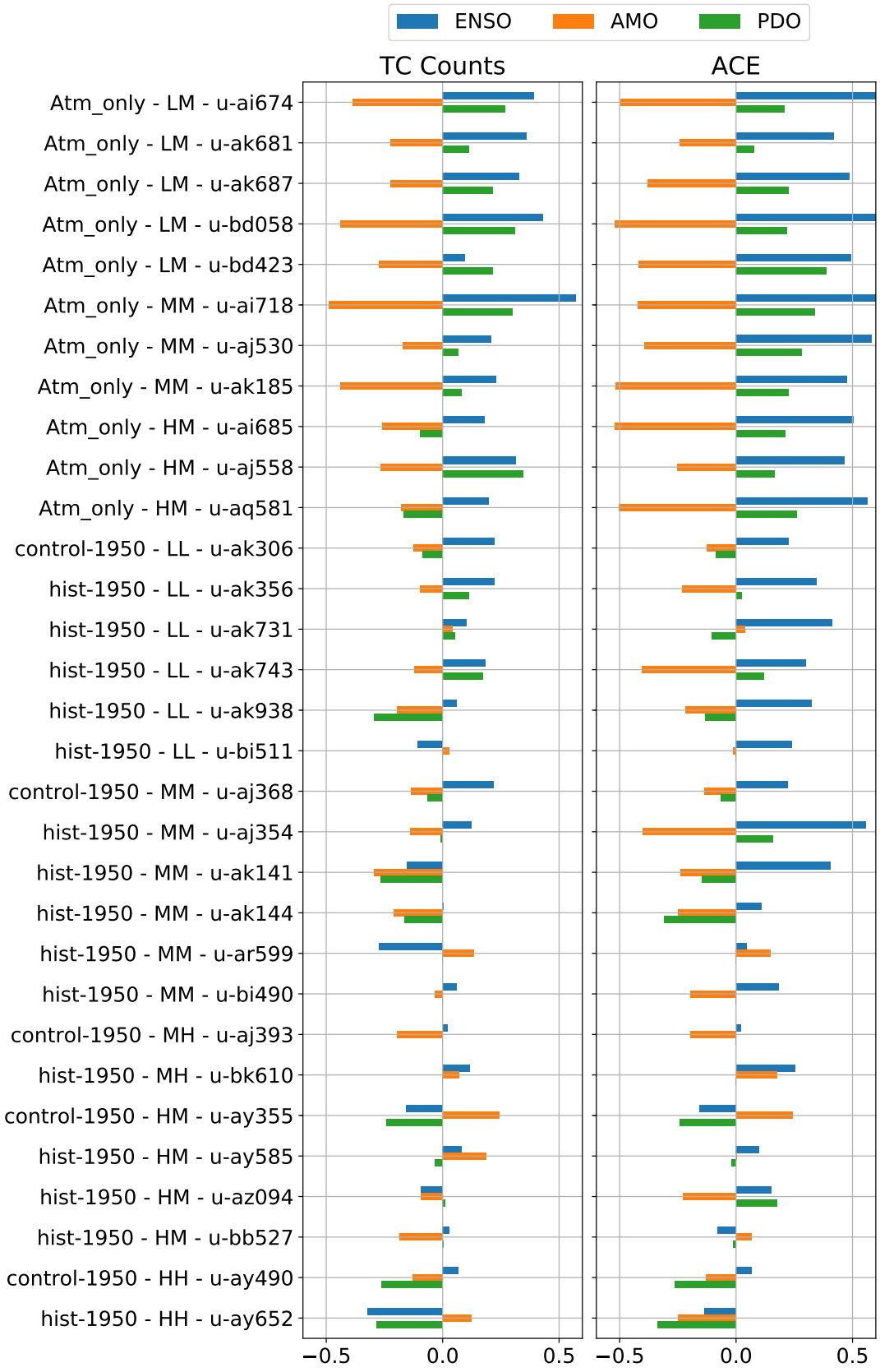

Figure 3.28: Pearson correlations between the time series of WPAC annual TC counts and ACE of models with the seasonal climate indices for the 1980-2013 period. Hatched bars indicate the correlations that are significant at the 90% CL.

(a) Locations of EOTs for all the model runs

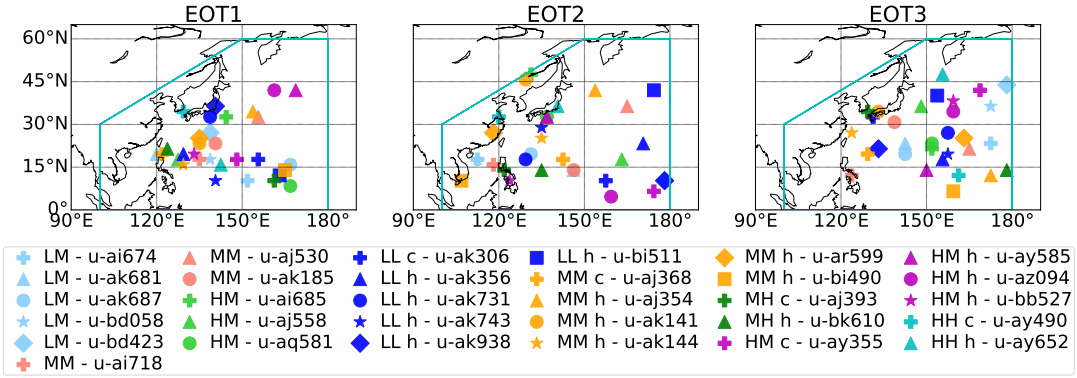

(b) SST regression patterns for the u-aq581 run

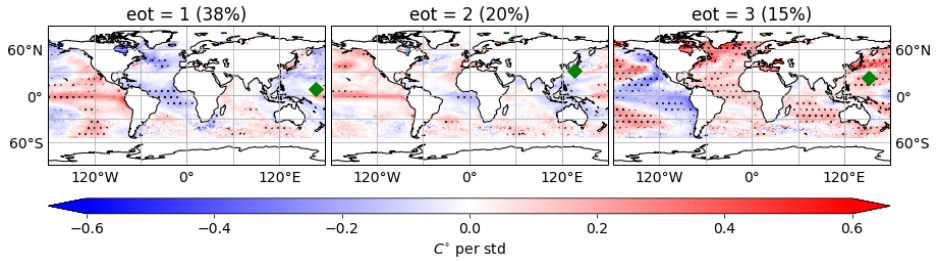

(c) VWS regression patterns for the u-aq581 run

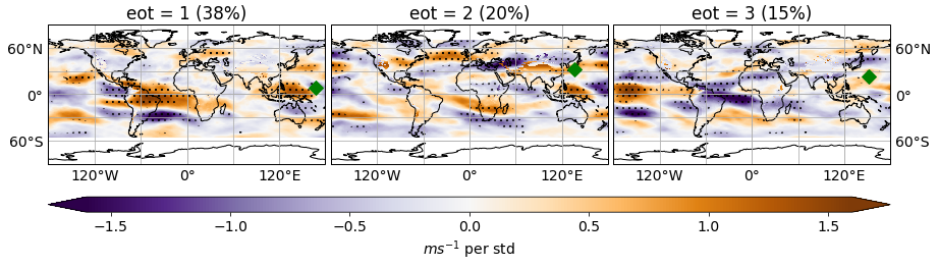

(d) Summary statistics about the Pearson correlation coefficients between the WPAC EOT time series for the different model simulations and the May-November averaged ENSO, AMO and PDO indices.

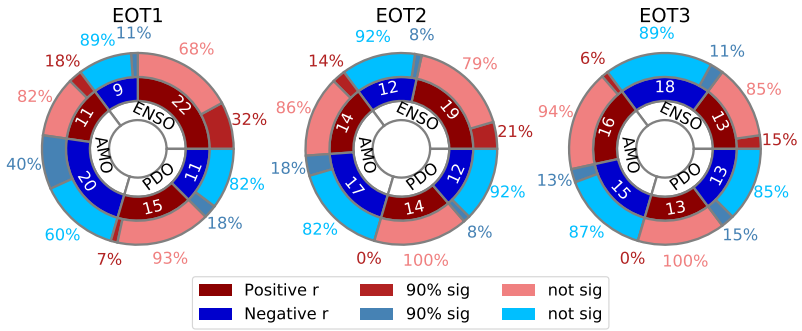

Figure 3.29: EOT results for TC variability in WPAC for the model simulations. Location of EOT is shown with green marker and significance at the 90% CL is indicated with dots on b and c. Period examined is 1980-2013. For the correlations dark red (blue) colors indicate how many of the 31 models have positive (negative) correlations with each index, medium red (blue) indicate how many of the dark red (blue) correlations are significant at the 90% CL, while light red (blue) indicate how many are not significant.

moderate correlations and anticorrelation with only 4 atm-only runs and 1 coupled run, respectively, in terms of counts. The time series of ACE is significantly moderately correlated with the index for only 2 atm-only runs and significantly anticorrelated with 3 of the coupled runs.

EOT results for this basin under the current climate for the model simulations show similarities with the EOT results for IBTrACS and the reanalyses, since the vast majority of EOT1s are located in the central and western part of the region examined. In addition, the distribution of percentage explained is similar to the one seen for the observations presented on figure 3.26. The locations for the first three EOTs for all the model runs are presented on figure 3.29a.

Compared to the robust connections established through the EOTs for the observations, forming a clear conclusion about which phenomena significantly influence TC activity in this region for the model simulations is a difficult task. A first look of this difficulty is observed through the Pearson correlations between the EOTs and the seasonally averaged climate indices. Even though for 22 and for 20 of the model runs positive and negative correlations are found between the EOT1s and ENSO and AMO, respectively, less than 40% of them are significant at the 90% CL, as seen from figure 3.29d. The majority of them are found for the atm-only runs. Even less significant connections are found for EOT2s and EOT3s.

EOT regression maps helped to establish some relationships with the climate indices. Figures 3.29b and 3.29c present the first three EOT SST and VWS regression maps for the u-aq581 run, one of the high-resolution atm-only simulations. For this particular run, EOT1 appears to be influenced by warm SSTs in an El-Niño-resembling pattern and cold AMO-related SSTs in the Atlantic region, while for EOT3 the opposite image can be seen, with cold SSTs in the the eastern and central Pacific and warm SSTs in the Atlantic. Activity at EOT1 also appears to be influenced by low VWS over the central Pacific, right below the ascent branch of the Walker Circulation during El-Niño conditions, whereas for EOT3 the regions of weak and strong regressions between the EOTs and the VWS field indicate that TC activity at that location is impacted by La-Niña conditions. Generally, from the EOT results it is seen that TC activity at EOTs located in the WPAC MDR and close to the date line is influenced mainly by El-Niño events through warm local SSTs and low VWS, whilst activity in the tropical western part of the region appears to be influenced

by La-Niña events.

3.6.3 Summary

As found from the different analysis tools utilised in the study, ENSO and PDO influence typhoon activity in the western part of the Pacific ocean in both IBTrACS and more than three reanalysis datasets. It is possible that the connecting mechanism to ENSO is related to westerlies and an expansion of the monsoon trough towards the east (Wang and Chan, 2002). Moreover, the change of phase of the AMO and the PDO has influenced the strength of different ENSO events, which consequently impacted TC activity in the basin during different decades. Results from EOT analysis on observations and model simulations indicate that TC variability in the basin has more than one main driver. Furthermore, analysis on model simulations shows that the frequency and ACE of TCs in the region, mainly for the atm-only runs, are significantly influenced by ENSO and the AMO. Lastly, from the EOT analysis on the model runs, it is found that, depending on the location of the EOT, different conditions associated with ENSO influence TC activity in the basin.

3.7 North Indian Ocean

3.7.1 Observations - Current Climate

The NIND is the second smallest region examined in the study after CPAC. For IBTrACS, around 10% of the northern hemisphere's TC activity, in terms of frequency, and around 2%, in terms of ACE, had its maximum intensity in this region under the current climate (fig. 3.2). The reanalysis products show a relatively good agreement by having around 10-13% of TC activity in the region in terms of frequency, while overestimating ACE with percentages ranging between 6-8%, due to a lot of missing wind speed data in IBTrACS.

There is an increase in activity in terms of counts after 1989 (fig. 3.30a), possibly related to better observational procedures, since prior to that year there were no reported missing data. Good agreement is established between the IBTrACS and the reanalyses, since significant moderate-to-strong and significant moderate correlations are found (not shown) in terms of counts and in terms of ACE (except for NCEP).

Power spectral analysis resulted in one significant peak at around 8 years for the IBTrACS time series of both ACE and counts (fig. 3.30b). For the combined reanalysis spectrum for both frequency and ACE, one significant peak can be seen at around 2 years. Similar information can be extracted from the wavelets. Figure 3.30c displays the mean reanalysis wavelet spectrum for the time series of TC counts in colors with the corresponding IBTrACS wavelet spectrum overlaid in black contours. It can be seen that the region of maximum power is at around 2010, which is also found in terms of ACE, with a periodicity of approximately 3 years. During that period two strong La-Niña events, separated by a strong El-Niño, occurred. In contrast, the region of maximum power for IBTrACS, with periodicity between 6-8 years, is located during the late 1990s, during which a very strong El-Niño event (1997-1998) was followed by a prolonged La-Niña. However, the fact that the periodicity found in IBTrACS is not observed on any of the reanalysis spectra leads to questions about the realism of the peak due to the poor observational record for this basin.

Correlations between the time series of frequency and ACE with the May-November averaged indices show mostly positive significant relationships with the AMM and AMO, and mostly moderate anticorrelations with ENSO and PDO (tab. 3.6). NCEP stands out once again with weak anticorrelations with ENSO, AMM and AMO and correlations

(a) Time series

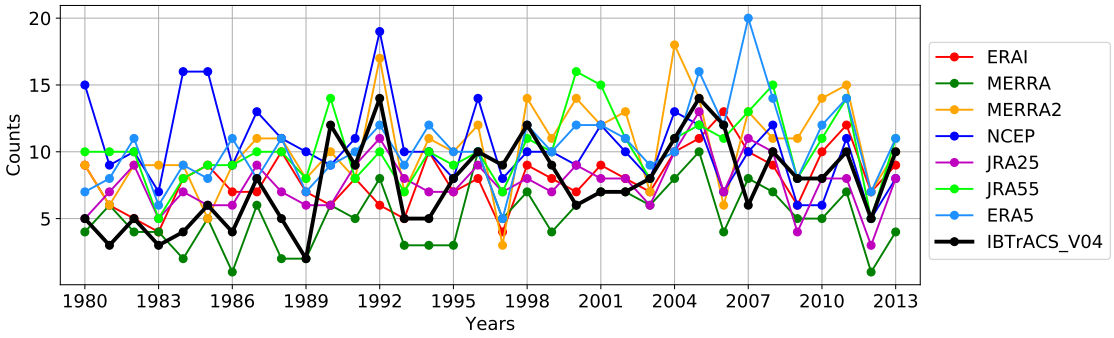

(b) Standard power spectrum

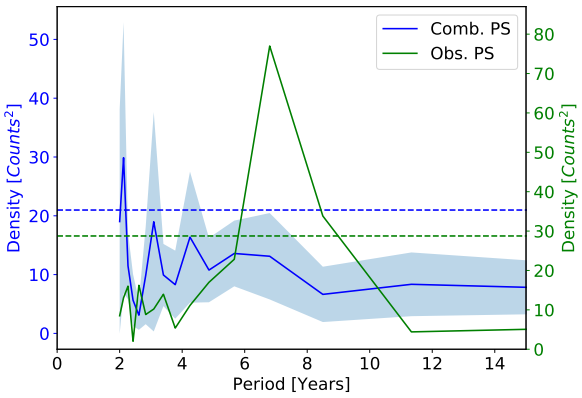

(c) Wavelet spectrum

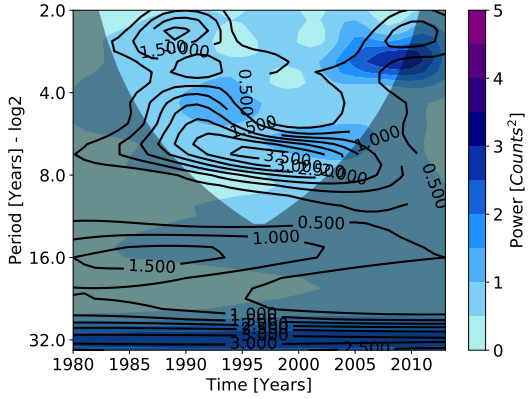

Figure 3.30: (a) Time series of TC counts for NIND; b) Standard power spectrum analysis for the time series. The individual reanalysis spectra are combined into one (blue line) and they are compared against the IBTrACS power spectrum (green line). The dashed lines indicate the 95% confidence level. The shaded area indicates the 95% confidence intervals for the combined spectrum; c) Mean of the seven reanalysis wavelet spectra (colours) and IBTrACS wavelet spectrum (black contours) of TC counts time series. The shaded area indicates the COI.

Table 3.6: Pearson correlations between the time series of NIND annual (a) TC counts and (b) ACE of IBTrACS and reanalyses with the seasonal climate indices for the 1980-2013 period. Correlations which are significant at the 90% CL are in bold.

	QBO	AMM	ENSO	AMO	PDO
IBTrACS	0.18	**0.45**	0.10	**0.36**	-0.17
ERAI	-0.03	**0.39**	**-0.42**	**0.53**	**-0.56**
MERRA	-0.12	**0.32**	0.02	0.24	-0.07
MERRA2	-0.16	**0.30**	-0.28	0.23	**-0.33**
NCEP	0.01	-0.22	-0.10	**-0.38**	0.17
JRA25	-0.11	0.13	-0.02	0.08	-0.02
JRA55	0.10	0.25	-0.29	**0.35**	**-0.54**
ERA5	-0.25	0.17	**-0.35**	**0.32**	**-0.46**

(a) TC counts

	QBO	AMM	ENSO	AMO	PDO
IBTrACS	0.10	**0.31**	-0.17	**0.37**	**-0.41**
ERAI	-0.15	0.17	**-0.43**	**0.30**	**-0.39**
MERRA	-0.17	**0.46**	-0.04	**0.35**	-0.05
MERRA2	-0.25	**0.31**	**-0.31**	**0.29**	-0.28
NCEP	0.15	-0.08	-0.20	-0.25	0.13
JRA25	-0.23	0.25	-0.04	0.22	0.04
JRA55	-0.07	0.19	-0.22	0.17	-0.15
ERA5	0.05	**0.32**	**-0.37**	**0.44**	**-0.32**

(b) ACE

with the PDO. Lastly, even though no significant correlations between the time series and the QBO index are found, for more than half of the reanalysis products the wavelet coherence between the QBO index and the individual reanalysis time series of TC counts shows significant regions within the 2-3 year power band, localised around the 1997-1998 El-Niño and the prolonged La-Niña event. It is possible that the intensity of those ENSO events significantly affected TC activity in the NIND ocean.

TC activity in this region is confined in the Bay of Bengal and the Arabian Sea as shown from the mean track densities on figures 3.1a and 3.1b. For EOT1, all the EOT1 base points are located in the Bay of Bengal with the exception of ERA5, which is located in the Arabian Sea, as evident on figure 3.31a. Results for this region did not reveal any robust influence from the climate indices. The percentage of variance explained by EOT1 for the different datasets is within the range 44-73%, while for EOT2 and EOT3 it drops to 12-31% and 6-20%, respectively (fig. 3.32). For this basin, 75% of the variability in the basin is covered by either two (for IBTrACS, MERRA and NCEP) or three (for ERAI, ERA5, MERRA2, JRA25 and JRA55) EOTs.

Spectral analysis of the EOT1 time series detects signals at ENSO's frequency, however the most interesting result is the power spectra for the second EOTs which has similar signals around seven years as the ones found in figure 3.30b. For some of the reanalyses,

(a) Locations for IBTrACS and reanalyses EOTs

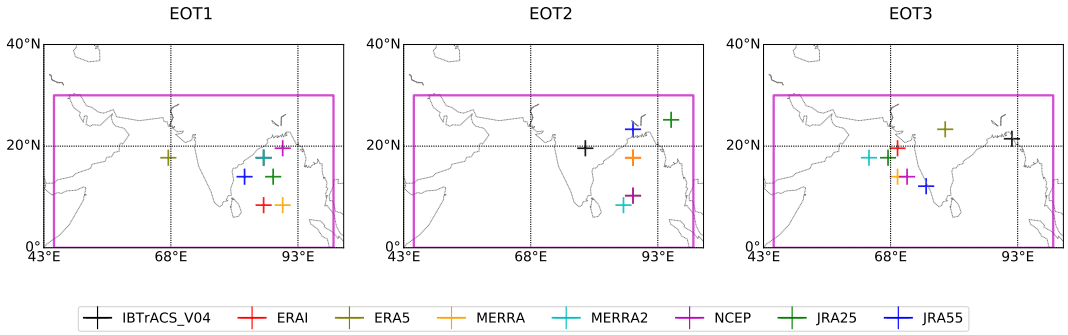

(b) SST regression patterns for ERA5. The HadISST SST field is regressed onto the ERA5 EOTs

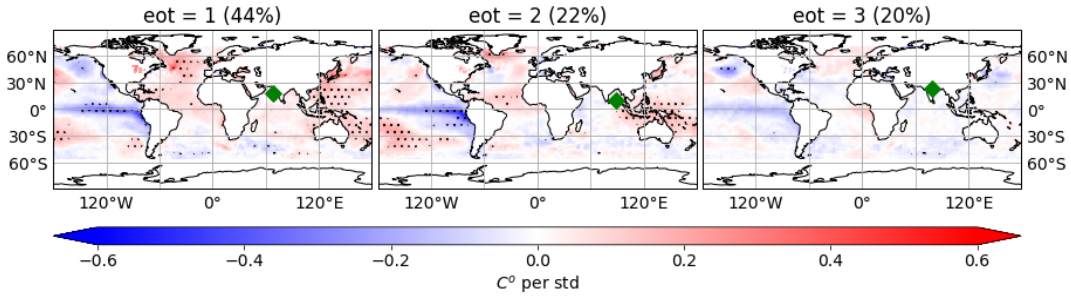

(c) VWS regression patterns for ERA5. The ERA5 VSW field is regressed onto the ERA5 EOTs

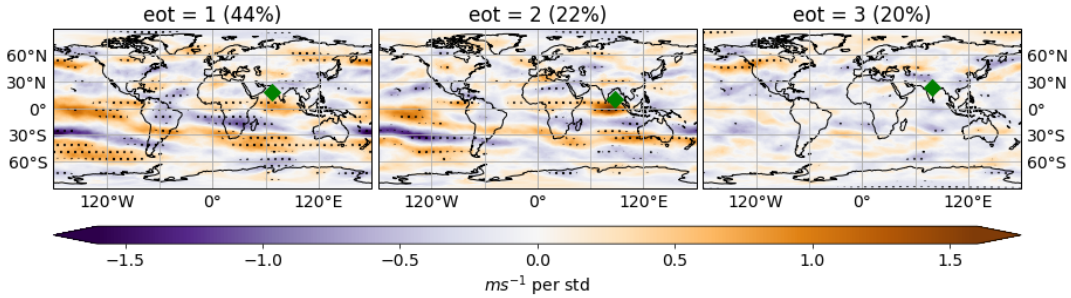

(d) Correlations between EOTs and May-November average climate indices

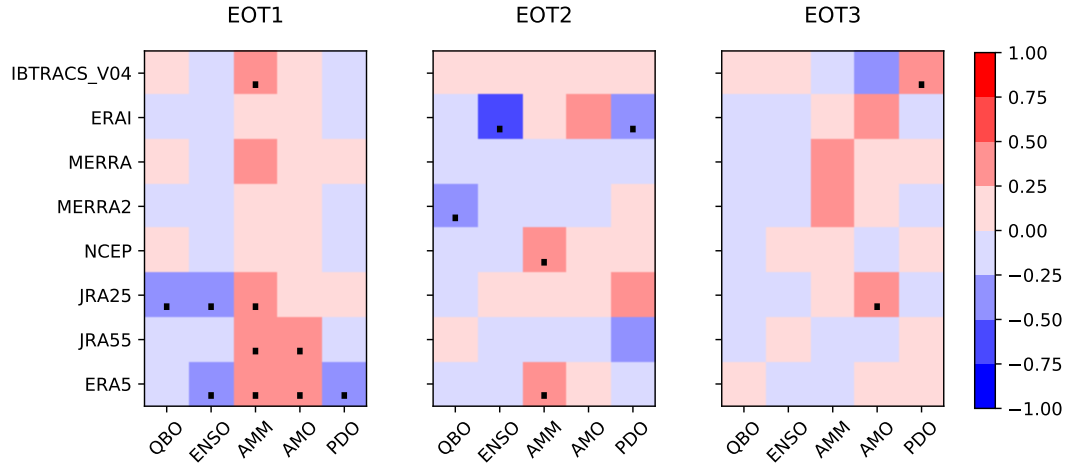

Figure 3.31: Results of EOT analysis for NIND under the current climate for IBTrACS and reanalyses. Locations of EOTs are indicated with a green marker on b and c. Significance at the 90% CL is indicated with dots on b, c and d.

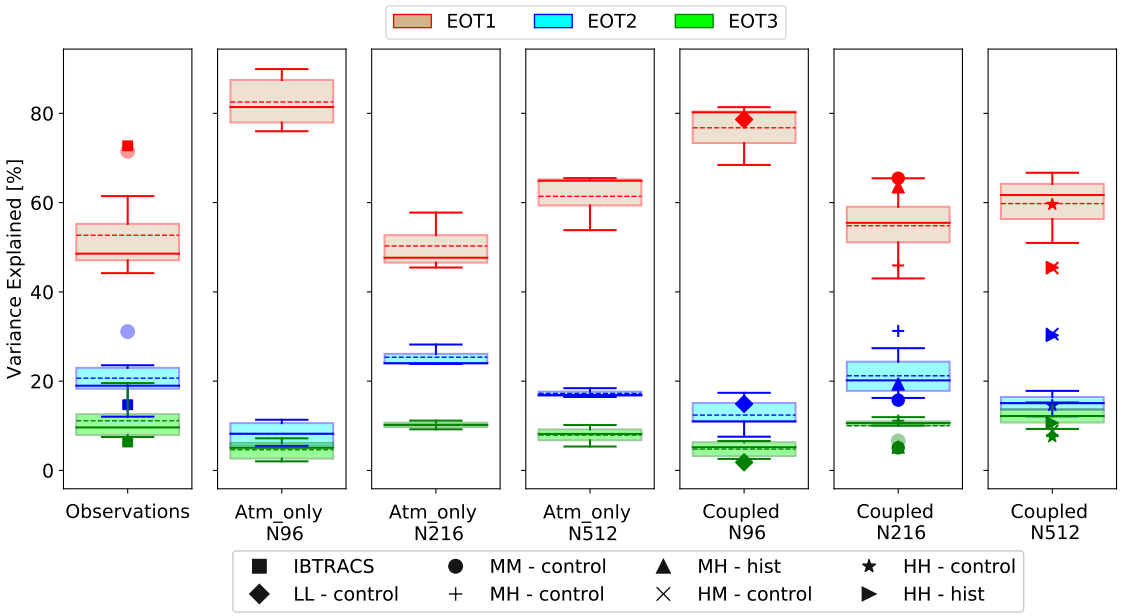

Figure 3.32: Percentage of variance explained by the EOTs under current climate for NIND. Column 1: Reanalyses (as an ensemble) against IBTrACS (■); Columns 2-4: ensemble of atm-only runs split by atmospheric resolution; Column 5: ensemble of LL historic runs against the control run (♦); Column 6: ensemble of MM historic runs against the MM control (●), MH control run (+) and MH historic run (▲); Column 7: ensemble of HM historic runs against HM control run (×), HH control run (★) and HH historic run (►). Faded circles (●) show outliers. Dotted lines show the ensemble means.

TC activity at EOT1 is found to be influenced by La-Niña conditions (either canonical or Modoki) with cold SSTs in the Eastern and Central Pacific and warm SSTs in the Western Pacific, such as the ones shown on figure 3.31b for ERA5. Such connections to La-Niña events have been found by Felton et al. (2013). Plus, enhanced VWS in the eastern and central regions of the Pacific ocean and south of India, possibly associated with the AMM, appear to affect TC activity in the ERA5 dataset as shown on figure 3.31c. The AMM connection is detected from the moderate positive correlations for the first two EOTs of ERA5 as seen on figure 3.31d. Moderate positive correlations are found between EOT1s and the AMO (AMM) for two (four) datasets. Even though, the cold phases of ENSO and PDO appear to influence some EOTs, no robust conclusion can be drawn about their influence on the activity in the basin.

It is possible that the main driver of this region's TC activity is more indirectly related to how the MJO and the monsoon seasons are influenced by the different modes of

interannual and decadal variability.

3.7.2 Models - Current Climate

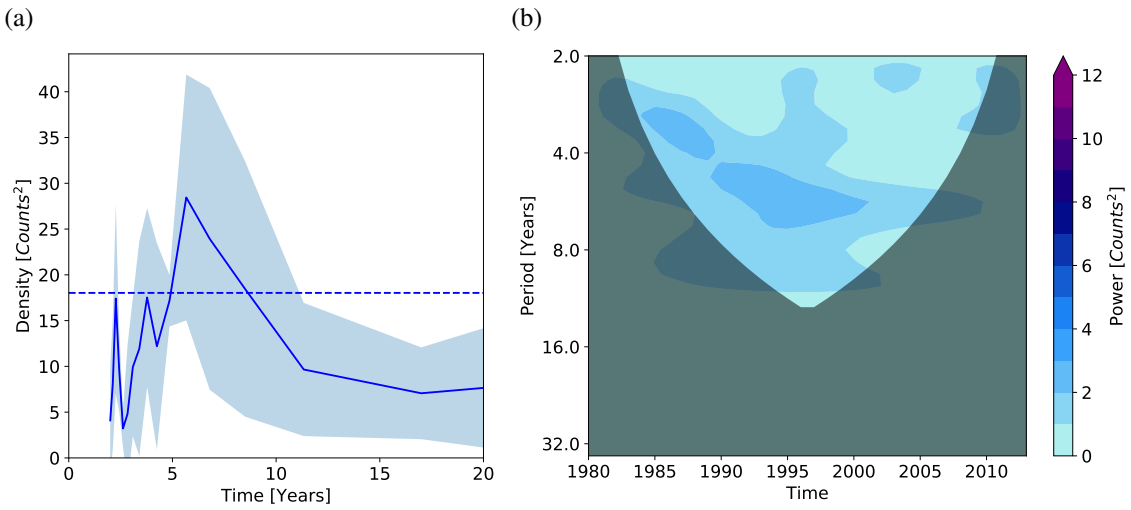

Figure 3.33: Spectral analysis on NIND TC counts for the atm-only HM runs: (a) Power spectrum: The spectra of the HM ensemble runs are combined into one (blue line). The dashed line indicates the 95% confidence level. The shaded area indicates the 95% confidence intervals for the mean power spectrum; (b) Wavelets: Colors indicate the mean spectrum for the ensemble of HM runs. The shaded area indicates the COI.

As found by Roberts et al. (2020a), TCs in the model simulations for this basin are more frequent than in observations. The NIND basin, however, is the only basin from the ones examined in the study for which model time series do not have significant correlations with the time series from the observations. Even though significant signals on interannual time scales are detected for some of the runs in the power spectrum, their overall quantity is smaller than the ones found in other basins. The distinct periodicity of approximately 7 years that was found in IBTrACS is detected in some of the power spectra of model runs, particularly the atm-only experiments as shown on figure 3.33a. Lastly, the region of maximum power in the combined wavelet spectrum of the time series of TC counts from the ensemble of HM atm-only runs has a similar periodicity as the significant peak in the power spectrum (fig. 3.33b).

Out of the 31 experiments examined in this study, only 5 of them show a significant connection to AMO in terms of frequency, 2 of them (coupled LL) showing anticorrelations

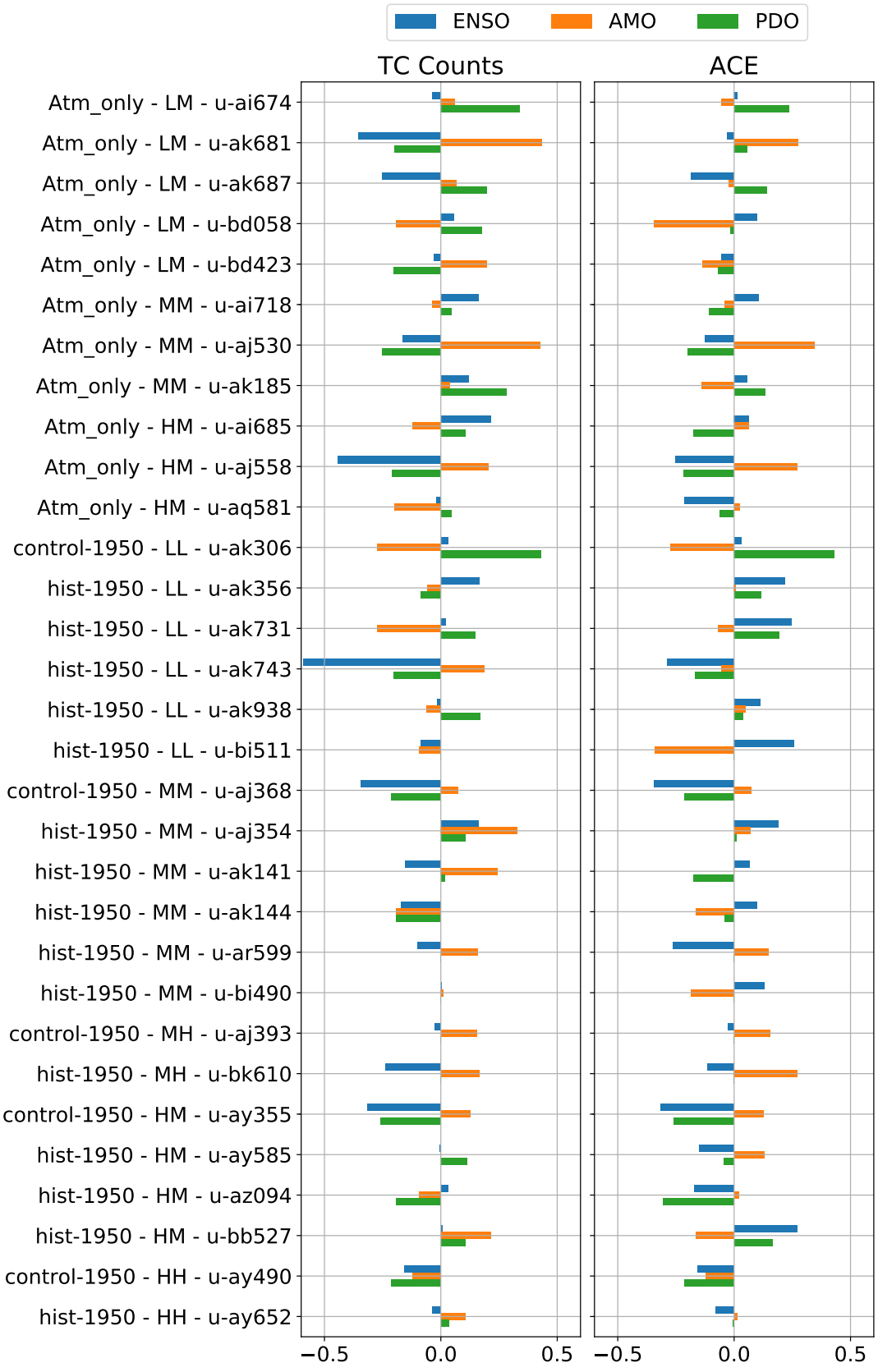

Figure 3.34: Pearson correlations between the time series of NIND annual TC counts and ACE of models with the seasonal climate indices for the 1980-2013 period. Hatched bars indicate the correlations that are significant at the 90% CL.

with AMO and thr3ee of them (1 atm-only LM, 1 atm-only MM and 1 coupled hist-1950 MM) had a positive relationship (fig. 3.34). A similar picture can be drawn for the relationship with ACE. On the other hand, ENSO's influence on TC activity in the basin appears to be minimal, since only 4 or less of the model runs, irrespective of resolution and configuration, showed a significant relationship with the May-November averaged index. The same situation occurs for the influence by the PDO, since only 2 of the experiments show a connection to the PDO index for both ACE and frequency.

EOT1 base points locations are generally closely located in the eastern side of the region, mainly in the Bay of Bengal or over India, for the majority of the model simulations, with the exception of one HM coupled hist-1950 run (u-ay585) which is positioned in the Arabian Sea (fig. 3.35a). In addition, the first three EOTs for all the N96 runs are located only in the Bay of Bengal, with no base points in the Arabian Sea. In contrast, for the N216 and N512 simulations, some of the EOT2s and EOT3s spread towards the Arabian Sea. Figure 3.35a presents the locations for all the model experiments.

Furthermore, the distribution of variance explained by the first EOTs for the N216 simulations (both atm-only and coupled) appears to have the most similarities with the observed distribution of variance compared to the ones from N96 and N512 runs, as shown on figure 3.32. EOT1s for N96 and N512 have a noticeable difference from EOT2s, which can perhaps be attributed to the fact that there are less TCs in the N96 runs, and therefore, less variability, since the TCs are mainly in the Bay of Bengal as seen from the mean track densities (fig. 3.1). For the N512 experiments, the reason for such a difference remains unknown.

The correlations between the EOT time series and the climate indices for the model simulations do not reveal any robust significant relationships with the climate modes, as shown from figure 3.35d, even though 18 of the models show positive (negative) correlations between EOT1 and AMO (ENSO). Following the same footsteps, the overwhelming majority of the regression maps does not provide any further insight on how the climate indices influence TCs in the basin. One of the few experiments for which some connection to the indices can be established from the SSTs and VWS is the u-bk610 (MH) coupled hist-1950 run. The corresponding SST and VWS maps are shown on figures 3.35b and 3.35c, respectively. For this particular run, the absence of significant known canonical patterns on the map for EOT1 is noticeable, whereas on map for EOT2, a cold SST tongue

(a) Locations of EOTs for all the model runs

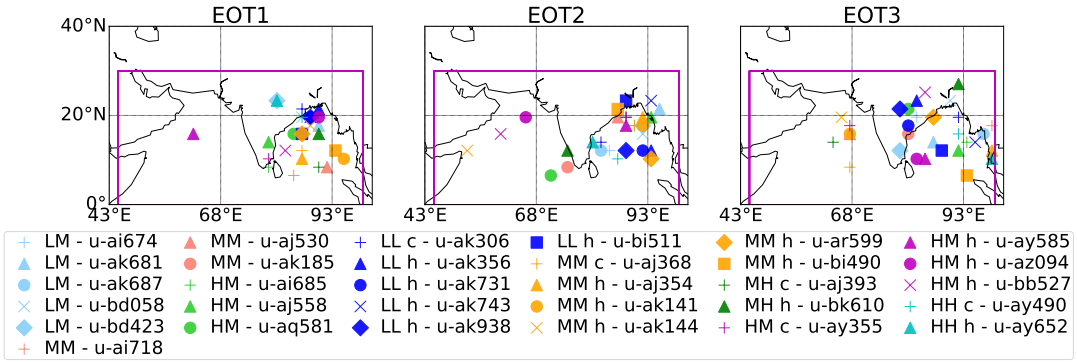

(b) SST regression patterns for the u-bk610 hist-1950 run

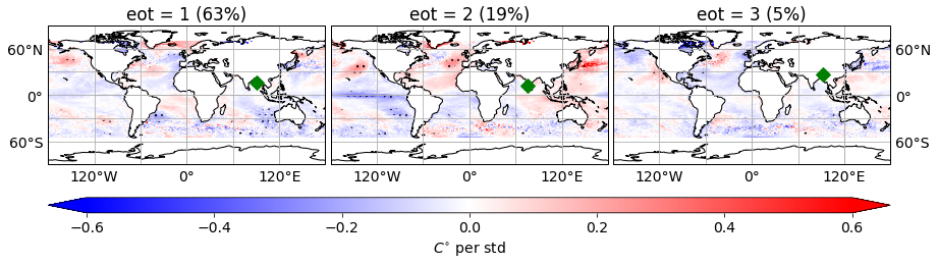

(c) VWS regression patterns for the u-bk610 hist-1950 run

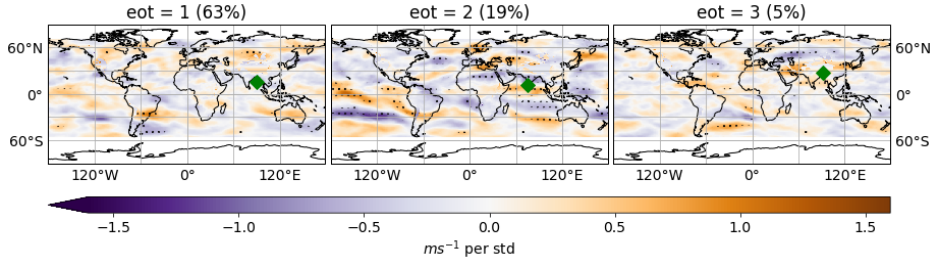

(d) Summary statistics about the Pearson correlation coefficients between the NIND EOT time series for the different model simulations and the May-November averaged ENSO, AMO and PDO indices.

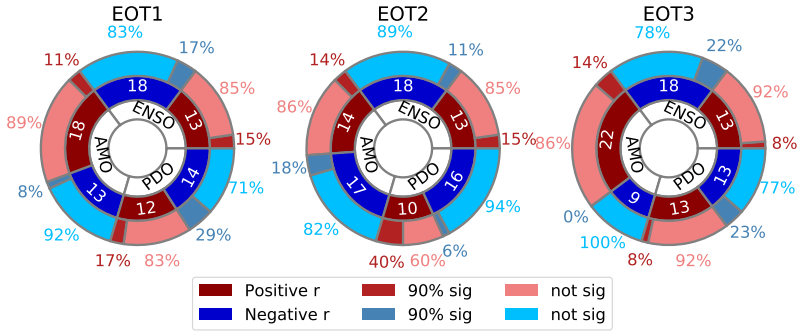

Figure 3.35: EOT results for TC variability in NIND for the model simulations. Location of EOT is shown with green marker and significance at the 90% CL is indicated with dots on b and c. Period examined is 1980-2013. For the correlations dark red (blue) colors indicate how many of the 31 models have positive (negative) correlations with each index, medium red (blue) indicate how many of the dark red (blue) correlations are significant at the 90% CL, while light red (blue) indicate how many are not significant.

in the eastern and central Pacific and warm SSTs in the northeastern Atlantic can be seen. This, along with strong VWS in the central Pacific and in the north Indian ocean and weak VWS over the north central Atlantic show that TC activity for this particular run is influenced by La-Niña and AMO-related conditions.

3.7.3 Summary

Even though connections between TC activity in the NIND basin and ENSO have been made in a few studies such as (Liu et al., 2021), results of the analysis performed on TC activity in the basin are characterised by the absence of significant connections to the climate indices examined in the study, in both observations and model simulations. It is possible, however, for the climate modes to influence TC activity indirectly, primarily via affecting the monsoon seasons as several studies have explored (A.A.Deo and D.W.Ganer, 2015; Goswami et al., 2006; Liu et al., 2021; Rajeevan et al., 2013).

3.8 Conclusion

In this chapter, the drivers of TC variability under the current climate (1980-2013) in the different NH basins are examined in IBTrACS, seven reanalysis datasets and a range of atmosphere-only and coupled simulations by HadGEM3-GC3.1. A range of techniques have been utilised for this investigation. The spectral methods (standard power spectrum and wavelets) have been used in order to detect any periodicities within the time series of TC activity. Additionally, the EOTs method has been used to analyse seasonal TC track densities and to identify canonical patterns of known modes of climate variability that influence TC activity on EOT regression patterns. Lastly, Pearson correlation coefficients were computed between the climate indices and time series of TC activity (counts, ACE and EOTs). Table 3.7 presents a summary of the results examined in this chapter on whether TCs in the different datasets are influenced by the climate modes that were examined. Given the large number of datasets and techniques utilised, a climate mode of variability is considered to have a clear influence on TCs if more than 75% of the analysis results showed a clear connection to the mode. If 50-75% of the results showed a connection to the mode, then there are indications of its influence on TCs. Otherwise, the climate mode is not associated with TC variability in the basin.

During the period examined, TC activity in the well-documented NATL region exhibits high variability, which has been found to be mainly driven, in all datasets, by warm Atlantic SSTs associated with the warm phases of the AMM and the AMO, as indicated by the results of the EOT regression analysis. In addition, further influence by the cold phases of ENSO and PDO, albeit with less robustness compared to the AMO, is exerted on Atlantic TCs via cold SSTs and enhanced VWS in the Pacific region. The influence of ENSO and AMM has been captured in all the different techniques used in the analysis, including the spectral analysis on EOT time series. As expected, the frequency of AMO and PDO was not captured by the spectral methods due to the short period that was examined. However, with the use of Pearson correlation coefficients and the EOT regressions patterns, their influence on TC activity in the basin has been identified.

Primary driver of the EPAC and CPAC TC activity is the warm phase of ENSO via warm SSTs and weak VWS in the eastern and central Pacific region, as has been established by the presence of associated canonical patterns on the EOT regression maps. Further evidence of this influence stems from the results of spectral analysis on the various time series as well as from Pearson correlations between the time series of TC activity and the May-November averaged index. Forming an opposite picture to the one for the NATL, the AMO has an influence on TC variability in the two regions, but with less robustness. A caveat of the analysis on the CPAC region is the fact that time series with very low amount of TCs are analysed. Therefore, it is crucial that more studies using both GCMs and better observations are undertaken in order to gain more confidence in the results for this particular region.

The typhoon activity in the WPAC region under the current climate in observations has been found to be influenced by the change of phase of the AMO and PDO, which lead to strengthening or weakening ENSO events during different decades. This result is primarily derived with the use of wavelets, which allow examination of power in both time and frequency. Even though, the periodicities of the two decadal modes were not captured by the spectral methods, the localisation of significant signals in the wavelet spectrum is associated with the change of phases of the two modes. Moreover, TC activity in both observations and models is found to be driven by more than one main driver.

Lastly, in contrast to the other basins, TC activity in the NIND region does not exhibit significant connections to the indices examined in the study, as it can be seen particularly

from the results on the analysis of the model simulations. For this basin it is necessary to investigate how the different modes of climate variability, namely ENSO, AMM, AMO and PDO, impact monsoon seasons and the Indian Dipole.

Table 3.7: Summary of which modes of variability influence each basin in the different datasets for the 1980-2013 period. YES: If more than 75% of the results examined in the chapter indicate the influence by a specific mode; YES*: if 50-75% of the results in the chapter indicate the influence by a specific mode; NO: if less than 50% of the results examined in the study indicate the influence by a specific mode; N/A: if the mode was not examined.

	NATL					EPAC					CPAC					WPAC					NIND				
	QBO	ENSO	AMM	AMO	PDO	QBO	ENSO	AMM	AMO	PDO	QBO	ENSO	AMM	AMO	PDO	QBO	ENSO	AMM	AMO	PDO	QBO	ENSO	AMM	AMO	PDO
IBTRACS	NO	YES	YES	YES	YES*	NO	YES	YES*	YES*	YES*	NO	YES*	YES	YES	NO	NO	YES	YES	YES	YES	NO	YES*	YES	YES	YES*
REANALYSES	NO	YES	YES	YES	YES*	NO	YES	NO	YES*	NO	NO	YES	YES	YES	NO	NO	YES	YES	YES	YES*	NO	NO	YES	YES	YES*
ATM_ONLY-LM	N/A	YES	N/A	YES	YES*	N/A	YES	N/A	YES*	NO	N/A	YES	N/A	YES	YES	N/A	YES	N/A	YES	NO	N/A	YES*	N/A	NO	NO
ATM_ONLY-MM	N/A	YES	N/A	YES	YES	N/A	YES	N/A	YES	YES*	N/A	YES*	N/A	YES	YES	N/A	YES*	N/A	YES*	NO	N/A	YES*	N/A	NO	NO
ATM_ONLY-HM	N/A	YES	N/A	YES	YES	N/A	YES	N/A	YES	NO	N/A	YES	N/A	YES	YES	N/A	YES	N/A	YES	NO	N/A	YES*	N/A	NO	NO
COUPLED-N96	N/A	YES*	N/A	NO	NO	N/A	YES*	N/A	NO	NO	N/A	YES*	N/A	YES*	NO	N/A	YES*	N/A	NO	NO	N/A	YES*	N/A	NO	NO
COUPLED-N216	N/A	YES*	N/A	YES	NO	N/A	YES*	N/A	YES*	NO	N/A	YES	N/A	YES*	NO	N/A	YES*	N/A	NO	NO	N/A	YES*	N/A	NO	NO
COUPLED-N512	N/A	YES*	N/A	YES	NO	N/A	YES	N/A	NO	NO	N/A	YES	N/A	NO	YES*	N/A	YES*	N/A	NO	NO	N/A	YES*	N/A	NO	NO

Chapter 4

Drivers of Decadal TC Variability

4.1 Introduction

This chapter presents results from the analysis of the drivers of TC activity on decadal time scales using centennial and multi-centennial time series of annual TC counts and ACE from a range of HadGEM3-GC3.1 simulations, along with track densities for 100 seasons. In terms of TC counts, time series and results from spectral analysis will be shown. In terms of ACE, for each basin, even though the time series and results from spectral analysis will be discussed, only figures of Pearson correlations with the climate indices will be presented. The drivers examined in the chapter are the SST and VWS fields from the different runs. For each basin, the multi-centennial ($\sim$ 595 years) time series of TC counts from the MM control run, along with the corresponding standard power and wavelet spectrum, will be displayed. For the NATL only, additional power spectra from 100-year-long time series will be presented in order to perform a comparison with the multi-centennial run.

Due to the nature of the atm-only experiments being forced by the same observed SSTs, all of them, irrespective of atm-resolution have identical climate indices. An example of the three climate indices analysed in this chapter for one of the HM atm-only runs, is shown on figure 4.1. The AMO has completed one cold phase from 1960 to around 2000 before shifting to a warm phase until the end of the period. The PDO shows one major complete warm phase between 1977 until almost 2010, while from 2020 onwards, the climate mode is in a cold phase. During the warm phase of the AMO, ENSO exhibits some of the strongest La-Niñas, and some of the smallest in duration El-Niños. The

longest in duration El-Niño occurs during the period right before the shift of the AMO, where the PDO is in a warm phase and the AMO is in a cold phase. In addition, the strongest El-Niño event occurs right after the shift of the AMO, while the PDO is still in a warm phase.

For the coupled simulations, the climate indices are unique compared to the atm-only runs. The different indices will not be individually described in this study, however, it is important to note that the warm and cold phases of the indices, especially for the two decadal modes, do not always exhibit the expected duration, i.e. 20-30 years for the PDO and 50-70 years for the AMO. For example, figures 4.2 and 4.3 display the monthly climate indices for the HM (u-ay355) and HH (u-ay490) coupled control runs, respectively. For the indices of the HM control run it can be seen that both the AMO and the PDO complete at least one full phase, i.e. the AMO being in a warm phase for almost 50 years, and the PDO being in a cold phase for almost 40 years. It is worth noting that the strongest El-Niño occurs during a small period when both the AMO and PDO monthly indices are in a warm phase (around 2020 on fig. 4.2). In contrast, for the HH coupled control run the AMO's warm and cold phases are noticeably shorter and the expected cycle of AMO is not captured. It is important to note, however, that the strongest ENSO events occur around the periods when the two decadal modes shift from one phase to the other.

Results from the atmosphere-only and coupled experiments show that the WPAC region is the most active tropical cyclone region both in terms of frequency and ACE, something that is also observed in the investigation of the drivers under the current climate. Summary statistics for the frequency and ACE of TCs in the basins of the NH are presented on figures 4.4 and 4.5, respectively. In addition, global TC counts and ACE are lower for the N216-resolution experiments than for the N512-resolution experiments. This result was expected as the skill in simulating TC-like features depends on resolution (Roberts et al., 2015). It is also observed that the counts for the N216-resolution experiments are lower than the counts in observations, in contrast to the counts for the higher-resolution experiment which appears to be within the range of counts found in IBTrACS and the reanalyses.

Standard power spectral analysis of the 100-year length time series of global TC counts shows that for all the model simulations, with the exception of four LM atm-only runs and the HM coupled runs, there is evidence of decadal TC variability, whereas in terms of

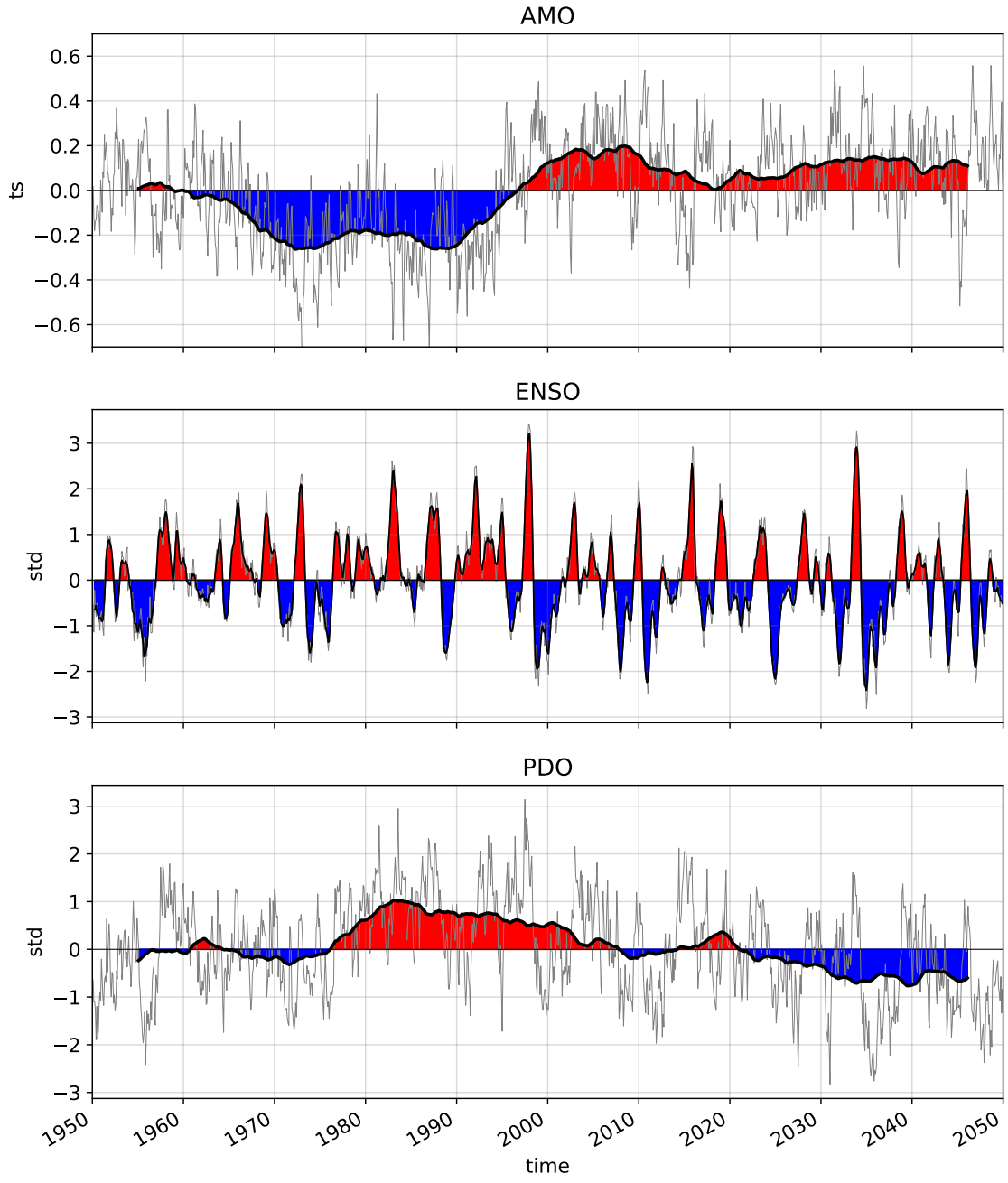

Figure 4.1: The AMO, ENSO and PDO indices for one of the HM atm-only experiments (u-ai685). The gray lines show the monthly indices, while the dark solid lines show the 5-month and 10-year running mean for ENSO and two decadal modes, respectively.

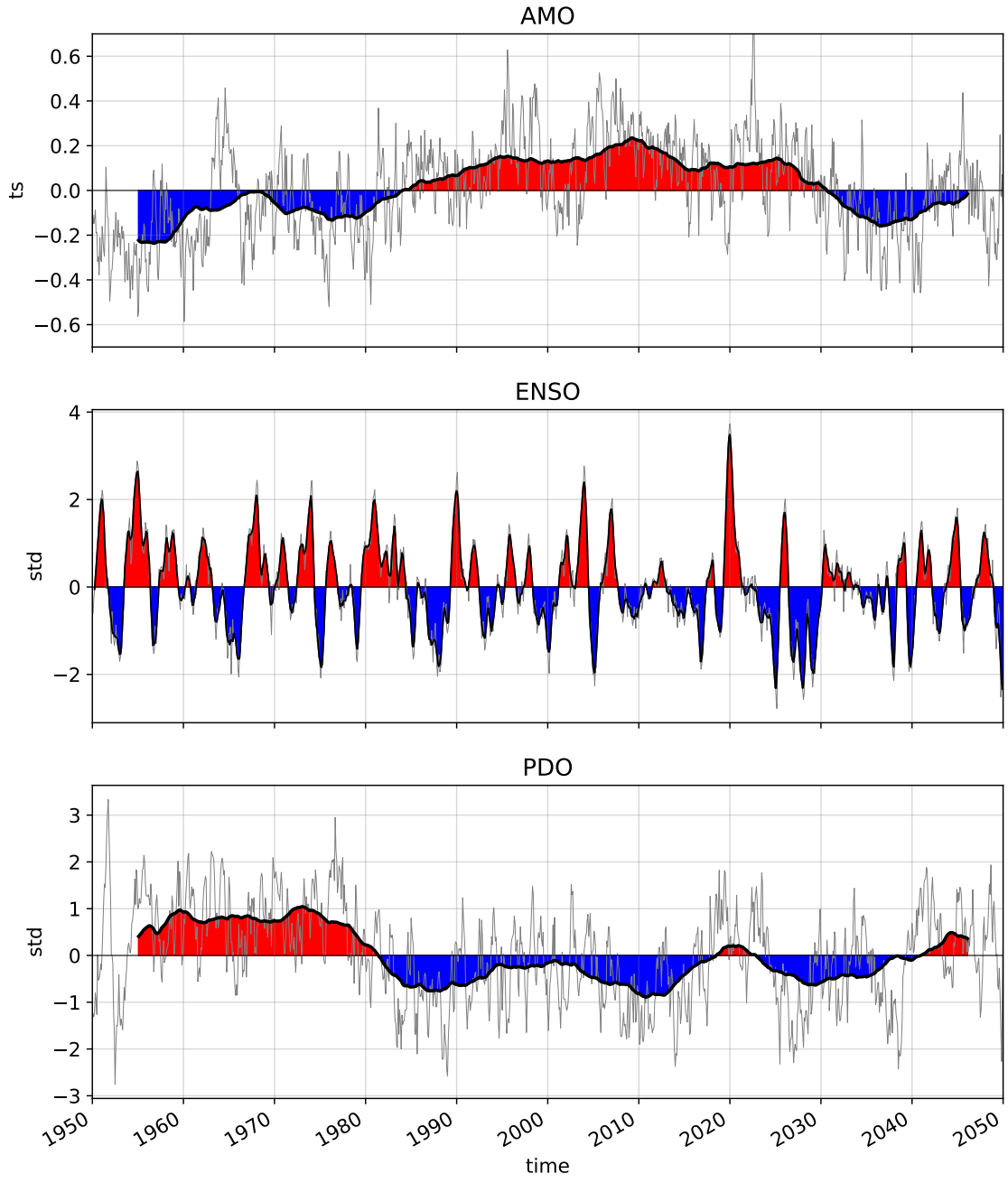

Figure 4.2: The AMO, ENSO and PDO indices for HM coupled control run (u-ay355). The gray lines show the monthly indices, while the dark solid lines show the 5-month and 10-year running mean for ENSO and two decadal modes, respectively.

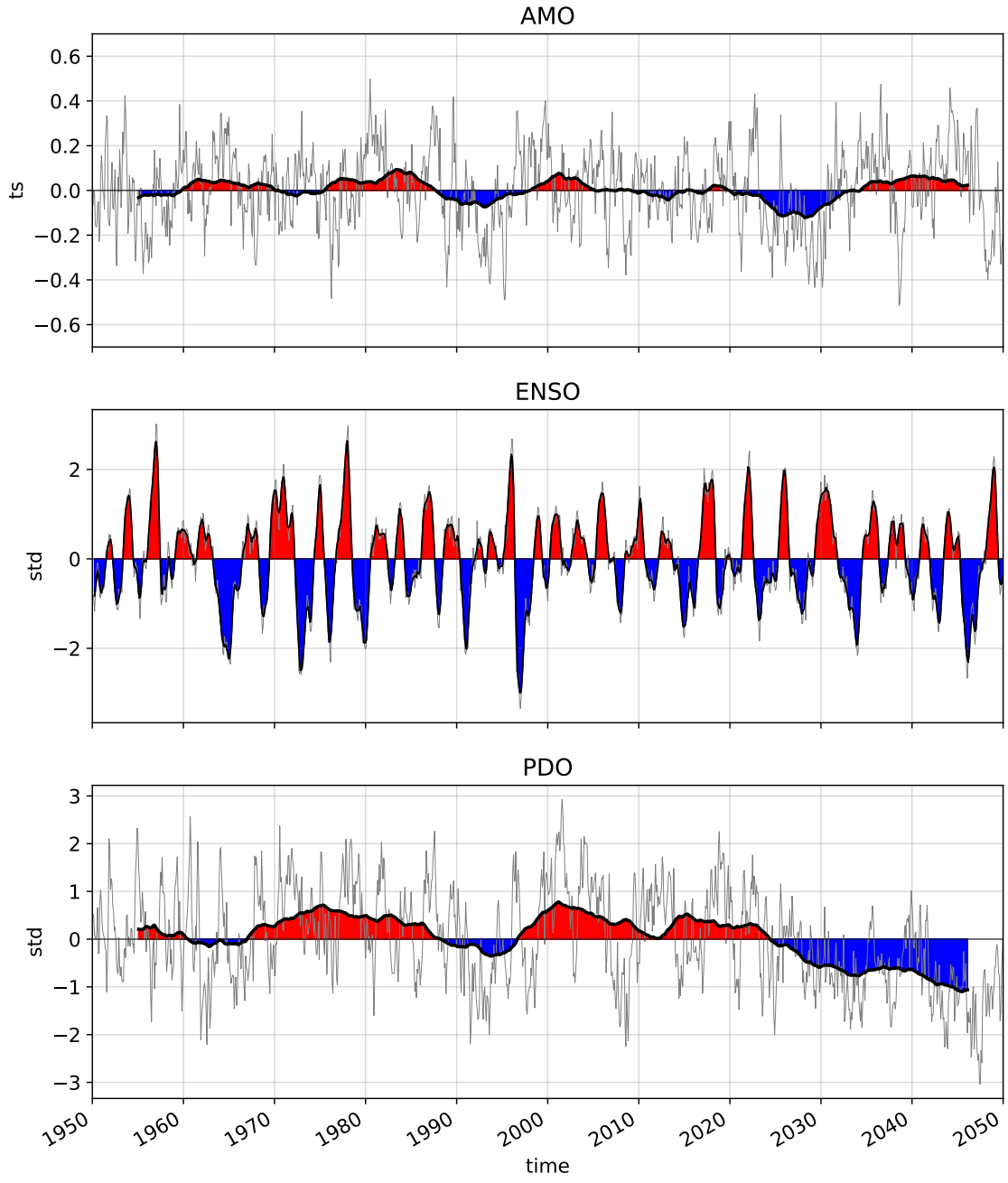

Figure 4.3: The AMO, ENSO and PDO indices for HH coupled control run (u-ay490). The gray lines show the monthly indices, while the dark solid lines show the 5-month and 10-year running mean for ENSO and two decadal modes, respectively.

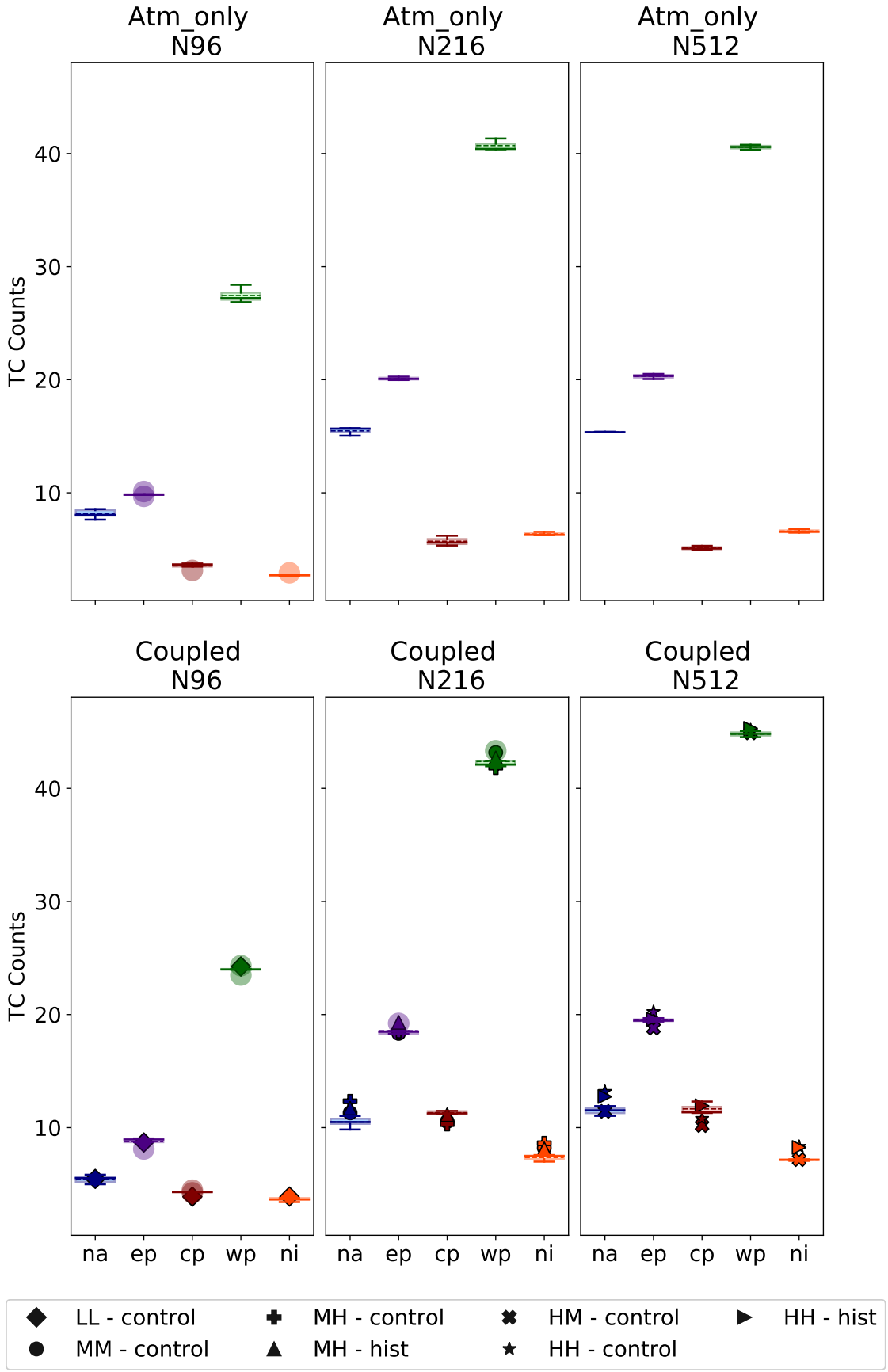

Figure 4.4: Summary statistics for the frequency of TCs in the different basins for the model experiments.

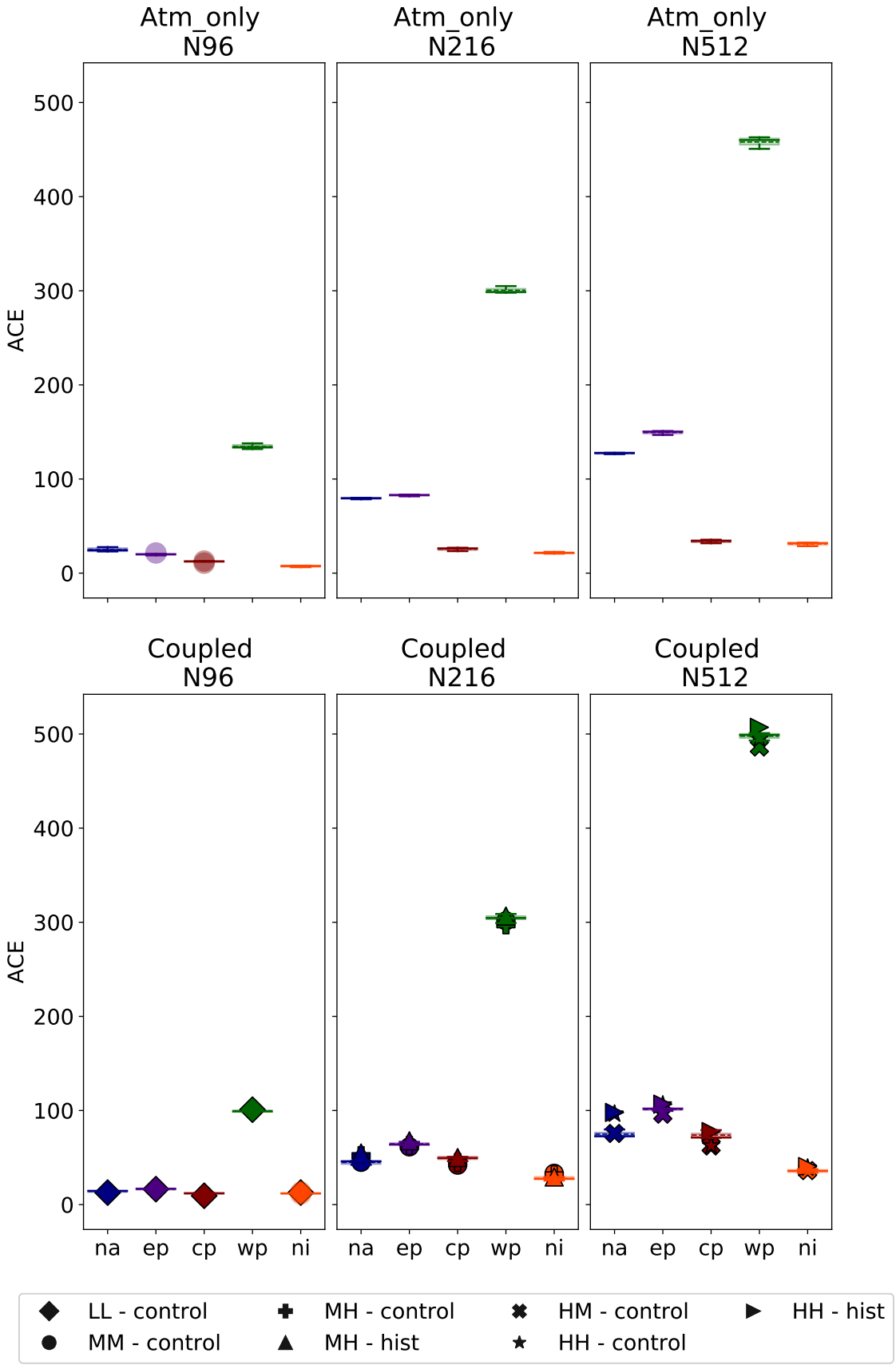

Figure 4.5: Summary statistics for the ACE of TCs in the different basins for the model experiments.

ACE, only a handful of the model simulations do not exhibit any significant periodicities on decadal time scales. It is impossible to efficiently summarise the results for the wavelet analysis, since the individual wavelet spectra show different significant regions localised at different periods and at different periodicities. It is important to note, however, that most of the wavelets have small significant regions on inter-annual time scales, while at least one experiment from each type of configuration and resolution, also displays significant signals on decadal time scales. It is observed that for the majority of these signals, despite their respective periodicities, they are localised near a change of phase of the two decadal modes, particularly towards the second half of the period examined.

The control-runs provide a unique opportunity to look at periodicities on decadal as well as on multi-decadal time scales, since they provide longer, more consistent records to work with. The five control-runs analysed in this study provide time series of annual TC counts and ACE for 600 (LL), 550 (MM), 200 (MH), 153 (HM) and 142 (HH) years. These time series are analysed using only the standard power spectrum method. Results for total TC counts and ACE from the LL and MM runs reveal significant peaks on multi-decadal time scales. Specifically, for both frequency and ACE, peaks can be observed at around 10, 15 and 20 years, while more signals are displayed for counts at around 30 years only for TC counts. The time series for the MH, HM and HH experiments are significantly shorter, therefore, even though significant peaks are found on decadal and multi-decadal time scales, they were at less quantities compared to the LL and MM runs.

Significant moderate anticorrelations for the atm-only experiments and weak anticorrelations for two coupled runs are observed between the AMO index and the time series of global TC counts. For ACE, moderate to strong anticorrelations with all the atm-only runs, and weak to moderate anticorrelations with at least 8 of the 20 coupled runs were found. Furthermore, the ENSO May-November averaged index has a significant positive influence on the NH's total ACE with all but the HH hist-1950 runs and significant positive correlations with at least half of the simulations in terms of counts. Interestingly, only the HH hist-1950 run was a weak anticorrelation with the climate mode. Lastly, the PDO May-November averaged index is significantly (weakly or moderately) correlated with time series of TC activity for 8 of the atm-only runs and significantly (weakly or moderately) anticorrelated with 4 and 7 of the coupled runs for counts and ACE, respectively.

4.2 North Atlantic

(a) Time series: annual TC counts (gray) and 10-year running mean

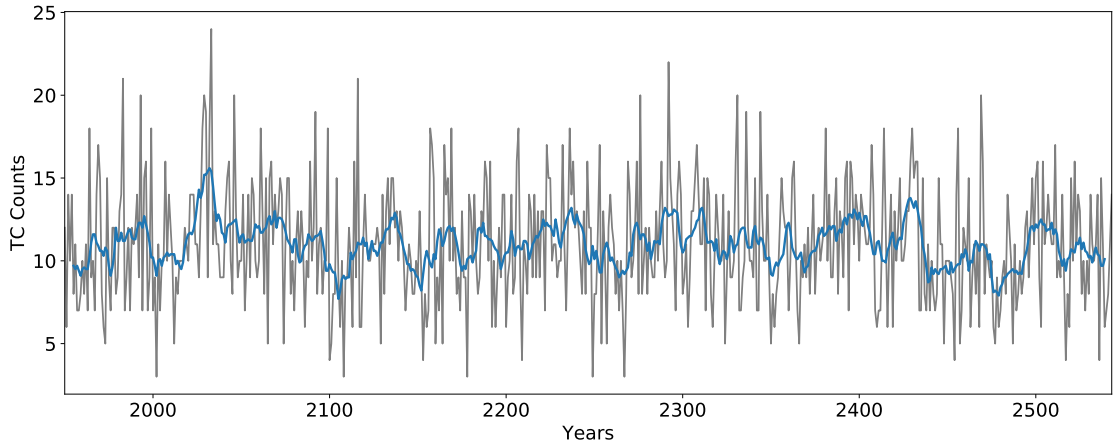

(b) Power spectrum with 95% confidence level (red dashed line)

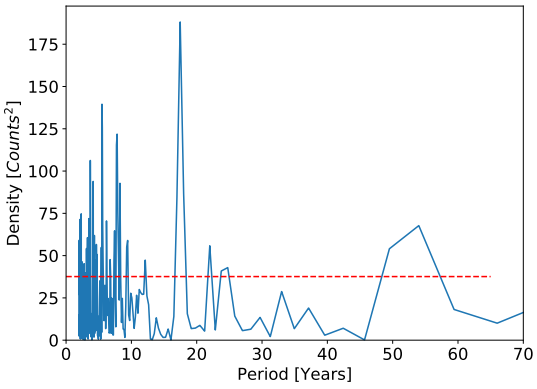

(c) Wavelet spectrum with COI (shaded area) and 95% confidence level (red contours)

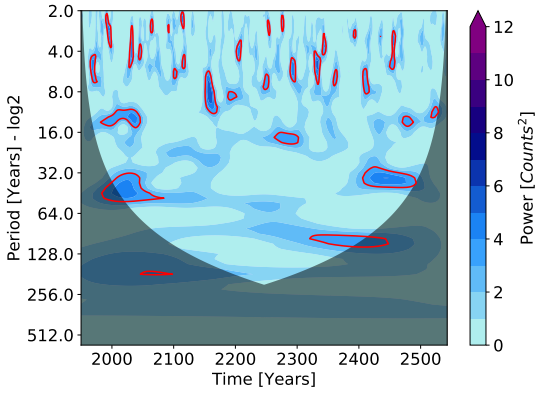

Figure 4.6: Results of spectral analysis for decadal TC variability in NATL annual counts for the multi-centennial MM control run.

Figure 4.6 presents the time series of annual NATL TC counts for the multi-centennial MM control run, along with the corresponding power spectral density and wavelet spectrum. Figure 4.7a displays the wavelet power spectrum of the multi-centennial time series of ACE for the NATL region. The distribution of power within certain bands (i.e. 2-8, 10-20, 20-40 and 40-70 years) is shown with KDEs (black lines) on figures 4.7b - 4.7e. The same time series was split into 5 100-year-long segments and for each segment the individual wavelet spectrum was computed. Following the same procedure as for the multi-centennial time series, for each wavelet spectrum the distribution of power within the above-mentioned bands was examined with KDEs which are presented with colored

lines on figures 4.7b - 4.7e.

It can be clearly seen that the different 100-year segments can capture the distribution of power within the 2-8 power band, which covers ENSO's periodicity, as effectively as the multi-centennial run. For longer periods, however, 100-year segments are not sufficient for adequately capturing multi-decadal variability, such as the one associated with the AMO, as indicated by the increasing spread of the KDEs on figures 4.7b - 4.7e. This clearly highlights the importance and necessity of longer climate simulations for investigating multi-decadal variability of both the climate as well as of TC activity.

All the individual standard power spectra of the 100-year long time series show significant peaks on interannual time scales, at similar periodicities to those observed for the current climate, pointing once again to QBO and ENSO influence on TC activity. Decadal signals are detected only in a couple of N96 and N512 atm-only experiments in terms of counts as shown on figure 4.8a. In contrast, for the time series of ACE, along with interannual signals, decadal signals (at ~10 years) were found for at least one ensemble member from each resolution. Such signals have been detected for all the coupled control runs with the exception of LL. For at least one hist-1950 ensemble member from each type of configuration, apart from the HH, similar signals were detected in the time series by the standard power spectrum analysis. Lastly, power spectra for the multi-centennial time series of counts and ACE from the control runs, revealed significant peaks around 20, 25 and 50 years (fig. 4.6b), periodicities which are linked to the decadal modes analysed in the study.

Results from the wavelet analysis of the 100-year long time series from the atm-only experiments show multiple significant regions on inter-annual time scales, within the 3-7-year band, as well as on decadal time scales within the 10-32-year band. The majority of the significant regions are observed within the last 50 years of the simulations, which is characterised by a warm AMO phase. Figure 4.8b presents the mean wavelet spectrum of the time series of TC counts from the HM atm-only runs. The maximum of the mean spectrum serves as an example of an inter-annual signal. Figure 4.8c shows wavelet spectra from the ACE time series of the N512 coupled runs. The mean wavelet spectrum for the ensemble of HM coupled hist-1950 runs is shown with colours on the left, with the wavelet spectrum of the HM control run shown with gray contours. The wavelet spectra of the HH control and hist-1950 runs are shown on the right with gray contours

(a) Wavelet Spectrum with COI (shaded area) and 95% confidence level (red contours)

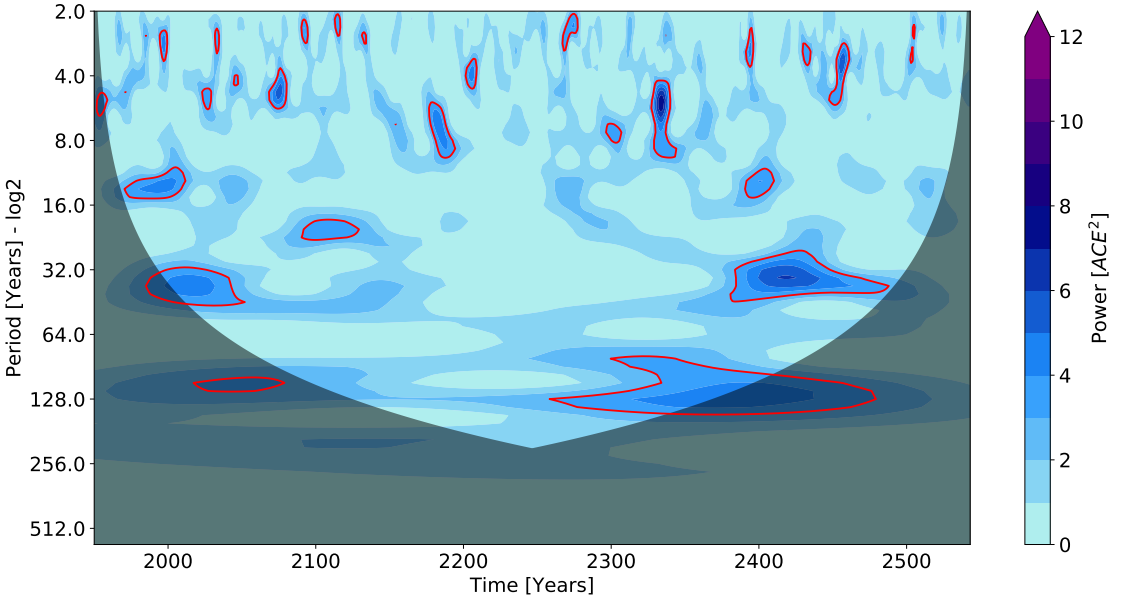

(b) 2-8-year band

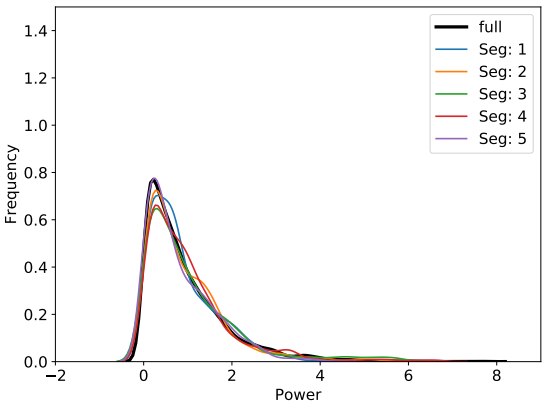

(c) 10-20-year band

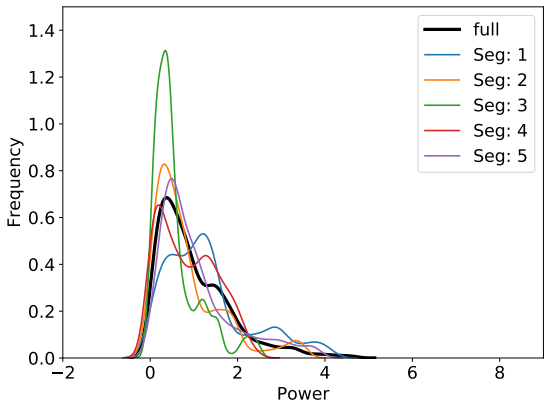

(d) 20-40 year band

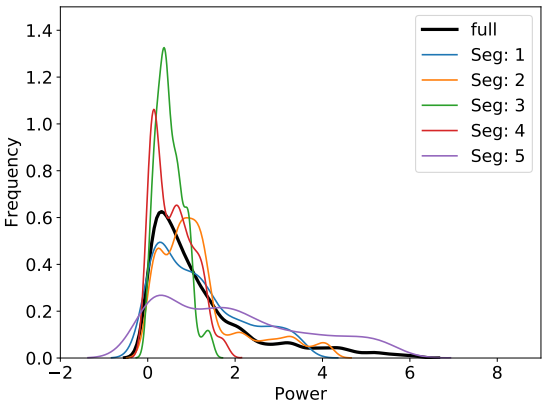

(e) 40-70 year band

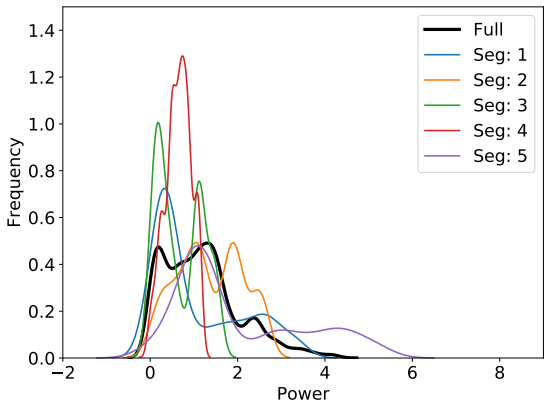

Figure 4.7: (a) Wavelet spectrum for the NATL time series of ACE of the multi-centennial MM control run; (b) - (e) KDEs for the wavelet power in different bands for the full run (black line) against KDEs for the wavelet power of 100-long segments of the run.

(a) Combined power spectrum of the HM atm-only time series of TC counts

(b) Mean wavelet spectrum of the HM atm-only time series of TC counts

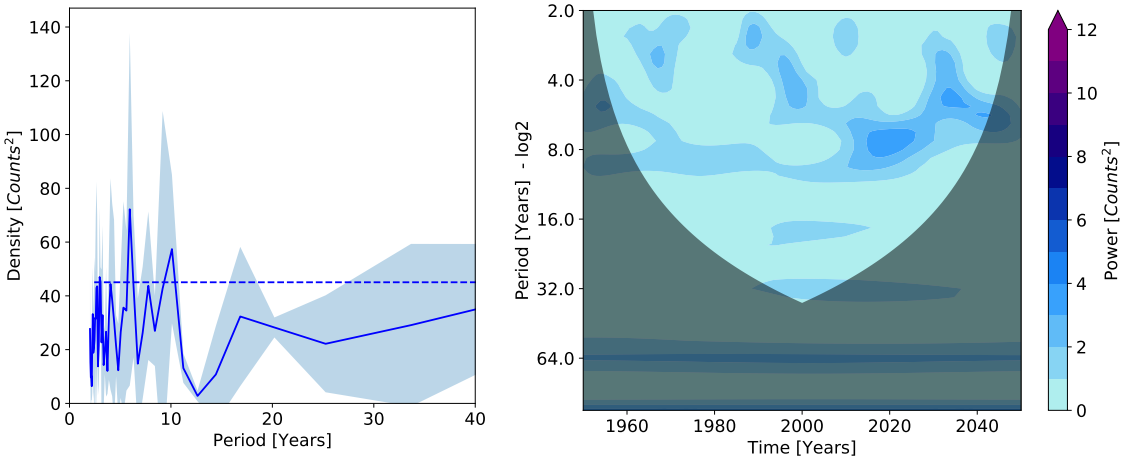

(c) Left: Mean wavelet spectrum of the time series of ACE from the ensemble of HM coupled hist-1950 runs (colours), and wavelet spectrum of the HM coupled control run (gray contours); Right: Wavelet spectrum of the HH coupled hist-1950 run (colours) and wavelet spectrum of the HH coupled control run (gray contours). The 95% significance level of each control run's wavelet spectrum is shown with red contours.

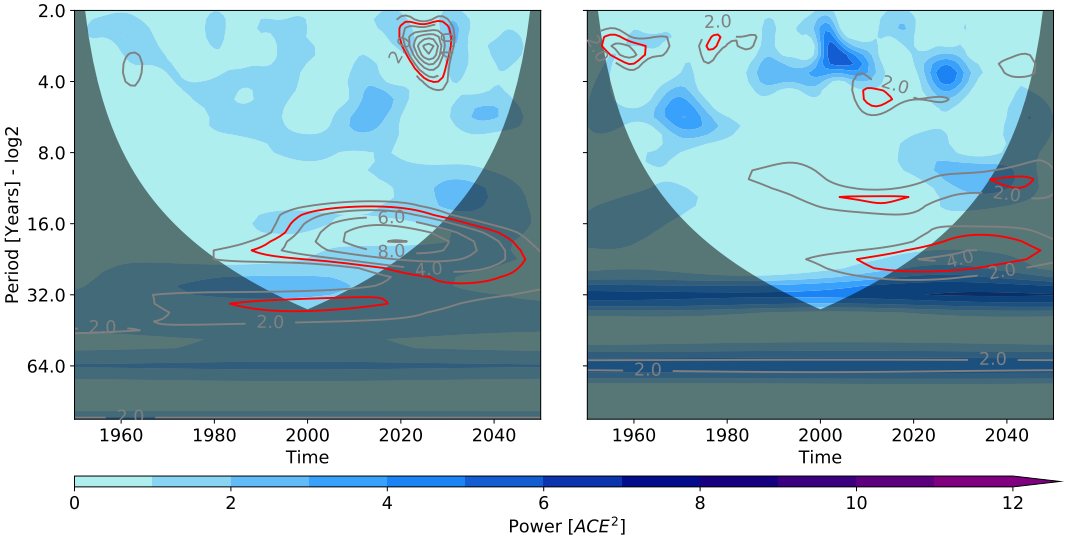

Figure 4.8: Results of spectral analysis of the 100-year long time series of TC activity for NATL.

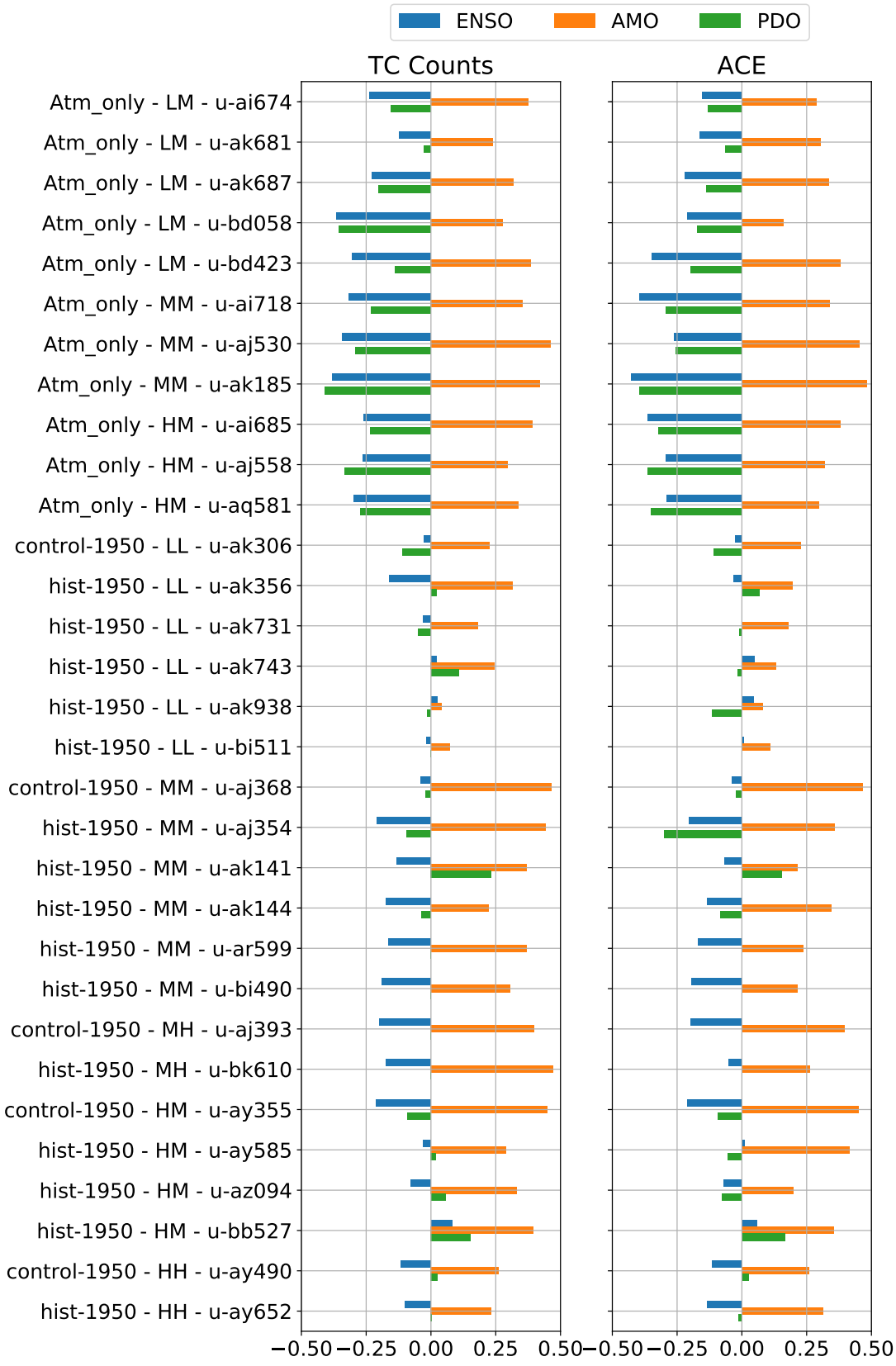

Figure 4.9: Pearson correlations between the time series of NATL annual TC counts and ACE of models with the seasonal climate indices for the 1950-2050 period. Hatched bars indicate the correlations that are significant at the 90% CL.

and colours, respectively. Significance at the 95% CL for the two control runs is shown with red contours.

In the wavelet spectra of both control runs significant decadal signals are shown spanning almost the entire last 50 years of the simulations (fig. 4.8c). For the HM control run, the significant region on inter-annual time scales is localised around the time period of the strongest El-Niño event and during a maximum in the AMO index (not shown). The significant region on decadal time scales covers a period during which the AMO is in a warm phase, the PDO is, for the majority of the period, in a cold phase and La-Niña events are more frequent. For the HH control run, forming a clear conclusion is more challenging. Examination of Pearson correlations between the time series of ACE and the climate indices for this particular run revealed significant correlation with the AMO and weak anticorrelation with ENSO (fig. 4.9). Therefore, it is possible that the significant region in the wavelet spectrum for this particular run shows that decadal variability of ACE during the last years of the simulation is mainly driven by the AMO.

As shown on figure 4.9, for the rest of the models, from the correlations between time series of ACE and counts with the climate indices it is found that for at least 28 of the simulations examined in terms of frequency, there is a weak to moderate positive correlation between AMO and TC activity in the basin. The same happens for at least 26 of the experiments in terms of ACE. Additionally, the May-November averaged ENSO index is significantly (weakly or moderately) anticorrelated with at least 8 out of the 11 atm-only experiments in both ACE and counts. Only a handful of coupled experiments show similar significant (mainly weakly) anticorrelations between the ENSO index and frequency and ACE. Furthermore, the time series of TC counts and ACE for 8 of the atm-only runs are significantly (weakly or moderately) anticorrelated with the May-November PDO index. Lastly, all the MM and HM experiments display this relationship for both metrics (frequency and ACE), whereas there is no robust influence on TC activity for the coupled experiments.

Upon examining the drivers of decadal variability using the EOTs method, just like for the case of the current climate, the EOT base points for all the low-resolution simulations examined in the study are positioned in the center or at the western side of the region (fig. 4.10a). Specifically, EOT1 for the coupled experiments are closely positioned east of Florida, while EOT1 for the atm-only runs are more spread out along the typical TC

(a) Locations of EOTs for all the model runs

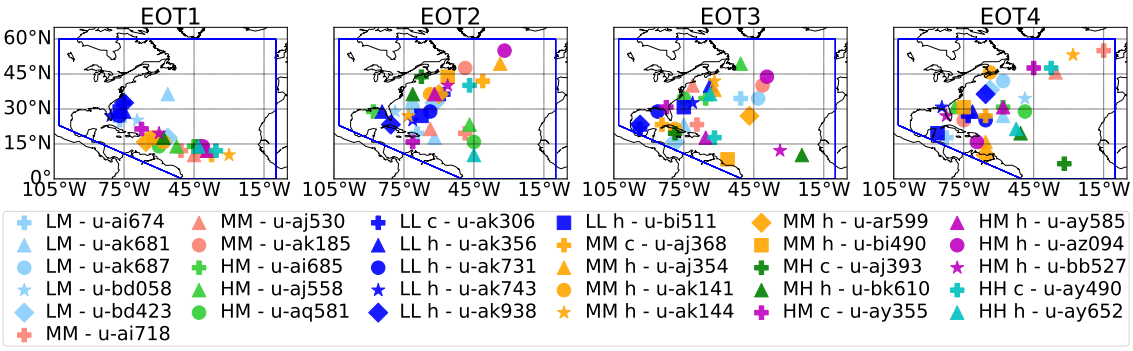

(b) SST regression patterns for the MM control run.

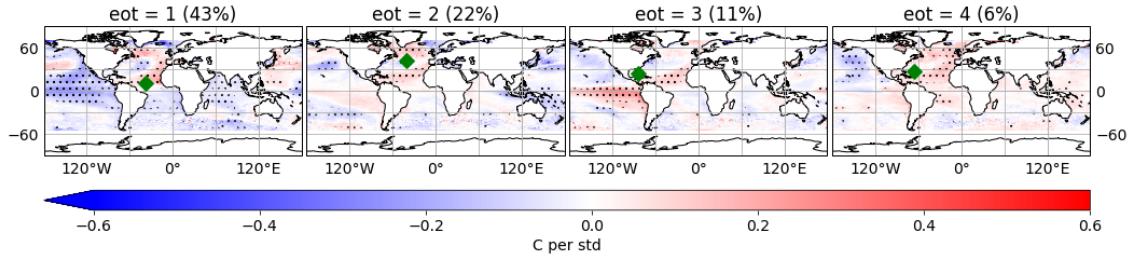

(c) VWS regression patterns for the MM control run

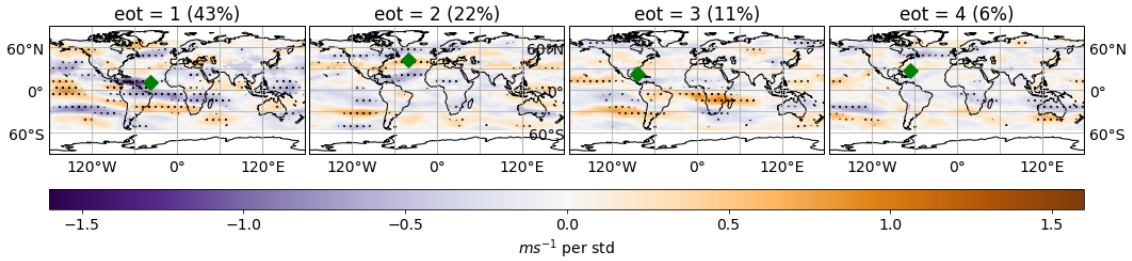

(d) Summary statistics about the Pearson correlation coefficients between the NATL EOT time series for the different model simulations and the May-November averaged ENSO, AMO and PDO indices.

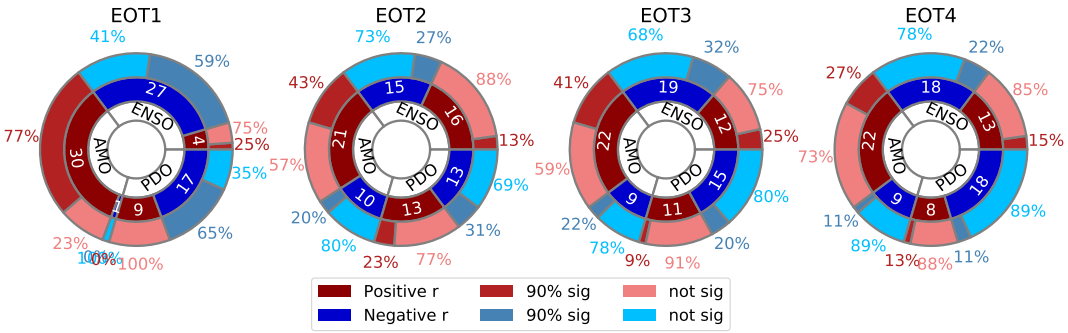

Figure 4.10: Results of EOT analysis for decadal TC variability in NATL. Location of EOT is shown with green marker and significance at the 90% CL is indicated with dots on b and c. Period examined is 1950-2050. For the correlations dark red (blue) colors indicate how many of the 31 models have positive (negative) correlations with each index, medium red (blue) indicate how many of the dark red (blue) correlations are significant at the 90% CL, while light red (blue) indicate how many are not significant.

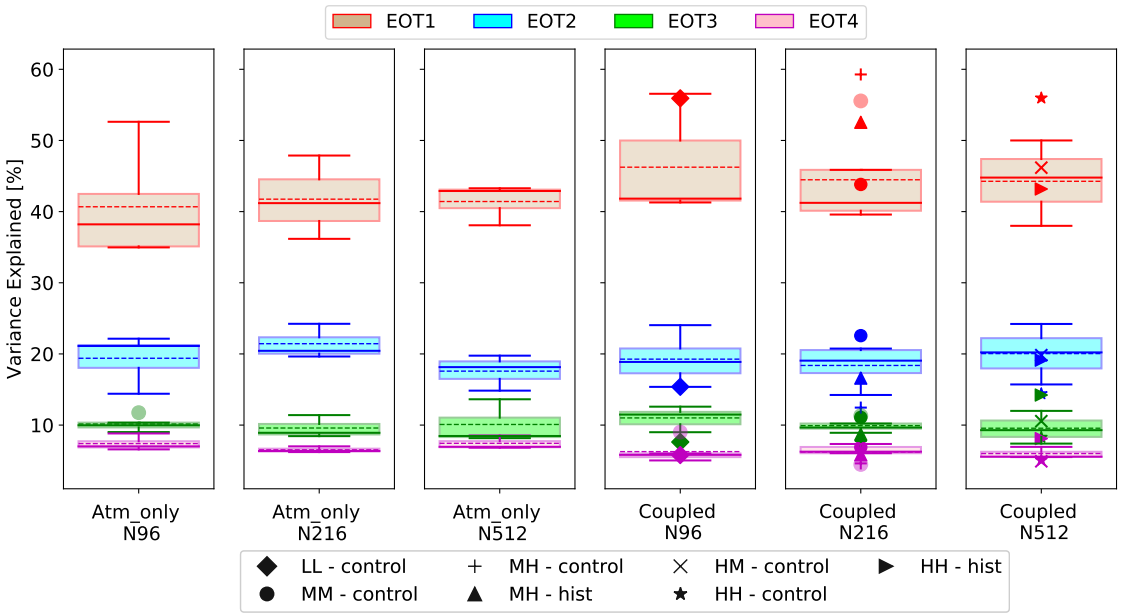

Figure 4.11: Percentage of variance explained by the EOTs for decadal variability for NATL. Column 1-3: ensemble of atm-only runs split by atmospheric resolution; Column 4: ensemble of LL historic runs against the control run (⧫); Column 5: ensemble of MM historic runs against the MM control (●), MH control run (+) and MH historic run (▲); Column 6: ensemble of HM historic runs against HM control run (×), HH control run (★) and HH historic run (►). Faded circles (●) show outliers. Dotted lines show the ensemble means.

path. Each EOT1 for the LL coupled runs explains more than 44% of the variance in the basin, while EOT1 for the atm-only experiments individually describe more than 35% (fig. 4.11). The EOT2 base points remain relatively in the same regions, while the percentage of variance explained drops to around 15-25%. The EOT1 base points for the higher-resolution experiments are generally located close together, either in the MDR or near the eastern coast of Cuba, while EOT2 base points spread out or move out of the tropical NATL region, as is the case for the N216 coupled EOT2s (fig. 4.10a). The distribution of variance explained by the EOTs for the higher-resolution experiments is similar to the one observed in the low-resolution experiment as shown on figure 4.11. It is important to note however that EOT1s for the MH and HH control runs (both positioned in the MDR, east of 45°W) explain the highest amount of variance compared to the rest of the model simulations in their category.

Results from Pearson correlations between the climate indices and the EOT time series

are presented on figure 4.10d. Generally, positive correlations (dark red) are found between the AMO and the EOT1 time series for 30 of the models (77% of which are significant at the 90% CL; semi dark red), indicating that increases in TC activity are influenced by the positive phase of the AMO. Furthermore, for 27 and for 17 of the models, negative correlations (dark blue) are observed between the EOT1 time series and the seasonal averaged ENSO and PDO indices, respectively, indicating that the cold phases of the two Pacific modes can also lead to increases in TC activity in the basin. More specifically, for all the model simulations except the LL coupled runs and two of the LM atm-only runs, EOT1s are significantly correlated with the seasonal average of the AMO index. In addition, 9 out of the 11 atm-only runs show significant anticorrelations with the seasonal average of the ENSO index, while 7 of them show similar relationships with the PDO. It appears that the skill of the model in capturing the long-term ENSO-teleconnections relationship for the NATL is stronger in the coupled experiments. Lastly, there is no robust conclusion from the correlations between the indices and EOT2, EOT3 and EOT4 time series, even though some connections with the indices, particularly with the AMO, can be seen.

Figures 4.10b and 4.10c show the EOT regression patterns when the SST and VWS fields of the MM control run are regressed onto the first four EOT time series for that particular run. The location of each EOT is indicated with a green marker, while the dots show where the regression coefficients are significant at the 90% CL. As shown on the regression maps, TC activity in the MDR for EOT1 is associated with warm local and cold Pacific SSTs, while simultaneously being linked to low VWS over the Atlantic branch of the ITCZ and increased VWS in the tropical Pacific. The EOT1 SST patterns resemble the canonical patterns of La-Niña, PDO and AMO in figures 1.1 (inverse) 1.4 (inverse), and 1.2, respectively. On the other hand, the overall VWS pattern appears to be the inverse of the pattern seen on figure 1.1, once again providing a link to La-Niña. Indeed, for this particular run, the EOT1 time series are significantly correlated with the Atlantic mode and anticorrelated with the two Pacific modes. Similar patterns can be observed in the regression maps for the runs which displayed such correlations with the climate indices. It is worth noting that for EOT3, the location of which lies in the Gulf of Mexico, warm SSTs, both in the MDR and in the eastern Pacific appear to influence TC activity, while the VWS pattern appears to be connected only to the warm phase of ENSO.

Taking all the above into account, it is concluded that TC activity in the MDR is influenced by local SSTs associated with the AMO, while also being influenced from low local VWS associated with the changes in the Walker circulation due to the cold phases of ENSO. In contrast, TC activity outside of the MDR and inside the Gulf of Mexico, can be more prone to the warm phases of ENSO.

4.3 Eastern Pacific

(a) Time series: annual TC counts (gray) and 10-year running mean

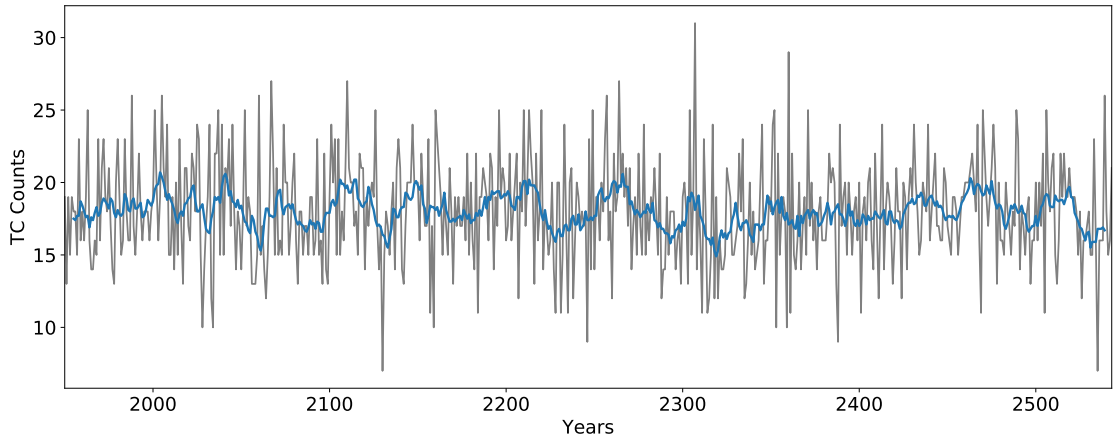

(b) Power spectrum with 95% confidence level (red dashed line)

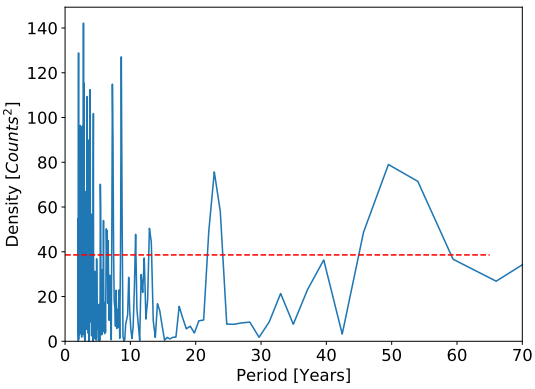

(c) Wavelet spectrum with COI (shaded area) and 95% confidence level (red contours)

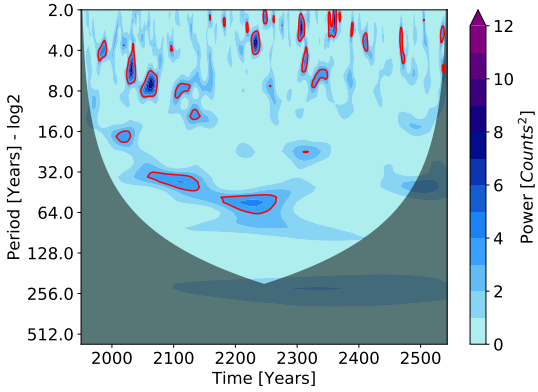

Figure 4.12: Results of spectral analysis for decadal TC variability in EPAC annual counts for the multi-centennial MM control run.

The standard power spectrum analysis on the 100-year-length time series of ACE and TC counts, reveals multiple peaks on interannual time scales. More importantly, for the range of model simulations examined, there is evidence of influence on the TC activity in the basin from phenomena with periodicities on decadal time scales, particularly periodicities within the 10-20 year band. Specifically, for the atm-only experiments, analysis of all N216 and N512 experiments detects decadal signals (near 10 years) for both ACE and TC counts, while for N96 such signals were observed for only three of the ensemble members in terms of counts and for only one member in terms of ACE. The LL control run does not exhibit any significant peaks on decadal time scales for ACE, in contrast to counts, while the majority of hist-1950 runs show similar significant peaks

at around 10-20 years in both metrics. The MM control and the two MH runs display a significant peak at around 20 years, for both ACE and frequency, while the majority of the ensemble of hist-1950 runs show periodicities in the 10-15 year band. Signals at around 10-15 years are also observed for the high-resolution experiments for both metrics, particularly the HM and HH control runs, as well as for at least one of the hist-1950 runs. Lastly, from the time series of the multi-centennial coupled control runs (fig. 4.12a), TC activity both in terms of counts (fig. 4.12b) and of ACE showed periodicities at around 15, 25 and 50 years. Significant regions at similar periodicities in the wavelet results appear for both frequency (fig. 4.12c) and ACE.

Correlating the time series of ACE and counts with the climate indices shows that the May-November averaged ENSO index is significantly (weakly to strongly) correlated with TC activity in the basin for both counts and ACE (fig. 4.13). In addition, ENSO has a greater influence on ACE compared to frequency for the coupled experiments. There is almost no significant relationship between TCs and ENSO for the low-resolution coupled runs. The AMO is significantly, moderately anticorrelated with TC activity in the EPAC (for both counts and ACE) for the MM and HM atm-only experiments. For the coupled experiments, the AMO appears to have a greater influence on ACE rather than frequency, particularly for the higher resolution (MM and above) experiments. The PDO is significantly positively (weak or moderate) correlated with the time series of TC activity for this basin for at least 6 of the atm-only experiments. In regards to the coupled runs, less than 3 of the simulations show a significant relationship with the PDO, mostly described with a weak or moderate anticorrelation.

For this region, the EOT1s from the model simulations, irrespective of their type (e.g. atm-only or coupled) and resolution, are positioned in locations similar to the ones found for the reanalyses (see fig. 3.13a). The locations of EOTs for model runs are shown on figure 4.14a. There is remarkable agreement for the position of EOT1s from the HM atm-only runs, all of which individually explain more than 66% of the variance in the basin (fig. 4.15). For the second, third and fourth modes, there is a greater spread in the basin, and a very low amount of variance explained. Furthermore, as was the case in the drivers under the current climate, there is a big difference between the amount of variance explained by EOT1s and EOT2s, particularly for the atm-only experiments (fig. 4.15). A minimum of two and, in a handful of cases, maximum of four EOTs are sufficient for

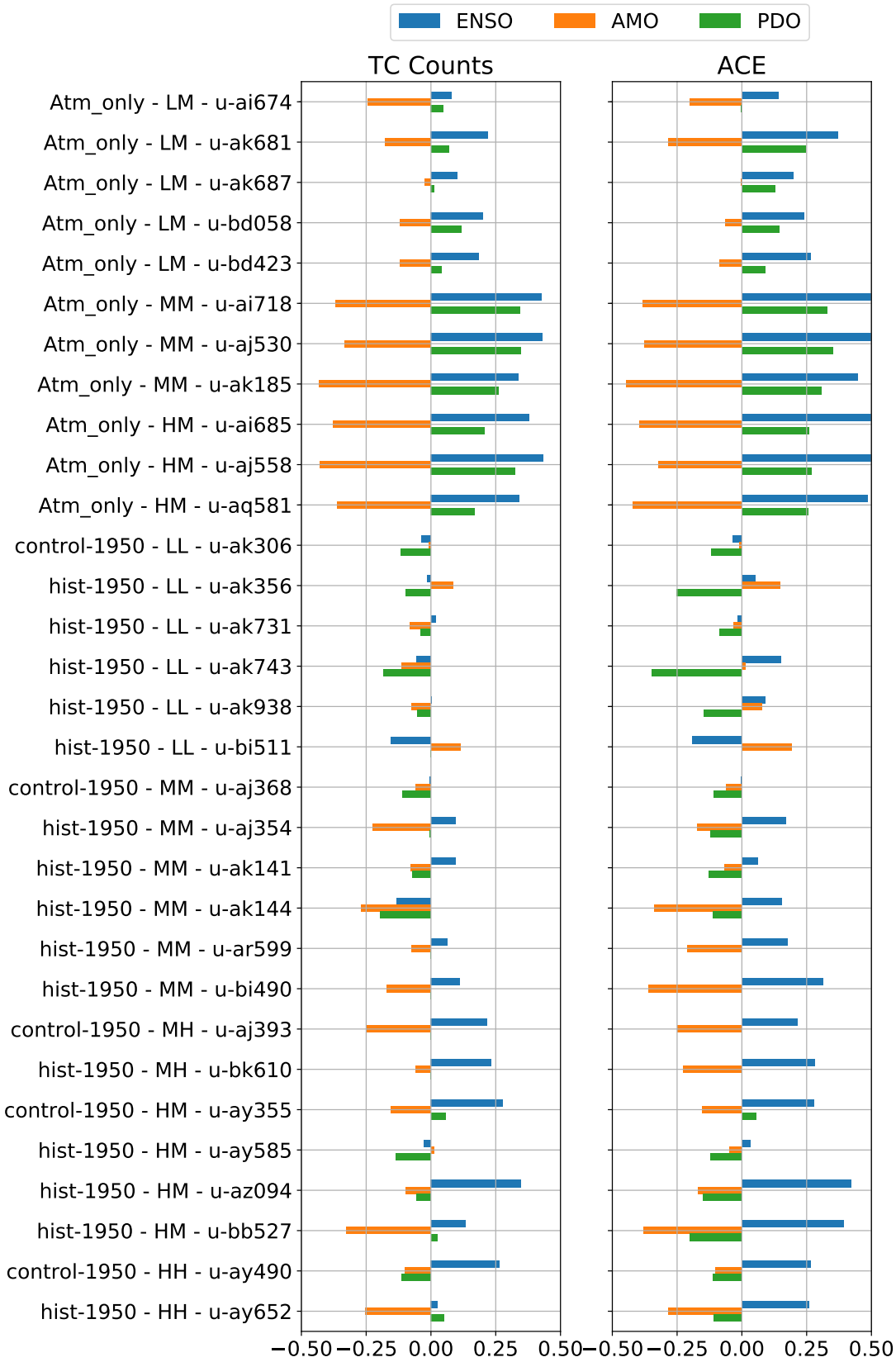

Figure 4.13: Pearson correlations between the time series of EPAC annual TC counts and ACE of models with the seasonal climate indices for the 1950-2050 period. Hatched bars indicate the correlations that are significant at the 90% CL.

(a) Locations of EOTs for all the model runs

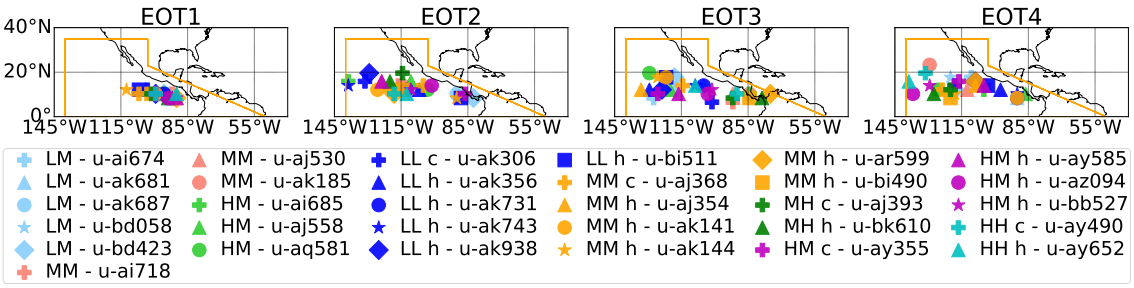

(b) SST regression patterns for the u-ai685 run

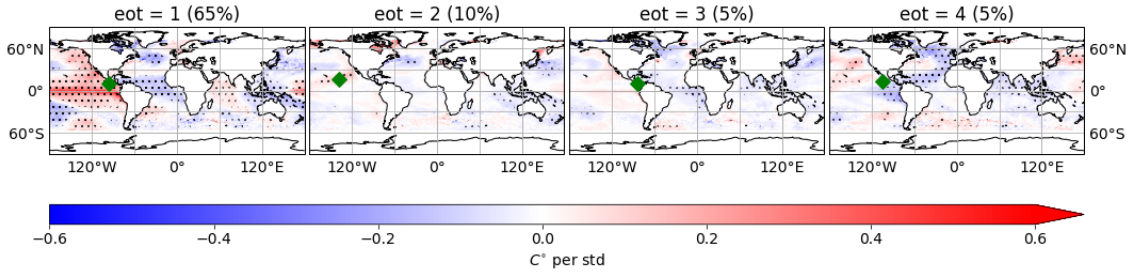

(c) VWS regression patterns for the u-ai685 run

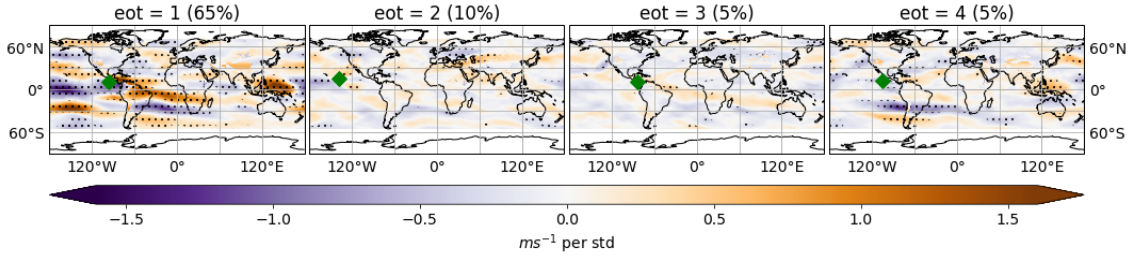

(d) Summary statistics about the Pearson correlation coefficients between the EPAC EOT time series for the different model simulations and the May-November averaged ENSO, AMO and PDO indices.

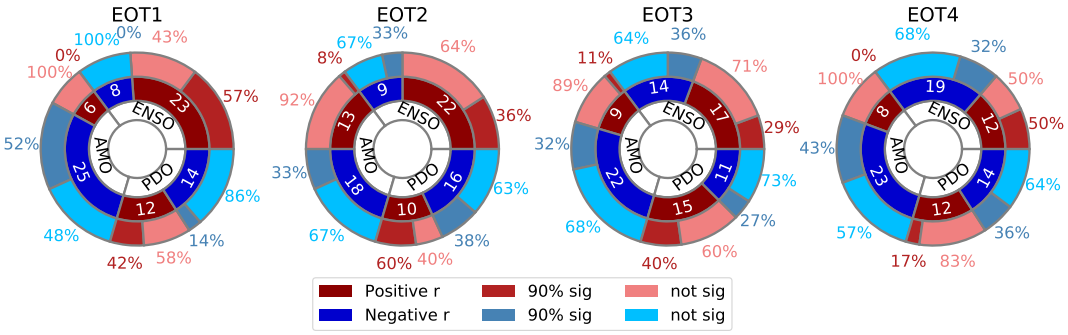

Figure 4.14: Results of EOT analysis for decadal TC variability in EPAC. Location of EOT is shown with green marker and significance at the 90% CL is indicated with dots on b and c. Period examined is 1950-2050. For the correlations dark red (blue) colors indicate how many of the 31 models have positive (negative) correlations with each index, medium red (blue) indicate how many of the dark red (blue) correlations are significant at the 90% CL, while light red (blue) indicate how many are not significant.

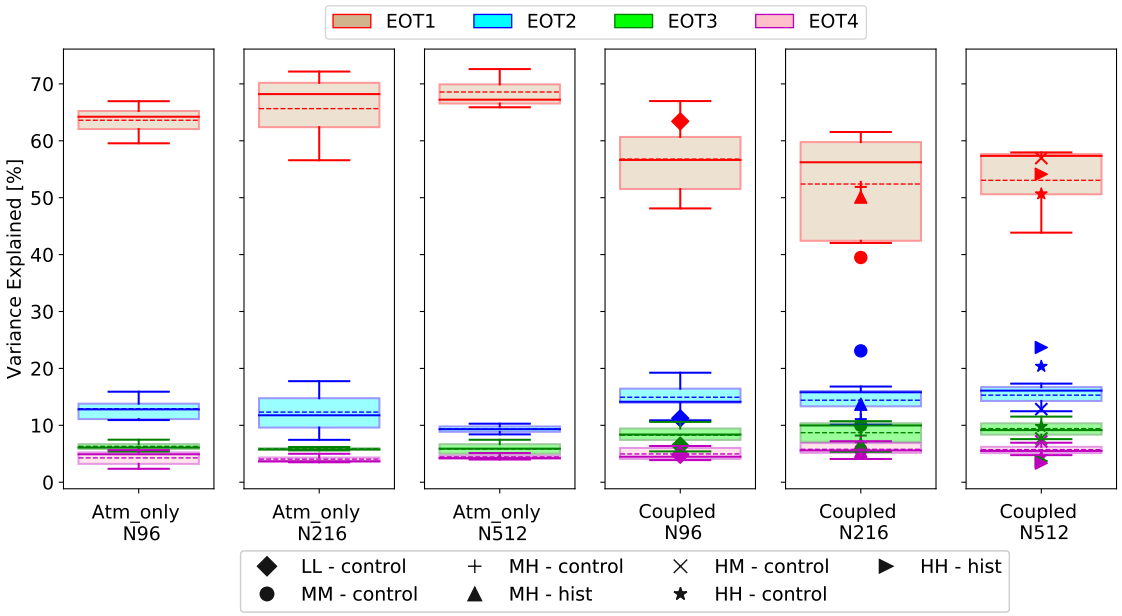

Figure 4.15: Percentage of variance explained by the EOTs for decadal variability for EPAC. Column 1-3: ensemble of atm-only runs split by atmospheric resolution; Column 4: ensemble of LL historic runs against the control run (⧫); Column 5: ensemble of MM historic runs against the MM control (●), MH control run (+) and MH historic run (▲); Column 6: ensemble of HM historic runs against HM control run (×), HH control run (★) and HH historic run (►). Faded circles (●) show outliers. Dotted lines show the ensemble means.

explaining at least 75% of the TC variability in the region.

Figures 4.14b and 4.14c show the SST and VWS regression maps, respectively, for one of the HM atm-only runs. From the SST regression maps, it can be seen that for this particular run, TC activity at the EOT1 location is influenced by all three climate indices (ENSO, AMO and PDO), with cold SSTs in the Atlantic, warm SSTs in the eastern and central tropical Pacific and a PDO-like SST pattern in the north Pacific. However, the corresponding VWS pattern is nearly identical to the VWS pattern associated with the positive ENSO phase for this run, with low vertical wind shear in the eastern and central tropical Pacific and increased VWS in the Atlantic ITCZ. Furthermore, the VWS shear in the Atlantic region appears to be a combination of the El-Niño VWS pattern and the cold AMO phase VWS pattern (inverse of figure 1.2).

From figure 4.14d, it can be seen that activity in the basin for 23 of the models is positively (significantly for 57% of them) correlated with the May-November average of

ENSO, while for 25 of the models it is anticorrelated (significantly for 52% of them) with the AMO. Out of the 26 runs for which the PDO index was calculated, 12 (14) of them showed a positive (negative) relationship with the EOT1 time series. TC activity for all the MM and HM atm-only experiments appear to be positively influenced by the two Pacific indices (ENSO and PDO), while also negatively affected by the Atlantic decadal mode.

4.4 Central Pacific

(a) Time series: annual TC counts (gray) and 10-year running mean

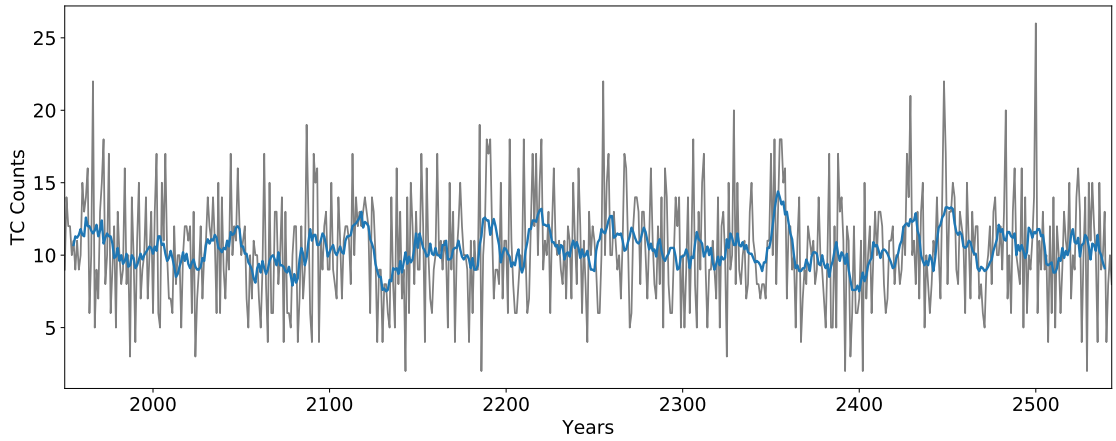

(b) Power spectrum with 95% confidence level (red dashed line)

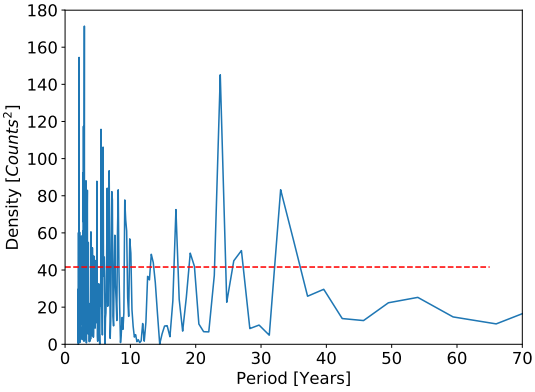

(c) Wavelet spectrum with COI (shaded area) and 95% confidence level (red contours)

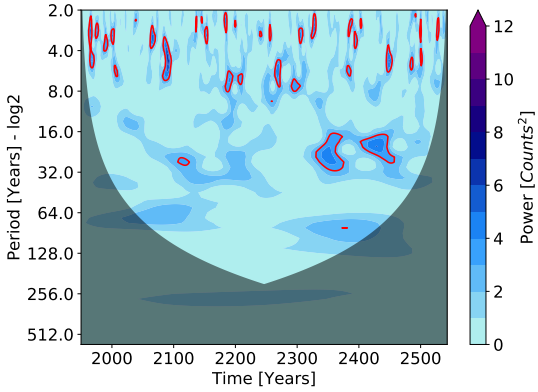

Figure 4.16: Results of spectral analysis for decadal TC variability in CPAC annual counts for the multi-centennial MM control run.

Apart from evidence of inter-annual variability in TC activity for the basin, standard power spectrum and wavelet analysis of the multi-centennial time series of ACE and counts (fig. 4.16a) from the coupled control runs did not reveal any significant peaks above 35 years (fig. 4.16b and 4.16c). For the 100-year long time series, decadal signals are observed for at least one of the ensemble of atm-only runs for both metrics (TC counts and ACE), irrespective of resolution. Regarding the coupled control runs, such signals for both counts and ACE are seen only in the power spectra of the HM and HH runs, while the MH run showed evidence of decadal variability only in TC counts and the MM and LL control runs revealed no decadal signals. For each type of resolution, except for the HM and HH runs, at least one of the ensemble members revealed significant decadal

periodicities.

From correlating the time series of ACE and counts with the climate indices, a robust significant, mainly moderate, correlation is found between the May-November averaged ENSO index and TC activity in the basin, as seen from both frequency and ACE on figure 4.17, for all the model experiments (except one LM run). The AMO appears to have a greater influence on frequency in the basin rather than ACE, particularly for the low-resolution atm-only simulations. Significant moderate anticorrelations with the time series of counts for all atm-only experiments and significant anticorrelations for 8 of the atm-only experiments in terms of ACE are observed. For the coupled runs, it appears that the AMO has a negative relationship with TCs for both frequency and ACE, particularly for the higher resolution simulations. Interestingly, the PDO has a positive influence on TC activity in the atm-only experiments (at least 9 of them being significant moderate correlations), but it has a significant weak or moderate anticorrelation with 7 of the coupled runs for both TC counts and ACE.

Due to the small size of this region, the locations of the EOT1 base points are similar to the ones seen for the observations, particularly for the higher-resolution experiments (fig. 4.18a). Once the influence of the first mode is removed, the EOTs start to spread out and often move out of the tropics. The obvious difference compared to the rest of the basins is in terms of the distribution of variance explained. There is a gradual decrease with increasing atmospheric resolution. In addition, CPAC is one of the basins for which the different EOTs explain similar amounts of variance for each mode, as evident from the thinness of the boxplots (fig. 4.19). Lastly, in order to explain 75% of the variability in the basin for the 100 years analysed, three to four EOTs are needed.

Figures 4.18b and 4.18c present the SST and VWS regression maps, respectively, for the first four EOTs for the HH coupled control run. The SST patterns for EOT1 and EOT3, which are both located in the tropics near $150°E$, reveal significant relationship with warm SSTs in the eastern and central Pacific, typically linked to El-Niño events. The corresponding VWS patterns closely resemble the El-Niño VWS canonical pattern shown on figure 1.1. Such patterns appear for at least one of the first three EOTs for all model experiments. Furthermore, the SST patterns associated with the cold phase of the AMO also appear in at least one of the first two EOTs for the majority of the models (not shown), while SSTs linked to the warm phase of PDO are present in almost all the EOT1s for the

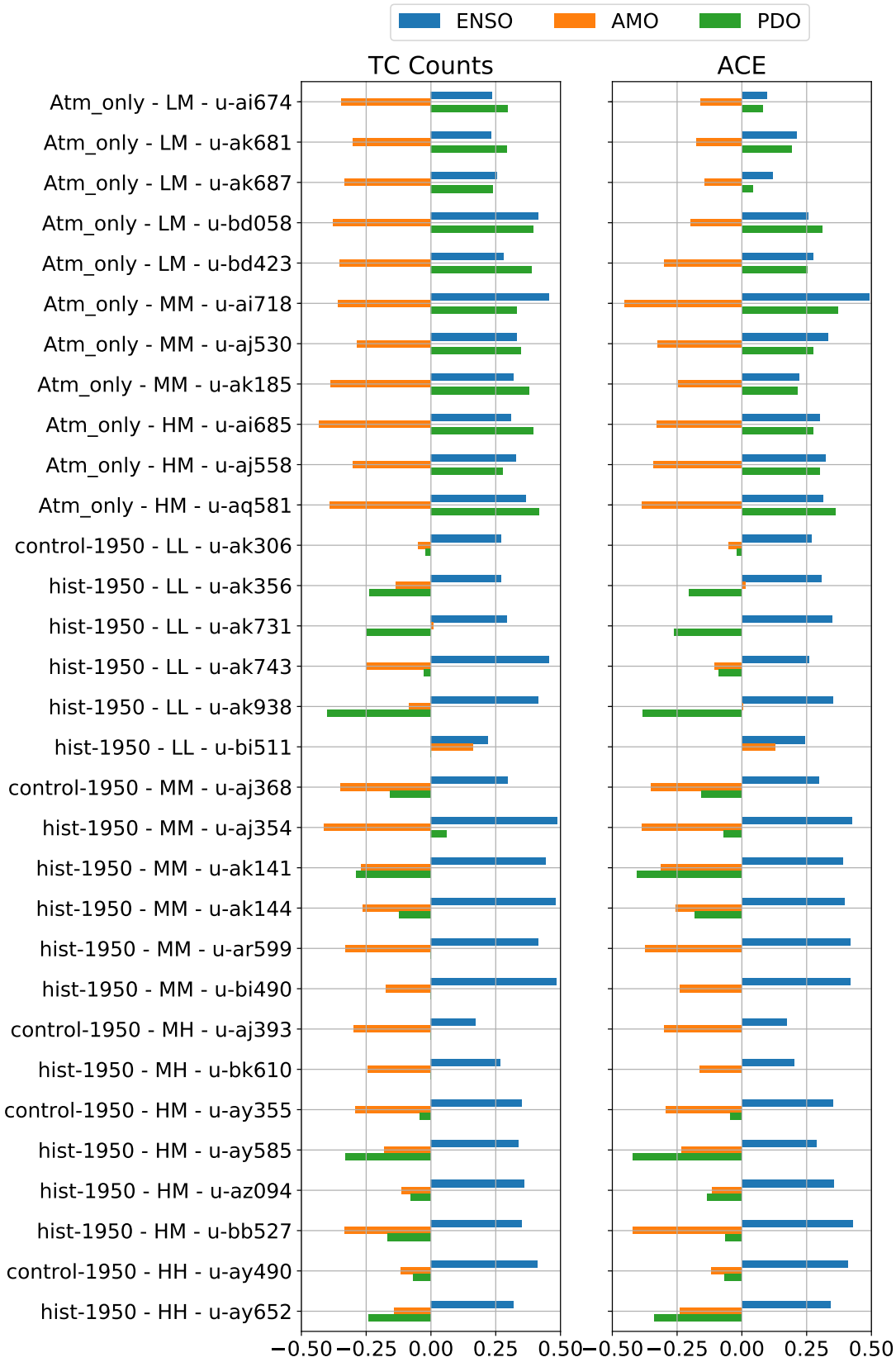

Figure 4.17: Pearson correlations between the time series of CPAC annual TC counts and ACE of models with the seasonal climate indices for the 1950-2050 period. Hatched bars indicate the correlations that are significant at the 90% CL.

(a) Locations of EOTs for all the model runs

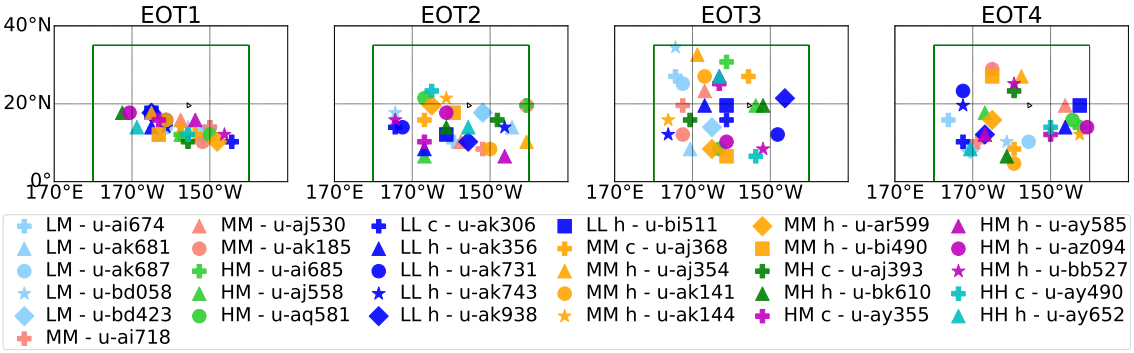

(b) SST regression patterns for the HH coupled control run

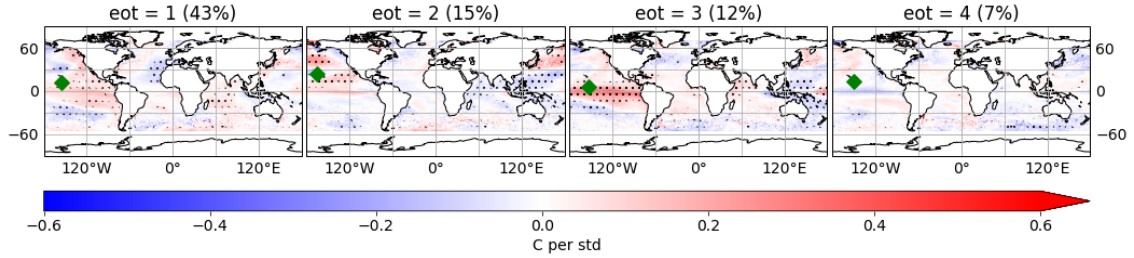

(c) VWS regression patterns for the HH coupled control run

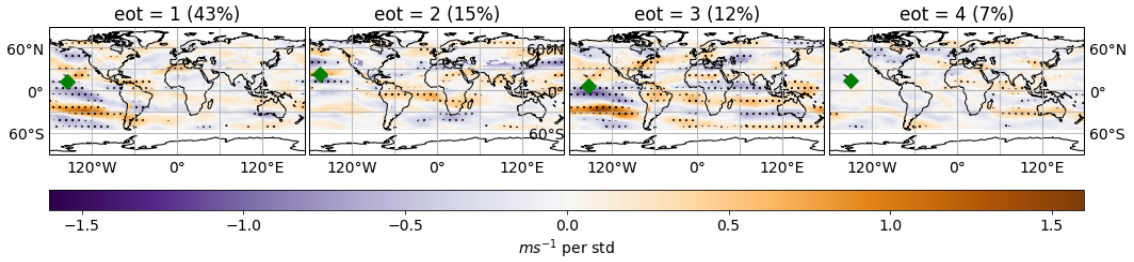

(d) Summary statistics about the Pearson correlation coefficients between the CPAC EOT time series for the different model simulations and the May-November averaged ENSO, AMO and PDO indices.

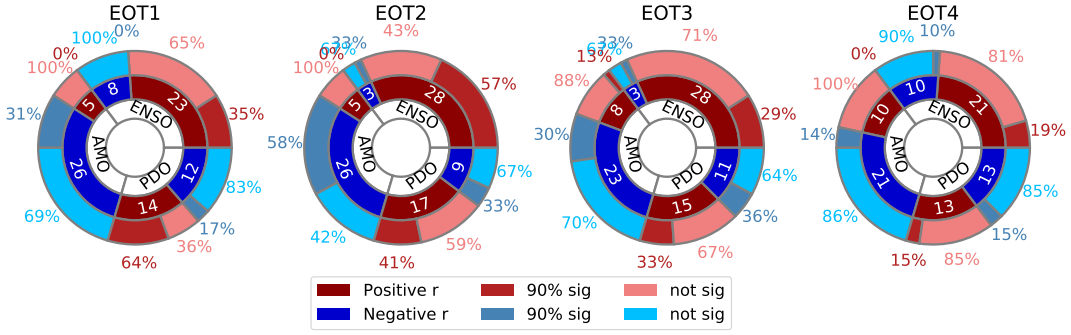

Figure 4.18: Results of EOT analysis for decadal TC variability in CPAC. Location of EOT is shown with green marker and significance at the 90% CL is indicated with dots on b and c. Period examined is 1950-2050. For the correlations dark red (blue) colors indicate how many of the 31 models have positive (negative) correlations with each index, medium red (blue) indicate how many of the dark red (blue) correlations are significant at the 90% CL, while light red (blue) indicate how many are not significant.

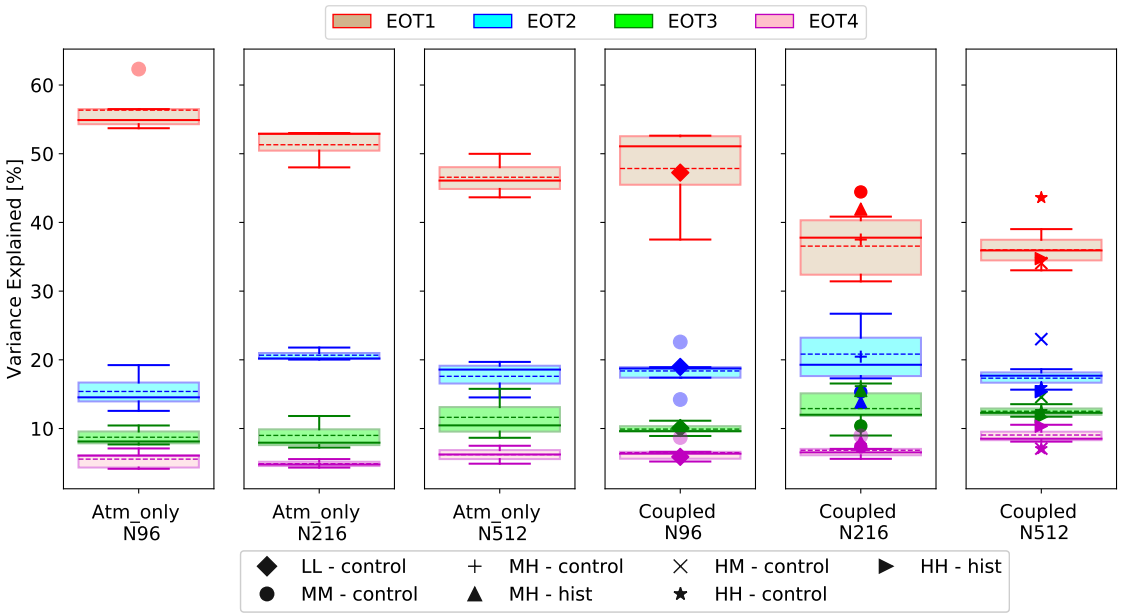

Figure 4.19: Percentage of variance explained by the EOTs for decadal variability for CPAC. Column 1-3: ensemble of atm-only runs split by atmospheric resolution; Column 4: ensemble of LL historic runs against the control run (♦); Column 5: ensemble of MM historic runs against the MM control (●), MH control run (+) and MH historic run (▲); Column 6: ensemble of HM historic runs against HM control run (×), HH control run (★) and HH historic run (►). Faded circles (●) show outliers. Dotted lines show the ensemble means.

atm-only experiments (not shown).

Figure 4.18d presents Pearson correlations between the climate indices and the EOT time series for the CPAC. Dark red (blue) colors indicate how many of the 31 models have positive (negative) correlations with each index, medium red (blue) indicate how many of the dark red (blue) correlations are significant at the 90% CL, while light red (blue) indicate how many are not significant. Activity at EOT1 base points, appears to have a positive relationship with ENSO and PDO in 23 and 14 of the models, respectively, while it is also negatively correlated with the AMO in 26 of the models, even though not all the relationships are significant. Significant anticorrelations are found between the seasonal average of the AMO and EOT1 for the LM, at least one of the MM and HM of the atm-only simulations, while significant positive correlations with the May-November averaged PDO index for 9 of the atm-only runs. In addition, for EOT2, the majority of the experiments are correlated with ENSO and anticorrelated with the AMO. This leads to the conclusion

that for the atm-only simulations, the AMO and the PDO, via SSTs appear to be important primary drivers for TC activity on decadal time scales in this basin for the atm-only runs, while ENSO is a secondary driver. For the coupled simulations, there is a larger number of models for which significant relationships are found between EOT2 and the indices of ENSO and AMO. Specifically, for 26 (28) of the runs negative (positive) correlations are found between EOT2 and AMO (ENSO), more of 55% of which are significant. It is, also, important to note that the vast majority of the EOTs power spectra have detected significant signals on decadal time scales between 10 and 20 years.

4.5 Western Pacific

(a) Time series: annual TC counts (gray) and 10-year running mean

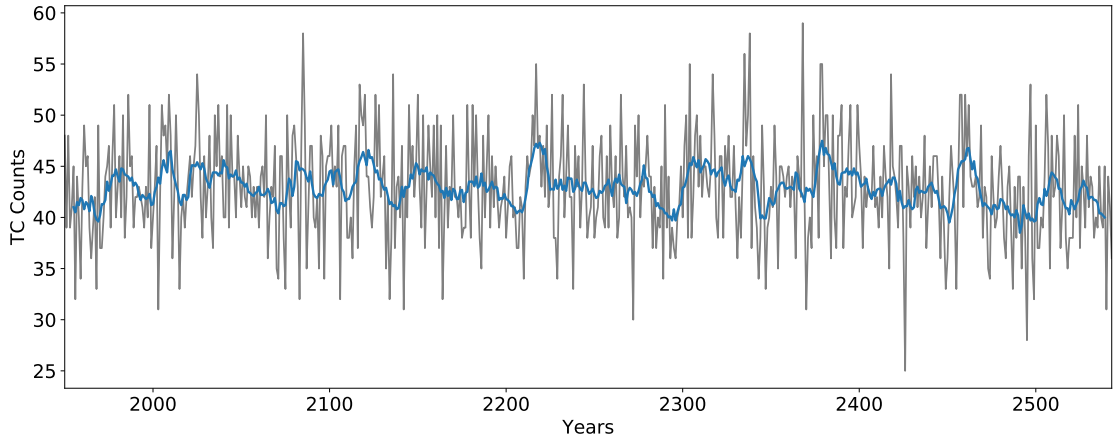

(b) Power spectrum with 95% confidence level (red dashed line)

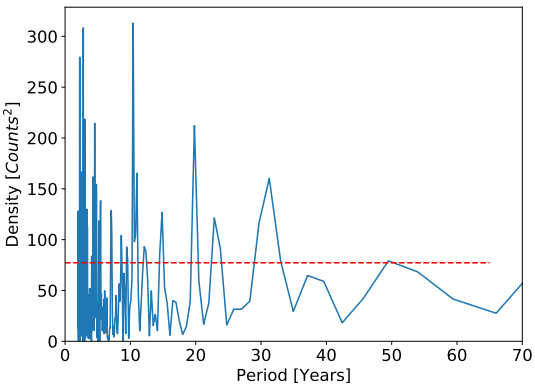

(c) Wavelet spectrum with COI (shaded area) and 95% confidence level (red contours)

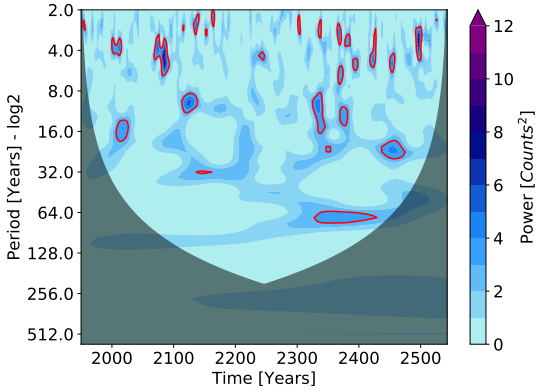

Figure 4.20: Results of spectral analysis for decadal TC variability in WPAC annual counts for the multi-centennial MM control run.

Upon analysing the time series with the standard spectral method, for all the LM runs for ACE there are signals on decadal time scales, in the 10-15 year band, whereas only a couple of the runs show similar signals for TC counts. For the MM experiments, even though significant peaks at periodicities above 10 years are found in all three individual power spectra for the time series of ACE, they are not powerful enough to show on the combined power spectrum. In addition, none of the spectra in terms of TC counts display such signals. In contrast, for both TC counts and ACE, in the individual spectra for the HM atm-only runs, as well as the combined, there is robust decadal TC variability. Absence of significant peaks above a 10-year periodicity is evident for the 100-year-long LL control run, but for at least 3 of the LL hist-1950 experiments in both metrics, powerful

decadal signals, enough to be shown on the combined spectrum, were detected. Evidence of decadal variability for the majority of MM runs both for ACE and TC counts, as well as only on the frequency of TCs in the basin for the MH runs, is shown from the power spectra. There is no evidence of decadal influence on ACE for the HH runs in contrast to the frequency of TCs, but for the control and for at least two of the ensemble of hist-1950 HM runs, such signals are detected for both metrics. Lastly, from the multi-centennial time series (fig. 4.20a), multiple peaks on multi-decadal time scales are observed, particularly for the LL and MM runs, but not above 40 years for the standard power spectrum (fig. 4.20b) and not above 65 years for the wavelet spectrum (fig. 4.20c), hinting at a connection to the PDO.

Only a handful of the 31 runs show a significant relationship between the May-November averaged ENSO index and the time series of counts from the Pearson correlation coefficients, as shown on figure 4.21. ENSO seems to have a greater influence on the energy associated with TCs, since a significant positive relationship can be seen for 28 of the runs. From this figure it can be seen that the correlations between the climate index and ACE are higher (in absolute value) compared to the correlations between the index and counts. This can be indicative of TCs in this basin having longer duration even if the occurrences decrease. ACE is a metric that takes into account and is affected by both the intensity and the duration of lifetime of TCs. It is possible to have similar amounts of ACE from a season with short-lived but very intense TCs and a season with long-lived but less intense TCs. In a vast basin, such as the WPAC, TCs can have longer life-cycles, compared to other basins. Environmental conditions such as warm SSTs can affect ACE by providing a steady flow of energy for the TCs and even prolonging their lifetime.

The May-November averaged AMO index shows a significant anticorrelation with the time series from both metrics for all atm-only experiments. However, in terms of the coupled runs, there is greater influence on ACE compared to frequency, since more significant, albeit weak, anticorrelations can be seen for the former metric than for the latter. For the period examined, the May-November averaged PDO index has a stronger influence on ACE compared to frequency, particularly for the atm-only experiments. Significant weak or moderate correlations are observed for at least 8 of the atm-only runs in terms of ACE, compared to 3 of them in terms of counts. Furthermore, significant weak, mostly negative correlations are found for 4 of the coupled runs for both metrics.

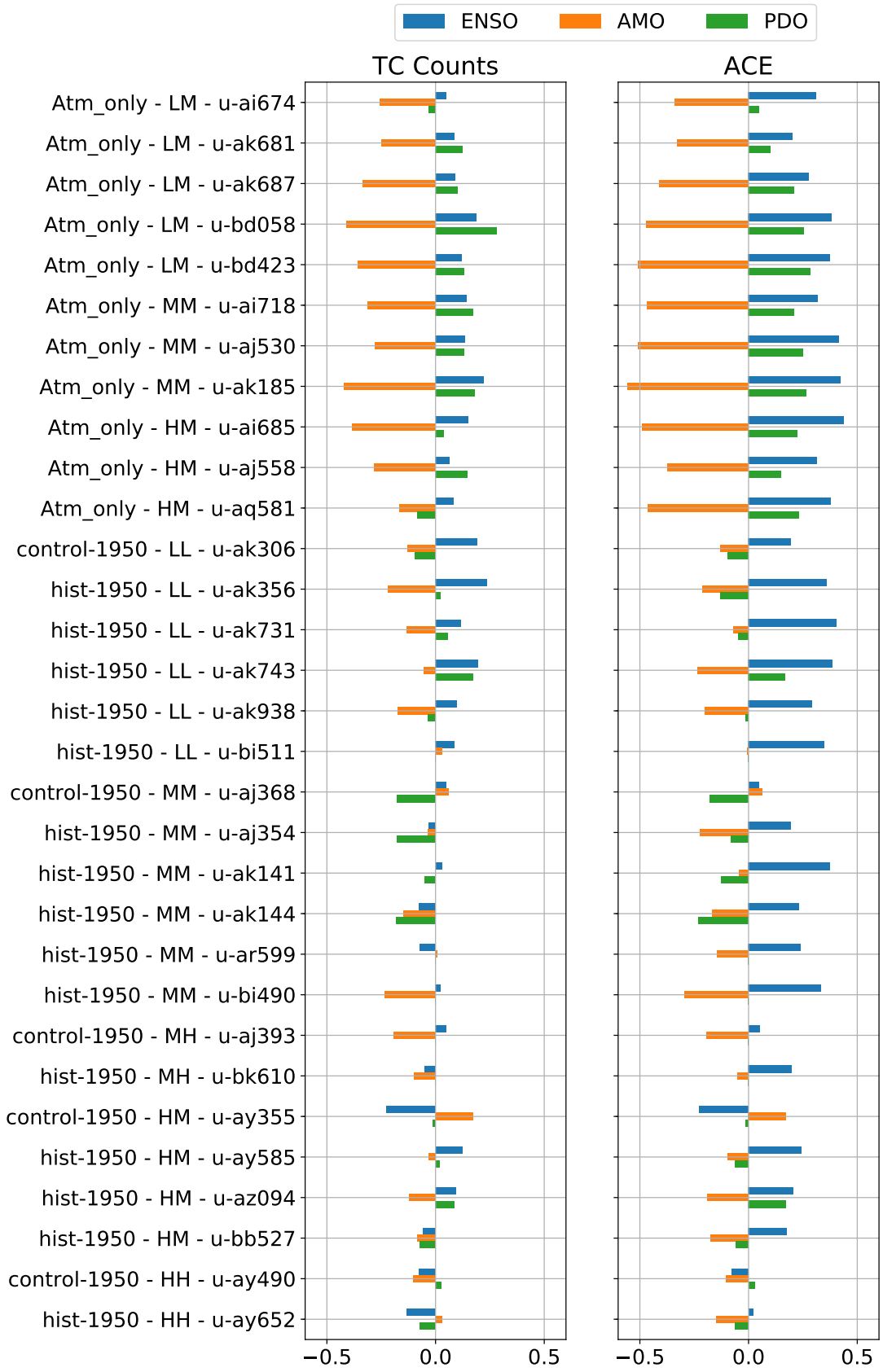

Figure 4.21: Pearson correlations between the time series of WPAC annual TC counts and ACE of models with the seasonal climate indices for the 1950-2050 period. Hatched bars indicate the correlations that are significant at the 90% CL.

(a) Locations of EOTs for all the model runs

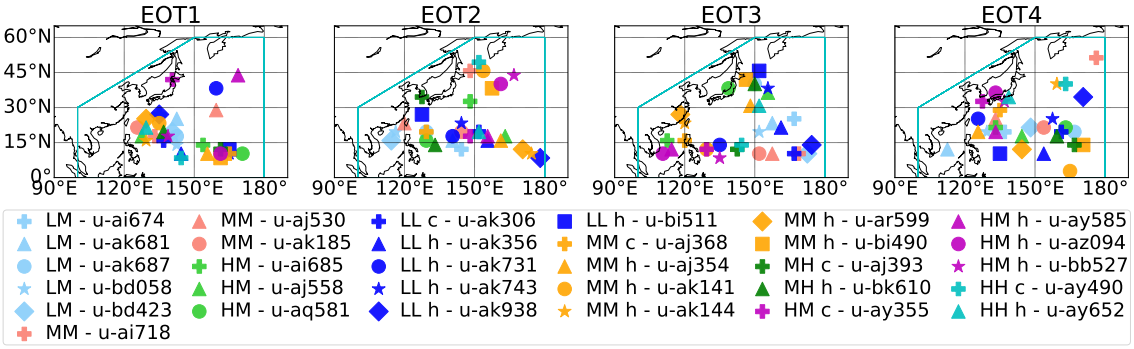

(b) SST regression patterns for the MM coupled control run

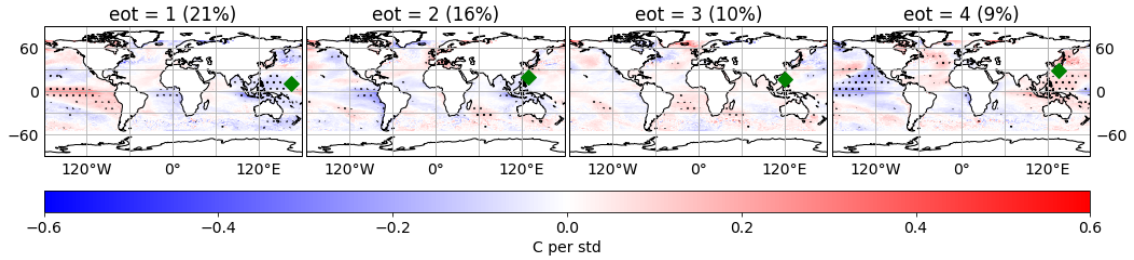

(c) VWS regression patterns for the MM coupled control run

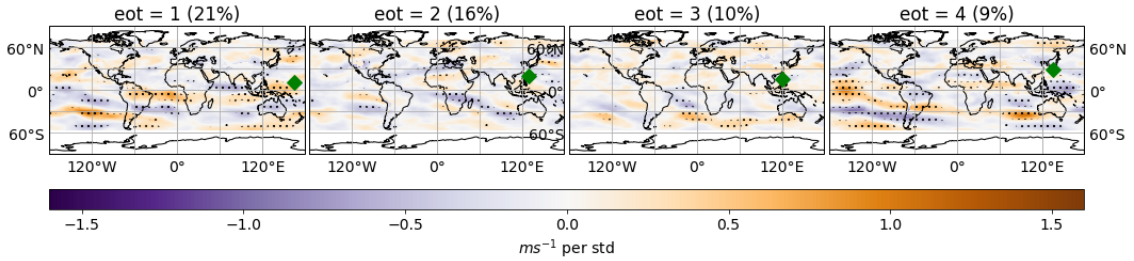

(d) Summary statistics about the Pearson correlation coefficients between the WPAC EOT time series for the different model simulations and the May-November averaged ENSO, AMO and PDO indices.

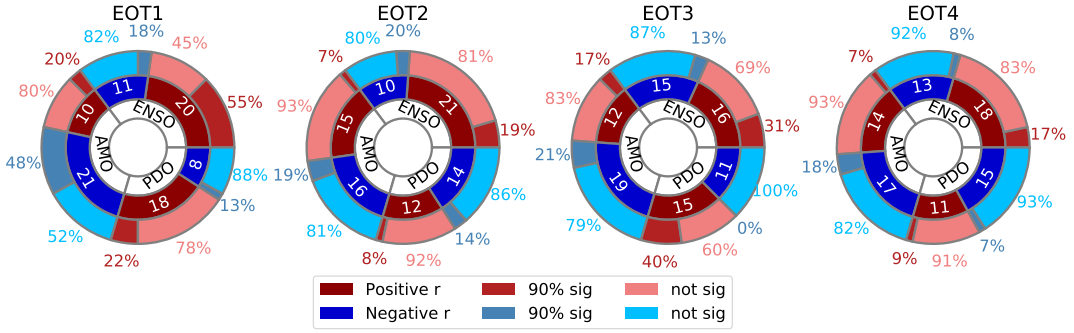

Figure 4.22: Results of EOT analysis for decadal TC variability in WPAC. Location of EOT is shown with green marker and significance at the 90% CL is indicated with dots on b and c. Period examined is 1950-2050. For the correlations dark red (blue) colors indicate how many of the 31 models have positive (negative) correlations with each index, medium red (blue) indicate how many of the dark red (blue) correlations are significant at the 90% CL, while light red (blue) indicate how many are not significant.

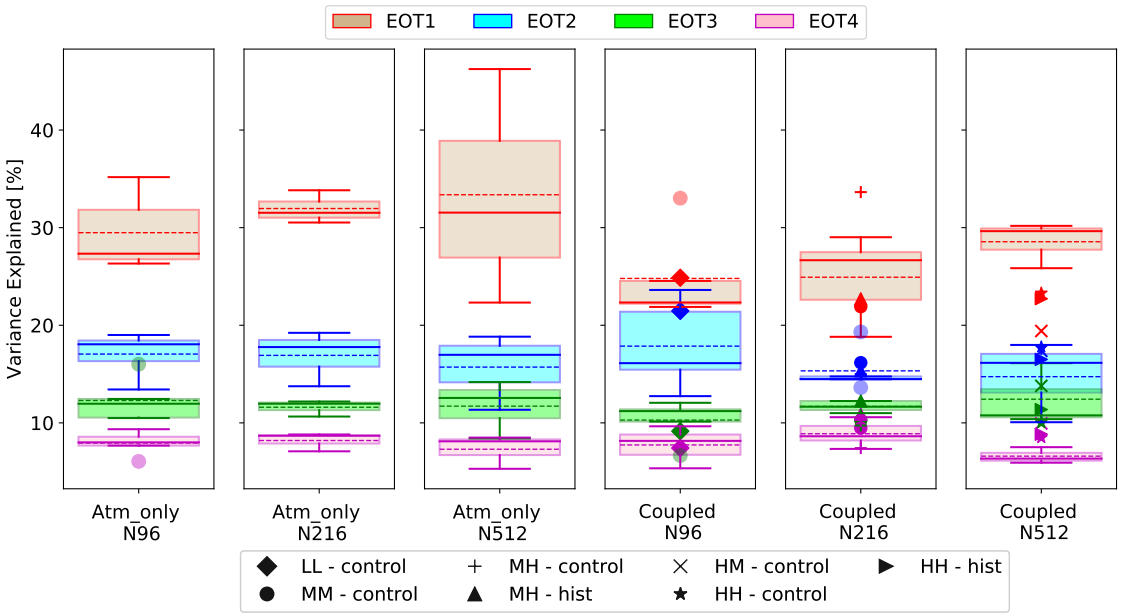

Figure 4.23: Percentage of variance explained by the EOTs for decadal variability for WPAC. Column 1-3: ensemble of atm-only runs split by atmospheric resolution; Column 4: ensemble of LL historic runs against the control run (♦); Column 5: ensemble of MM historic runs against the MM control (●), MH control run (+) and MH historic run (▲); Column 6: ensemble of HM historic runs against HM control run (×), HH control run (★) and HH historic run (►). Faded circles (●) show outliers. Dotted lines show the ensemble means.

The EOT1 base points for the low-resolution atm-only experiments are clustered in the tropical region over Japan (fig. 4.22a), in contrast to EOT1 base points for the LL coupled runs which are spread in the basin similarly to the observations (fig. 4.22a). For the N216 simulations, EOT1 base points for the coupled runs are clustered in two different locations as seen on figure 4.22a, the tropical region over Japan and the tropical region between $150-180^{\circ}E$, whereas EOT1 for the N216 atm-only and the N512 runs are once again spread out in the basin. Just like the case for the observations, it becomes extremely difficult to summarise information regarding the location of EOTs since the base points are not clustered. In addition, individual EOT1 describe less than 40% variance in the basin for all the model simulations, except for the ones for N512 atm-only experiments as displayed on figure 4.23. The similarity in the distribution of percentage of variance explained and the locations of EOTs by the model simulations with the ones for observations, further reinforces the argument that there is more than one main driver of TC variability in the

basin. Lastly, compared to the other basins, in order to explain at least 75% of the variance in the basin for decadal time scales, it is necessary to use at least five EOTs. It is important to note at this point, that for at least one of the EOTs analysed, power spectral analysis of the time series, resulted in significant decadal periodicities.

The SST and VWS regression patterns for this particular basin are more difficult to interpret, due to the greater spread between the EOTs from the different experiments, but also because in some cases, EOTs from different runs are found to be in similar locations whilst the resulting regression patterns are not similar (not shown). For the vast majority of the atm-only experiments SST regression patterns show significant warm SSTs in the eastern and central tropical Pacific, associated with ENSO. Whether this result is partially or primarily attributed to the overestimation of the trend in 2015-2050 for these experiments, is unknown for the moment. In addition, for 8 of the 11 atm-only runs, significant cold SSTs, associated with the Atlantic modes are observed.

SST and VWS regression maps for the first 4 EOTs of the MM coupled control run are presented on figures 4.22b and 4.22c, respectively. For the coupled runs, warm SSTs for the LL (significant), MM (significant) and MH and cold SSTs for the HM (significant) and HH control runs are observed from the regression maps. Furthermore, results from the hist-1950 runs irrespective of resolution are split, since half of them display warm SSTs in the Pacific while the rest display cold SSTs. For the MM control run, EOT1 is located in the tropical eastern part of the region analysed (fig. 4.22). Warm SSTs in the equatorial eastern and central Pacific and cold SSTs in the western part of the region, resembling the El-Niño-Modoki canonical pattern, are observed for EOT1. Furthermore, the VWS pattern corresponds to a weak pattern associated with the warm phase of ENSO as seen on figure 1.1. For the remaining EOTs, EOT2 and EOT4 display cold SSTs in the eastern equatorial and central Pacific, patterns linked to the cold phases of the two Pacific modes (ENSO and PDO).

TC activity at EOT1 for 20 and 18 of the models is positively correlated with the seasonal averaged ENSO and PDO, respectively, as shown on figure 4.22d. For 21 of the models TCs are anticorrelated with the AMO. More specifically, the vast majority of atm-only simulations show a significant positive relationship to the May-November averaged ENSO index, as well as a significant anticorrelation with the seasonal average of the AMO. EOT3 for two of the LM and two of the MM atm-only runs, show positive

correlations with both of the Pacific indices and anticorrelation with the AMO. For these particular simulations, the influence by the AMO can be also seen for one of the first two EOTs.

4.6 North Indian

(a) Time series: annual TC counts (gray) and 10-year running mean

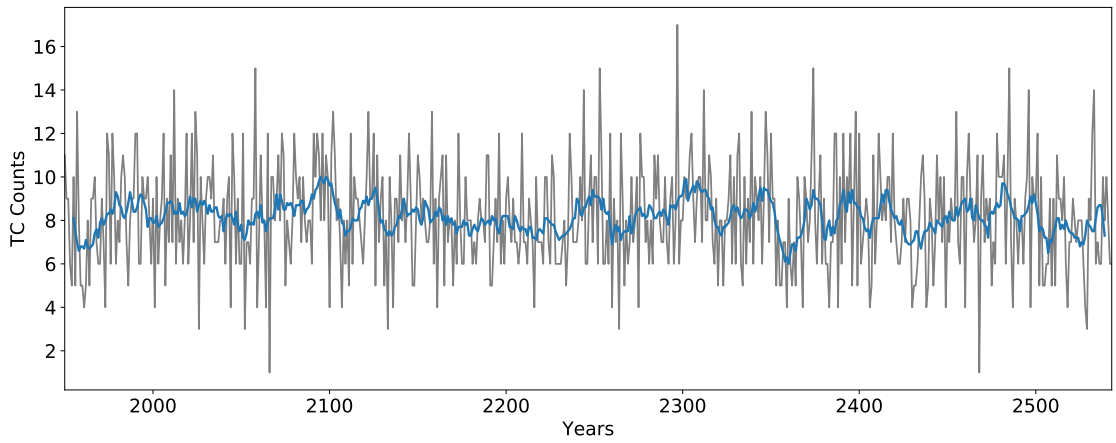

(b) Power spectrum with 95% confidence level (red dashed line)

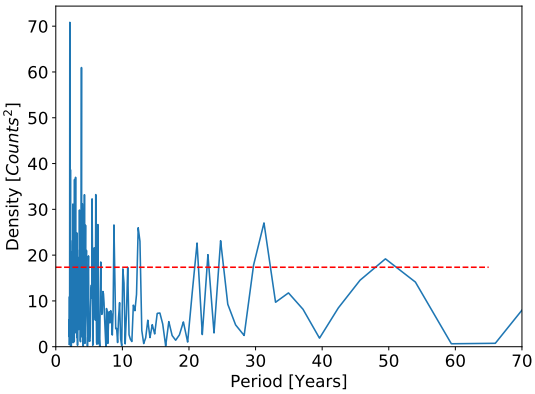

(c) Wavelet spectrum with COI (shaded area) and 95% confidence level (red contours)

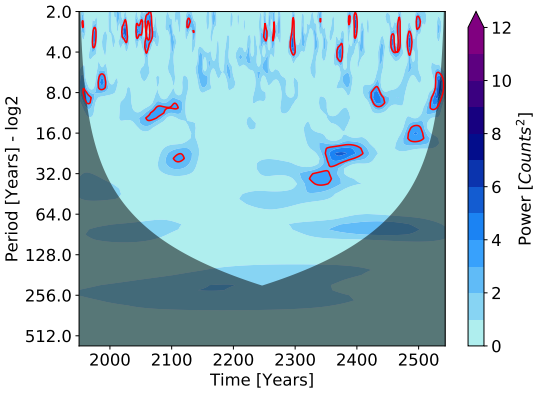

Figure 4.24: Results of spectral analysis for decadal TC variability in NIND annual counts for the multi-centennial MM control run.

The overall analysis of TC activity in this basin results in no robust conclusions about drivers of decadal TC variability. The standard power spectrum analysis of the ACE time series from the multi-centennial coupled control runs shows significant peaks at around 50-years, a periodicity typically linked to the AMO. In terms of counts (fig. 4.24a), decadal signals (at around 30 years) are detected by both the standard method and the wavelets only for the LL and MM control runs (fig. 4.24b and fig. 4.24c).

For the 1950-2050 period, at least one of the LM and HM atm-only individual spectra are able to detect periodicities at decadal time scales for both metrics, something that is not seen for the MM runs. For the power spectra of ACE and counts for the LL control run,

there is a significant signal on decadal time scales, however the validity of it is questioned, since it is associated with periodicities of above 20 years, an uncommon result based on the results for the other basins. At least one of the hist-1950 experiments, however, showed signals at decadal time scales (~10-13 years). Nevertheless, there is evidence of decadal variability on the MH control experiment, but not for the MM runs for both metrics. Lastly, decadal variability on TC activity in the basin was found for both metrics in HM and HH control runs as well as for at least one of the corresponding hist-1950 runs.

Just like for the rest of the basins, the time series of annual ACE and TC counts are correlated with the three climate indices. No robust conclusion can be drawn from the correlations between the ENSO index and the time series for this basin (fig. 4.25). Only a handful of the model simulations show a significant (mostly weak) anticorrelation between the time series of ACE and the ENSO index, while the same is observed for 8 of the runs in terms of frequency. A similar picture can be drawn for the influence by the AMO, with only a few weak relationships between the time series and the index. Perhaps, it is important to note that for the MH hist-1950 there is a significant, moderate positive relationship with both the May-November and the yearly averaged AMO index in both metrics. The yearly averaged index seems to have a greater influence on the frequency of TCs compared to ACE for some of the coupled MM and MH runs. Lastly, no robust conclusion can be formed about the PDO's influence on TC activity, since significant coefficients between the index and the time series are found for less than 5 of the simulations.

The locations of EOTs for all the model runs are presented on figure 4.26a. For coupled runs, irrespective of resolution, the EOT1 base points are clustered in the Bay of Bengal. In contrast, for the atm-only experiments, with increasing resolution, there is a greater spread between the EOT1s, even though they remain in the eastern part of the region. For the low-resolution runs, both atm-only and coupled, none of the first four EOT base points are positioned in the Arabian Sea, compared to the EOTs for the higher resolutions. In terms of variance explained by the first EOTs, the amount explained by EOT1s of low-resolution experiments is noticeably higher compared to the corresponding EOTs for the higher resolution experiments (see fig. 4.27), similar to the distributions for the EOTs under the current climate (fig. 3.32). Furthermore, the amount of variance explained by EOT2s for the N96 runs drops noticeably to below 15%. Two EOTs were sufficient for explaining 75% of the variance in the basin for the low-resolution runs, while three to four

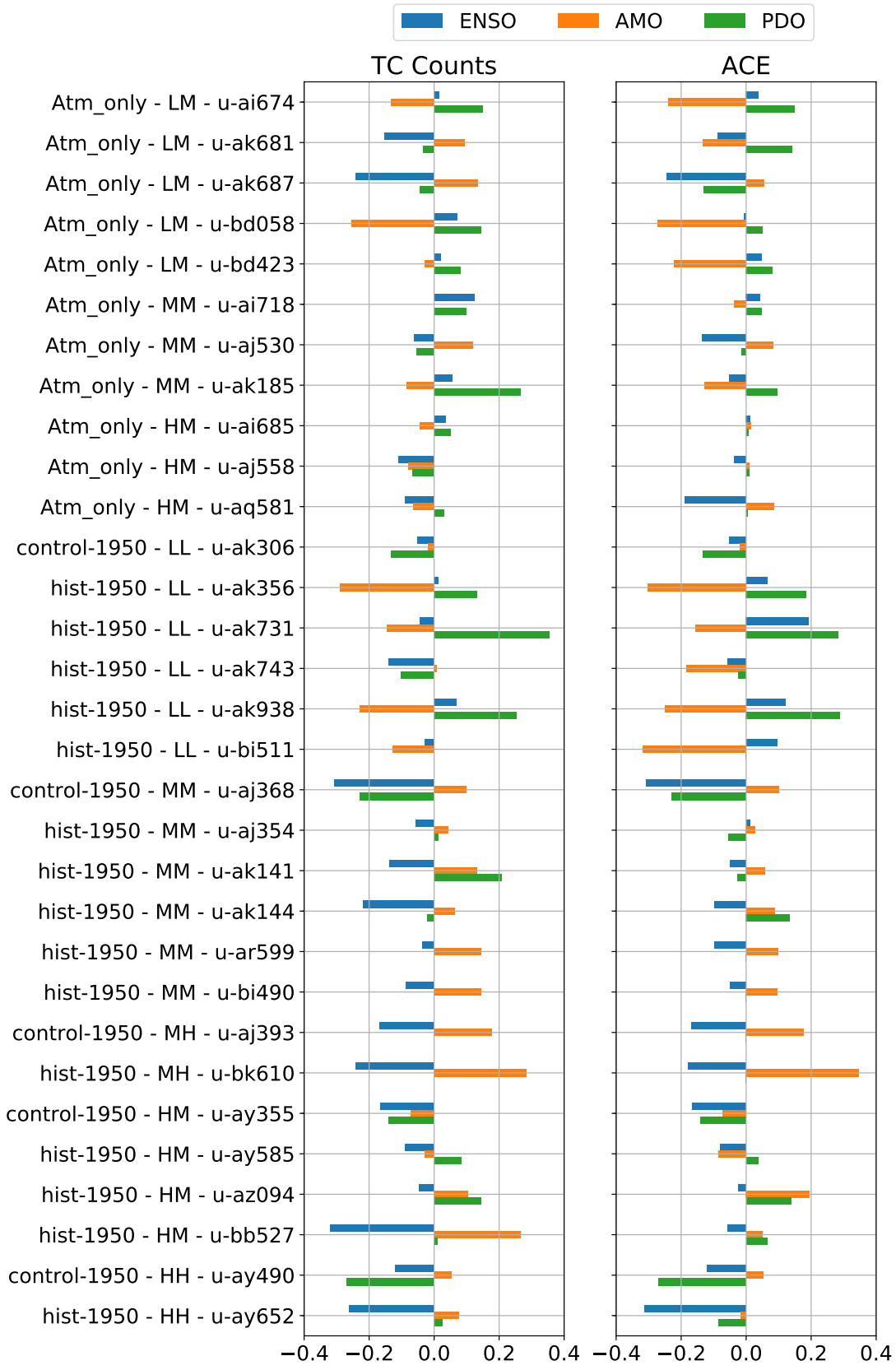

Figure 4.25: Pearson correlations between the time series of NIND annual TC counts and ACE of models with the seasonal climate indices for the 1950-2050 period. Hatched bars indicate the correlations that are significant at the 90% CL.

(a) Locations of EOTs for the N96 (LL) coupled runs

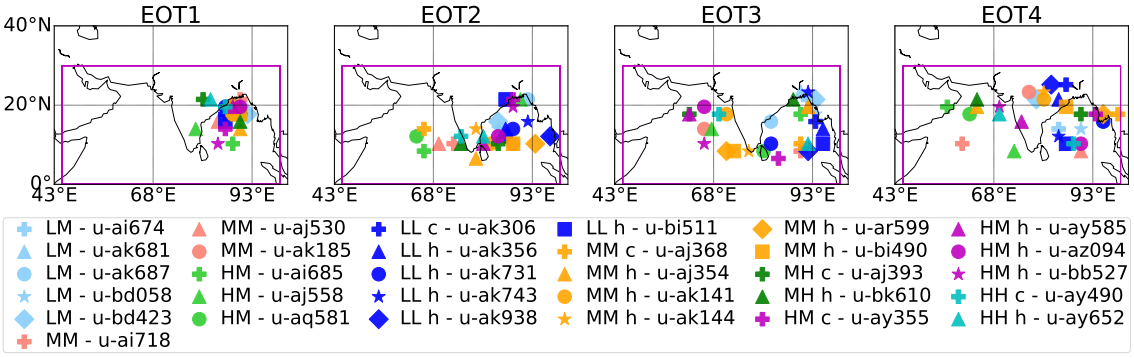

(b) SST regression patterns for the u-ak356 hist-1950 run

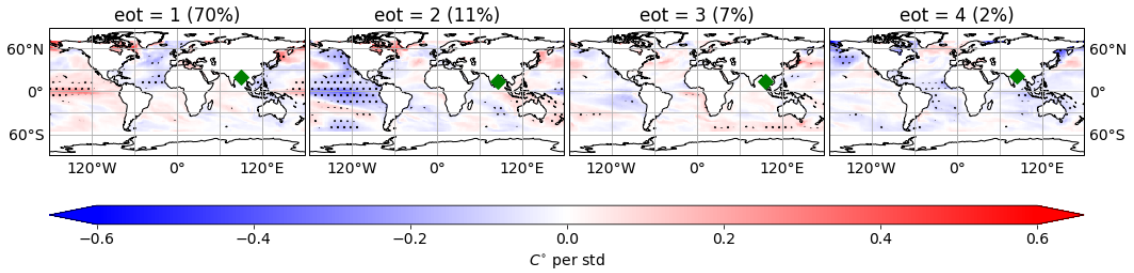

(c) VWS regression patterns for the u-ak356 hist-1950 run

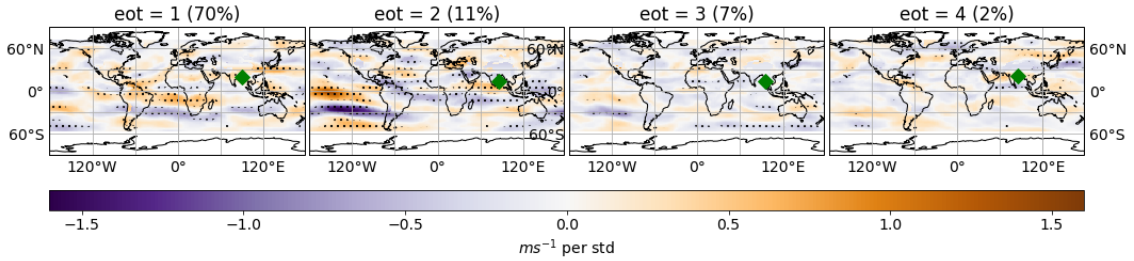

(d) Summary statistics about the Pearson correlation coefficients between the NIND EOT time series for the different model simulations and the May-November averaged ENSO, AMO and PDO indices.

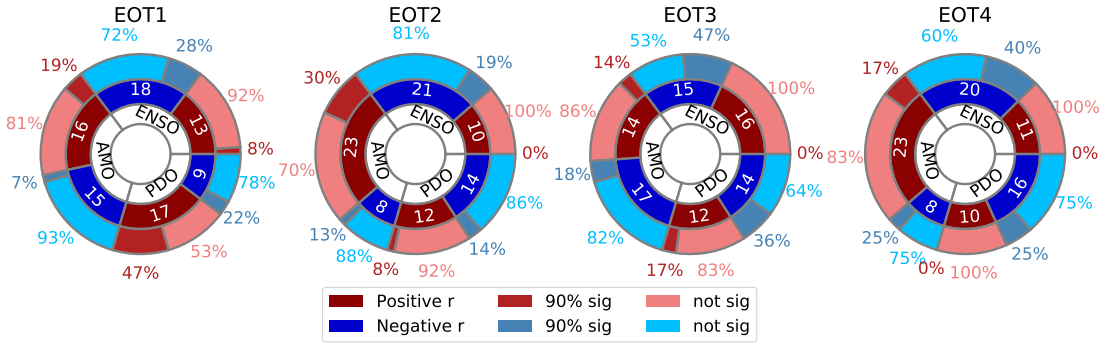

Figure 4.26: Results of EOT analysis for decadal TC variability in NIND. Location of EOT is shown with green marker and significance at the 90% CL is indicated with dots on b and c. Period examined is 1950-2050. For the correlations dark red (blue) colors indicate how many of the 31 models have positive (negative) correlations with each index, medium red (blue) indicate how many of the dark red (blue) correlations are significant at the 90% CL, while light red (blue) indicate how many are not significant.

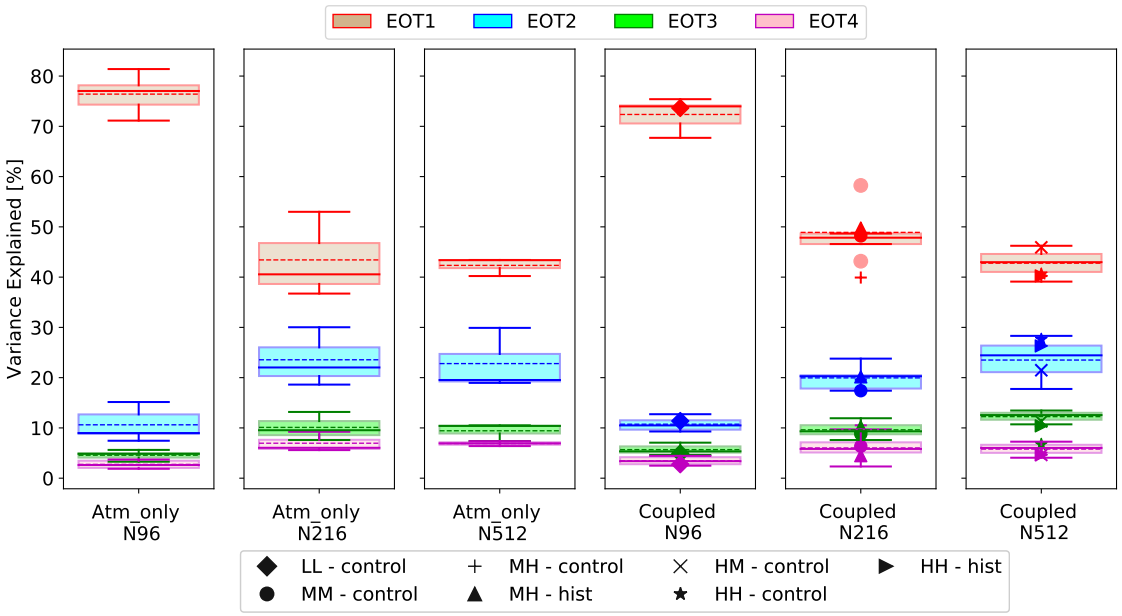

Figure 4.27: Percentage of variance explained by the EOTs for decadal variability for NIND. Column 1-3: ensemble of atm-only runs split by atmospheric resolution; Column 4: ensemble of LL historic runs against the control run (♦); Column 5: ensemble of MM historic runs against the MM control (●), MH control run (+) and MH historic run (▲); Column 6: ensemble of HM historic runs against HM control run (×), HH control run (★) and HH historic run (►). Faded circles (●) show outliers. Dotted lines show the ensemble means.

EOTs were needed for the rest of the simulations.

No robust connection to the climate indices can be extracted from the SST and VWS regression maps or from the Pearson correlation coefficients between the EOTs and the indices. Figures 4.26b and 4.26c present SST and VWS regression maps for the first 4 EOTs for the u-ak356 (LL hist-1950) run, one the few simulations for which known canonical patterns were displayed on regression maps. For this particular basin, activity at the Bay of Bengal appears to be influenced by warm SSTs and weak VWS in the central Pacific and cold SSTs accompanied by strong VWS in Atlantic MDR. Pearson correlations between EOT1 and the climate indices showed significant positive (negative) correlation with the May-November averaged ENSO (AMO) index. Once the influence of EOT1 is removed, EOT2, which is still positioned in the Bay of Bengal but explains considerably less variance, appears to be influenced by cold SSTs and strong VWS linked to La-Niña. It is important to note that these results are not representative of the relationship between

TC activity in the NIND ocean and the climate indices. They just serve as an example of isolated influence on TC activity by the climate indices examined in the study. Lastly, very few significant correlations or anticorrelations are found for the 31 model simulations as shown on figure 4.26d. In the future, it is worth investigating the connection to interannual climate indices and particularly to the Indian Dipole.

4.7 Conclusion

This chapter is dedicated to examining the drivers of the decadal variability of TCs in the different basins. Table 4.1 presents a summary of the results examined in this chapter on whether decadal variability of TCs is influenced by known modes of variability, particularly ENSO, AMO and PDO. Spectral analysis of the full length of multi-centennial coupled control runs showed clear evidence of decadal periodicities within the time series of frequency and ACE in the different basins. These periodicities have been associated in the literature with the periodicities of the AMO (around 50-70 years) and the PDO (around 20-30 years).

TC activity in the Atlantic during the 1950-2050 period is influenced, with a high degree of confidence, by the AMO via warm local SSTs, as was evident by the SST regression patterns. ENSO additionally affects Atlantic hurricanes via changes in the Walker Circulation, a conclusion that was derived by both the SST and VWS regression patterns. The AMO's influence is robust in all the simulations examined, with the exception of the N96 coupled runs. Pearson correlation coefficients between the time series of TC activity (counts, ACE, EOTs) with the climate indices further support this conclusion.

In contrast, ENSO and AMO's impact on TC activity in the EPAC region is more robustly observed for the atm-only experiments, especially the N216 and N512 runs. ENSO has a greater influence than AMO on the N216 and N512 coupled simulations in terms of ACE and frequency. However, both AMO (via cold SSTs) and ENSO (via warm SSTs and weak VWS) drive TC variability in the basin.

For the CPAC region very robust correlation (anticorrelation) with the ENSO (AMO) index is found across the model experiments for frequency, ACE and EOT time series. In contrast, the PDO has a positive relationship with TCs in the atm-only experiments and a mainly negative one for the coupled runs. It is worth reminding that results for this basin

must be considered carefully since the amount of TCs analysed is considerably small. As can be seen from table 4.1, based on the analysis ENSO and PDO have a more robust influence on TC activity in the basin compared to the AMO.

For the WPAC region, the AMO is significantly anticorrelated with both the frequency and ACE in atm-only experiments, while ENSO and PDO are correlated mainly with ACE. The robustness is not observed for the coupled runs. Even though the analysis of the drivers of decadal TC variability for this basin is challenging due to the vast size of the region examined, there are indications of ENSO and AMO influence for the coupled experiments. TC activity in the atm-only experiments is evidently influenced by both ENSO and AMO, while there are indications of PDO influence. The Pacific decadal mode does not appear to have a significant influence on TC activity for the coupled experiments.

Lastly, similarly to the investigation under the current climate, decadal variability of TCs in the NIND region has no robust connection to the climate indices (ENSO, AMO and PDO). There are indications of ENSO influence, but it is recommended to investigate the connection to interannual climate indices such as the Indian Dipole and especially how ENSO, AMO and PDO might influence the Indian Dipole and the monsoon seasons.

Table 4.1: Summary of which modes of variability influence each basin in the HadGEM3-GC3.1 simulations for the 1950-2050 period. YES: If more than 75% of the results examined in the chapter indicate the influence by a specific mode; YES*: if 50-75% of the results in the chapter indicate the influence by a specific mode; NO: if less than 50% of the results examined in the study indicate the influence by a specific mode; N/A: if the mode was not examined.

	NATL			EPAC			CPAC			WPAC			NIND		
	ENSO	AMO	PDO	ENSO	AMO	PDO	ENSO	AMO	PDO	ENSO	AMO	PDO	ENSO	AMO	PDO
ATM_ONLY-LM	YES	YES	NO	YES	NO	NO	YES	YES	YES	YES	YES	YES*	YES*	YES*	NO
ATM_ONLY-MM	YES	YES	YES	YES	YES	YES	YES*	YES	YES	YES	YES	YES*	YES*	NO	NO
ATM_ONLY-HM	YES	YES	YES	YES	YES	YES	YES	NO	YES	YES	YES	NO	YES*	NO	NO
COUPLED-N96	YES	YES	NO	YES	NO	YES*	YES	NO	YES	YES	YES*	NO	YES*	YES*	YES*
COUPLED-N216	YES	YES	NO	YES	YES	YES*	YES	YES*	YES*	YES*	YES*	NO	YES*	NO	NO
COUPLED-N512	YES	YES	NO	YES	YES	NO	YES	YES*	YES*	YES*	YES*	NO	YES*	NO	NO

Chapter 5

Drivers of TC Activity under Climate Change

5.1 Introduction

As mentioned in sections 1.6.3 and 1.7, several studies have examined how TCs might change in a warming climate. In this chapter, in order to assess the influence of a warming climate on the variability of TCs, we examine the differences between the drivers of TC activity between the control and the historic HadGEM-GC3.1 experiments during the first 30 years of the coupled model simulations (1950-1980, hereafter referred to as P1) with the drivers during the last 30 years (2020-2050, hereafter referred to as P2), and how they connect with the climate indices. General comments about TC representation will be made for the atm-only runs, however, results presented will be focused only on the coupled runs. A brief description will be made of the results for whole NH activity before addressing TC activity in the different regions individually. Lastly, it must be noted that, even though the spectral methods have been used for analysing time series of TC activity in the two periods and they reveal significant periodicities mainly on interannual time scales, their results do not have any contribution in assessing the impact of climate change on TC activity. Therefore, in this chapter results from the spectral methods will not be included. Lastly, in this chapter the correlations between the climate indices and the time series of annual TC counts and ACE will be discussed, but no figures will be presented.

5.2 NH Activity

Figures 5.1 and 5.2 present the difference in global mean track densities in the two periods examined for the LL, MM and HH control and historic runs as well as global mean track densities (of equal or greater than 2 TCs per reason per unit area) for the two runs during P1 and P2. It can be seen that for the historic run there are greater differences in mean track densities between the two periods compared to the control run.

Figure 5.3 shows the difference in the average annual number of TCs and ACE in terms of total NH activity for P1 (green) and P2 (purple). The model simulations with common resolution are taken as an ensemble, and are presented as a boxplot. The different control runs and the stand-alone hist-1950 runs are indicated by symbols. These results for both metrics of TC activity show once again how increases in model resolution can lead to better simulation of TC activity. Furthermore, with increasing resolution, there is a more gradual increase in the mean annual ACE, whereas in terms of TC counts, the annual average of TCs in the NH for the N216 simulations is either slightly less or on the same level with the N512 simulations as seen on figure 5.3.

For the atm-only runs, differences between the two periods reveal an overall global decrease in P2, for both metrics, in the annual means of TC activity in the NH. In contrast, for the coupled runs, the ensemble means of annual ACE as well as ACE for the individual control (except HH) experiments, and the MH and HH historic runs show an increase in P2 compared to P1 (fig. 5.3b). In terms of frequency, the ensemble means of annual TC counts remain relatively the same, the control runs show slight increases, whereas the MH and HH hist-1950 runs show slight decreases (fig. 5.3a). These results are in agreement with studies suggesting an increase in more intense TCs (Knutson et al., 2015; Manganello et al., 2014; Murakami et al., 2015; Roberts et al., 2020b, 2015; Wehner et al., 2015; Yamada et al., 2017) whilst the frequency of TCs remains stable or shows slight decrease (Christensen et al., 2013).

Upon examining the metrics of total TC activity in the NH further, correlations between the time series (of TC counts and ACE) and the climate indices (ENSO, AMO and PDO) show that the seasonal ENSO's influence is greater on ACE compared to counts in both periods examined. In addition, the ENSO's influence is greater for P2 than for P1. Specifically, for P1, there is almost no significant relationship between the seasonal ENSO index and TC frequency. However, for all the LL coupled runs, 4 N216 runs, 3 N512 runs

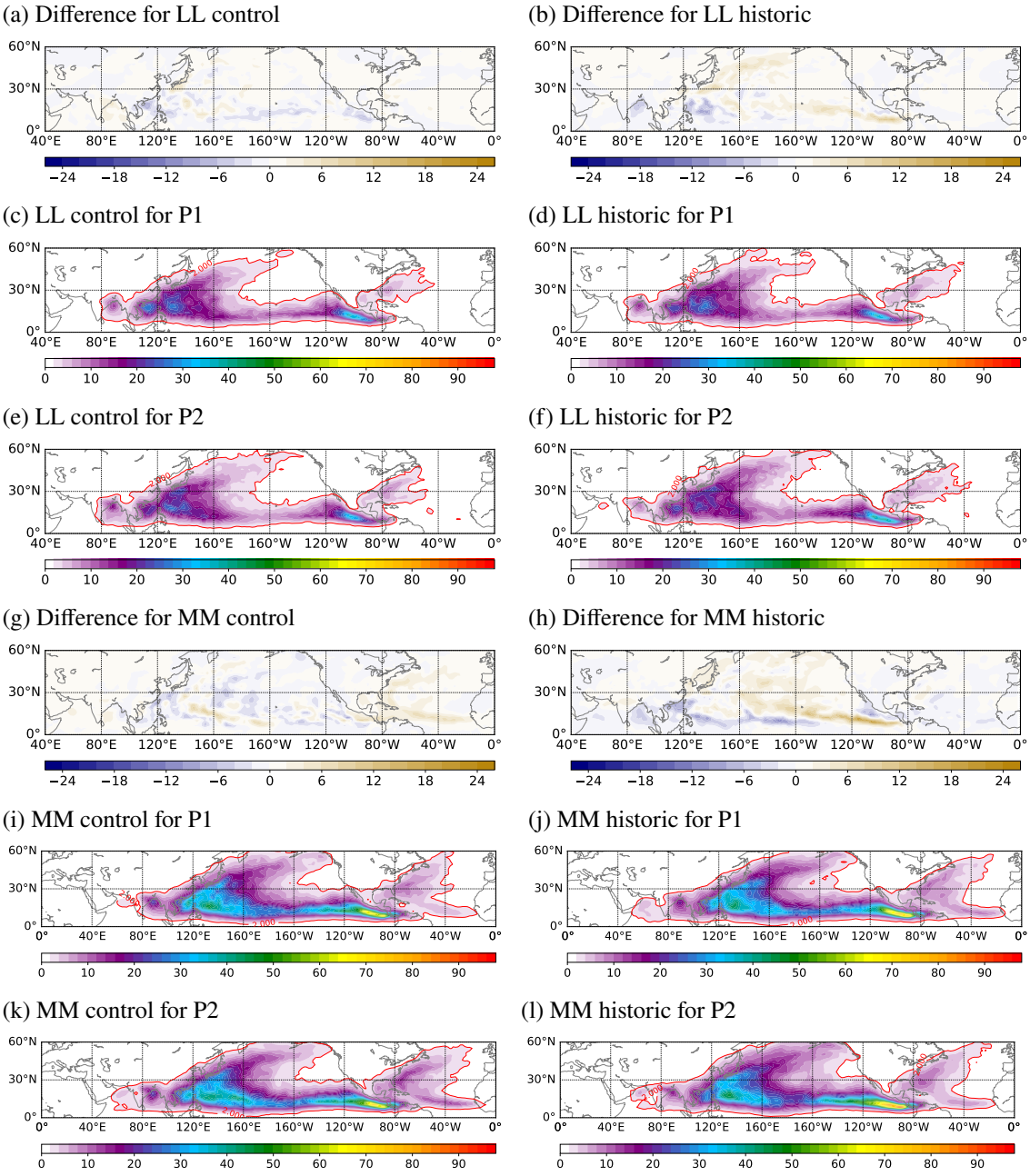

Figure 5.1: (a) - (b) Difference in mean track density for the LL control and historic runs; (c) - (f) Mean track density during the P1 and P2 periods for the LL control and historic runs; (g) - (h) Difference in mean track density for the MM control and historic runs; (i) - (l) Mean track density during the P1 and P2 periods for the MM control and historic runs; Red contour indicates where the mean track density is greater that 2 TCs per season, per unit area.

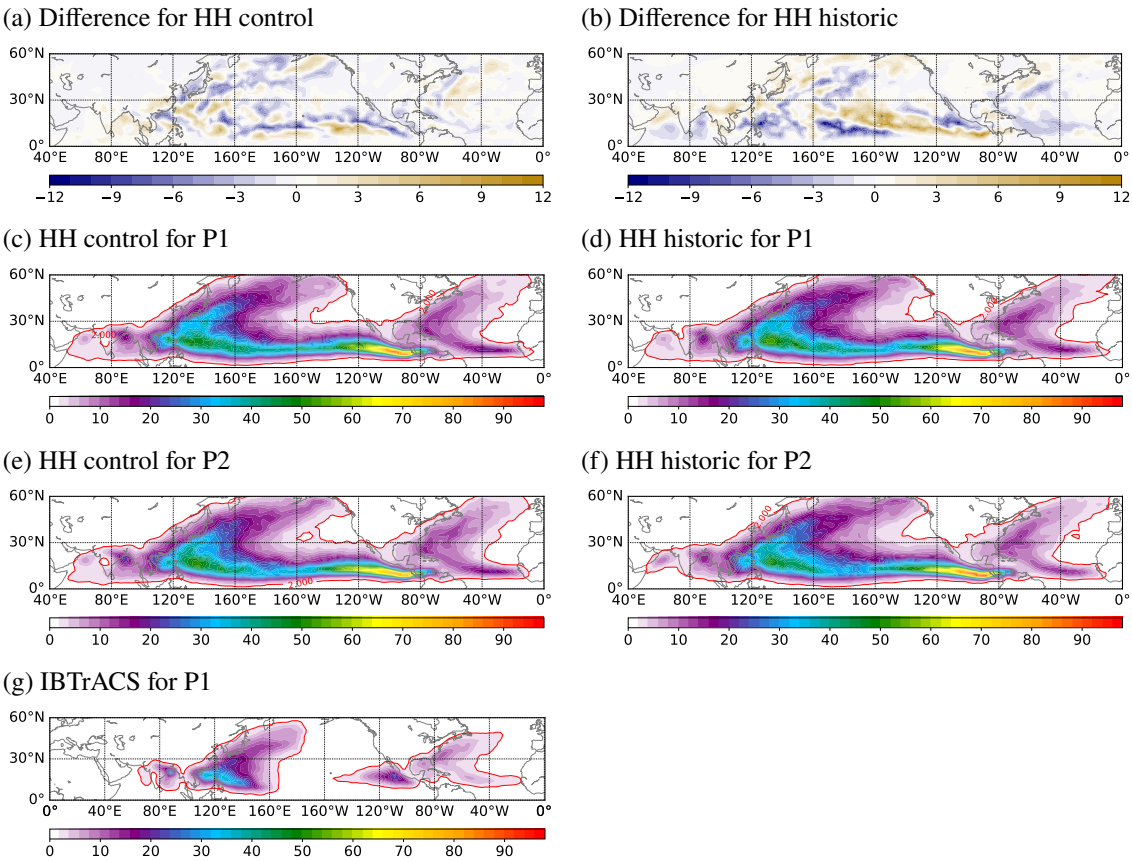

Figure 5.2: (a) - (b) Difference in mean track density for the HH control and historic runs; (c) - (g) Mean track density during the P1 and P2 periods for the HH control and historic runs, as well as for IBTrACS during P1. Red contour indicates where the mean track density is greater that 2 TCs per season, per unit area.

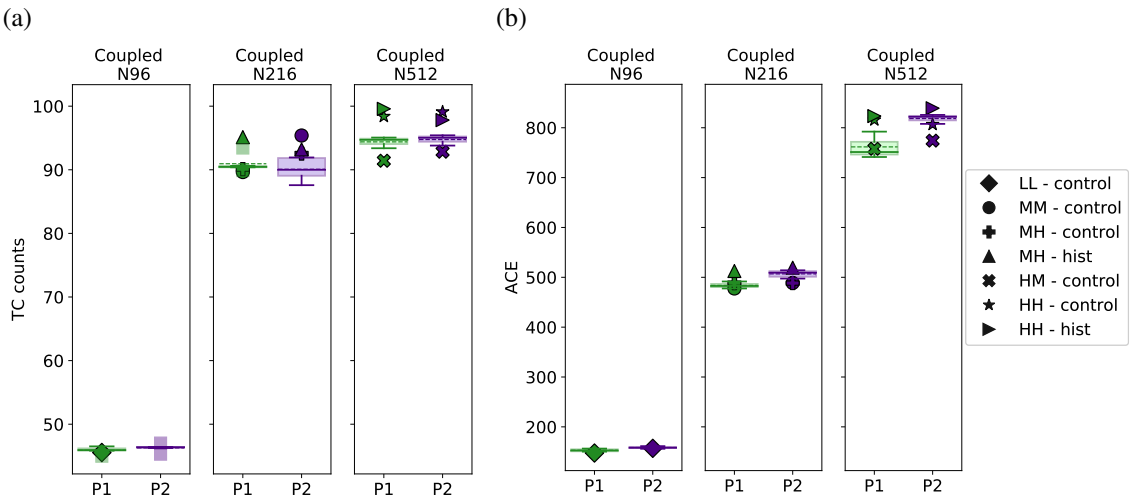

Figure 5.3: Annual average of (a) TC counts and of (b) ACE in the NH for P1 (green) and P2 (purple). Column 1: ensemble of LL historic runs against the control run (⧫); Column 2: ensemble of MM historic runs against the MM control (●), MH control run (✚) and MH historic run (▲); Column 3: ensemble of HM historic runs against HM control run (✖), HH control run (★) and HH historic run (►). Faded squares (■) show outliers. Dotted lines show the ensemble means.

and 3 of the LM and MM atm-only runs, there is a moderate or strong positive correlation with the seasonal ENSO index. For P2, the global ACE is significantly, moderately or strongly, correlated with ENSO for at least 22 out of the 31 runs examined. In terms of frequency, for all the MM and HM atm-only experiments, significant (mostly moderate) positive correlations are observed with the seasonal ENSO index. Interestingly, none of the time series of total NH TC counts for the coupled control runs show a significant relationship with the index. Moreover, the AMO's influence on TCs is stronger in P2 compared to the other period, which is particularly obvious for the atm-only runs. Even though there is not a robust influence by the AMO for P1, the AMO has a significant moderate anticorrelation with ACE in all but one of the hist-1950 LL coupled runs. For the later period, the May-November AMO averaged index is significantly, moderately anticorrelated with the time series of counts (ACE) in 4 (6) out of the 6 higher-resolution atm-only experiments. Lastly, the PDO index has a more robust connection to TC activity during P2 period compared to P1, mainly for the atm-only runs, since the number of significant relationships with the index increase from one period to the other. There is no robust conclusion from the coupled runs.

5.3 North Atlantic

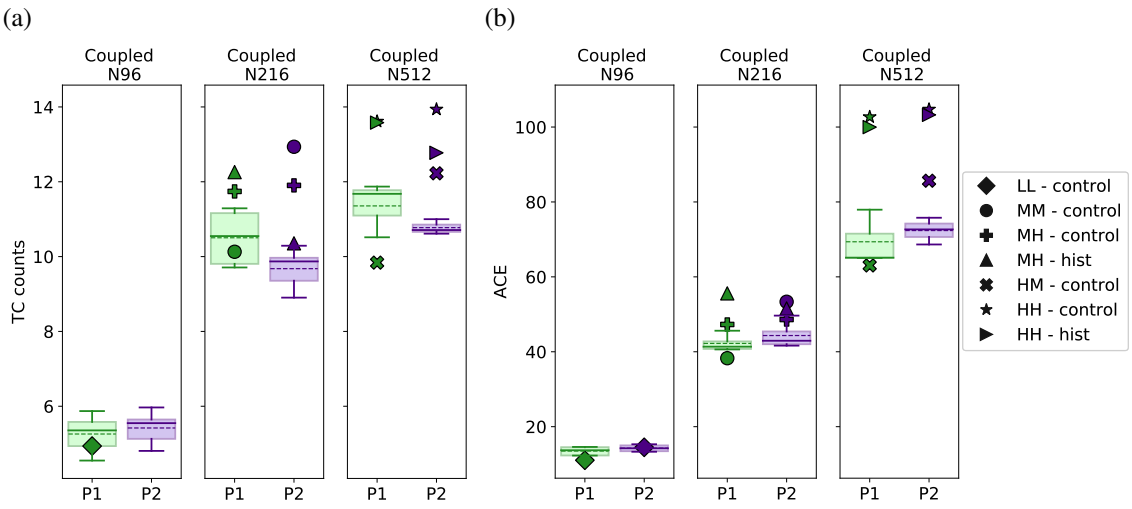

Figure 5.4: Annual average of (a) TC counts and of (b) ACE in NATL for P1 (green) and P2 (purple). Column 1: ensemble of LL historic runs against the control run (♦); Column 2: ensemble of MM historic runs against the MM control (●), MH control run (✚) and MH historic run (▲); Column 3: ensemble of HM historic runs against HM control run (✖), HH control run (★) and HH historic run (►). Faded squares (■) show outliers. Dotted lines show the ensemble means.

The differences in the average annual number of TC counts and ACE for the NATL region in P1 and P2 are presented in figures 5.4a and b, respectively. An increase can be seen for the annual average NATL ACE in P2 compared to P1 for all the ensembles examined, as well as for the control-1950 and hist-1950 runs shown with markers, except for the MH hist-1950. In terms of TC counts, the annual means for the atm-only ensembles irrespective of resolution, as well as for the LL coupled runs, show increases during P2. Lastly, the annual means for the coupled N216 and N512 ensembles and the MH and HH hist-1950 runs decrease. For the atm-only runs, it is found that, in terms of frequency the MM and HM have similar annual averages, whilst in terms of ACE the N512 show much higher means, a result which is in agreement with Roberts et al. (2020b). It is possible that this difference between ACE and frequency is attributed to having more intense TCs in the basin in a warming climate, particularly for HadGEM3.

By correlating the time series (of TC counts and ACE) with the seasonally averaged climate indices for the two periods, no robust influence from ENSO on TC activity in

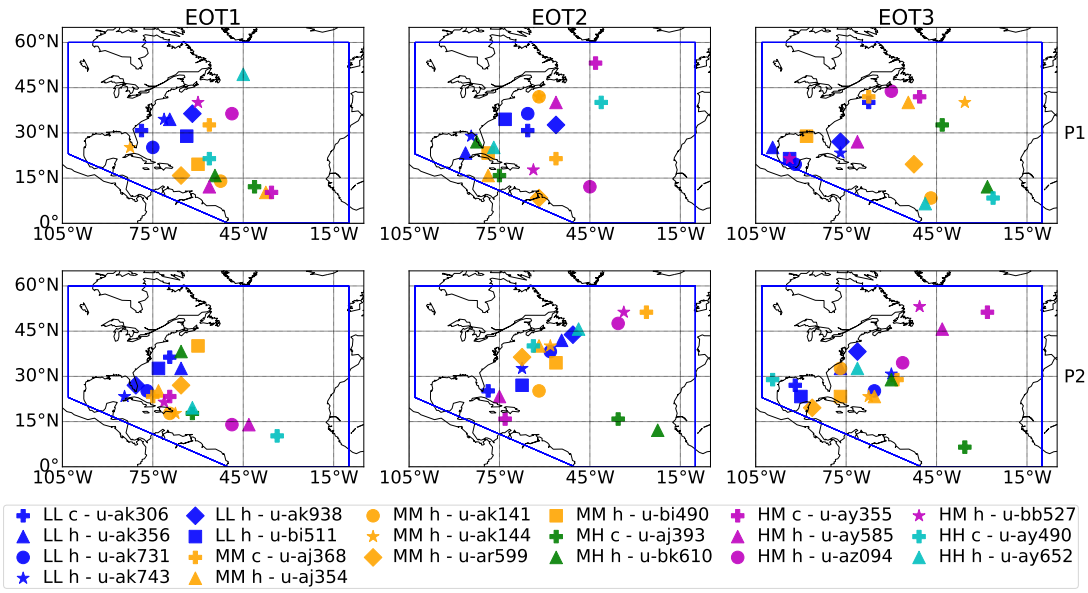

Figure 5.5: EOT locations for the coupled simulations for TC activity in NATL during P1 (top) and P2 (bottom). The different colors indicate the simulations of a given resolution, while the symbols differentiate the runs for each resolution. For each color, the first symbol indicates the control run, and the remaining symbols indicate the corresponding hist-1950 runs.

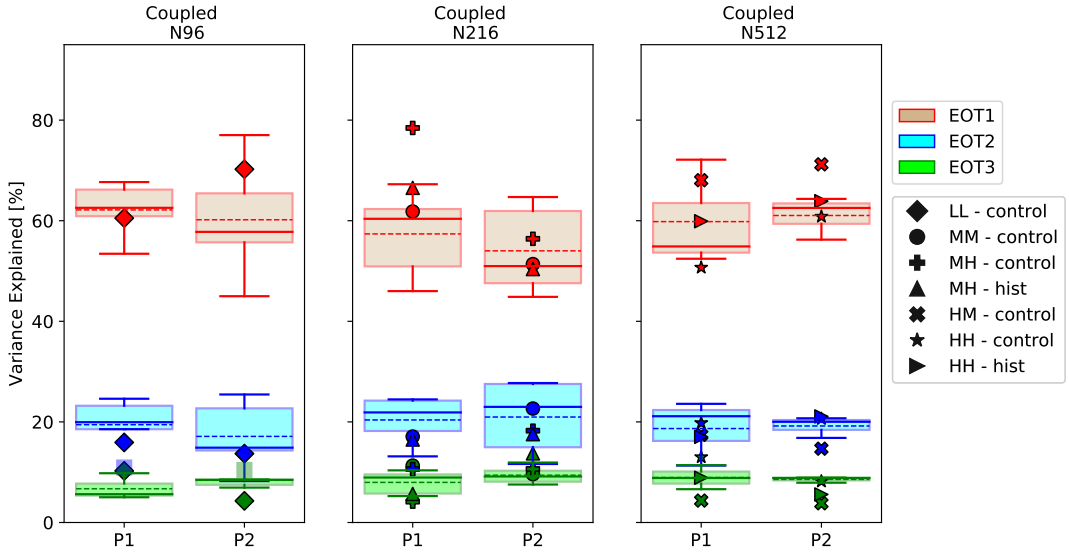

Figure 5.6: Amount of variance explained by EOTs during P1 and P2 for NATL. Column 1: ensemble of LL historic runs against the control (♦); Column 2: ensemble of MM historic runs against the MM control (●), MH control (✚) and MH historic run (▲); Column 3: ensemble of HM historic runs against HM control (✖), HH control (★) and HH historic run (►). Faded squares (■) show outliers. Dotted lines show the ensemble means.

the NATL basin during P1 is detected, since less than 5 experiments show a significant connection (anticorrelation) to the index. Even for P2, less than 10 runs (the majority of them being atm-only runs) showed a significant connection to ENSO.

The AMO's influence on TCs appears to be stronger in P2 compared to P1. There is no robust conclusion from the correlations for the influence of the AMO on the frequency of TC activity in the region during P1. In contrast, for at least one run from each configuration and resolution, a significant, moderate or strong positive correlation can be seen between the May-November averaged AMO index and the time series of counts and ACE. For P2 more model simulations are significantly, moderately or strongly correlated with the AMO index, compared to P1. Only one of the LL hist-1950 runs has an anticorrelation with the climate mode, however this coefficient is weak and not significant.

The PDO appears to have a greater influence on TC activity during P2 compared to P1, mainly for the atm-only runs, since the number of significant moderate anticorrelations between the May-November averaged PDO index and the time series increase from 2 to 5 (2 to 6) for frequency (ACE). No significant connection to the climate mode is found for TC counts in the coupled simulations during the two periods examined. However, in terms of ACE, two of the coupled runs show significant, moderate anticorrelations with the index during P1, while 4 of the coupled models show significant correlations during P2.

Track densities for both periods reveal once again that TCs in the N96 runs are concentrated in the western part of the region (not shown). For the N216 and N512 runs, track densities extend in the MDR as well, and in the majority of the runs examined two distinct regions of maximum mean track density are observed as shown on figure 5.2; one in the MDR and one along the East Coast of the US.

Analysing the locations for EOT1s is a complicated matter since no consensus can be observed about how they differ between the two periods. Figure 5.5 presents the locations for the first three EOTs for all the coupled runs. The different colors indicate the simulations of a given resolution, while the symbols differentiate the runs for each resolution. For each color, the first symbol indicates the control run (for example LL c - u-ak306), and the remaining symbols indicate the corresponding hist-1950 runs (for example LL h - u-ak356). The top row presents the results for P1 and the bottom row presents the results for P2. The N96 EOTs are positioned in the western part of the region

along the east coast of the US, due to the concentration of track densities, between 20 and 40N in both periods (fig. 5.5). The vast majority of N216 EOTs for P1 are positioned in the MDR or in the Caribbean, with the exception of the MM control run which is in the middle of the subtropical Atlantic (fig. 5.5). For P2, the majority of N216 EOT1s move towards the north or northeast, while one of the MM hist-1950 EOT1s moves from Florida towards the Caribbean and EOT1 for the MM control run moves above Cuba (fig. 5.5). One base point of the MM and the MH hist-runs move out of the tropics during P2 (fig. 5.5). The N521 EOT1s are spread out in the basin during P1, but the majority of them relocate to below $25°N$. The HM control run is an exception since the associated EOT1 during P1 is positioned in the MDR, but relocates towards Cuba during P2 as shown on figure 5.5. As was the case in the previous chapters, EOT2s and EOT3s are more spread out in the basin and, as seen on figure 5.5, most of them are outside the tropics and along the path that most TCs take as they re-curve and undergo extra-tropical transition. The mean variance explained by EOT1 from the ensemble of hist-1950 in the N96 and N216 experiments decreases in P2, whereas the variance for EOT1 of the N512 ensemble runs increases during P2 (fig. 5.6). Lastly, the overall distribution of variance explained by the first three EOTs remains similar to the ones observed in the previous chapters.

Examining the influence of SSTs and VWS proves to be no easier task, therefore, only EOT1 is considered, particularly the ones positioned below $30°N$. Results show that for the different control runs during P1, when EOT1 is located between $60°W$ and 0 and below $30°N$, TC activity is associated with significant warm SSTs in the Atlantic as seen in figure 5.7a. If the EOT is located above $15°N$, the VWS appears to be not an important driver (not shown). However, if the EOT1 is within the same longitudinal range and below $15°N$, as is the case on figure 5.7a, then TC activity is additionally associated with cold (sometimes significantly) SSTs in the eastern Pacific and weak VWS over the Caribbean (fig. 5.7c).

During P2, when EOT1 for the control runs are below $30°N$ and between $75°W$ and $65°W$, as shown on figure 5.7e, TC activity at the base points is associated with warm SSTs both in the Atlantic MDR (significantly), in an AMO-resembling pattern, and in the eastern equatorial Pacific. Additionally, it appears that TC activity at those base points is influenced by low VWS over the Caribbean (fig. 5.7g). Conversely, if the longitudinal range is between $65°W$ and 0, TC activity is associated with cold SSTs in the Atlantic

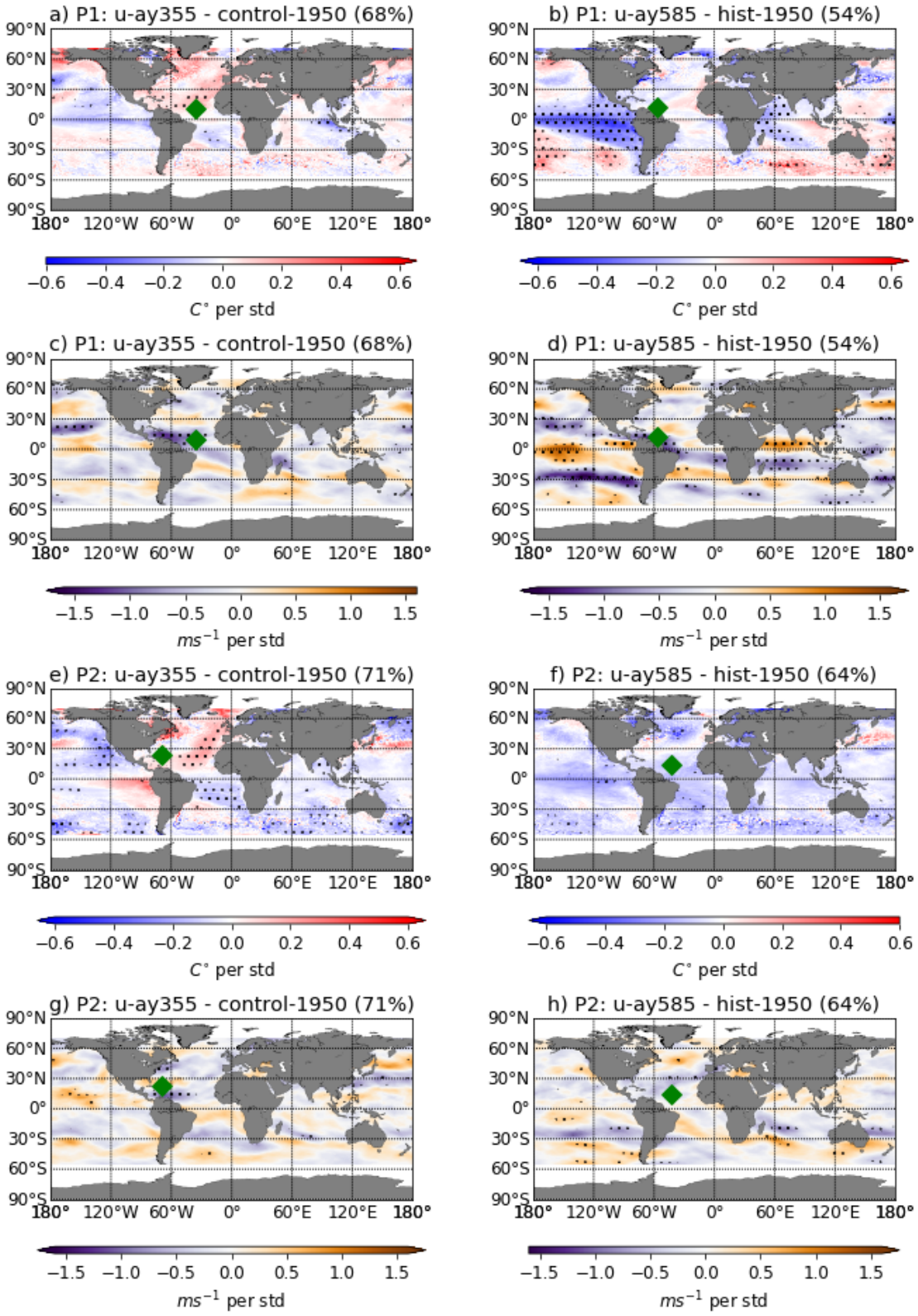

Figure 5.7: EOT1 SST and VWS regression maps for the HM control-1950 (left) and one hist-1950 (right) runs during P1 and P2 for NATL. Plots in blue/red colours indicate the SST maps. Plots in purple/orange colours indicate the VWS maps. Location of EOT is indicated with a green marker. Significance at the 90% CL is indicated with dots.

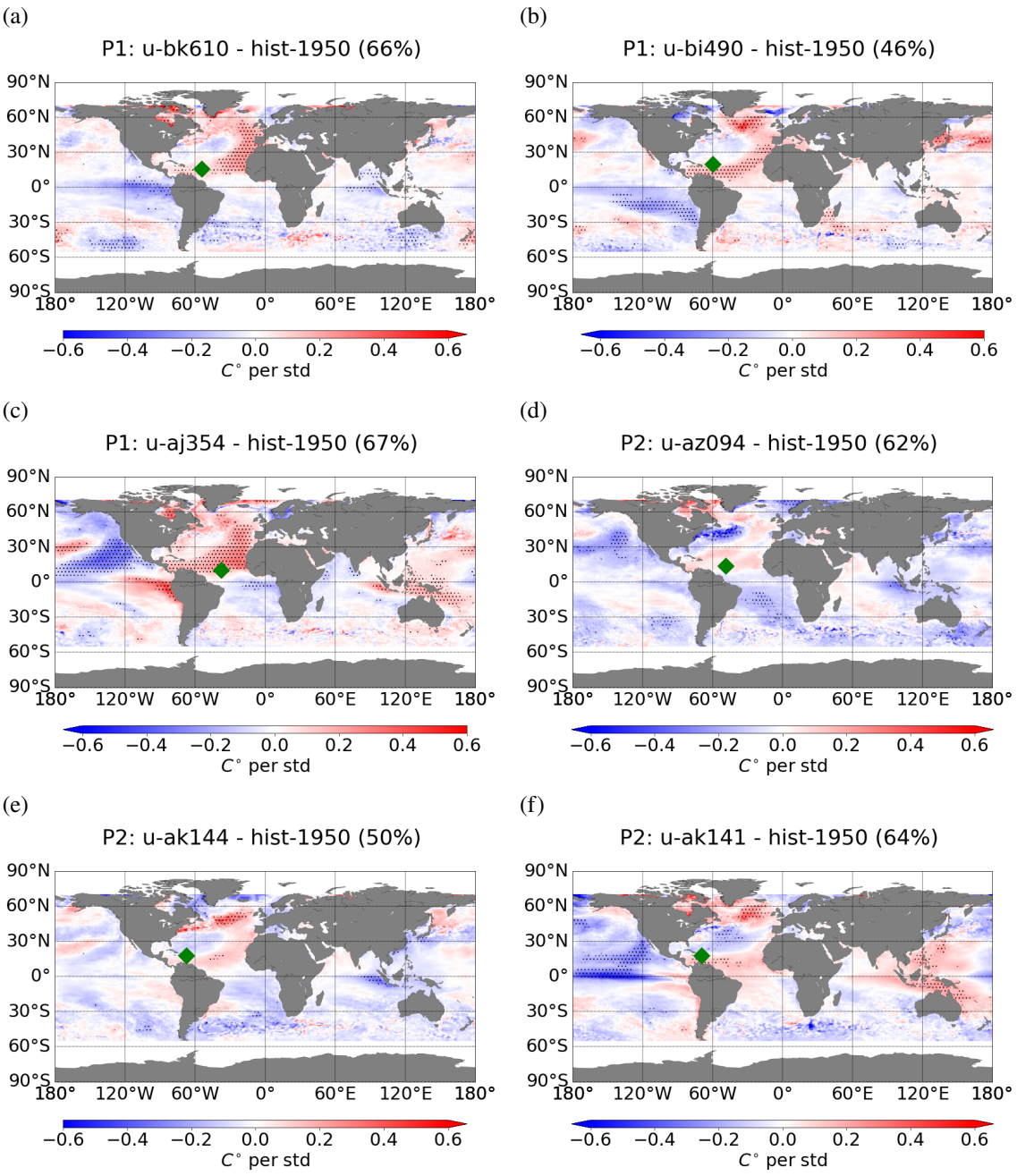

Figure 5.8: Examples of EOT1 SST regression maps for the NATL region; (a)-(c) for P1; (d)-(f) for P2

and the Pacific (not shown) and low VWS over the Caribbean and the Atlantic ITCZ (not shown).

Results for the SST and VWS show that depending on the location of each EOT, different conditions can influence the TC activity. Therefore, in order to study the drivers associated with EOT1 for the historic runs during P1, it is important to separate the EOTs by location into three cases:

1. Between 75 and 60 $°W$:
   (a) Between 20 and 15 $°N$: TC activity is associated with only cold SSTs in the Pacific (not shown)
   (b) Other latitudes: No known pattern is observed
2. Between 60 and 45 $°W$:
   (a) Below 15 $°N$: TC activity is either influenced by significant cold Pacific SSTs as (fig 5.7b) or by warm AMM-resembling Atlantic SSTs (fig. 5.8a).
   (b) Between 15 and 20 $°N$: TC activity is significantly connected to both warm SSTs in Atlantic and cold SSTs in Pacific (fig. 5.8b) and low VWS over the Caribbean as shown on (fig 5.7d).
   (c) Between 20 and 30 $°N$: No EOT1s are found
3. Between 45 $°W$ and 0:
   (a) below 15 $°N$: TC activity is mostly significantly associated with warm Atlantic and warm eastern Pacific SSTs (fig. 5.8c), in addition to low VWS over Caribbean and the Atlantic ITCZ and strong VWS in central Pacific (fig 5.7d).
   (b) Other latitudes: No EOT1s are found

For P2, the EOT1s are split into two main categories depending on their longitudinal coordinates:

1. Between 60 $°W$ and 0: 2 EOT1s are found, but no known canonical patterns are observed (fig. 5.8d)
2. Between 75 and 60 $°W$: the majority of EOT1s are located within this region

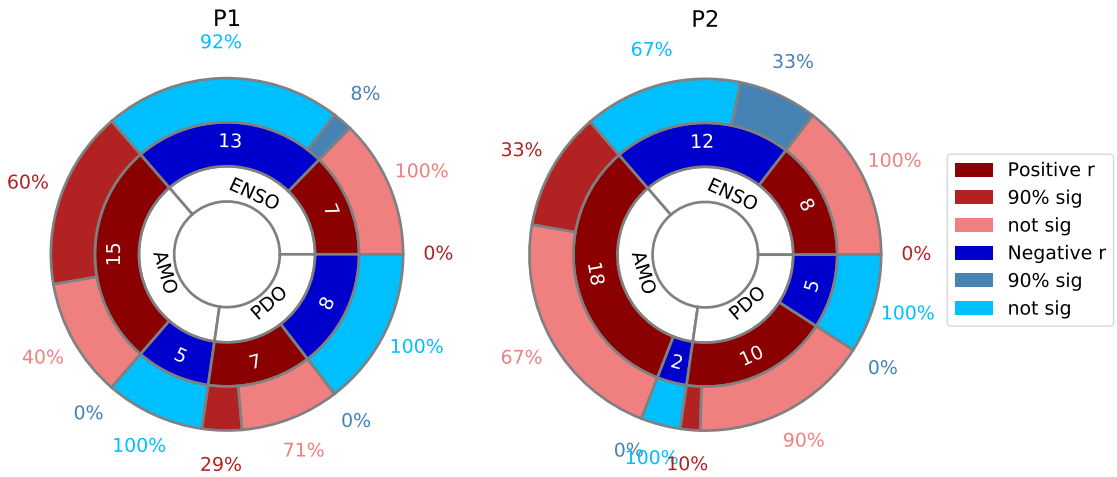

Figure 5.9: Summary statistics about the Pearson correlation coefficients between the NATL EOT time series for the 20 coupled model simulations and the May-November averaged ENSO, AMO and PDO indices during P1 and P2. Dark red (blue) colors indicate how many of the runs have positive (negative) correlations with each index, medium red (blue) indicate how many of the dark red (blue) correlations are significant at the 90% CL, while light red (blue) indicate how many are not significant.

(a) Below 15 $^{\circ}N$: No EOT1s are found

(b) between 15 and 30 $^{\circ}N$: 6 EOTs are found, 2 of which are not linked to any known patterns (fig. 5.8e), whilst 4 of them show only cold SSTs in the central equatorial Pacific (fig. 5.8f) accompanied by low VWS over the Caribbean and strong VWS in the central Pacific (not shown).

Generally, TC activity at the majority of EOT1s for both periods is positively correlated with the seasonally averaged AMO index and anticorrelated with ENSO as shown on figure 5.9. Specifically, during P1, for 15 of the experiments positive correlations are computed between the EOT1 time series and AMO, 9 of which are significant. This number increases to 18 during P2, 6 of which are significant. It is important to note that the majority of the significant correlations are seen for the higher-resolution (MM and above) runs. Similarly, during P1, 13 of the model runs are anticorrelated with ENSO, but only 1 of them is significant at the 90% CL. In contrast, during P2, 12 of the experiments show anticorrelations, 4 of which are significant. For PDO, during P1, EOT1s for 7 (8) of the runs are positively (negatively) anticorrelated with the index, but only 1 of the correlations is significant. During P2, however, 10 (5) are positively (negatively) correlated with the

index. One notable difference between the two periods is that the control experiments switch signs from one period to the other, i.e. the LL, HM and HH switch from positive to negative, and the MM switches from negative to positive correlations.

5.4 Eastern Pacific

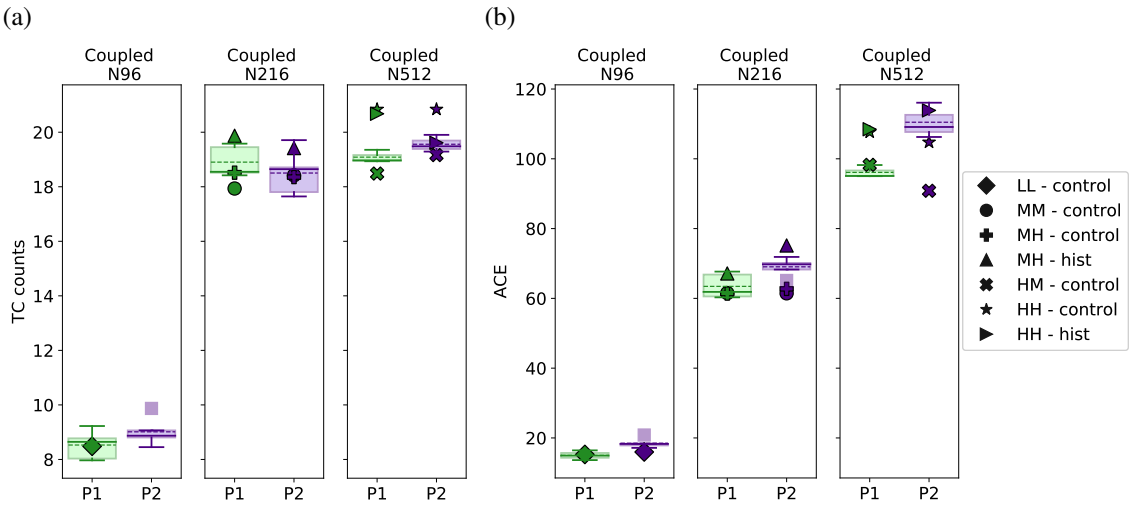

Figure 5.10: Annual average of TC counts (a) and of ACE (b) in EPAC for P1 (green) and P2 (purple). Column 1: ensemble of LL historic runs against the control run (⧫); Column 2: ensemble of MM historic runs against the MM control (●), MH control run (✚) and MH historic run (▲); Column 3: ensemble of HM historic runs against HM control run (✖), HH control run (★) and HH historic run (►). Faded squares (■) show outliers. Dotted lines show the ensemble means.

Annual averages of EPAC TC counts and ACE for P1 and P2 are presented in figure 5.10. For the atm-only runs there is a decrease in terms of TC counts for all resolutions and a decrease in terms of ACE, except for the N512 runs. For the coupled runs, the ensemble means are slightly higher in P2 for both ACE and TC counts. In terms of the runs indicated with markers, for TC frequency, decreases can be observed for the LL and MH control runs, as well as for the MH and HH historic runs. Increases can be seen for the MM, HM and HH control runs for the frequency of TCs, whereas the exact opposite is observed in terms of ACE.

Just as for the NATL, ENSO's influence on EPAC TC activity is greater in P2 compared to P1 as detected by the Pearson correlations, and the influence is more evident in terms of ACE rather than counts for both periods. More specifically, in P1 only 4 of the atm-only and 1 of the coupled runs display a significant relationship to ENSO in terms of counts, while for ACE the numbers correspond to 6 atm-only and 7 coupled runs. In contrast, during P2, ENSO's positive influence on TC activity in the basin is evident from the

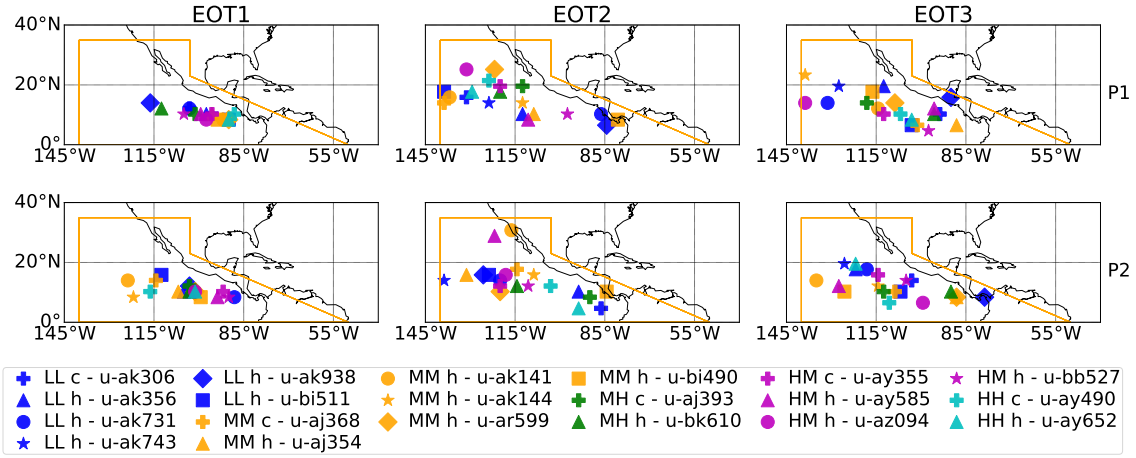

Figure 5.11: EOT locations for the coupled simulations on EPAC TC activity during P1 (top) and P2 (bottom). The different colors indicate the simulations of a given resolution, while the symbols differentiate the runs for each resolution. For each color, the first symbol indicates the control run, and the remaining symbols indicate the corresponding hist-1950 runs.

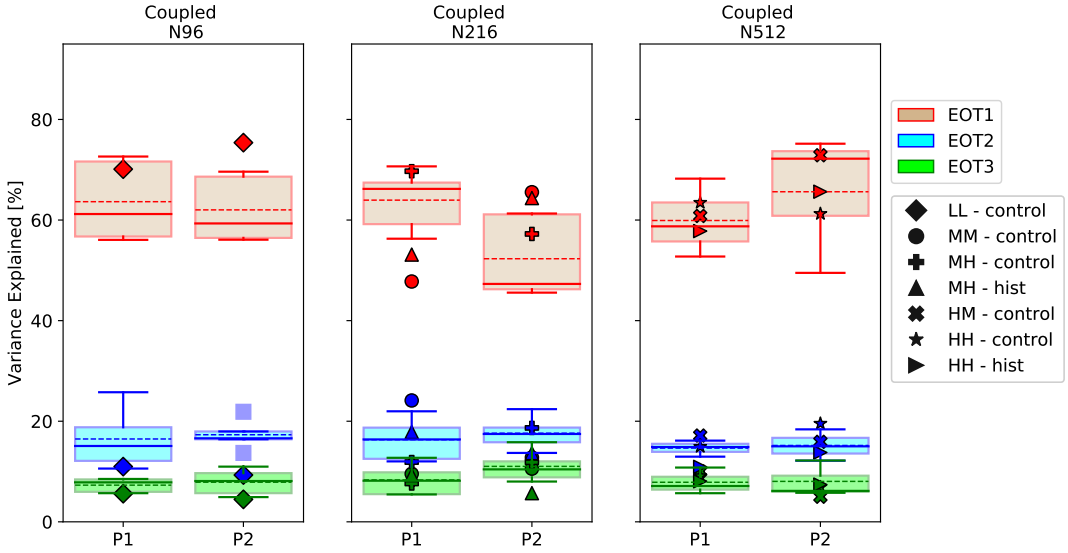

Figure 5.12: Amount of variance explained by EOTs during P1 and P2 for EPAC. Column 1: ensemble of LL historic runs against the control (♦); Column 2: ensemble of MM historic runs against the MM control (●), MH control (✚) and MH historic run (▲); Column 3: ensemble of HM historic runs against HM control (✖), HH control (★) and HH historic run (►). Faded squares (■) show outliers. Dotted lines show the ensemble means.

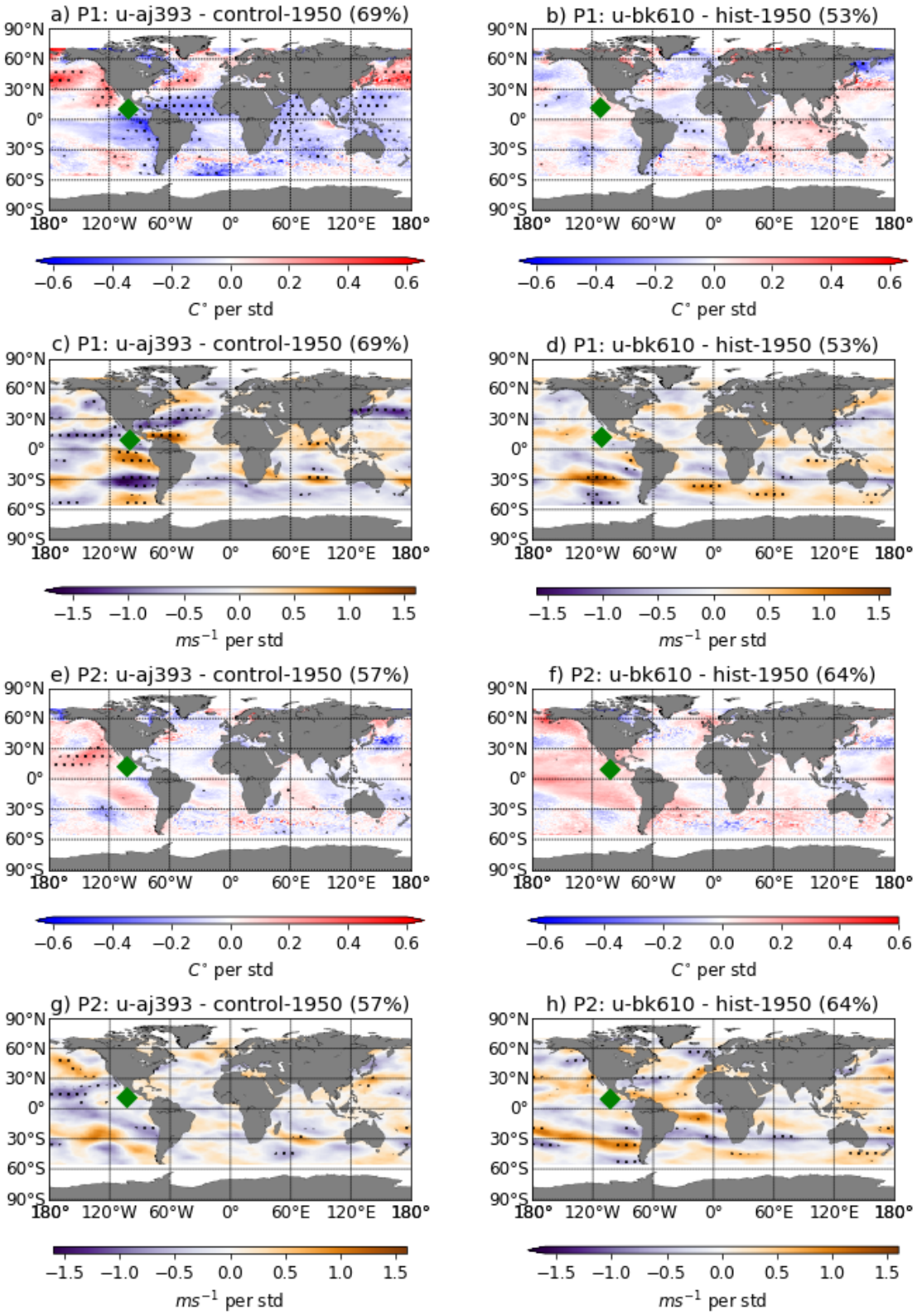

Figure 5.13: EOT1 SST and VWS regression maps for the MH control-1950 (left) and one hist-1950 (right) runs during P1 and P2 for EPAC. Plots in blue/red colours indicate the SST maps. Plots in purple/orange colours indicate the VWS maps. Location of EOT is indicated with a green marker. Significance at the 90% CL is indicated with dots.

correlations for all 6 higher-resolution atm-only and for 12 coupled runs in terms of ACE, in addition to 7 atm-only and 13 coupled runs in terms of frequency.

Similarly to ENSO, AMO has a stronger influence on TCs in the EPAC for both metrics in P2 and its influence can be particularly observed for the atm-only experiments. In detail, the AMO index is significantly moderately anticorrelated with 1 (2) atm-only run in terms of frequency (ACE) during P1, while it is significantly moderately or strongly anticorrelated with 7 atm-only runs for both metrics in P2. For the coupled runs, the index is significantly moderately anticorrelated with 5 (4) runs in terms of TC counts (ACE) during P1, but only with 4 runs for both metrics during P2.

PDO's influence on TC activity in at least 4 of the atm-only experiment is found for both periods examined, for both metrics from significant, moderate or strong correlations with the May-November averaged index. The index displays significant moderate anticorrelations with only 3 of the coupled runs for P1 and with only 1 coupled run for P1 in terms of TC counts. In terms of ACE, the PDO index appears to have a lesser significant influence during P2 on the atm-only runs.

The locations for the first three EOTs for the coupled runs are presented in figure 5.11. The different colors indicate the simulations of a given resolution, while the symbols differentiate the runs for each resolution. For each color, the first symbol indicates the control run, and the remaining symbols indicate the corresponding hist-1950 runs. The top row presents the results for P1 and the bottom row presents the results for P2. It can be seen that during P1 all N216 EOT1s are localised below $20°N$ and between 115 and 85 $°W$, whereas during P2 the majority of them move westwards. The same can be seen for EOT1 for the low-resolution experiments, however for the N512 the EOT1s remain clustered between 105 and 85 $°W$ and below $15°N$ with the exception of the HH control run which moves westwards during P2. This westward shift is associated with the spread of the maximum of the mean track density towards the west in the future period as seen from figure 5.2. All the EOT2 and EOT3 base points, irrespective of resolution, are spread out over the entire basin as seen in figure 5.11 and there is no robust conclusion about how their locations differ from one period to the other.

Figure 5.12 presents how the distribution of variance explained by the first three EOTs changes from P1 to P2. It can be seen that for the LL and MM experiments, the percentage of variance explained by EOT1 for the control runs increases from P1 to P2, whereas the

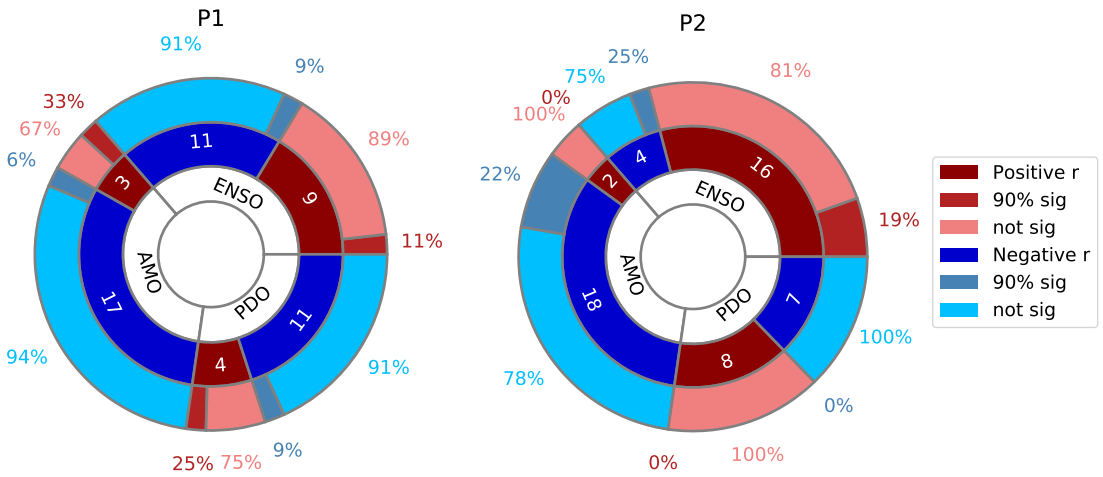

Figure 5.14: Summary statistics about the Pearson correlation coefficients between the EPAC EOT time series for the 20 coupled model simulations and the May-November averaged ENSO, AMO and PDO indices during P1 (left) and P2 (right). Dark red (blue) colors indicate how many of the runs have positive (negative) correlations with each index, medium red (blue) indicate how many of the dark red (blue) correlations are significant at the 90% CL, while light red (blue) indicate how many are not significant.

ensemble mean of the percentage reduces. In contrast, for the MH runs the amount of variance explained by the control run drops, while the corresponding percentage for the hist-1950 run increases. Moreover, for all the HM as well as the HH hist-1950 runs the amount of variance increases, whereas the percentage for the HH control run decreases. These differences, particularly the opposite changes between control and historic runs, albeit interesting, appear to be unrelated to the changes in the EOT1 positions from one period to the other. Lastly, the overall distribution of percentage between the first three EOTs for this basin is similar to the ones observed in chapters 3.4.2 and 4.3.

Examining SSTs and VWS for the control runs reveal that, during P1, EOT1 for 3 of the control runs are significantly (at the 90% CL) associated with cold SSTs in the equatorial Pacific as shown on figure 5.13a, while the remaining two (specifically the MM and HM) are linked to warm SSTs (not significant) in the same area (not shown). In addition, as can be seen on the same figure, in some of the control runs linked to cold Pacific SSTs, cold Atlantic SSTs appear to additionally influence TC activity (fig. 5.13a). Contributing to this, VWS in an AMM-resembling pattern (inverse of fig. 1.3), confined in the western part of the Atlantic can be seen (fig. 5.13c), while the eastern and central

tropical Pacific are characterised by low VWS. It is possible that TC activity at that specific location during P1 is more susceptible to conditions occurring in the Atlantic MDR and Gulf regions simply due to proximity. In contrast, during P2, activity for all EOTs for the control runs are associated with warm SSTs in the eastern and central Pacific and cool SSTs in the Atlantic. Significance for the Pacific SSTs is seen only for the MH control run (fig. 5.13e), which is additionally significantly associated with low VWS over the central Pacific (fig. 5.13g).

Results from the hist-1950 runs during both periods appear to not be of significance. The only conclusion that can be drawn from the results is that during P1 activity at the first base points is almost equally linked to warm and cool SSTs in the Pacific and simultaneously linked to mostly cool SSTs in the Atlantic as seen from figure 5.13b. The VWS appears to be not an important local driver as seen from figure 5.13d. In contrast to P1, during P2 a greater number of runs are found to be associated with warm Pacific SSTs, while the amount of runs associated with cool SSTs in the Atlantic remain relatively the same. Such conditions can be seen on figure 5.13f. This difference between the two periods might be one of the impacts of a warming climate.

Figure 5.14 presents summary statistics for the Pearson correlations between the EOT1 time series and the three seasonally averaged climate indices (ENSO, AMO and PDO) for EPAC TC activity during P1 and P2. Generally, it can be seen that activity associated with the EOT1 base points is anticorrelated with the AMO index during both periods with more than 17 of the runs, even though only a small portion of them are significant. In contrast to the stability observed for the Atlantic mode, ENSO has a greater, positive influence on TC activity during P2 compared to P1, since during P1 9 of the runs are positively correlated with EOT1, whereas this number increases to 16 during P2. This change can be particularly seen for the higher resolution runs and similarly to the AMO, only a small portion of the correlations are significant. The relationship with the decadal Pacific mode follows the relationship with ENSO, since the number of the models for which the EOT1s are correlated with the index increase. It is important to note, however, that during P2 there are no significant relationships with the PDO index.

5.5 Central Pacific

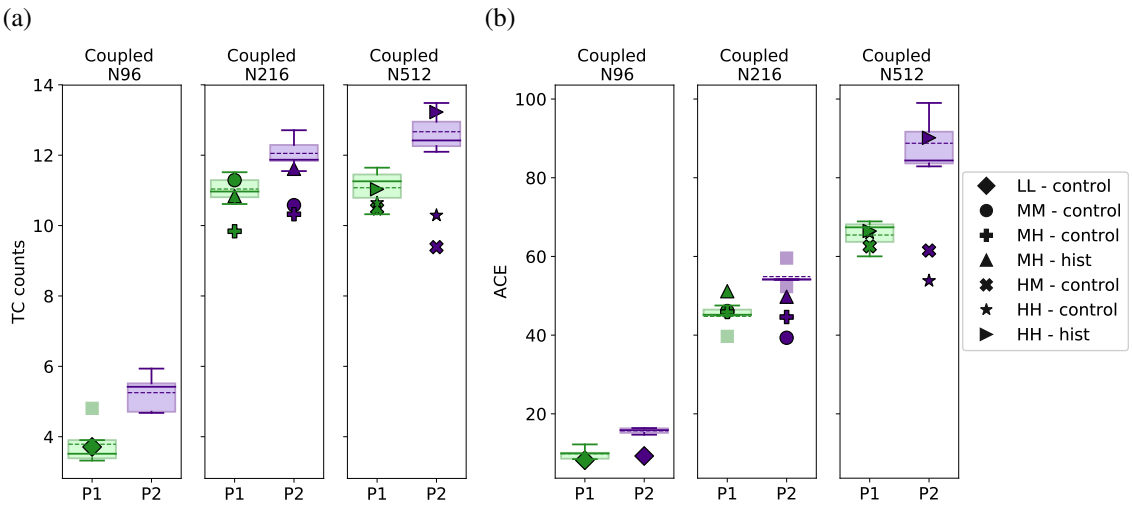

Figure 5.15: Annual average of TC counts (a) and of ACE (b) in CPAC for P1 (green) and P2 (purple). Column 1: ensemble of LL historic runs against the control run (♦); Column 2: ensemble of MM historic runs against the MM control (●), MH control run (✚) and MH historic run (▲); Column 3: ensemble of HM historic runs against HM control run (✖), HH control run (★) and HH historic run (►). Faded squares (■) show outliers. Dotted lines show the ensemble means.

Figure 5.15 presents how the annual mean of TC counts and ACE changes for the historic and future periods. Results show decreases in both the mean annual number of CPAC TC counts and ACE for atm-only runs, whereas increases are detected for both metrics for the ensembles of coupled hist-1950 runs. Furthermore, for both metrics the annual means of TC activity for the LL control and the HH hist-1950 run slightly increase in P2, whilst for the MM, HM and HH control runs they decrease. Lastly, even though the annual average frequency of the MH runs increases, the opposite is shown for the annual average of ACE.

The CPAC basin is the basin in which TC activity is mostly influenced by the ENSO index for both metrics (TC counts and ACE). TC activity in this basin is significantly positively influenced by ENSO. The key difference between the two periods examined is that for P1, only two atm-only LM and one atm-only MM experiments showed significant positive correlations with ENSO, while for P2 all the atm-only MM and HM runs displayed such relationships (not shown). For the coupled runs, however, the number of experiments

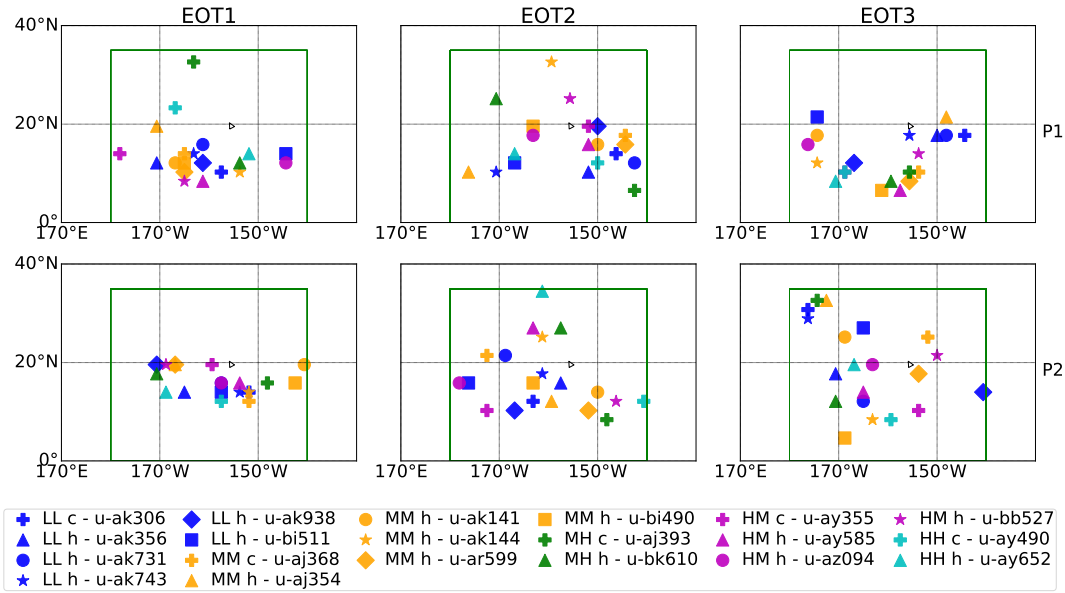

Figure 5.16: EOT locations for the coupled simulations on CPAC TC activity during P1 (top) and P2 (bottom). The different colors indicate the simulations of a given resolution, while the symbols differentiate the runs for each resolution. For each color, the first symbol indicates the control run, and the remaining symbols indicate the corresponding hist-1950 runs.

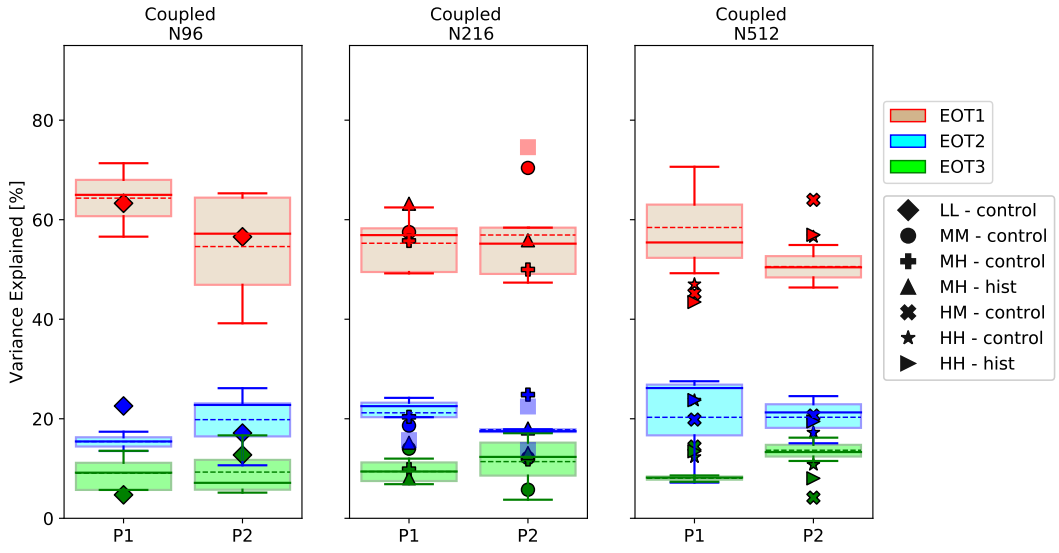

Figure 5.17: Amount of variance explained by EOTs during P1 and P2 for CPAC. Column 1: ensemble of LL historic runs against the control (♦); Column 2: ensemble of MM historic runs against the MM control (●), MH control (✚) and MH historic run (▲); Column 3: ensemble of HM historic runs against HM control (✖), HH control (★) and HH historic run (►). Faded squares (■) show outliers. Dotted lines show the ensemble means.

that are significantly influenced by ENSO reduce from 15 to 13 and from 17 to 13 in terms of counts and ACE, respectively.

In terms of the influence by the decadal modes, for the relationship with the AMO, there is a greater influence from the May-November averaged index during P2 compared to P1. For both metrics and and both periods, significant moderate or strong anticorrelations are found. For this basin, the number of significant correlations between the seasonal PDO index and the time series of TC counts increases for the atm-only runs, whereas in terms of ACE the increase is noticeable for the coupled runs as well. What is particularly noteworthy for this basin is that in both metrics and in both periods the vast majority of atm-only runs are positively correlated with the index, whilst most of the coupled runs are anticorrelated, indicating how the coupling of GCMs can impact how the coupled climate modes might influence TC activity.

The EOT analysis does not provide a clear understanding of how drivers of TC variability in this ocean basin change in a warming climate in the coupled simulations of HadGEM3-GC3.1. However, an attempt will be made to document the results. Figure 5.16 presents the locations for the first three EOTs for all the coupled runs. The different colors indicate the simulations of a given resolution, while the symbols differentiate the runs for each resolution. For each color, the first symbol indicates the control run, and the remaining symbols indicate the corresponding hist-1950 runs. The top row presents the results for P1 and the bottom row presents the results for P2. A general observation from the EOT1 base points of the coupled runs is that for both periods the base points are spread in the basin, except for the EOT1 for the high resolution runs. The N512 EOT1s during the future period concentrate below $20°N$ and between 170 and $150°W$.

Figure 5.17 presents the distribution of variance explained by the first three EOTs for the different coupled simulations. The drop in the mean variance explained by the ensemble of historic runs is consistent across atmospheric resolutions. The same occurs for the LL control and the two MH runs, whereas for the rest of the runs the amount of variance explained increases. In general, the overall distribution of variance during P1 and P2 is similar to the one seen in previous chapters for TC activity in the CPAC region.

Even though there are no particular differences between the drivers of TC activity during the two periods that can be observed systematically through the regression maps, figure 5.18 presents, as an example, SST and VWS regression maps for the MM control run

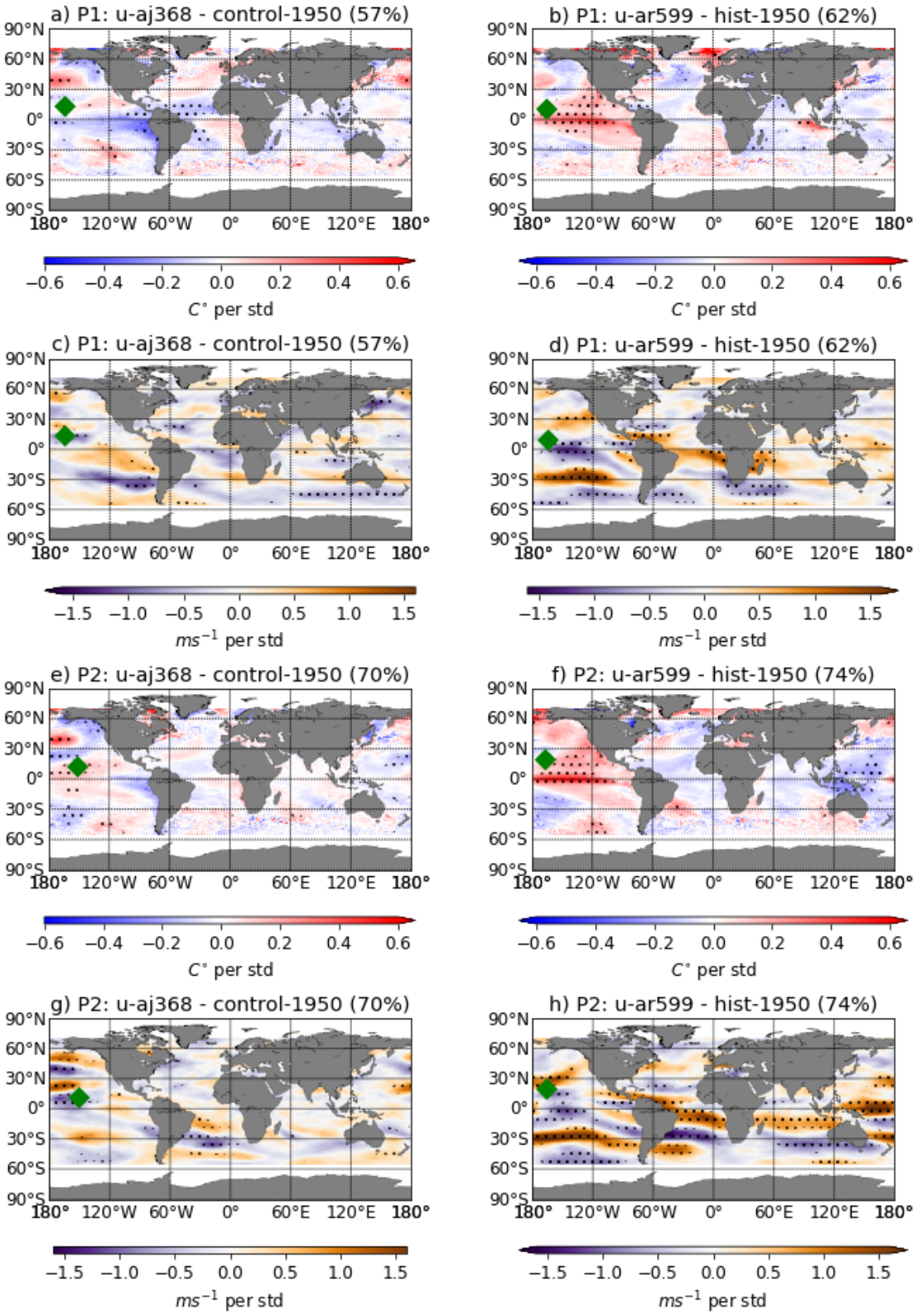

Figure 5.18: EOT1 SST and VWS regression maps for the MH control-1950 (left) and one hist-1950 (right) runs during P1 and P2 for CPAC. Plots in blue/red colours indicate the SST maps. Plots in purple/orange colours indicate the VWS maps. Location of EOT is indicated with a green marker. Significance at the 90% CL is indicated with dots.

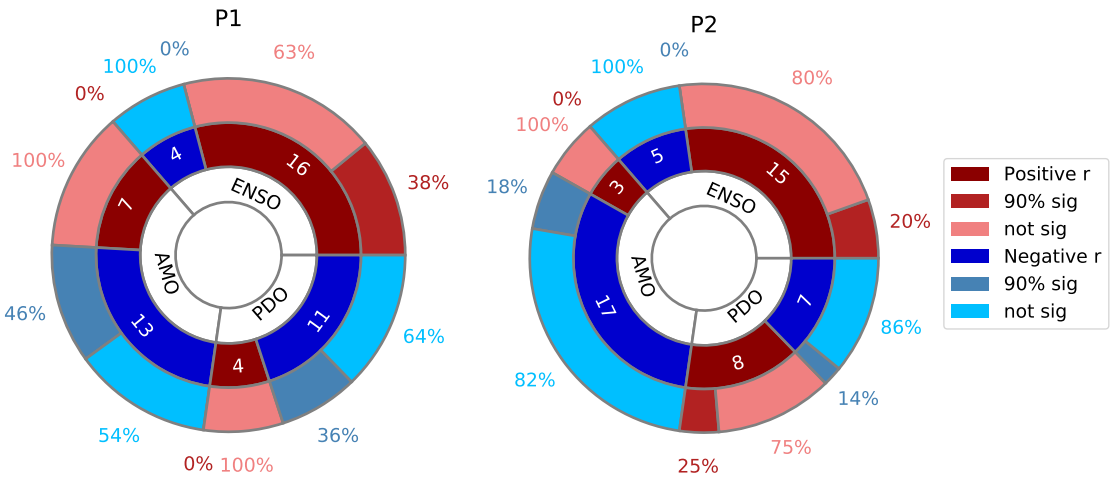

Figure 5.19: Summary statistics about the Pearson correlation coefficients between the CPAC EOT time series for the 20 coupled model simulations and the May-November averaged ENSO, AMO and PDO indices during P1 and P2. Dark red (blue) colors indicate how many of the runs have positive (negative) correlations with each index, medium red (blue) indicate how many of the dark red (blue) correlations are significant at the 90% CL, while light red (blue) indicate how many are not significant.

and one of the corresponding historic runs. No connection is found between the location of EOT1 and how they are influenced by the two drivers. The vast majority of runs during both periods are mainly linked to warm SSTs in the eastern and central Pacific and cool SSTs in the Atlantic region as shown on figures 5.18a, b, e and f. Where the influence by the SSTs is significant, further influence by VWS is observed, mainly described by low VWS over the equatorial Pacific and strong VWS over the Atlantic ITCZ, as shown on figures 5.18d, g and h.

Figure 5.19 displays the summary statistics for the Pearson correlations between the seasonally averaged climate indices and the EOT time series. In general, during P1, EOT1 is anticorrelated with the two decadal modes (AMO and PDO) and correlated with ENSO. Similar relationships can be been for AMO and ENSO during P2, but for PDO 4 of the model runs switch from negative to positive signs. Just as was observed for the two previous basins only a small amount of the correlations are significant at the 90% CL.

5.6 Western Pacific

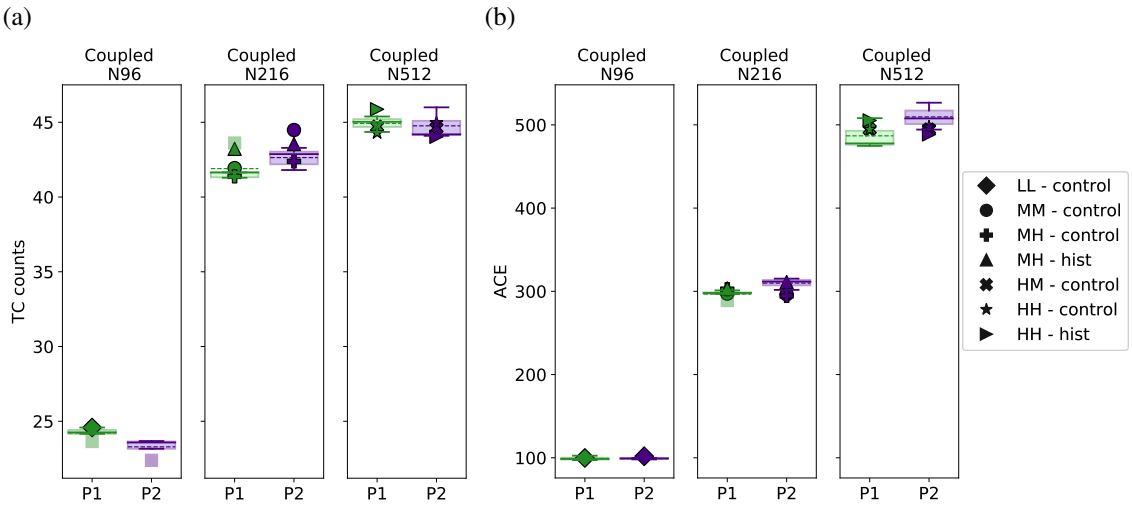

Figure 5.20: Annual average of TC counts (a) and of ACE (b) in WPAC for P1 (green) and P2 (purple). Column 1: ensemble of LL historic runs against the control run (♦); Column 2: ensemble of MM historic runs against the MM control (●), MH control run (✚) and MH historic run (▲); Column 3: ensemble of HM historic runs against HM control run (✖), HH control run (★) and HH historic run (►). Faded squares (■) show outliers. Dotted lines show the ensemble means.

The annual averages of TC counts and ACE in the coupled model simulations for WPAC for the two periods examined are displayed on figure 5.20. For the atm-only runs, the mean annual frequency and ACE decrease in a warming climate. For the coupled runs, a decrease in the LL ensemble mean annual frequency of TCs can be seen, whereas the mean annual ACE remains relatively the same. On the other hand, increases in the ensemble means for N216 for both metrics can be seen, as well as for the N512 ensemble mean for ACE, whereas a decrease in the N512 ensemble mean for TC counts is observed. For the simulations indicated by markers, the mean TC frequency increases for the MM and HH control runs as well as the MH hist-1950 run, whereas slight decreases are observed for the HM control and HH hist-1950 runs. In contrast, the annual mean ACE decreases for the MH control and the HH hist-1950, increases for the MH hist-1950 run and remains relatively the same for the MM, HM and HH control runs.

There is no robust influence from ENSO on the frequency of TCs in the WPAC region during P1, since from the 6 significant correlation coefficients found between ENSO and

the time series of counts, 4 of them describe a negative relationship with the index, while the remaining 2 describe a positive relationship. In terms of ACE however, all the LL coupled runs as well as half of the N216 coupled runs show a significant moderate positive relationship with the seasonal index. In P2, only 4 out of the 31 the correlations computed show a significant positive influence on the time series of counts from the seasonal ENSO index. In contrast, for ACE at least half of the runs, the majority of whom are atm-only, are significantly moderately or strongly correlated with the index.

Of the two decadal modes, the AMO exerts a greater influence on TC activity during P2 compared to P1, particularly for ACE as seen from significant anticorrelations between the time series (of TC counts and ACE) and the index. On the other hand, the May-November averaged PDO index appears to have a significant (weak or moderate) anticorrelation with 5 out of the 31 model simulations examined in terms of counts and with 3 out of 31 model simulations in terms of ACE during P2.

TC track densities appear to generally move towards the north/northwest during the future period as shown from the locations of regional maxima on figure 5.2, which are in agreement with other studies (Kossin et al., 2016, 2014; Roberts et al., 2020b). Following the EOT analysis results from the other two Pacific regions, it is nearly impossible to find a robust connection between the position of EOTs in the two periods examined, except perhaps for the N512 experiments. Figure 5.21 presents how the first three EOTs of the coupled model experiments are distributed in the basin. The different colors indicate the simulations of a given resolution, while the symbols differentiate the runs for each resolution. For each color, the first symbol indicates the control run, and the remaining symbols indicate the corresponding hist-1950 runs. The top row presents the results for P1 and the bottom row presents the results for P2. In contrast to what is shown by the mean track densities, the majority of the EOT1 base points move southeast during P2 with the exception of the HH control run, which moves outside of the tropics. For the rest of the EOTs, irrespective of the experiments' resolution, EOT2 base points are spread in the entire basin, while EOT3 base points move closer to the continent.

The overall distribution of variance explained by the first three EOTs is presented in figure 5.22 and follows a similar pattern to that in chapters 3.6.2 and 4.5 since there is generally small difference between EOT1 and EOT2. The LL control and ensemble mean percentage of variance explained is lower during P1. In contrast, the amount of variance

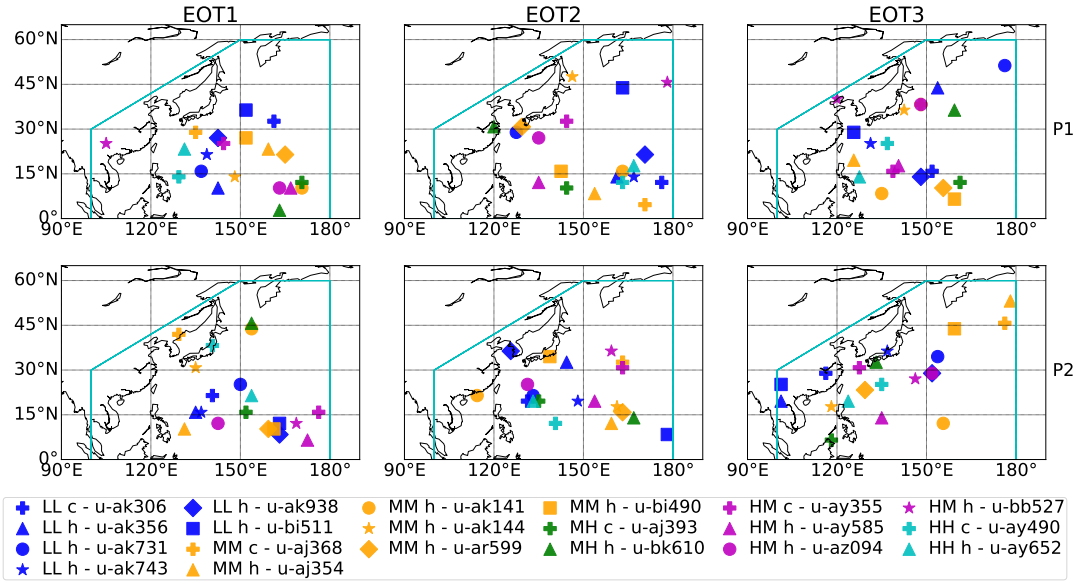

Figure 5.21: EOT locations for the coupled simulations on WPAC TC activity during P1 (top) and P2 (bottom). The different colors indicate the simulations of a given resolution, while the symbols differentiate the runs for each resolution. For each color, the first symbol indicates the control run, and the remaining symbols indicate the corresponding hist-1950 runs.

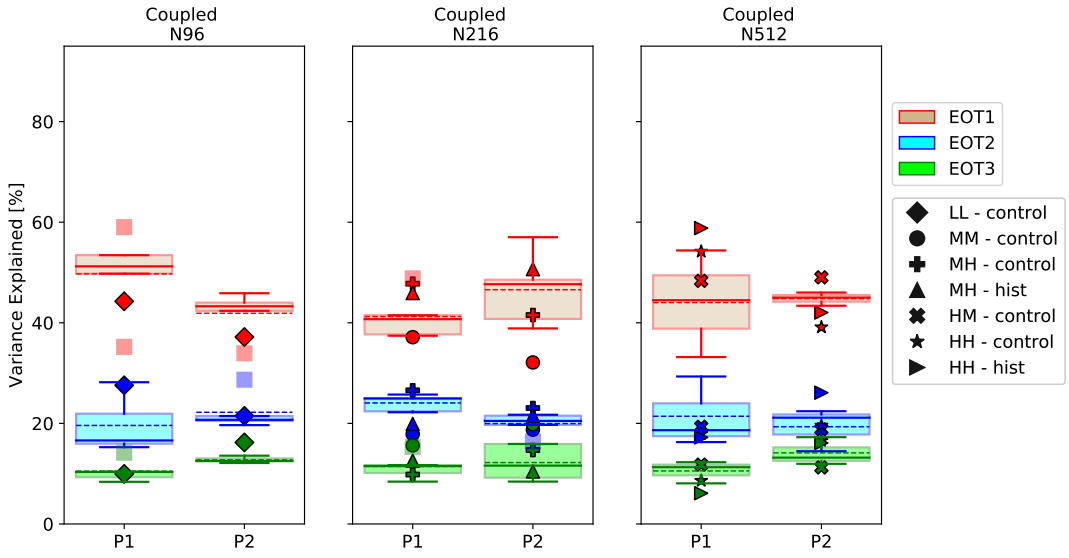

Figure 5.22: Amount of variance explained by EOTs during P1 and P2 for WPAC. Column 1: ensemble of LL historic runs against the control (♦); Column 2: ensemble of MM historic runs against the MM control (●), MH control (✚) and MH historic run (▲); Column 3: ensemble of HM historic runs against HM control (✖), HH control (★) and HH historic run (►). Faded squares (■) show outliers. Dotted lines show the ensemble means.

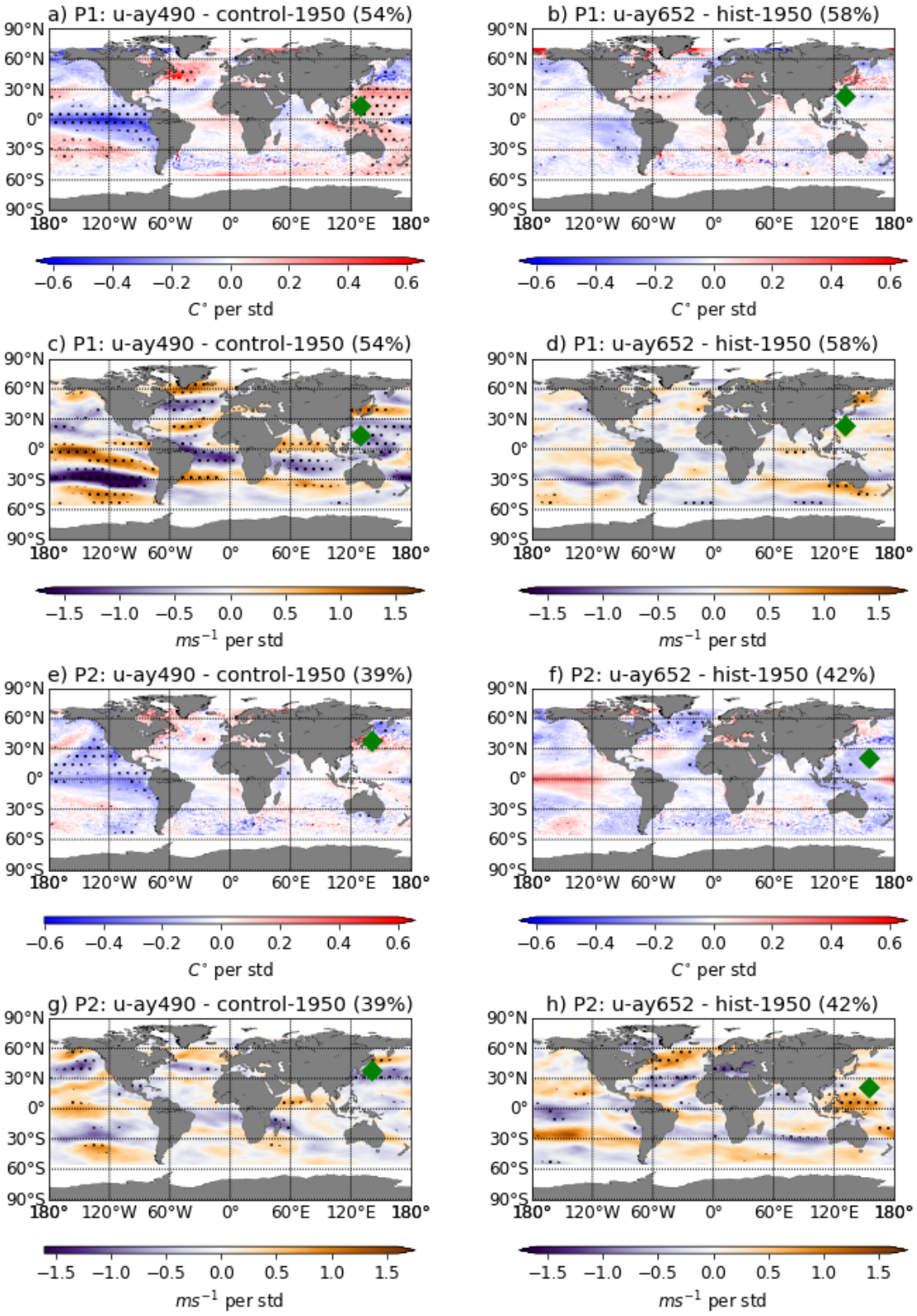

Figure 5.23: EOT1 SST and VWS regression maps for the HH control-1950 (left) and one hist-1950 (right) runs during P1 and P2 for WPAC. Plots in blue/red colours indicate the SST maps. Plots in purple/orange colours indicate the VWS maps. Location of EOT is indicated with a green marker. Significance at the 90% CL is indicated with dots.

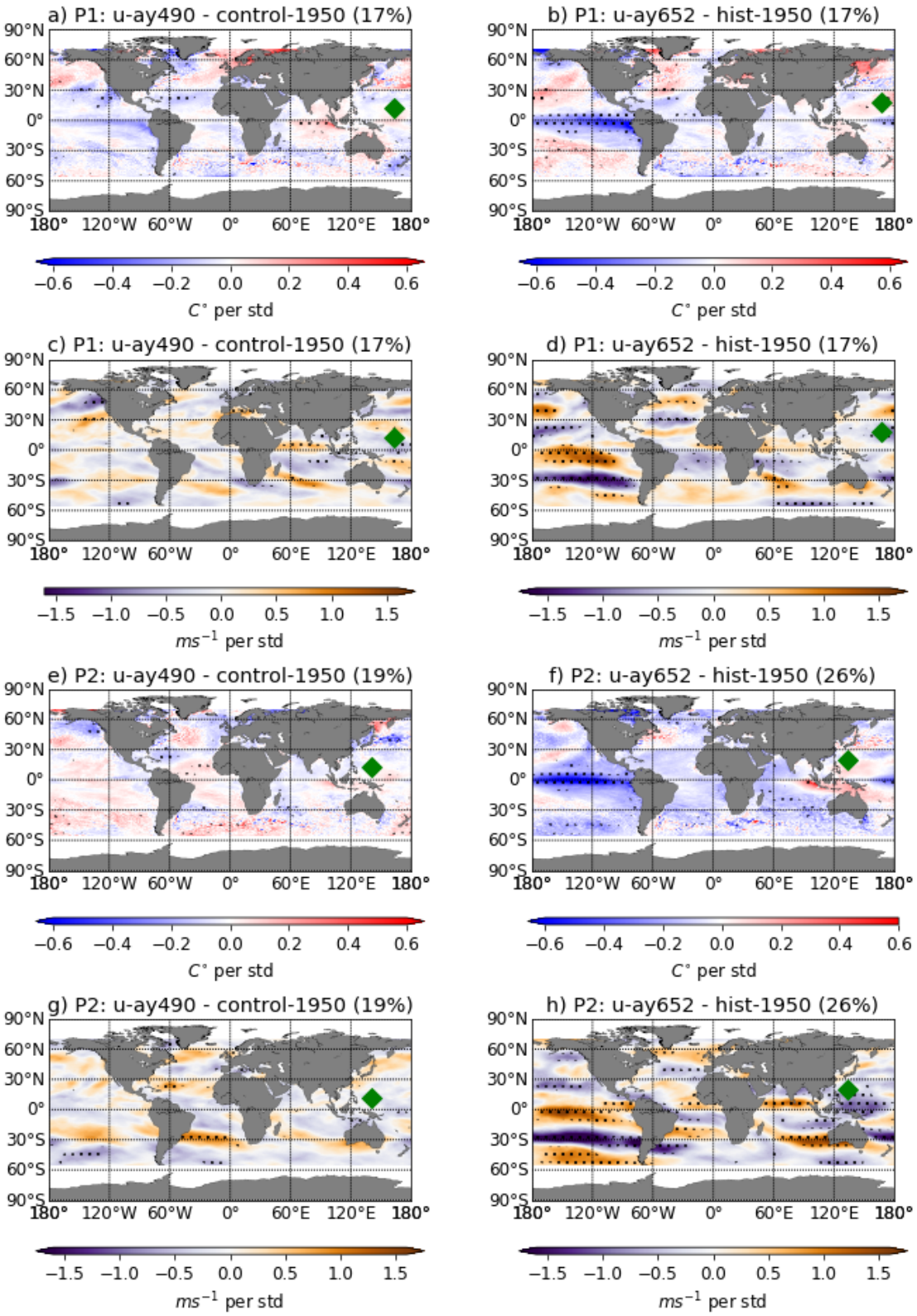

Figure 5.24: Same as fig. 5.23 but for EOT2

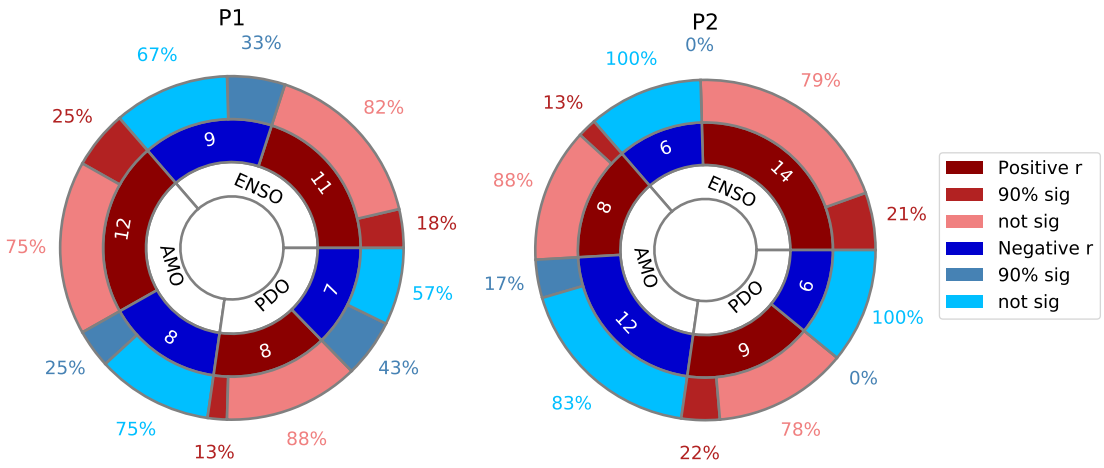

Figure 5.25: Summary statistics about the Pearson correlation coefficients between the WPAC EOT time series for the 20 coupled model simulations and the May-November averaged ENSO, AMO and PDO indices during P1 and P2. Dark red (blue) colors indicate how many of the runs have positive (negative) correlations with each index, medium red (blue) indicate how many of the dark red (blue) correlations are significant at the 90% CL, while light red (blue) indicate how many are not significant.

explained by the MM ensemble and the MH hist-1950 run shows an increase, whereas the percentages for the MM and MH control runs show a decrease. For the N512 experiments the ensemble mean remains the same, the amount of variance for the HM control run increases slightly and for the two HH runs it decreases.

The SST and VWS regression maps show that during P1, 3 of the EOT1 base points for the control runs that are positioned in the western part of the region are associated with warm (cold) SSTs in the west (equatorial eastern and central) Pacific as shown on figure 5.23a, as well as weak (strong) VWS over the same regions as displayed on figure 5.23c. For P2, no robust conclusion can be drawn from the SST regression maps, however, the EOT1 base points appear to be located in regions of weak VWS. In contrast, EOT1s for the different historic runs appear to be positioned in regions between warm and cool SSTs and strong and weak VWS as shown from figures 5.23b, f, d and h, respectively.

As indicated by the amount variance explained by the EOTs, for this basin it is important to investigate more EOT modes once the influence of EOT1 is removed. Figure 5.24 presents SST and VWS regression maps for EOT2 for the same runs as in 5.23. It appears that the conditions influencing the control run in EOT1 now influence EOT2 for the historic run. In addition, the conditions influencing EOT2 during P1 are similar to the

conditions influencing EOT2 during P2 considering that the latter is positioned near the continent. The conditions are described by significant cold La-Niña-resembling patterns in the eastern and central Pacific accompanied by strong VWS, causing TCs to form and develop further west. It is possible that the difference between the two periods for EOT2 indicates that in a warming climate, during La-Niña events, the variability of TCs will be further confined in the western part of the region.

The most striking observation from figure 5.25, which presents the summary statistics for the Pearson correlation coefficients between the EOTs and the ENSO, AMO and PDO indices, is the fact that very few significant relationships with the indices are found during both periods. Moreover, it appears that the number of correlations and anticorrelations with the AMO index reverse from one period to the other, whereas the relationships with ENSO and PDO remain relatively the same.

5.7 North Indian Ocean

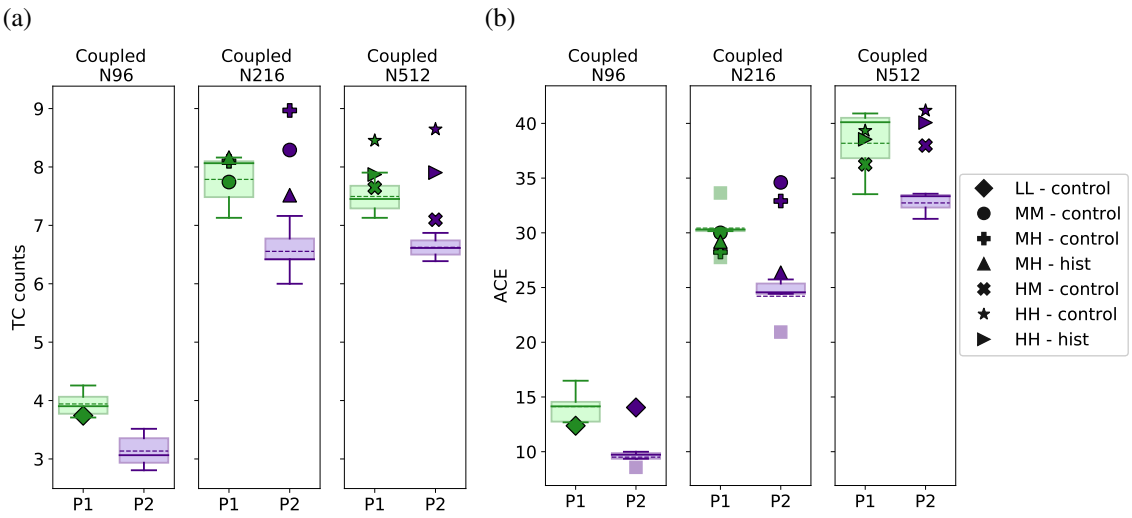

Figure 5.26: Annual average of TC counts (a) and of ACE (b) in NIND for P1 (green) and P2 (purple). Column 1: ensemble of LL historic runs against the control run (♦); Column 2: ensemble of MM historic runs against the MM control (●), MH control run (✚) and MH historic run (▲); Column 3: ensemble of HM historic runs against HM control run (✖), HH control run (★) and HH historic run (►). Faded squares (■) show outliers. Dotted lines show the ensemble means.

The ensemble means for annual number of TCs and ACE in the NIND region decrease in terms of the coupled runs (fig. 5.26) and the atm-only N96 runs. For the N216 atm-only runs the ensemble mean of annual frequency stays the same but the corresponding mean for ACE decreases, whereas for the N512 experiments the mean frequency drops and ACE increases. For the individual experiments, for both metrics, increases for the LL control, MM control, MH control, HH control and HH hist-1950 runs are observed from one period to the other. In contrast, the annual means for the MH hist-1950 run decrease, while the average number of yearly counts for the HH control run increases and ACE increases.

Even though no robust influence from ENSO is observed for TC activity in the NIND region, significant moderate anticorrelations are found for some of the coupled runs in both metrics and for both of the periods examined in this chapter. The differences between the two periods which were found for the other basins, are not observed for TC activity in this basin. Just like in the case of current climate, no robust conclusion can be formed about which climate modes, especially in a changing climate, can influence TC activity

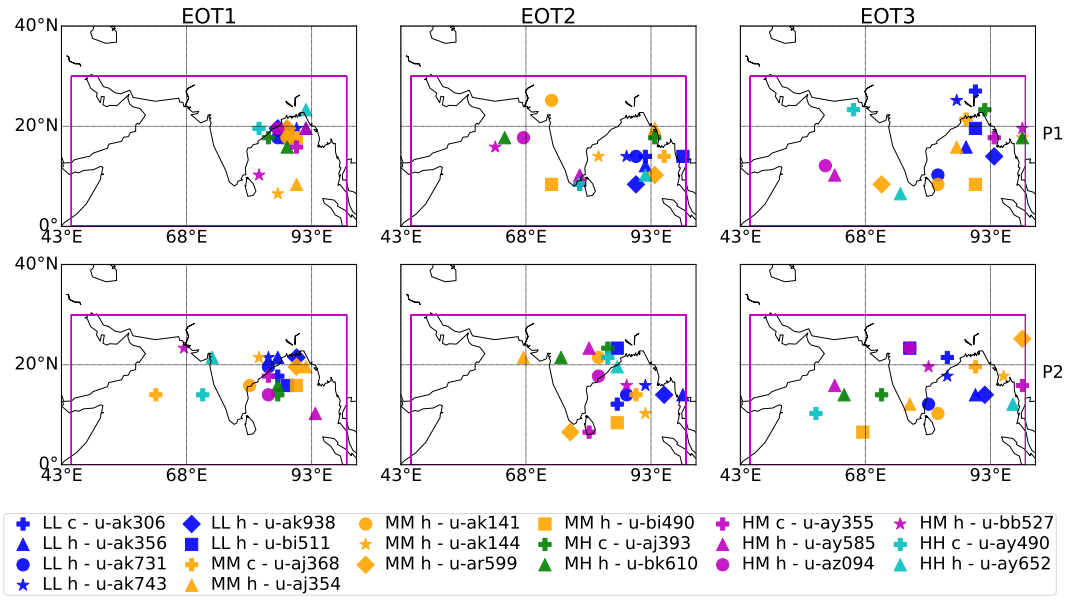

Figure 5.27: EOT locations for the coupled simulations on NIND TC activity during P1 (top) and P2 (bottom). The different colors indicate the simulations of a given resolution, while the symbols differentiate the runs for each resolution. For each color, the first symbol indicates the control run, and the remaining symbols indicate the corresponding hist-1950 runs.

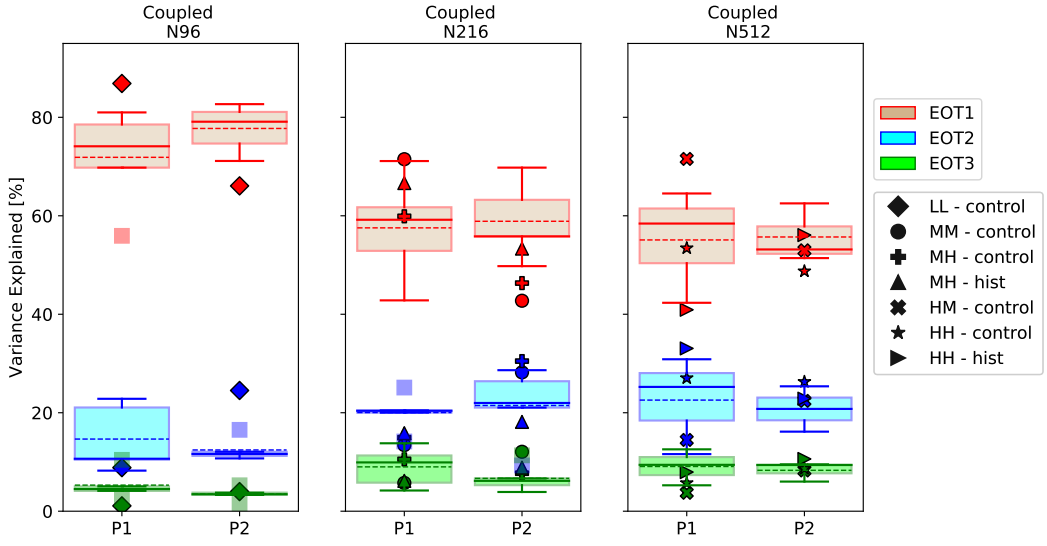

Figure 5.28: Amount of variance explained by EOTs during P1 and P2 for NIND. Column 1: ensemble of LL historic runs against the control (♦); Column 2: ensemble of MM historic runs against the MM control (●), MH control (✚) and MH historic run (▲); Column 3: ensemble of HM historic runs against HM control (✖), HH control (★) and HH historic run (►). Faded squares (■) show outliers. Dotted lines show the ensemble means.

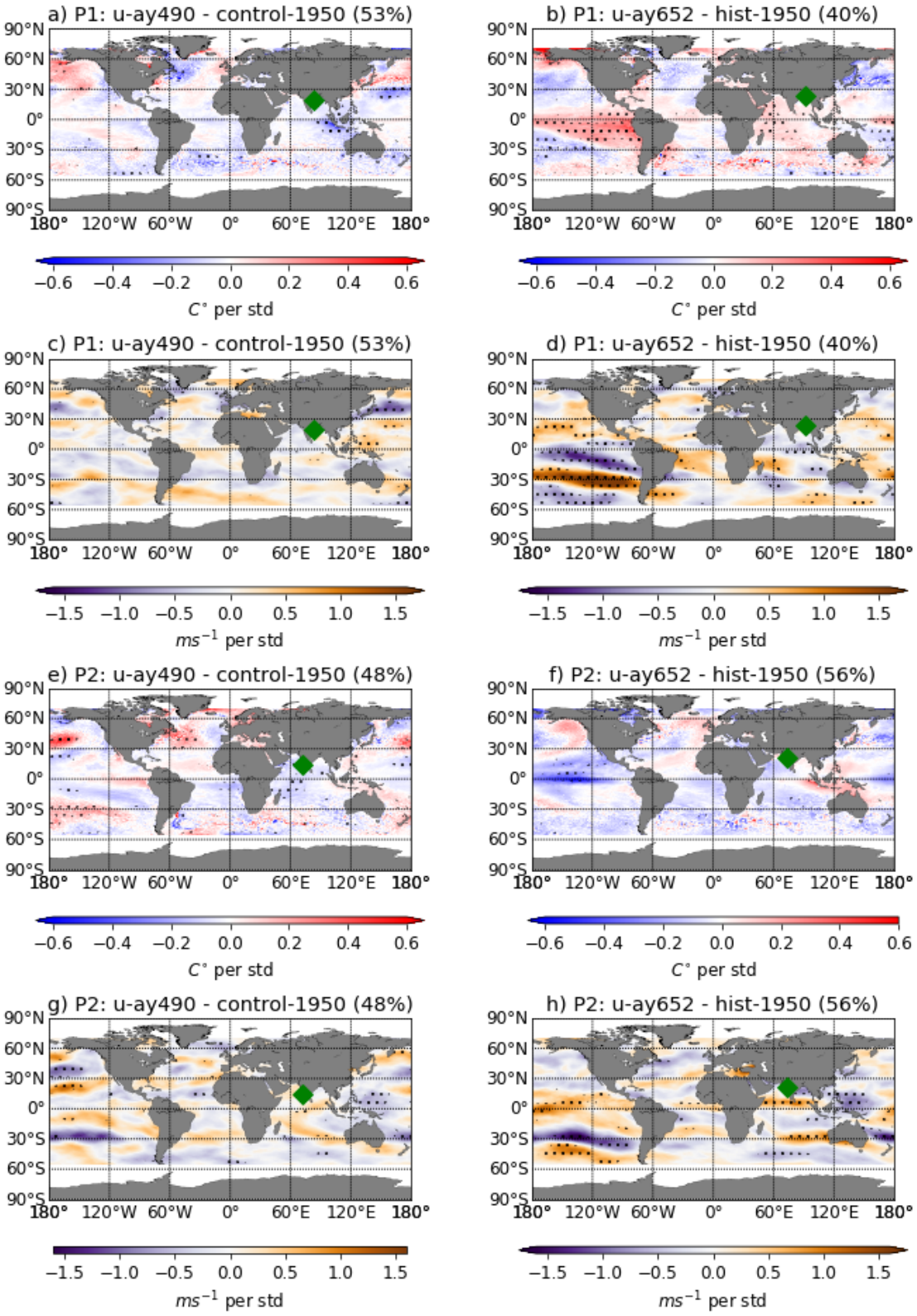

Figure 5.29: EOT1 SST and VWS regression maps for the HH control-1950 (left) and one hist-1950 (right) runs during P1 and P2 for NIND. Plots in blue/red colours indicate the SST maps. Plots in purple/orange colours indicate the VWS maps. Location of EOT is indicated with a green marker. Significance at the 90% CL is indicated with dots.

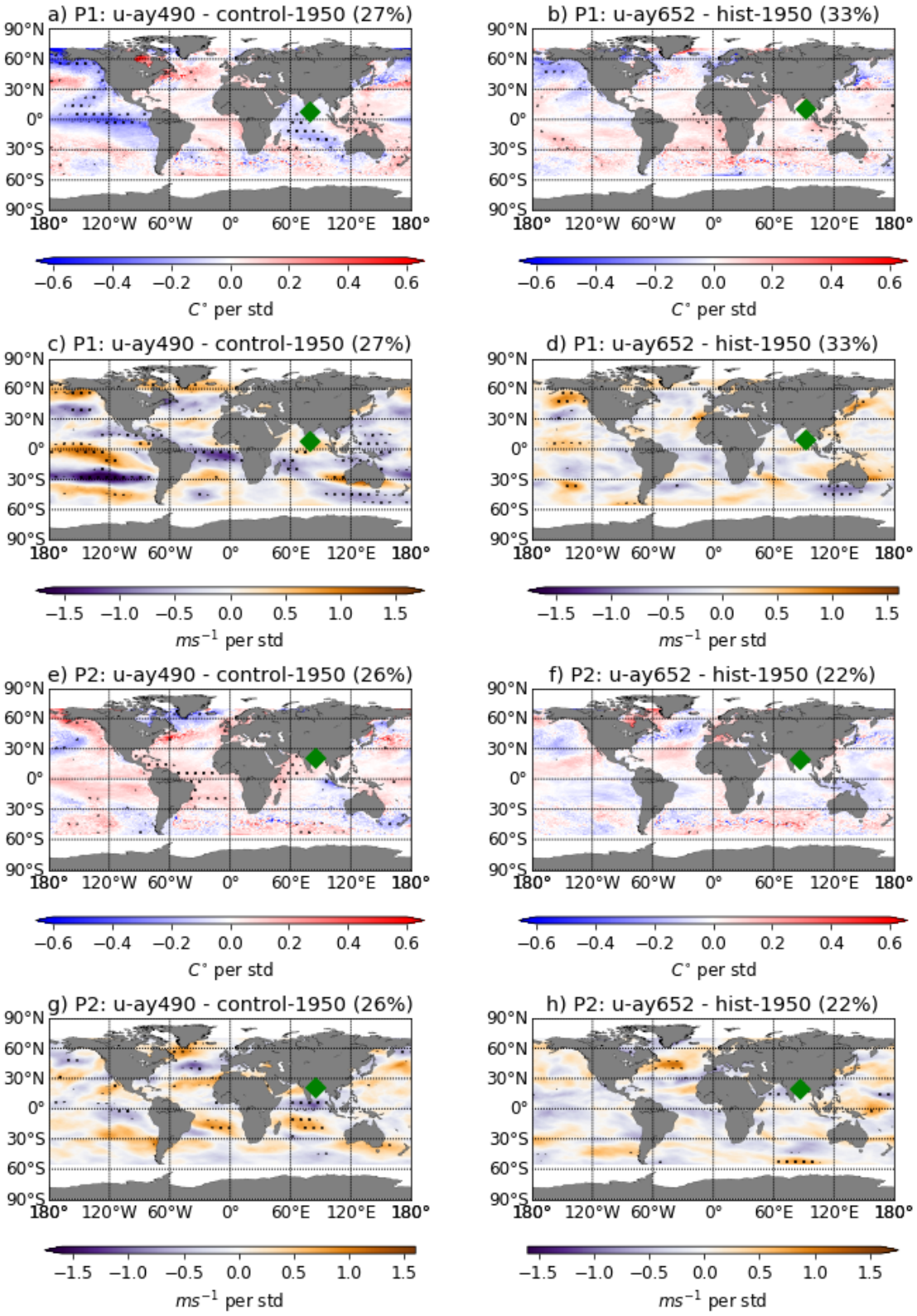

Figure 5.30: EOT2 SST and VWS regression maps for the HH control-1950 (left) and one hist-1950 (right) runs during P1 and P2 for NIND. Plots in blue/red colours indicate the SST maps. Plots in purple/orange colours indicate the VWS maps. Location of EOT is indicated with a green marker. Significance at the 90% CL is indicated with dots.

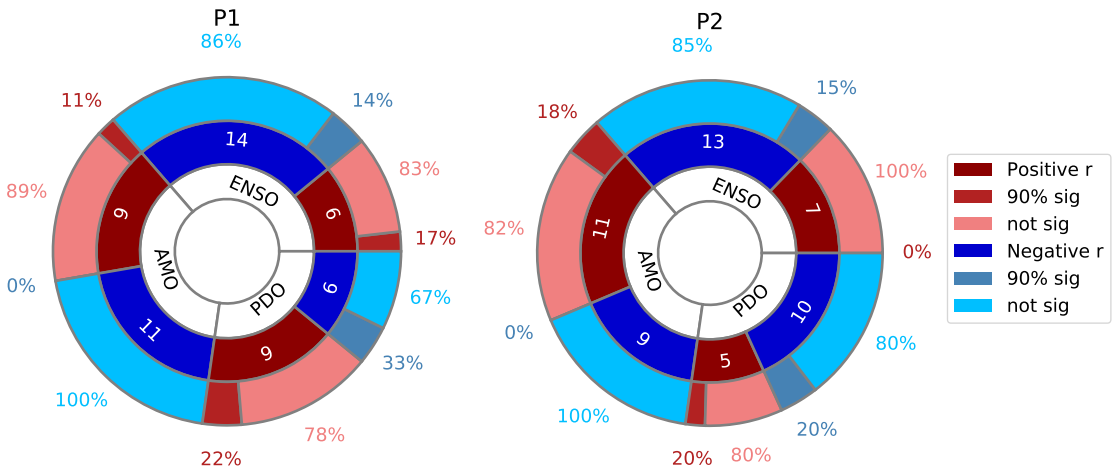

Figure 5.31: Summary statistics about the Pearson correlation coefficients between the NIND EOT time series for the 20 coupled model simulations and the May-November averaged ENSO, AMO and PDO indices during P1 and P2. Dark red (blue) colors indicate how many of the runs have positive (negative) correlations with each index, medium red (blue) indicate how many of the dark red (blue) correlations are significant at the 90% CL, while light red (blue) indicate how many are not significant.

in the this region. Even from the few significant relationships found from the Pearson correlation coefficients, there is no agreement on whether the AMO is positively or negatively anticorrelated with TC activity. For P1, there is no PDO influence observed for any of the atm-only experiments in both metrics, while there are contradictory significant correlations for some of the coupled simulations. For P2, two of the atm-only runs display significant positive correlations with the May-November averaged PDO index. For the coupled runs, only 2 of them display a significant, this time negative, correlation with the index.

Even though it appears that during P2, the control runs have more TCs in the Bay of Bengal than the historic runs, compared to P1 (fig. 5.2), results of EOT analysis appear to be inconclusive. Figure 5.27 presents the locations for the first three EOTs for all the coupled runs. The different colors indicate the simulations of a given resolution, while the symbols differentiate the runs for each resolution. For each color, the first symbol indicates the control run, and the remaining symbols indicate the corresponding hist-1950 runs. The top row presents the results for P1 and the bottom row presents the results for P2. For the N96 runs, all EOT1 base points are clustered very close in the Bay of Bengal during both periods examined. This result is expected since, according to the mean track

density above 2 TCs per season per unity area over the period examined, there are no track densities in the Arabian Sea (fig. 5.1c - 5.1f). For the N216 experiments, during P1 all the EOT1s are once again in the Bay of Bengal, but they are not as closely located as in the case of the N96 experiments. During P2, all EOT1s for the historic runs are clustered again in the Bay of Bengal, but EOT1 for the MM control run is located in the Arabian Sea (fig. 5.27). These results are linked back to the track densities, since in both periods, the majority of TCs are in the Bay of Bengal but, the mean track densities extend in the Arabian Sea (in contrast to the N96 runs), as seen on figures 5.1i - 5.1l. In addition, compared to the historic runs, it seems like the MM control run has more TCs in the Arabian Sea during P2 (fig. 5.1i -5.1k), which might explain why EOT1 for that particular run is not in the same location as the ones for the historic runs. For the N512 simulations, EOT1s during P1 are again in the eastern part of the NIND region, the majority of them being in the Bay of Bengal, as shown on figure 5.27. During P2, EOT1s are no longer collectively in the eastern part of the region, since for half of the simulations examined (specifically one HM historic run and the two HH runs), EOT1s are located in the Arabian Sea or near the west coast of India. During both periods, the HM historic runs show more TCs in the Arabian Sea than the corresponding control run (not shown). In addition, the HH control run has more TCs both in the Bay of Bengal and the Arabian Sea than the HM control run (not shown). Lastly, during P2 there are more TCs in both areas for both HH runs compared to P1 (fig. 5.2), which is perhaps the reason why more EOT1s are in the Arabian Sea during P2 compared to P1.

The overall distribution of variance explained by the first three EOTs as presented on figure 5.28, is similar to the ones shown in chapters 3.7.2 and 4.6. It can be seen that, irrespective of resolution, all the ensemble means of the amount variance explained by EOT1 increase during P2. In contrast, for all the individual runs shown with markers, except the HH hist-1950 (which is the one relocating in the Arabian Sea), the percentages of variance explained drop during P2.

Based on the differences between the SST and VWS regression maps for the control and historic runs during the two periods examined, no robust conclusion can be drawn about how a warming climate will impact TCs in the region. An example of this is shown on figures 5.29 and 5.30, which present the SST and VWS regression maps for the first two EOTs, respectively, for the HH control and corresponding historic run.

For the control run EOT1, which is located in the eastern part of India, is associated with cold SSTs in the northern subtropical Pacific in both periods (fig. 5.29a and e) accompanied by negative PDO-resembling VWS conditions (fig. 5.29 c and g). The regression patterns are the reverse of the patterns shown on figure 1.4. The only difference between the two periods is that EOT1 during P2 is located in the Arabian Sea and the significant regressions are largely in the central north Pacific, whereas during P1 the same conditions extended in the northwestern part of the basin. In contrast, EOT1 for the HH historic run during P1, is located over the continent above the Bay of Bengal and it is associated with significant warm equatorial and southern Pacific SSTs (fig. 5.29b) in the eastern and central Pacific, accompanied by weak VWS conditions over the same region (5.29d). During P2, EOT1 is located over the west coast of India near the Arabian Sea, and it is significantly linked to cold SSTs (fig. 5.29f) and strong VWS (fig. 5.29h) in the central equatorial Pacific.

For this region and for the two high-resolution runs, it is found that the EOT2s explain more than 20% of the variance once the influence from the first mode is removed, deeming it necessary to look at the conditions linked to the second modes. During P1, TC activity at EOT2 for the HH control run appears to be associated with cold equatorial SSTs in the eastern and central Pacific (fig. 5.30a), accompanied by strong VWS conditions over the same region (fig. 5.30c). During P2, however, EOT2 is significantly linked to warm SSTs in the Arabian Sea and to weak VWS in the tropical NIND region. For the HH historic run, EOT2 is not associated with any significant conditions (fig. 5.30b and f), whereas during P2, EOT2 is in relatively the same position as EOT1 during P1, but it does not appear to be related to any significant conditions either (fig. 5.30d and h).

This lack of robust conclusions can be further observed from the Pearson correlations coefficients between the EOTs and the climate indices. Only a handful of the coefficients are significant, and the number of correlations and anticorrelations with the AMO index reverse from P1 to P2. In addition, the overall anticorrelation with ENSO remains almost constant between the two periods, whereas the relationship with PDO reverses as seen from the summary statistics on figure 5.31.

5.8 Conclusion

In summary, the impact of climate change on the drivers of TC activity, particularly SSTs and VWS, is assessed by comparing the drivers between control and historic runs during the 1950-1980 period with those during the 2020-2050 period. Table 5.1 presents the main impacts of climate change on TC activity regarding changes in intensity, frequency or shifts the activity in the region. Information on any clear influence by the climate modes of variability or SST and VWS connection is also included.

Results for the NATL region show an overall increase in TC ACE, whereas they appear to be inconclusive about whether there is a north/northeast or south shift of TC activity in a warming climate. In addition, the influence of SSTs and VWS associated with climate modes on historic and future runs depends on the locations of EOT1 base points, with TC activity generally correlated with the decadal Atlantic mode and anticorrelated with ENSO. A westward shift in the future is found for TC activity in the EPAC region, but no robust conclusion is formed on which SST or VWS conditions are the main source of influence. In addition, an increase in the ensemble means of both ACE and frequency for the coupled runs has been found. For TC activity in the CPAC region, an increase in activity is found for the coupled simulations during the 2020-2050 period. Additionally, TC activity is found to be generally driven by warm SSTs in the central Pacific and cold SSTs in the Atlantic. For TC activity in the WPAC region, an increase in the ensemble mean of ACE for the coupled N216 and N512 experiments and a poleward shift of TC activity was found. However, results have been inconclusive regarding the dynamic and thermodynamic drivers of this basin's activity in a warming climate. Lastly, for the NIND region, results are inconclusive except for a decrease in the ensemble means of ACE and frequency for the coupled experiments.

Admittedly, a warming climate can lead to stronger TCs since warmer SSTs can provide more favourable conditions for TC formation as well as a greater source of energy useful for intensification. Investigating climate indices with a length of only 100 years limits our ability to examine how climate indices might be impacted by a warmer climate, and by extend how the corresponding climate modes might influence TC activity in the different basins. Studies such as the one by Freund et al. (2020), which investigates the impact of warming patters on El-Niño in CMIP5 and CMIP6 models, are essential in understanding these future changes.

Table 5.1: Summary of the main impacts of climate change on the different basins from the HadGEM3-GC3.1 simulations.

	NATL	EPAC	CPAC	WPAC	NIND
Changes in intensity or frequency	Increase in ACE	Increase in ACE and frequency ensemble means for coupled runs	Increase in activity	Increase in ACE ensemble means for coupled N216 and N512 runs	Decrease in ACE and frequency ensemble means for coupled runs
Shift in activity	North/northeast or southern shift	Westward shift	x	Poleward shift	x
Notes	Activity correlated with AMO and anticorrelated with ENSO	No robust conclusion on SST and VWS influence	Activity driven by warm central Pacific SSTs and cold Atlantic SSTs	No robust conclusion on SST and VWS influence	No robust conclusion on SST and VWS influence

Chapter 6

Development of a simple, open-source hurricane wind risk model for Bermuda with a sensitivity test on decadal variability

Abstract A hurricane-catastrophe model was developed for assessing risk associated with hurricane winds for Bermuda by combining observational knowledge with property value and exposure information. The sensitivity of hurricane wind risk to decadal variability of events was tested. The historical record of hurricanes passing within 185km of Bermuda was created using IBTrACS. A representative exposure dataset of property values was developed by obtaining recent governmental Annual Rental Value data, while Miller et al. (2013) provided a vulnerability relationship between increasing winds and damage. With a probabilistic approach, new events for 10,000 years were simulated for three different scenarios using (1) the complete record of annual TC counts; (2) two high-frequency periods and; (3) two low-frequency periods. Exceedance probability curves were constructed from event loss tables, focusing on aggregating annual losses from damaging events. Expected losses of low-frequency scenarios were less than losses of high-frequency scenarios or when the whole historical record was used. This framework suffers from uncertainties due to different assumptions, and biases within IBTrACS. Small data sizes limit our ability to conduct a formal model validation and results should be interpreted in this context. In the future, sensitivity tests on the different components of

the model will be performed.

6.1 Introduction

Tropical cyclones (TCs) belong to the category of weather systems which bring severe damage and destruction across many regions of the planet in respect to rain, winds and storm surge. Studies by McCarthy et al. (2015) and Goldenberg et al. (2001) have shown that TC activity around the globe undergoes important variability through the decades. Insurance and re-insurance companies can be particularly impacted by TCs, especially in countries that are more likely to see a TC making landfall.

Table 6.1 provides information about the ten costliest Atlantic hurricanes (Kishore et al., 2018; NOAA, 2020a; U.s. Bureau of Labor Statistics, n.d.). It can be seen that four of them occurred during the last Atlantic hurricane seasons (2017 and 2018) while nine of them occurred during the past twenty years. The columns indicate: name; year; maximum achieved intensity; total numbers of fatalities; total cost in billions of US dollars unadjusted for inflation; and adjusted total cost for 2017 in billions of US dollars. Deaths and damage costs refer to the total numbers of fatalities (direct and indirect) and damages across all the affected areas and countries. It should be highlighted that when thinking about damage and impact from a hazard, it is useful to use a metric of the affected area's wealth, for example the Gross Domestic Product (GDP). Hurricane Maria (2017) can be seen as a notable example: even though the total damage caused by the hurricane was around $91.6 bn, the impact on Dominica was way more significant than the impact on the United States. The damage after adjusting for inflation was 244% of Dominica's 2017 GDP. In addition, the uncertainty and large range of fatalities (particularly in Puerto Rico) caused by Hurricane Maria can be attributed to the fact that the assessment of deaths was difficult to perform and to that many people died because of delays (or inability) in receiving medical care (Kishore et al., 2018).

Insurance and re-insurance companies often use catastrophe models to quantify the risk associated with hurricanes. A catastrophe model is used for assessing financial impacts of catastrophes, for estimating physical damages of properties and assigning probabilities to the range of potential outcomes (RMS, 2020). There are three main components: hazard (in this case, information about tropical cyclones), exposure (information about

properties) and vulnerability (information about the damage a property can get). The goal of catastrophe modelling is to combine the three main components for the estimation of financial loss from hazards.

The aim of the study is to combine what is known from the historical hurricane record with information about property values, exposure and vulnerability in order to develop a hurricane catastrophe risk model to assess the risk for Bermuda. It is worth noting that the intent of this study is not to rigorously reproduce the methodology of traditional catastrophe model development used by insurers and re-insurers. However, we use the conceptual process as a guide to develop our hurricane wind risk model. Figure 6.1 presents time series of annual numbers of tropical cyclones. The red line indicates the time series for the whole North Atlantic basin, while the black bars present the number of storms that came within 185km (or 100nm) of Bermuda. The historical record of hurricanes is created by using the International Best-Track Archive for Climate Stewardship (IBTrACS) (Knapp et al., 2010). Recent Annual Rental Value (ARV) data, taken from the Bermuda Government (Land Valuation Department, 2019), are used for the development of a representative dataset of property values for each of the thirty-six electoral constituencies in Bermuda. Miller et al. (2013) have performed damage analysis for Hurricane Fabian (2003) that shows the estimation of damage functions incorporating effects of topography. The study concluded that when topographic effects are taken into consideration for the near-surface wind speeds, there is a correlation between increasing damage and elevation.

6.2 Methodology

6.2.1 Data

For the purposes of this study, IBTrACS was used for obtaining a historical record for storms that have impacted Bermuda. In addition, ARV data from the Bermuda Government, are used for developing a representative dataset of property values for each of the thirty-six electoral constituencies in Bermuda.

Table 6.1: Top 10 costliest Atlantic Hurricanes (as of 2019)

NAME	YEAR	Category	Deaths	Cost in bn	Cost 2017 in bn
Katrina	2005	5	1200	$125	$164.9
Harvey	2017	4	68	$125	$129.5
Maria	2017	5	estimates up to > 8500	$91.6	≥ $94.9
Irma	2017	5	47	$77.2	$66.5
Sandy	2012	3	233	$68.7	$76.3
Ike	2008	4	103	$38	$43.3
Wilma	2005	5	23	$27.4	$34.4
Andrew	1992	5	26	$27.3	$47.6
Ivan	2004	5	92	$26.1	$33.9
Michael	2018	5	74	$25.1	$25.1 (US)

6.2.1.1 Best-track Dataset (Observations)

IBTrACS is a combination of the best track data taken from different agencies such as the Regional Specialized Meteorological Centers (RSMCs), the Tropical Cyclone Warning Centers (TCWCs) as well as other national agencies. The IBTrACS-ALL (v03r03) dataset, which includes data taken from all agencies, is used for this study. Full details can be found in Knapp et al. (2010). Data are available since 1877 until 2018. The agencies provide information about the best estimated position of each storm in terms of longitude and latitude in addition to reporting wind speed and mean sea level pressure (MSLP) values. The different agencies use different wind-averaging periods and the values are reported in knots. For the North Atlantic data are derived from the Hurricane Databases (HURDAT2) and they are provided at 6-hour intervals. The wind speeds are 1-min sustained winds at 10m and they have been converted from knots to meters per second (multiplied by 1.94).

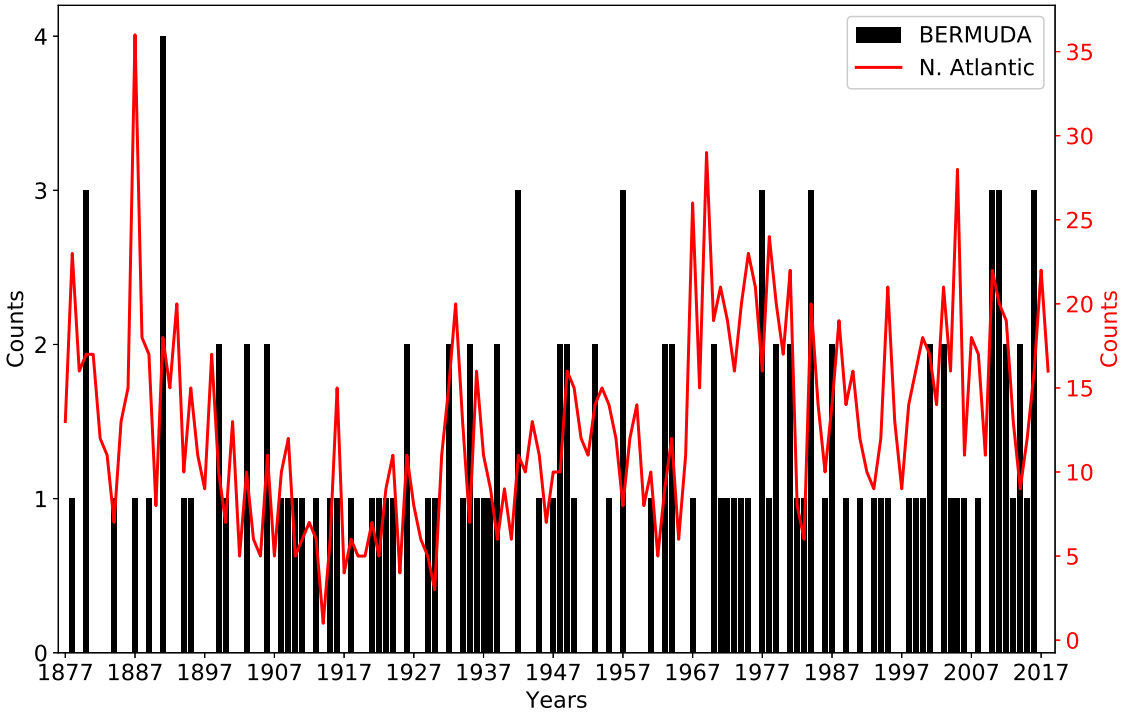

Figure 6.1: Time series of annual numbers of tropical cyclones. Red line shows the time series for the whole North Atlantic basin. The black bars show the time series of storms that came within 185km of Bermuda.

6.2.2 Exposure

6.2.2.1 Annual Rental Value Data

The Government of Bermuda's Land Valuation Department collects information about locations, types of property, size of living accommodation, size of any ancillary accommodation, amenities and characteristics (Land Valuation Department, 2019). They provide the Land Valuation List which includes location, type and annual rental value (ARV) data. The ARV data used in this study are from 2009, but accessed in 2019, since more recent data were unavailable. A few representative examples of the ARV data are shown in Table 2.1. In order to protect the householders' personal information, the addresses displayed on the table are anonymized. The annual rental value is converted to estimated actual property value (PV) by multiplying by a factor of 50.

In operational catastrophe models developed for re/insurance applications, building parameters such as construction type and number of stores are often used as second-order modifiers. In the case of the current analysis, secondary modifiers such as property type

and location are available in the ARV dataset, and could be used in future to refine and enhance this modelling framework.

Table 6.2: Examples for the ARV data.

2009 ARV	PV	Description	Address (not real)	Parish
$15.600	780.000	APARTMENT	5 HARRY STREET HM01	CITY OF HAMILTON
$21.600	1.080.000	SHOP	8 HARRY STREET HM01	CITY OF HAMILTON
$13.800	690.000	APARTMENT	2 RONALD ROAD HM38	DEVONSHIRE
$33.600	1.680.000	HOUSE	8 FRED LANE MA12	SANDYS
$40.800	2.040.000	HOUSE	11 FLER LANE GE14	ST. GEORGE'S

6.2.3 Bermuda's Historical Record of Hurricanes

The first step of the process was to obtain a historical record of hurricanes that have either made landfall or that have been in close proximity to Bermuda. Therefore, by using the complete record for IBTrACS (1877 - 2018), for every year, for every storm, every track point which came within 185km of Bermuda (32.39°N, 64.68°W) along with the wind speed information is kept for further analysis. The choice of 185km is based on the threat parameter used by the Bermuda Weather Service (BWS, 2020). The process is summarised on figure 6.2 (left). Figure 6.2 (right) presents all the points that were kept for further analysis. Bermuda is indicated with a black cross.

For each point that is kept, the distance from Bermuda is calculated by using the Haversine formula given by:

$$d = r * c \tag{6.1}$$

where $r = 6371km$ is the Earth's radius and c is given by:

$$c = 2 * \arctan(\frac{\sqrt{a}}{\sqrt{1-a}}) \tag{6.2}$$

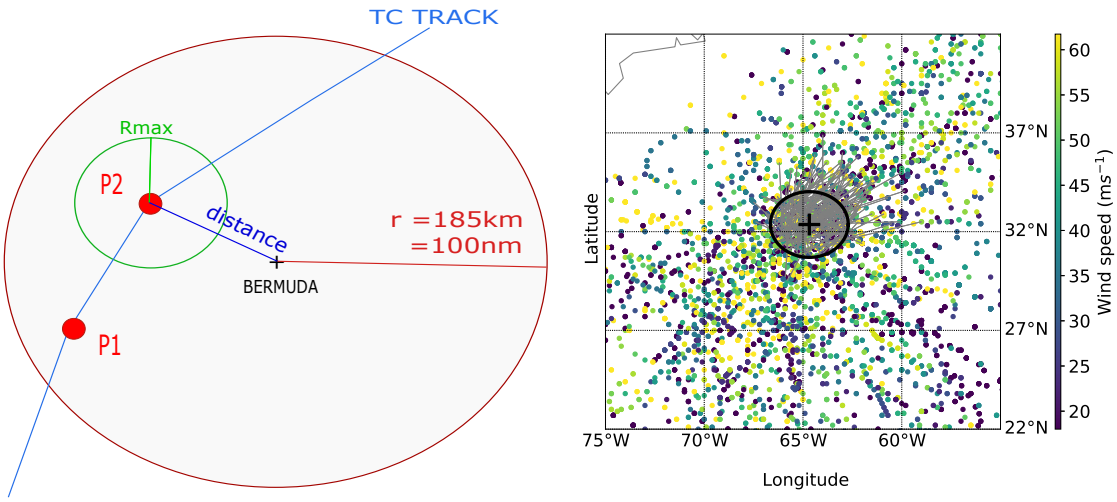

Figure 6.2: Left: Schematic of the methodology for creating the dataset of storms for Bermuda. Right: Tropical cyclones that passed within 185km from Bermuda (black cross).

where

$$a = \sin^2(\frac{\phi_2 - \phi_1}{2}) + \cos(\phi_1) * \cos(\phi_2) * \sin^2(\frac{\lambda_2 - \lambda_1}{2}) \tag{6.3}$$

with ϕ_1 and λ_1 the latitude and longitude coordinates of the storm track point in radians and ϕ_2 and λ_2 the latitude and longitude coordinates of Bermuda in radians. For each point, a radius of maximum wind (r_{max}) was chosen as followed:

$$r_{max} = \begin{cases} 200km, & v \leq 17ms^{-1} \\ 125km, & 18 \leq v \leq 32ms^{-1} \\ 95km, & 32 < v \leq 42ms^{-1} \\ 50km, & 42 < v \leq 49ms^{-1} \\ 30km, & 49 < v \leq 58ms^{-1} \\ 25km, & 58 < v \leq 70ms^{-1} \\ 20km, & v > 70ms^{-1} \end{cases} \tag{6.4}$$

where v is the intensity from IBTrACS. The values for r_{max} were chosen empirically based on a collection of data from H*WIND (NOAA, 2020b) which included tropical cyclones that affected Bermuda during the period 2006-2014. Then for each point that was saved,

the intensity of the storm at Bermuda is calculated by:

$$v_{BDA} = \begin{cases} v * \sqrt{\frac{r_{max}}{d}}, & d > r_{max} \\ v, & d \leq r_{max} \end{cases} \tag{6.5}$$

where d is given by the aforementioned Haversine formula. The first part of equation 6.5 is a variation of the Rankine Vortex (Holland et al., 2010). Afterwards, for each year, for each storm, the point with the highest estimated intensity at Bermuda is retained. Eventually, all the points of the highest estimated intensities for all the storms that passed within 185km of Bermuda are obtained. By sorting the data according to distance and fitting a logarithmic curve, a relationship between the distance of a storm from Bermuda and its estimated wind speed at Bermuda is obtained. The relationship is presented in figure 6.3 and it is described by:

$$f(x) = 63.1 - 8.05 * \ln(x), \tag{6.6}$$

where x is the distance (d) in km and $f(x)$ is the wind speed in ms^{-1}.

A very important component of a catastrophe model is the relationship between wind and damage. According to Sealy and Strobl (2017) the appropriate way to simulate the relationship is by varying the damage of the property with the cubic power of the wind speed. For the purposes of this study, a damage index, f, proposed by Emanuel (2011) is used for the calculation of the proportion of damage as a function of wind speed, V:

$$f = \frac{u_i^3}{1 + u_i^3} \tag{6.7}$$

where

$$u_i = \frac{MAX[(V_i - V_{thresh}), 0]}{V_{half} - V_{thresh}} \tag{6.8}$$

where V_i is the estimated wind speed at Bermuda (calculated by equation 6.6), V_{thresh} is the wind speed below which no damage occurs and V_{half} is the value of wind speed at which half of the property is damaged. Different studies (Elliott et al., 2015; Emanuel, 2011; Sealy and Strobl, 2017) have used a threshold of around $25.7ms^{-1}$ (50kts) for V_{thresh}, while for V_{half} different values were chosen based on the nature of each study. For this study, in order to choose appropriate thresholds, the data by Miller et al. (2013) were used. They found a threshold of approximately $37.5ms^{-1}$ for the occurrence of roof damage.

Therefore, by using $V_{thresh} = 37.5ms^{-1}$ and by varying V_{half} to best fit the Miller et al. (2013) data (see figure 6.4), it was found that at $V_{half} = 95ms^{-1}$ half of the property was damaged.

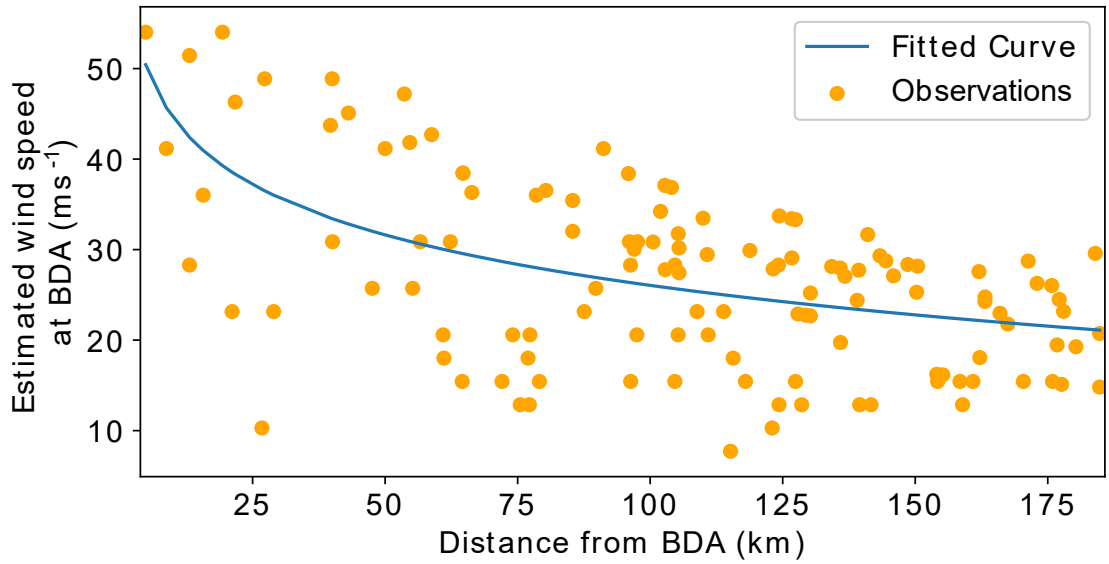

Figure 6.3: Plot of estimated wind speeds at Bermuda against the distance from Bermuda (orange line). The blue line indicates a fitted logarithmic curve.

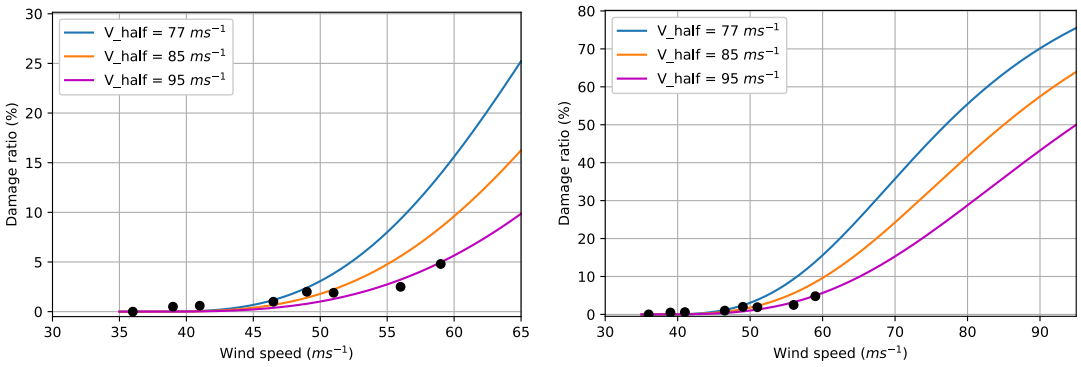

Figure 6.4: Relationship between damage and wind speed. Black dots indicate an estimate of the Miller et al. (2013) figure 12 data. Left: Fitting the data with the different damage index curves by varying V_{half}; Right: projection of the different curves that were fitted to the data.

6.2.4 Generating New Datasets

The next step of the study involved using the historical record of annual number of storms for Bermuda shown in figure 6.1 to generate new random events. In order to do that, the probability of a number of hurricanes occurring was calculated. Previous studies (Emanuel, 2011; Jagger et al., 2001; Klotzbach, 2010; Scherb et al., 2015; Sealy and Strobl, 2017) have suggested using the Poisson distribution since it provides a simple method for computing the probability of hurricane occurrence. The Poisson distribution is given by:

$$P(X = k) = \frac{\lambda^k}{k!} \exp -\lambda \tag{6.9}$$

where λ is taken as the average annual number of hurricanes ($\mu = 0.86$) for Bermuda from the historical record. Afterwards, random events (fig. 6.6) for the period of ten thousand years were generated from the Poisson distribution. To each event, a randomly generated number for distance (in km) between 0 and 185 was assigned. Then, by using equations 6, 7 and 8 a wind speed and a damage ratio value are calculated and assigned to each event. Eventually, by using the PV data, the potential loss for each event can be estimated and then the sum of all the losses in each year is calculated. The process of generating the new datasets is summarized in figure 6.5.

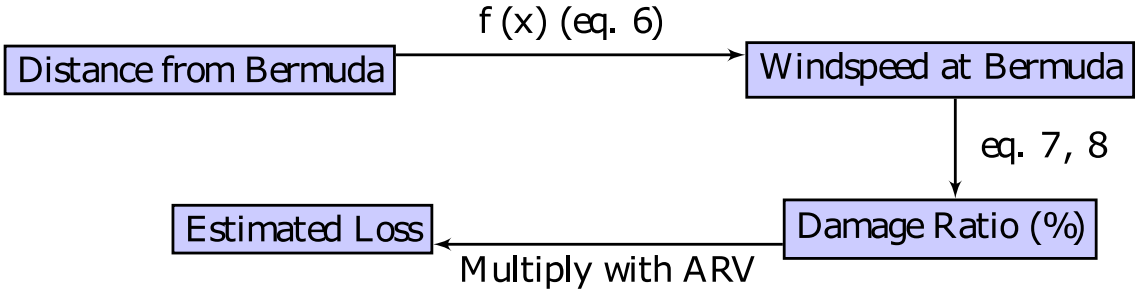

Figure 6.5: Schematic of the process of generating the new datasets

6.2.5 Incorporating Decadal Variability

Numerous studies have shown that on decadal time scales TC activity in the North Atlantic can be influenced by the Atlantic Multidecadal Oscillation (AMO) through variations of sea surface temperatures (Goldenberg et al., 2001; Hallam et al., 2021; Mann et al., 2021; McCarthy et al., 2015; Murakami et al., 2020; Ting et al., 2019). The associated warm

and cold phases of the AMO can last for 20-40 years and they can lead, either directly or via modulation of other modes, such as the El-Niño Southern Oscillation (ENSO), to more or less active hurricane seasons (Klotzbach and Gray, 2008; Knight, 2005; Zhang and Delworth, 2006). Therefore, the final step of the study was to test the model for different climate scenarios. In order to do that, different time periods with either increased or decreased TC activity within the time series were examined. The different periods were chosen based on the following steps:

1. Find the mean (μ_{all}) of the time series for the annual number of tropical storms in Bermuda.

2. Calculate the 10-year moving average of the time series (centred–red solid line in figure 6.7).

3. Find the mean of the 10-year moving average (μ_{10} – red dashed line in figure 6.7).

4. For high-frequency phases, take at least 10 consecutive years for which the 10-year moving average is greater than μ_{10}. Two high frequency phases were found: 1973-1989 and 1999-2014.

5. For low-frequency phases, take at least 10 consecutive years for which the 10-year moving average is less or equal than μ_{10}. Two low-frequency phases were found: 1882-1895 and 1897-1930.

Then, for each phase, by using the mean of the phase, new events were randomly generated by following the process outlined in section 6.2.4.

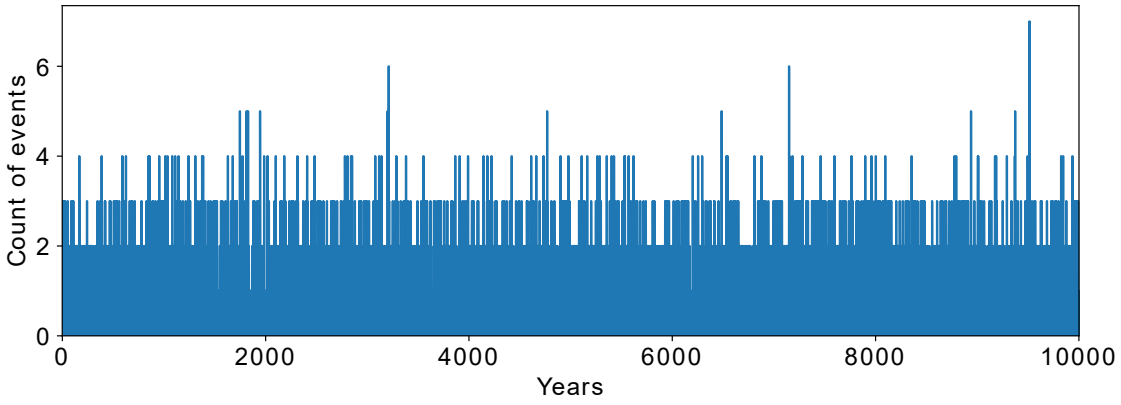

Figure 6.6: Time series of simulated events for 10000 years.

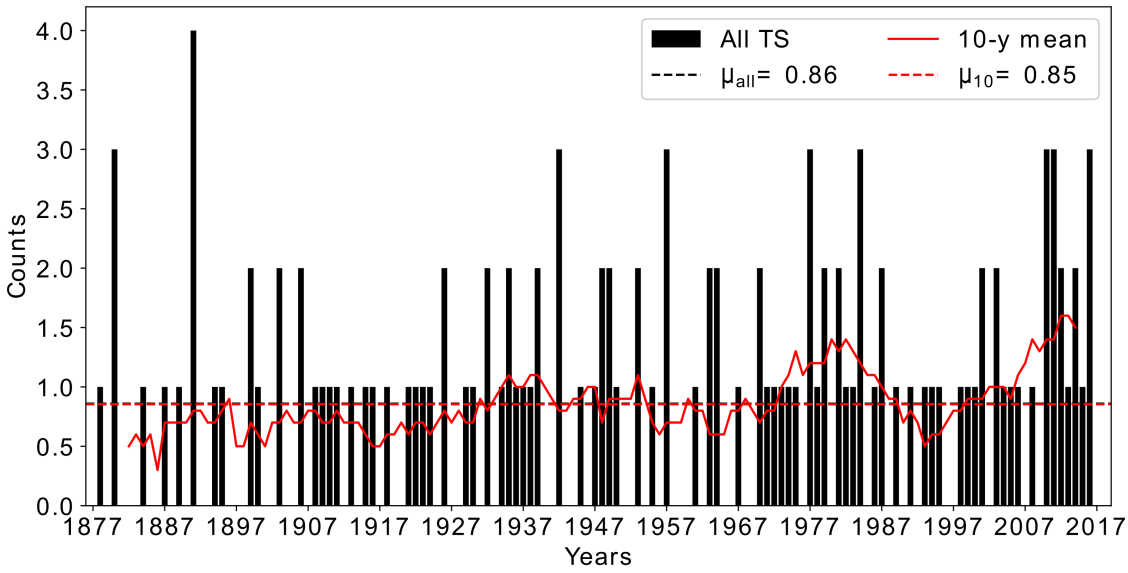

Figure 6.7: Time series for Bermuda (black bars). The 10-year moving average is shown with the red solid line and its mean is shown with the dashed red line.

6.3 Results

The output of a catastrophe model is the loss amount from a catastrophic peril. This is given in the form of an Event Loss Table – the format and a data sample is shown in Table 6.3. By looking at the time series of simulated events on figure 6.6, the maximum number of events in a single year in that scenario is seven individual events. Therefore, for Table 6.3 column 1 corresponds to the year number, columns 2 to 8, correspond to the losses from the individual events and column 9 corresponds to the amount of loss in a year (the sum of losses from the individual events). It can be seen that there were years with no events (e.g. year 7), years with a single non-damaging event (e.g. year 1), years with a single damaging event (e.g. year 0), years with multiple non-damaging events (e.g. year 4), years with multiple damaging events (e.g. year 8) and years with both damaging and non-damaging events (e.g. year 3). From this tabulated output one can construct an Exceedance Probability (EP) curve. The EP curve describes the annual probability that an amount of loss will be exceeded. For constructing the EP curves we focus on aggregating annual losses. If a more granular analysis were needed, effort would have been made to establish a specific identifier for each event. However, it is worth noting here that the model output has been constructed from an Aggregate Exceedance Probability (AEP) perspective, and neglects further analysis of individual contributions to the annual losses

Table 6.3: Example Event Loss Table

Year	Event1	Event2	Event3	Event4	Event5	Event6	Event7	Sum
0	14512670	-	-	-	-	-	-	14512670
1	0	-	-	-	-	-	-	0
2	0	0	-	-	-	-	-	0
3	0	0	0	10238454	-	-	-	10238454
4	0	0	0	0	-	-	-	0
5	45319873	-	-	-	-	-	-	45319873
6	0	8749651	45319873	-	-	-	-	54069523
7	-	-	-	-	-	-	-	0
8	13099546	14512670	-	-	-	-	-	27612216
9	16005999	0	-	-	-	-	-	16005999
10	0	10238454	-	-	-	-	-	10238454

(Occurrence Exceedance Probability (OEP)). A future refinement would be to assess the variability of loss events on an annual basis via an OEP analysis.

Figure 6.8 presents the Cumulative Distribution Function (CDF) of expected losses on all properties in all parishes of Bermuda when the whole time series of annual counts of tropical storms for Bermuda is used for simulating new events. The histogram (empirical results) indicates the actual losses from events that were intense enough to cause damage, meaning events that had an estimated wind speed at Bermuda greater than $37.5ms^{-1}$ (based on Miller et al. (2013)). The black dashed line indicates the theoretical CDF, meaning what one would expect to observe if there was an infinite amount of damaging events. Non-damaging events were excluded from the analysis, but we present all the model output. For example, by looking at the histogram from the empirical results, there is a 21.9% chance that during a year with at least one damaging event, losses will exceed $1bn.

Examination of the decadal variability of TCs revealed two high-frequency and two low-frequency phases. High-phases A and B correspond to the periods 1973-1989 (with mean μ=1.18) and 1999-2014 (with mean μ=1.31), respectively, during which the 10-year moving average was greater than the mean of the 10-year moving average. Low-phases

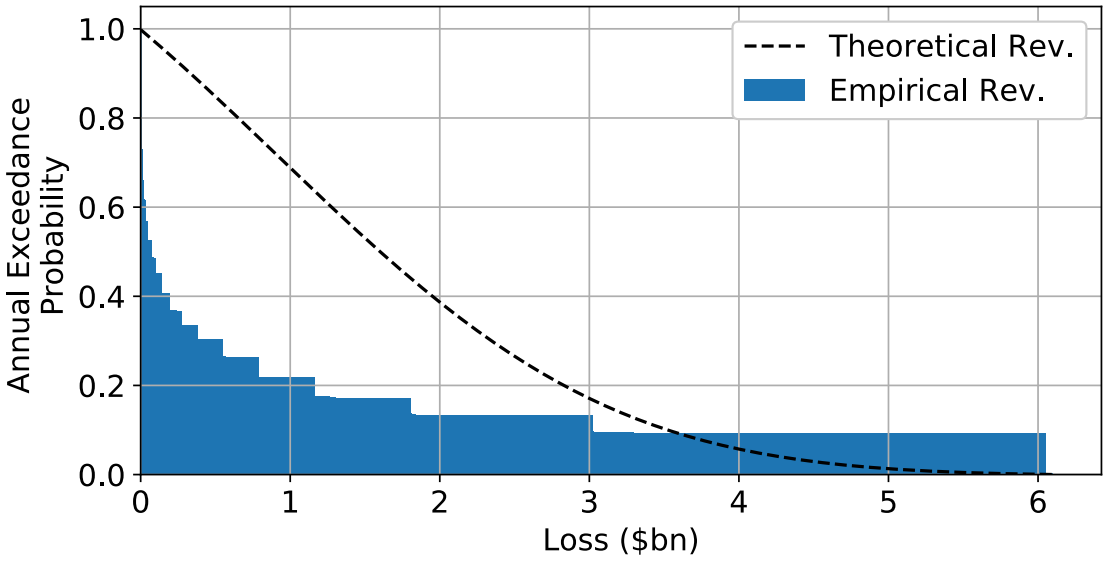

Figure 6.8: Cumulative distribution function (CDF) of expected AEP losses on all properties, all parishes of Bermuda when the 1877-2018 record for Bermuda was used for simulating new events. The histogram indicates the empirical CDF of losses from damaging events.

A and B correspond to the periods 1882-1895 (with mean μ=0.64) and 1897-1930 (with mean μ=0.68), respectively, during which the 10-year moving average was less or equal than the mean of the 10-year moving average.

For each one of the four phases the mean was calculated and used as described in section 2.4 to find the Poisson rate probability of number of events occurring, from which new events were randomly generated for each phase. Empirical and theoretical CDFs were plotted for each phase, as well as for the CDF shown in figure 6.8 (hereafter referred to as no-phase), and are shown in figure 6.9.

Results showed that losses from damaging events sampled from both high-frequency scenarios were larger than the losses from damaging events sampled from the two low-frequency scenarios and the no-phase scenario. In addition, the annual exceedance probabilities for low-phase B were smaller than the ones for low-phase A, while the probabilities for high-phase B were greater than the ones for high-phase A. It should be noted that, since the process of simulating new events is random, the output of the model will not always resemble the results presented here.

Furthermore, the amount of simulated events is dependent on the average annual number of hurricanes. For this study, the means of the different phases ranged from 0.64

Table 6.4: Exceedance probability and return period values for different loss amounts.

	No-Phase		**High-A**		**High-B**		**Low-A**		**Low-B**	
Loss ($bn)	EP (%)	RP (Yr)	EP (%)	RP (Yr)	EP (%)	RP (Yr)	EP (%)	RP (Yr)	EP (%)	RP (Yr)
0.50	84.8	1.2	85.2	1.2	85.5	1.2	84	1.2	83.1	1.2
1.00	68.9	1.5	69.3	1.4	70.1	1.4	67.4	1.5	65.7	1.5
2.00	38.7	2.6	40.0	2.5	41.2	2.4	36.7	2.7	33.7	3
3.00	17.1	5.8	18.3	5.5	19.4	5.2	15.4	6.5	13.1	7.6
4.00	5.7	17.8	6.6	15.3	7.2	13.9	4.9	20.6	3.7	27.2
5.00	1.3	75.9	1.8	54.5	2.1	47.4	1.2	86.6	0.7	138.5

to 1.13 hurricanes per year. It is expected that a significantly higher annual average will result in significantly increased number of simulated events, and thus to larger losses. Lastly, it is important to highlight that, based on equation 6, the highest wind speed of a simulated event can be up to $63.1ms^{-1}$, while the lowest damaging wind speed is $37.5ms^{-1}$. It is certain that if the former value were higher or if the latter value were lower, the resulting EP curves would be very different, showing greater losses particularly in a high-frequency scenario. In future work, the sensitivity of the model on both the effect of the average annual rate of hurricanes and the estimated wind speed at Bermuda will be explored.

Information about return periods (RP) of catastrophic events can be obtained from EP curves. The return period (in years) corresponds to 1/EP. Table 6.4 presents examples of EP values and the corresponding RPs for all five scenarios shown in figure 6.9 for six different loss amounts. The loss amounts are shown in column 1, EPs and RPs for the no-phase scenario are in columns 2 and 3, for the two high-phase scenarios in columns 4-7 and for the two low-phase scenarios in columns 8-11. For example, in the no-phase scenario there is a 5.7% probability that an amount of $4bn will be exceeded in a year with at least one damaging event. This probability corresponds to a RP of around 17.5 years. The probability that the same amount will be exceeded rises for both high-frequency scenarios and dips for both low-frequency scenarios.

Table 6.5: Loss amounts for different return period values.

RP	**EP**	**Loss ($bn)**				
(Years)	**(%)**	No-Phase	High-A	High-B	Low-A	Low-B
5	**20**	2.8	2.9	3	2.7	2.6
10	**10**	3.5	3.6	3.7	3.4	3.2
25	**4**	4.3	4.4	4.5	4.1	3.9
50	**2**	4.7	4.9	5	4.6	4.4
75	**1.3**	5	5.2	5.3	4.9	4.7
100	**1**	5.2	5.4	5.5	5.1	4.8
200	**0.5**	5.5	5.8	6	5.5	5.2

Table 6.5 presents examples of estimated losses for certain return periods of catastrophic events. The first and second columns indicate the return periods and corresponding exceedance probabilities, while expected losses for each scenario are shown in the remaining columns. For example, a once-in-two-hundred-years catastrophic event is expected to cause $5.5bn worth of damage across all parishes and all types of buildings in a no-phase scenario, compared to $6bn in a high-phase B scenario. These losses are halved for a catastrophic event with a return period of once-per-five-years.

Event Loss Tables and EP curves provide the ability to yield indicative return periods of threshold loss events (or changes in magnitude of losses for a given return period). This is very important for insurance and re-insurance companies since they are provided with necessary information that can help in the process of decision making.

6.4 Limitations and Future Work

This study serves as a simple catastrophe model for assessing annual hurricane wind risk in Bermuda, with a scientifically informed sensitivity test on long-term frequencies. It does not intend to reproduce traditional catastrophe modelling methodologies widely used by insurance and re-insurance companies, but to merely serve as a guide for the development of a hurricane wind risk model.

The process of building a catastrophe model entails various sources of uncertainties in

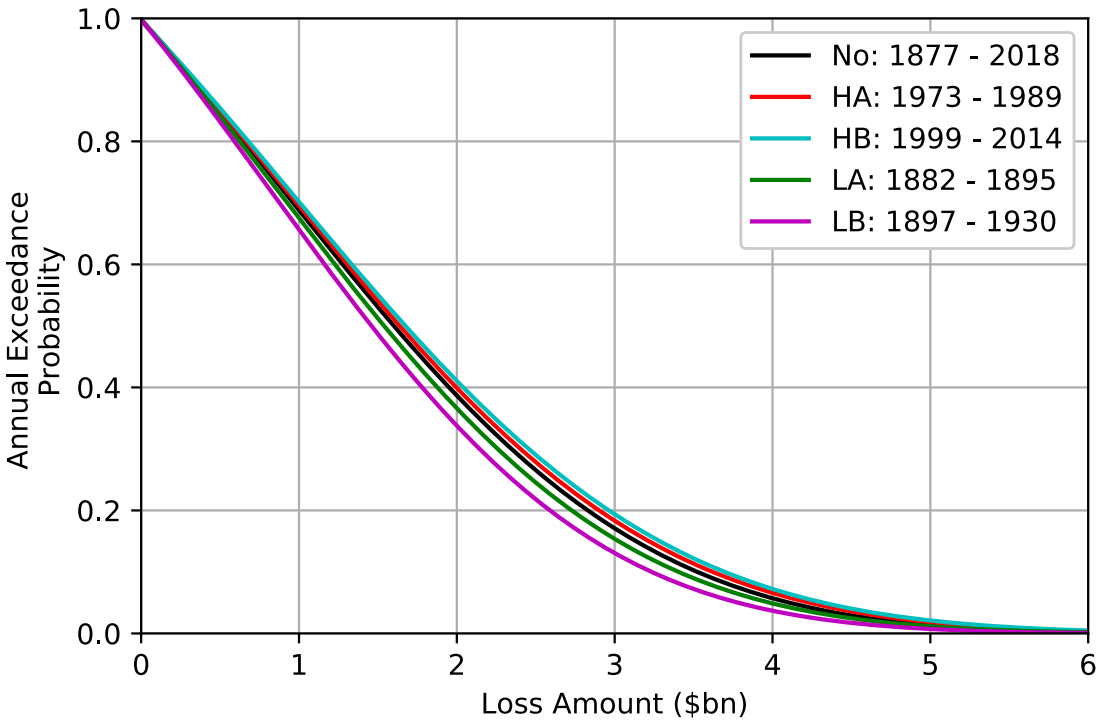

Figure 6.9: EP curves for all five scenarios.

all the different components. Firstly, a key limitation of the study is the use of the observational record. Despite the fact that the record for the North Atlantic basin is considered to be the longest and most comprehensive record compared to other basins (Strachan et al., 2013), it suffers from homogeneity problems due to changes in operational procedures (Landsea, 2007), whose most important source of uncertainty is the observational error (Tolwinski-Ward, 2015). In addition, evaluation of the model with historical losses is problematic, as there are only a few very recent official reports from damaging storms affecting Bermuda that can be used for calibration purposes. So, not only are the basin-wide statistics a source of uncertainty, the damaging impacts in Bermuda are insufficient to effect a useful calibration of the model.

Secondly, different decisions made in the process of exploring the relationship between the distance of a storm from Bermuda and the estimated intensity at the country (see section 6.2.1.1) is another source of uncertainty. These decisions include the arbitrary choices for r_{max}, the use of the variation of the Rankine vortex, the different conversions and the curve fitting. In the future it would be really beneficial to explore different techniques for simulating hurricane intensity such as the ones outlined in Holland et al. (2010), Justus et al. (1978) and Jagger and Elsner (2006). In addition, wind asymmetries, the exclusion

of which can have a negative impact on TC risk assessment (Alvehag and Söder, 2011; Pahwa, 2007), could be addressed following suggestions by studies such as Olfateh et al. (2017) and Chang et al. (2020).

Thirdly, it is important to highlight the lack of studies in Bermuda that explore the relationship between the intensity of a storm and the proportion of damage on properties. Since the vulnerability component of a catastrophe model is of great importance, there is a necessity for more studies like Miller et al. (2013) to be conducted in future catastrophic events, since they will provide an opportunity for updates and sensitivity tests on this model framework.

Lastly, the impact of decadal variability of TCs on potential losses has been examined only in terms on frequency. It will be of great interest to explore the impact in terms of intensity as well. The reasoning behind this comes from the fact that, particularly for the North Atlantic basin, it has been shown that even during low-activity hurricane seasons, very intense tropical cyclones can cause a lot of damage and destruction should they make landfall.

6.5 Discussion

We have developed a simple model for the assessment of hurricane wind risk. Despite the limitations of the study outlined above, this methodology may be useful for jurisdictions with limited availability of property exposure or vulnerability datasets. In the absence of a set of robust engineering studies or readily available property exposure data, assessments of the variability of risk can still be achieved, especially for small island jurisdictions. In our study, we utilized a real estate dataset and a published damage survey as the bases for development of exposure and vulnerability inputs, respectively. The hazard portion of this model is constructed by randomly generating multiple location-centric events that are constrained using the historical record. However, this approach is simple compared to the Monte Carlo simulations used to develop the stochastic storm track datasets in commercial catastrophe models (RMS, 2019). Our method can quickly and easily be applied to assess the variability of wind hazard in different climate regimes, such as ENSO or the NAO, or can utilize other input such as historical anecdotal document archives (e.g. Chenoweth and Divine (2008)), climate model simulations of future storm regimes (e.g. Wehner

et al. (2015)) or geological proxy datasets, such as those provided in Wallace et al. (2014). The simple nature of the model may also be of benefit in quick sensitivity tests of modelled losses to changes in hazard, vulnerability or exposure. This may be especially useful for the purposes of teaching different aspects of risk and its estimation. The code underlying the model itself is written in Python, and it is accessible freely via Github here `https://github.com/PinelopiLoizou/Risk_Model`.

Chapter 7

Concluding Remarks and Future Work

7.1 Introduction

Tropical cyclones are known for causing severe damage and destruction, including loss of life, across many regions of the planet. Understanding which dynamic and thermodynamic conditions mainly drive their inter-annual and decadal variability is crucial for decision makers. The focus of the present Ph.D. study is to understand which processes drive the variability of TCs and to assess any evidence of anthropogenic influence. Different tools, including the standard power spectrum method, wavelets and EOTs method have been applied to multiple datasets - IBTrACS, seven recent reanalysis products (ERAI, ERA5, MERRA, MERRA2, NCEP, JRA25, JRA55) and a range of atm-only and coupled simulations from HadGEM3-GC3.1 for current and future climate. As outlined in chapter 1.1, the aims of the study are to:

1. Understand what drives the natural variability of TCs and to detect evidence of anthropogenic influence.

2. Separate and attribute the impact of natural variability and anthropogenic influence on the variability of TCs.

3. Understand the nature of natural variability under various forcing scenarios and compare this with a scenario of changing forcing.

4. Explore how decadal variability is related to known modes of variability.

By investigating TC variability in the current climate in certain basins understanding some of the drivers of the natural variability of TCs, namely the SSTs and VWS, and exploring the relationship of inter-annual and decadal variability to known modes of variability is addressed. Additionally, the response of TC activity in the different regions of the NH under different forcing scenarios was investigated by comparing TC activity in the first 30 years against the last 30 years of the model simulations.

7.2 Synthesis of Results

7.2.1 Understand what drives the natural variability of TCs and detect any evidence of anthropogenic influence

The connection between the variability of TCs in the different basins and some of the known modes of variability was examined throughout the study. However, in order to address this research question, we particularly focus on the results examined in chapter 3. The drivers of natural variability under the current climate (1980-2013) were investigated in IBTrACS, the reanalysis products and the different model simulations.

TC activity in the well-documented NATL region exhibits high variability compared to the other basins. In both observations and model simulations, TC activity in the basin undergoes inter-annual variability as found by examining the present climate in the different datasets. This interannual variability is driven primarily by the AMO via warm local SSTs. Further influence on Atlantic hurricanes is exerted by the cold phases of ENSO and the PDO via cold SSTs and enhanced VWS in the Pacific regions, conditions linked to the displacement of the Walker Circulation during such events.

Primary driver of TC activity in the EPAC region is the warm phase of ENSO via warm SSTs and weak VWS in the eastern and central Pacific regions under the current climate. ENSO's influence has been robust across the majority of techniques applied on the different datasets. The AMO (via cold Atlantic SSTs) also appears to have an important influence on this basin's activity, albeit with less robustness compared to ENSO.

Similarly to the EPAC, TC activity in the CPAC region under the 1980-2013 period is driven primarily by ENSO via its warm phase and by the AMO via its cold phase. The PDO does not appear to influence TC activity in observations and reanalysis products, but

it has a consistent presence, especially by influencing TCs in the basin via its warm phase, in the atm-only experiments.

The WPAC basin is the region known to have the majority of TC activity in the NH. Typhoon activity in the basin has been found to be driven by more than one main driver in both observations and models. Under the current climate TC variability is linked to the strengthening or weakening of ENSO events according to the change in the phases of the AMO and PDO. The Atlantic decadal mode also appears to have an influence on the basin's activity, in observations, reanalyses and atm-only experiments. PDO's influence is only observed for TC activity in IBTrACS and reanalyses.

Consistent results are found of analysis regarding TC activity in the NIND ocean, since in the different periods and datasets examined in the study TC variability in the basin was not linked significantly to the climate modes of variability. The overall conclusion for TC variability in this basin is that, in order to understand the main drivers, it is necessary to investigate the connection to interannual climate modes such as the Indian Dipole. It is also recommended to examine how climate modes such as ENSO, AMO and PDO might influence the Indian Dipole and the monsoon seasons.

Even though the present study has examined the potential impact of climate change on the variability of TCs (discussed in section 7.2.2), it does not provide a clear detection of evidence of major anthropogenic influence on the variability of TCs. Increases in SSTs are of course observed in both observations and model simulations (due to the nature of the experimental design). A warmer climate can have an impact on the conditions that favour TC formation and intensification. However, in order to fully understand the potential impact of climate change and whether or not anthropogenic influence will take a leading role in influencing TC activity, it is crucial to assess how the known modes of variability will vary in a warming climate.

7.2.2 "Separate and attribute the impact of natural variability and anthropogenic influence on the variability of TCs" and "Understand the nature of natural variability under various forcing scenarios and compare with a scenario of changing forcing"

In this section we address whether research questions 2 and 3 have been answered with the investigation performed in the study. The two questions are combined in order to avoid re-iteration of the main conclusions.

The impact of natural variability has been examined in chapters 3 (the synthesis of which is discussed in section 7.2.1) and 4 (the synthesis of which is discussed in section 7.2.3), whereas the impact of climate change has been examined in chapter 5. By comparing results of the analysis on coupled control-1950 runs against results for the hist-1950 runs during P1 (1950-1980) and P2 (2020-2050) in scenarios with anthropogenic forcing, results show an overall increase in NATL TC intensity but they appear inconclusive on whether there is a north/northeast or south shift of TC activity. EOT analysis shows that influence by the dynamic and thermodynamic drivers examined in the study depends on the location of EOTs, but is generally associated with AMO and ENSO. A westward shift is found for TC activity in the EPAC region as well as an increase in ACE irrespective of the resolution, but no robust conclusion is formed on which SST or VWS conditions are the main source of influence. For the CPAC region, an increase in both frequency and ACE of TCs is found but there are no particular differences between the drivers of TC activity in the current and future climate. For this particular basin, it is important to note that results must be considered with caution since only a small amount of TCs are analysed. Under climate change, a slight increase in ACE and a poleward shift of WPAC TC activity in the basin was found, a result in agreement with the literature (IPCC, 2019). Lastly, similarly to section 7.2.1, results for the NIND basin appear inconclusive about how climate change can impact TC activity in the basin.

7.2.3 Explore how decadal variability is related to known modes of variability

Chapter 4 was dedicated in examining the drivers of natural decadal TC variability. Spectral methods (standard power spectrum and wavelets) were applied onto centennial

and multi-centennial time series of annual counts and ACE from a range of atm-only and coupled simulations by the HadGEM3-GC3.1 GCM in order to detect decadal periodicities associated with the AMO and PDO within the time series. The EOTs method was applied on centennial seasonal (May-November) TC track densities. SST (detrended) and VWS fields were regressed onto the EOT time series in an effort to identify any known canonical patterns, which would further indicate the influence of known modes of variability on the variability of TCs. Lastly, spectral analysis of EOT time series and Pearson correlation coefficients between the time series of TC activity (count, ACE, EOTs) and the seasonally averaged indices complement the analysis.

For the NATL basin, TC activity has been found to undergo decadal variability, a result that is in agreement with studies such as Goldenberg et al. (2001) and McCarthy et al. (2015). This decadal variability is primarily driven by AMO and ENSO, a result that was robustly observed by the analysis performed on model simulations irrespective of resolution and configuration. Indications of additional PDO influence have been shown from the MM and HM atm-only runs. The decadal variability of TCs in the basin is positively correlated with the AMO and anticorrelated with both ENSO and PDO, i.e. a warm AMO and cold ENSO and PDO phases lead to increases in NATL hurricane activity, while the opposite leads to decreases in activity.

For the EPAC region, primary driver of the basin's TC decadal variability is ENSO via local warm SSTs and weak VWS as was evident by all the techniques applied on the model simulations. The AMO appears to additionally drive the basin's activity, at least in the higher resolution runs via cold Atlantic SSTs, associated with Walker Circulation conditions during El-Niño events. Lastly, there are indications of influence by the PDO's warm phase, albeit with less robustness across the different simulations.

Decadal variability in the CPAC region is driven by the warm phase of ENSO across the model experiments. PDO also appears to be a main source of influence, however, the climate index is correlated with TC activity in the atm-only experiments and anticorrelated in the coupled experiments. A possible explanation for this difference is that the SSTs that are used for the computation of the PDO index are prescribed in the atm-only experiments. Lastly, there are strong indications of additional AMO influence on the basin's activity, particularly the cold phase of the decadal Atlantic mode.

Typhoon activity in the WPAC has been found once again to be driven by more than

one main driver. The decadal variability in the atm-only experiments is correlated with the warm phases of ENSO and PDO and anticorrelated with the AMO. However, the presence of the PDO is less robust than the influence of the other two modes.

Finally, results of the analysis on the NIND's activity on decadal timescales remains consistent with the results on the drivers of the current climate. TC activity in the basin cannot be linked significantly to the climate indices. There are indications of ENSO's influence on TCs in the basin, but this is most likely due to the fact that ENSO's high frequency is easily captured in long time series by the spectral methods. It is once again recommended to examine the relationship between the modes already examined in this study (ENSO, AMO, PDO) and the Indian Dipole and monsoon seasons.

7.3 Limitations and Future Work

The methodology used in the present study relies on a range of datasets. Observations of TCs are the primary source of knowledge of the variability of TCs, but their records, apart from being short in length, suffer from biases and homogeneity issues. Reanalyses can reduce uncertainties, however the records used in the study are also short. Centennial reanalyses such as the ERA-20C (Poli et al., 2016) are available, but their low resolution and proneness to unreal trends due to changes in the observational system (Poli et al., 2015) are not ideal for our area of research. Model simulations provide longer, more consistent records to work with, especially for the investigation of decadal variability. In this study, centennial and multi-centennial runs were analysed and it was found that it is important, if not necessary, to have longer climate simulations for the investigation of decadal variability.

Regarding the tools utilised in the study, the spectral methods are simple tools which allow the easy and quick detection of periodicities within the time series, whereas the EOTs method is a more complex, computationally expensive and quantitative tool, which enables the temporal and spatial investigation of variability of TCs in this study but depends on track densities computed from relatively small annual TC samples. By using a range of tools on multiple datasets more confidence is provided especially where results are consistent between datasets and methods.

Following the framework of the study, future work can extend in various ways. Pri-

marily, as evident particularly from the analysis on model simulations, it is imperative to examine the relationship between TC variability and different climate indices. A caveat of the study is that only a few climate indices are examined, especially for the model simulations, since only the May-November averaged ENSO, AMO and PDO indices were taken into consideration. Moreover, for certain basins such as the NATL, it is worth examining lagged effects, such as how the December-February averaged ENSO can impact TC variability in the basin. In addition, it is possible that some of the decadal variations of TC activity, particularly in the NIND region, are more indirectly related to modes of decadal variability through modulation of interannual modes. In the future, it would be beneficial to examine how the decadal modes, as simulated in the model, can impact interannual modes such as QBO, the MJO and the Indian Dipole and then examining their impact on TC activity.

Furthermore, the regression of two different fields, SSTs and VWS, onto the EOT time series provides important results in linking dynamic and thermodynamic conditions associated with modes of climate variability to TC variability. However, taking into consideration the conditions that favour TC formation and intensification, it is important to examine more drivers such as humidity and low-level vorticity following the same analysis. Apart from providing additional information on drivers of TC variability which will enable the scientific community to form a better understanding, it is possible that, for some basins, for example the WPAC, the lack of significant relationships with SSTs and VWS linked to the climate indices examined, might be improved by examining more drivers. Lastly, in the present study only the seasonal SST and VWS fields are examined, therefore in the future lagged regressions, i.e. as regressing the December-February SST field onto the EOT time series, can be explored.

The different tools utilised in the present study have provided us with important information on what drives the variability of TC activity with a certain degree of confidence, since TC activity is examined in a range of datasets using the same analysis. Even though a part of the analysis, namely the EOT regression, is computationally expensive, performing this analysis in the future on simulations from different models, particularly of multiple ensemble members with finer resolution, can perhaps help in improvements in better TC representation in climate models and in examining model uncertainty. In addition, the different ensemble members of HadGEM3-GC3.1 are examined separately in order to in-

crease the amount of simulations examined. It is worth repeating the same analysis on the ensemble means, which will also allow researchers to examine different models. Lastly, the number of ensemble members used in the present study is small, particularly for the high resolution runs. Having a larger ensemble can be useful in additional confidence in the results presented.

The focus of this study is on the regions in the NH, but TCs in the SH should not be neglected. It is important for scientists to better observe and study not only TC activity in the SH, but also how the different climate modes can influence TC variability in the SH, especially since the SH hemisphere is covered by more water than land. It is agreeable amongst the scientific community that there are biases in the observational procedures in the SH compared to the NH, particularly because the former is less densely inhabited. However, conditions that can affect TCs in the NH hemisphere, can also impact TCs in the SH. Therefore, understanding the drivers of TC variability in the world as a whole can perhaps further benefit our understanding in the two hemispheres individually.

Lastly, TCs do cause severe damage and destruction in many regions of the planet. Providing insurance and re-insurance companies, who are strongly impacted by TCs, with impact-related mitigation and planning information based on understanding what drives the variability of TCs, is incredibly important. A simple model for assessing the hurricane wind risk associated with Bermuda was developed as part of the present study. Despite the model's simplicity and limitations, the framework of the study may be useful for jurisdictions with limited availability of property exposure or vulnerability datasets, since it can be easily applied in investigating the variability of TC intensity in different climate regimes. Future work on this model should focus on sensitivity tests on the various model components.

Appendix

Figure 7.1 presents a comparison between the wavelet and Hilbert spectra both for the ERA5 NATL time series of annual TC counts as well as for the mean reanalysis spectrum of the NATL time series of counts. It can seen that despite the fact that the Hilbert spectrum is more localised than the wavelet spectrum, the locations of high power within the Hilbert spectrum are in similar regions to the wavelet spectrum. These regions are within the 2 to 8 year power band, indicating an ENSO influence on TCs. Results from this analysis show complementary results between the two spectral methods in the majority of datasets and individual regions, with very few exceptions, providing greater confidence in the results by the wavelet analysis.

Figure 7.2 presents the wavelet spectra for the time series of NATL TC counts of the full LL and HM coupled control runs along with the KDEs of the power in the 2-8, 10-20, 16-32, 32-75 year band. Even though the range of the runs is different, it can be seen that there is more power in the wavelet spectrum on decadal time scales. Furthermore, the KDEs are able to reflect the distribution of power within certain bands. For example, for the HM control run, the majority of power is within the 16-32 year band. This can be seen from the the corresponding KDE since it has a larger tail compared to the rest.

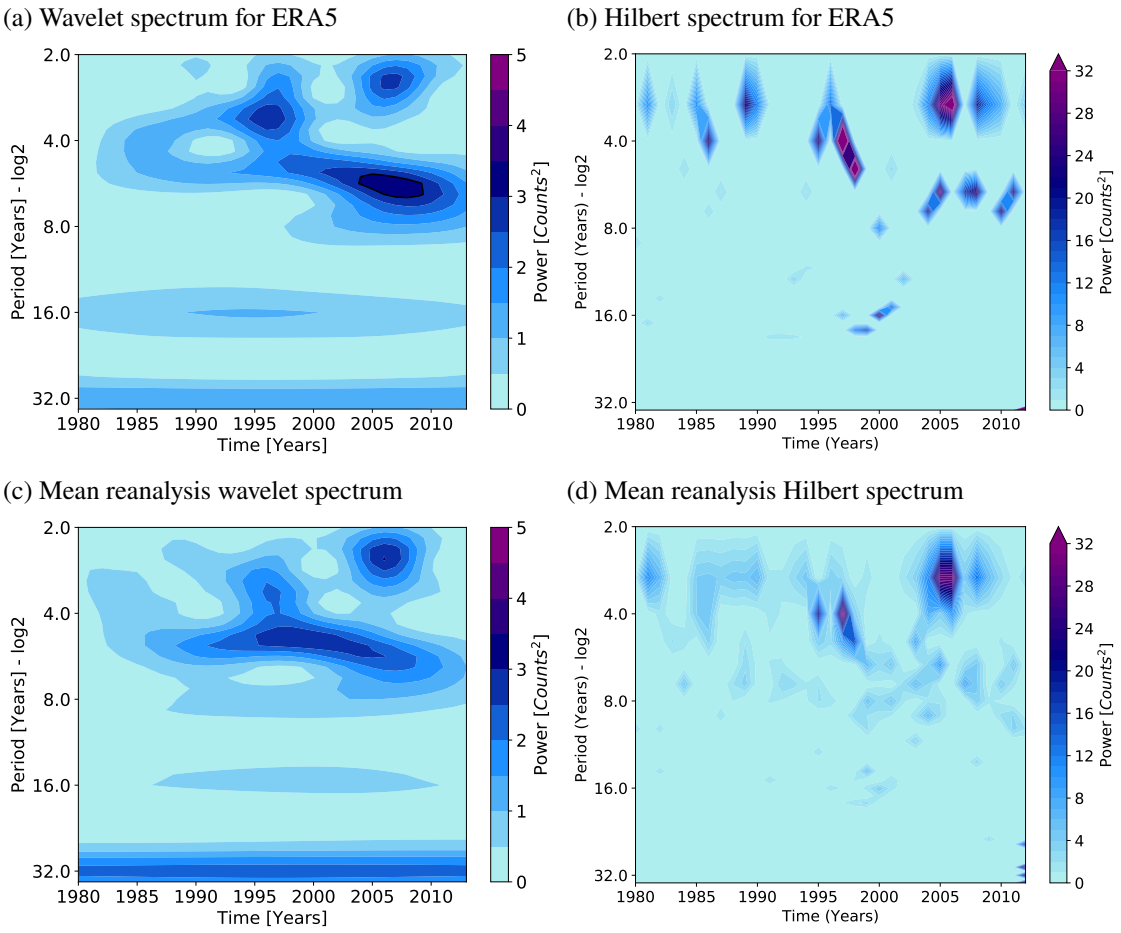

Figure 7.1: Comparison between wavelet and Hilbert spectrum for NATL TC counts

(a) Wavelet spectrum for LL control run

(b) KDEs for different power bands in a

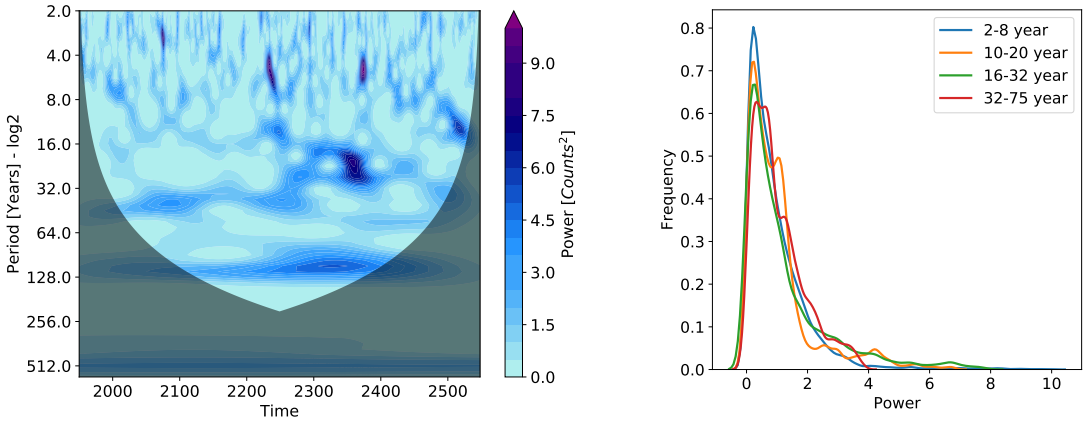

(c) Wavelet spectrum for HM control run

(d) KDEs for different power bands in c

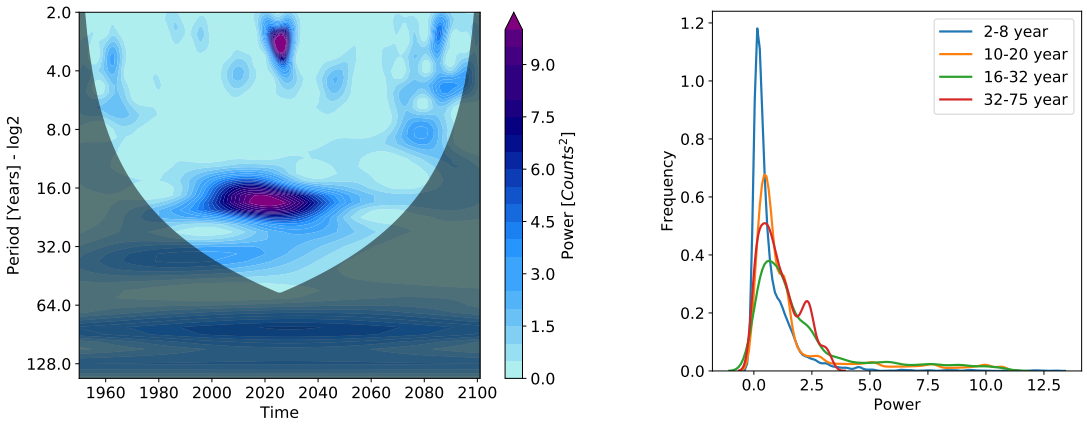

Figure 7.2: Wavelet spectra for the full LL and HM coupled control runs and corresponding KDEs for the 2-8, 10-20, 16-32 and 32-75 year power band.

List of Tables

List of Figures

Bibliography

A.A.Deo and D.W.Ganer (2015), 'Variability in Tropical Cyclone Activity Over Indian Seas in Changing Climate', International Journal of Science and Research (IJSR) **4**(5), 880–885.
URL: *https://www.ijsr.net/archive/v4i5/SUB153371.pdf*

Alvehag, K. and Söder, L. (2011), 'A reliability model for distribution systems incorporating seasonal variations in severe weather', IEEE Transactions on Power Delivery **26**(2), 910–919.
URL: *http://ieeexplore.ieee.org/document/5669368/*

Amaya, D. J., DeFlorio, M. J., Miller, A. J. and Xie, S.-P. (2017), 'WES feedback and the Atlantic Meridional Mode: observations and CMIP5 comparisons', Climate Dynamics **49**(5-6), 1665–1679.
URL: *http://link.springer.com/10.1007/s00382-016-3411-1*

Baldwin, M. P., Gray, L. J., Dunkerton, T. J., Hamilton, K., Haynes, P. H., Randel, W. J., Holton, J. R., Alexander, M. J., Hirota, I., Horinouchi, T., Jones, D. B. A., Kinnersley, J. S., Marquardt, C., Sato, K. and Takahashi, M. (2001), 'The quasi-biennial oscillation', Reviews of Geophysics **39**(2), 179–229.
URL: *http://doi.wiley.com/10.1029/1999RG000073*

Barcikowska, M., Feser, F. and von Storch, H. (2012), 'Usability of Best Track Data in Climate Statistics in the Western North Pacific', Monthly Weather Review **140**(9), 2818–2830.
URL: *http://journals.ametsoc.org/doi/10.1175/MWR-D-11-00175.1*

Bell, G. D. and Chelliah, M. (2006), 'Leading Tropical Modes Associated with Interannual and Multidecadal Fluctuations in North Atlantic Hurricane Activity', Journal of

Climate **19**(4), 590–612.
URL: *https://journals.ametsoc.org/jcli/article/19/4/590/31180/Leading-Tropical-Modes-Associated-with-Interannual*

Bell, R., Hodges, K., Vidale, P. L., Strachan, J. and Roberts, M. (2014), 'Simulation of the global ENSO-tropical cyclone teleconnection by a high-resolution coupled general circulation model', Journal of Climate **27**(17), 6404–6422.

Bengtsson, L., Hodges, K. I. and Esch, M. (2007), 'Tropical cyclones in a T159 resolution global climate model: Comparison with observations and re-analyses', Tellus, Series A: Dynamic Meteorology and Oceanography **59 A**(4), 396–416.

Besonen, M. R., Bradley, R. S., Mudelsee, M., Abbott, M. B. and Francus, P. (2008), 'A 1,000-year, annually-resolved record of hurricane activity from Boston, Massachusetts', Geophysical Research Letters **35**(14), L14705.
URL: *http://doi.wiley.com/10.1029/2008GL033950*

Bhatia, K., Vecchi, G., Murakami, H., Underwood, S. and Kossin, J. (2018), 'Projected response of tropical cyclone intensity and intensification in a global climate model', Journal of Climate **31**(20), 8281–8303.

Bjerknes, J. (1966), 'A possible response of the atmospheric Hadley circulation to equatorial anomalies of ocean temperature', Tellus **18**(4), 820–829.
URL: *http://tellusa.net/index.php/tellusa/article/view/9712*

Bloom, S. C., Takacs, L. L., da Silva, A. M. and Ledvina, D. (1996), 'Data Assimilation Using Incremental Analysis Updates', Monthly Weather Review **124**(6), 1256–1271.
URL: *http://journals.ametsoc.org/doi/10.1175/1520-0493(1996)124%3C1256:DAUIAU%3E2.0.CO;2*

Booth, B. B. B., Dunstone, N. J., Halloran, P. R., Andrews, T. and Bellouin, N. (2012), 'Aerosols implicated as a prime driver of twentieth-century North Atlantic climate variability', Nature **484**(7393), 228–232.
URL: *http://www.nature.com/articles/nature10946*

Bosilovich, M., Akella, S., Coy, L., Cullather, R., Draper, C., Gelaro, R., Kovach, R., Liu, Q., Molod, A., Norris, P., Wargan, K., Chao, W., Reichle, R., Takacs, L., Vikhliaev,

Y., Bloom, S., Collow, A., Firth, S., Labow, G., Partyka, G., Pawson, S., Reale, O., Schubert, S. D. and Suarez, M. (2015), 'MERRA-2 : Initial Evaluation of the Climate', NASA/TM–2015-104606/Vol. 43, NASA Technical Report Series on Global Modeling and Data Assimilation **43**(September), 139.

Boucharel, J., Jin, F., Lin, I. I., Huang, H. and England, M. H. (2016), 'Different controls of tropical cyclone activity in the Eastern Pacific for two types of El Niño', Geophysical Research Letters **43**(4), 1679–1686.
URL: *https://onlinelibrary.wiley.com/doi/10.1002/2016GL067728*

Brandon, C. M., Woodruff, J. D., Lane, D. P. and Donnelly, J. P. (2013), 'Tropical cyclone wind speed constraints from resultant storm surge deposition: A 2500 year reconstruction of hurricane activity from St. Marks, FL', Geochemistry, Geophysics, Geosystems **14**(8), 2993–3008.
URL: *http://doi.wiley.com/10.1002/ggge.20217*

Briegel, L. M. and Frank, W. M. (1997), 'Large-Scale Influences on Tropical Cyclogenesis in the Western North Pacific', Monthly Weather Review **125**(7), 1397–1413.
URL: *http://journals.ametsoc.org/doi/10.1175/1520-0493(1997)125%3C1397:LSIOTC%3E2.0.CO;2*

Burgers, G. and Stephenson, D. B. (1999), 'The "normality" of El Niño', Geophysical Research Letters **26**(8), 1027–1030.
URL: *http://doi.wiley.com/10.1029/1999GL900161*

BWS (2020), 'BWS Glossary'.
URL: *http://www.weather.bm/glossary/glossary.asp*

Camargo, S. J. (2013), 'Global and regional aspects of tropical cyclone activity in the CMIP5 models', Journal of Climate **26**(24), 9880–9902.

Camargo, S. J., Robertson, A. W., Barnston, A. G. and Ghil, M. (2008), 'Clustering of eastern North Pacific tropical cyclone tracks: ENSO and MJO effects', Geochemistry, Geophysics, Geosystems **9**(6), n/a–n/a.
URL: *http://doi.wiley.com/10.1029/2007GC001861*

Camargo, S. J., Robertson, A. W., Gaffney, S. J., Smyth, P. and Ghil, M. (2007), 'Cluster Analysis of Typhoon Tracks. Part II: Large-Scale Circulation and ENSO', Journal of Climate **20**(14), 3654–3676.
URL: *http://journals.ametsoc.org/doi/10.1175/JCLI4203.1*

Camargo, S. J. and Sobel, A. H. (2010), 'Revisiting the influence of the quasi-biennial oscillation on tropical cyclone activity', Journal of Climate **23**(21), 5810–5825.
URL: *http://journals.ametsoc.org/doi/10.1175/2010JCLI3575.1*

Camargo, S. J., Sobel, A. H., Barnston, A. G. and Klotzbach, P. J. (2010), The Influence of Natural Climate Variability on Tropical Cyclones, and Seasonal Forecasts of Tropical Cyclone Activity, pp. 325–360.
URL: *http://www.worldscientific.com/doi/abs/10.1142/9789814293488_0011*

Caron, L. P., Boudreault, M. and Bruyère, C. L. (2015), 'Changes in large-scale controls of Atlantic tropical cyclone activity with the phases of the Atlantic multidecadal oscillation', Climate Dynamics **44**(7-8), 1801–1821.
URL: *http://www.nature.com/articles/srep12358 http://link.springer.com/10.1007/s00382-014-2186-5*

Chan, J. C. (2008), 'Decadal variations of intense typhoon occurrence in the western North Pacific', Proceedings of the Royal Society A: Mathematical, Physical and Engineering Sciences **464**(2089), 249–272.

Chan, J. C. L. (2000), 'Tropical Cyclone Activity over the Western North Pacific Associated with El Niño and La Niña Events', Journal of Climate **13**(16), 2960–2972.
URL: *http://journals.ametsoc.org/doi/abs/10.1175/1520-0442%282000%29013%3C2960%3ATCAOTW%3E2.0.CO%3B2*

Chan, J. C. L. (2007), 'Interannual variations of intense typhoon activity', Tellus A: Dynamic Meteorology and Oceanography **59**(4), 455–460.
URL: *https://www.tandfonline.com/doi/full/10.1111/j.1600-0870.2007.00241.x*

Chan, J. C. L. and Holland, G. J. (1989), 'Observing and Forecasting Tropical Cyclones - Where Next?', Bulletin of the American Meteorological Society **70**(12), 1560–1563.
URL: *https://www.jstor.org/stable/26227763*

Chang, D., Amin, S. and Emanuel, K. (2020), 'Modeling and Parameter Estimation of Hurricane Wind Fields with Asymmetry', Journal of Applied Meteorology and Climatology **59**(4), 687–705.
URL: *https://journals.ametsoc.org/view/journals/apme/59/4/jamc-d-19-0126.1.xml*

Chenoweth, M. and Divine, D. (2008), 'A document-based 318-year record of tropical cyclones in the Lesser Antilles, 1690-2007', Geochemistry, Geophysics, Geosystems **9**(8).
URL: *http://doi.wiley.com/10.1029/2008GC002066*

Chiang, J. C. H., Kushnir, Y. and Giannini, A. (2002), 'Deconstructing Atlantic Intertropical Convergence Zone variability: Influence of the local cross-equatorial sea surface temperature gradient and remote forcing from the eastern equatorial Pacific', Journal of Geophysical Research **107**(D1), 4004.
URL: *http://doi.wiley.com/10.1029/2000JD000307*

Chiang, J. C. H. and Vimont, D. J. (2004), 'Analogous Pacific and Atlantic Meridional Modes of Tropical Atmosphere–Ocean Variability*', Journal of Climate **17**(21), 4143–4158.
URL: *http://journals.ametsoc.org/doi/10.1175/JCLI4953.1*

Choi, Y., Ha, K.-J., Ho, C.-H. and Chung, C. E. (2015), 'Interdecadal change in typhoon genesis condition over the western North Pacific', Climate Dynamics **45**(11-12), 3243–3255.
URL: *http://link.springer.com/10.1007/s00382-015-2536-y*

Christensen, J. H., Kanikicharla, K. K., Aldrian, E., An, S. I., Albuquerque Cavalcanti, I. F., de Castro, M., Dong, W., Goswami, P., Hall, A., Kanyanga, J. K., Kitoh, A., Kossin, J., Lau, N. C., Renwick, J., Stephenson, D. B., Xie, S. P., Zhou, T., Abraham, L., Ambrizzi, T., Anderson, B., Arakawa, O., Arritt, R., Baldwin, M., Barlow, M., Barriopedro, D., Biasutti, M., Biner, S., Bromwich, D., Brown, J., Cai, W., Carvalho, L. V., Chang, P., Chen, X., Choi, J., Christensen, O. B., Deser, C., Emanuel, K., Endo, H., Enfield, D. B., Evan, A., Giannini, A., Gillett, N., Hariharasubramanian, A., Huang, P., Jones, J., Karumuri, A., Katzfey, J., Kjellström, E., Knight, J., Knutson, T., Kulkarni, A., Kundeti, K. R., Lau, W. K., Lenderink, G., Lennard, C., Leung, L. y. R.,

Lin, R., Losada, T., Mackellar, N. C., Magaña, V., Marshall, G., Mearns, L., Meehl, G., Menéndez, C., Murakami, H., Nath, M. J., Neelin, J. D., van Oldenborgh, G. J., Olesen, M., Polcher, J., Qian, Y., Ray, S., Reich, K. D., de Fonseca, B. R., Ruti, P., Screen, J., Sedláček, J., Solman, S., Stendel, M., Stevenson, S., Takayabu, I., Turner, J., Ummenhofer, C., Walsh, K., Wang, B., Wang, C., Watterson, I., Widlansky, M., Wittenberg, A., Woollings, T., Yeh, S. W., Zhang, C., Zhang, L., Zheng, X. and Zou, L. (2013), Climate Phenomena and their Relevance for Future Regional Climate Change, in Intergovernmental Panel on Climate Change, ed., 'Climate Change 2013 - The Physical Science Basis', Vol. 9781107057, Cambridge University Press, Cambridge, pp. 1217–1308.
URL: *https://www.cambridge.org/core/product/identifier/CBO9781107415324A036/type/book_part*

Chu, P. S. and Wang, J. (1997), 'Tropical cyclone occurrences in the vicinity of Hawaii: Are the differences between El Niño and non-El Niño years significant?', Journal of Climate **10**(10), 2683–2689.

Chu, P. S. and Zhao, X. (2004), 'Bayesian change-point analysis of tropical cyclone activity: The central North Pacific case', Journal of Climate **17**(24), 4893–4901.

Cione, J. (2012), Hurricane intensity and inner-core SST: Warmer is not always better, in '30th Conference on Hurricanes and Tropical Meteorology'.

Clark, J. D. and Chu, P. S. (2002), 'Interannual variation of tropical cyclone activity over the Central North Pacific', Journal of the Meteorological Society of Japan **80**(3), 403–418.

Czaja, A., van der Vaart, P. and Marshall, J. (2002), 'A Diagnostic Study of the Role of Remote Forcing in Tropical Atlantic Variability', Journal of Climate **15**(22), 3280–3290.
URL: *http://journals.ametsoc.org/doi/10.1175/1520-0442(2002)015%3C3280:ADSOTR%3E2.0.CO;2*

Dee, D. P., Uppala, S. M., Simmons, A. J., Berrisford, P., Poli, P., Kobayashi, S., Andrae, U., Balmaseda, M. A., Balsamo, G., Bauer, P., Bechtold, P., Beljaars, A. C., van de Berg, L., Bidlot, J., Bormann, N., Delsol, C., Dragani, R., Fuentes, M., Geer, A. J., Haimberger, L., Healy, S. B., Hersbach, H., Hólm, E. V., Isaksen, L., Kållberg, P.,

Köhler, M., Matricardi, M., Mcnally, A. P., Monge-Sanz, B. M., Morcrette, J. J., Park, B. K., Peubey, C., de Rosnay, P., Tavolato, C., Thépaut, J. N. and Vitart, F. (2011), 'The ERA-Interim reanalysis: Configuration and performance of the data assimilation system', Quarterly Journal of the Royal Meteorological Society **137**(656), 553–597.

DeMaria, M. (1996), 'The Effect of Vertical Shear on Tropical Cyclone Intensity Change', Journal of the Atmospheric Sciences **53**(14), 2076–2088.
URL: *http://journals.ametsoc.org/doi/10.1175/1520-0469(1996)053%3C2076:TEOVSO%3E2.0.CO;2*

Denniston, R. F., Villarini, G., Gonzales, A. N., Wyrwoll, K. H., Polyak, V. J., Ummenhofer, C. C., Lachniet, M. S., Wanamaker, A. D., Humphreys, W. F., Woods, D. and Cugley, J. (2015), 'Extreme rainfall activity in the Australian tropics reflects changes in the El Niño/Southern Oscillation over the last two millennia', Proceedings of the National Academy of Sciences of the United States of America **112**(15), 4576–4581.

Denommee, K. C., Bentley, S. J. and Droxler, A. W. (2014), 'Climatic controls on hurricane patterns: A 1200-y near-annual record from Lighthouse Reef, Belize', Scientific Reports **4**, 1–7.

Deser, C., Alexander, M. A., Xie, S.-P. and Phillips, A. S. (2010), 'Sea Surface Temperature Variability: Patterns and Mechanisms', Annual Review of Marine Science **2**(1), 115–143.
URL: *http://www.annualreviews.org/doi/10.1146/annurev-marine-120408-151453*

Dong, B., Sutton, R. T. and Scaife, A. A. (2006), 'Multidecadal modulation of El Niño–Southern Oscillation (ENSO) variance by Atlantic Ocean sea surface temperatures', Geophysical Research Letters **33**(8), L08705.
URL: *http://doi.wiley.com/10.1029/2006GL025766*

Dunstone, N. J., Smith, D. M., Booth, B. B., Hermanson, L. and Eade, R. (2013), 'Anthropogenic aerosol forcing of Atlantic tropical storms', Nature Geoscience **6**(7), 534–539.
URL: *http://dx.doi.org/10.1038/ngeo1854*

Dvorak, V. F. (1973), 'A technique for the analysis and forecasting of tropical cyclone intensities from satellite pictures', NOAA Technical Memorandum NESS 45 **45**(45), 25.

Dvorak, V. F. (1975), 'Tropical Cyclone Intensity Analysis and Forecasting from Satellite Imagery', Monthly Weather Review **103**(5), 420–430.
URL: *http://journals.ametsoc.org/doi/10.1175/1520-0493(1975)103%3C0420:TCIAAF%3E2.0.CO;2*

Dvorak, V. F. (1984), Tropical cyclone intensity analysis using satellite data. noaa tech.rep. 11, 45 pp.

Dvorak, V. F. (1995), 'Tropical clouds and cloud systems observed in satellite imagery: Tropical cyclones.workbook vol. 2. noaa/nesdis, 359 pp'.

Elliott, R. J., Strobl, E. and Sun, P. (2015), 'The local impact of typhoons on economic activity in China: A view from outer space', Journal of Urban Economics **88**, 50–66.
URL: *https://linkinghub.elsevier.com/retrieve/pii/S0094119015000340*

Emanuel, K. (2008), 'The Hurricane—Climate Connection', Bulletin of the American Meteorological Society **89**(5), ES10–ES20.
URL: *http://journals.ametsoc.org/doi/10.1175/BAMS-89-5-Emanuel https://journals.ametsoc.org/doi/10.1175/BAMS-89-5-Emanuel*

Emanuel, K. (2011), 'Global warming effects on U.S. hurricane damage', Weather, Climate, and Society **3**(4), 261–268.

Emanuel, K. A. (2013), 'Downscaling CMIP5 climate models shows increased tropical cyclone activity over the 21st century', Proceedings of the National Academy of Sciences of the United States of America **110**(30), 12219–12224.

Evan, A. T. and Camargo, S. J. (2011), 'A Climatology of Arabian Sea Cyclonic Storms', Journal of Climate **24**(1), 140–158.
URL: *http://journals.ametsoc.org/doi/10.1175/2010JCLI3611.1*

Evan, A. T., Kossin, J. P., 'Eddy' Chung, C. and Ramanathan, V. (2011), 'Arabian Sea tropical cyclones intensified by emissions of black carbon and other aerosols', Nature **479**(7371), 94–97.
URL: *http://www.nature.com/articles/nature10552*

Felton, C. S., Subrahmanyam, B. and Murty, V. S. N. (2013), 'ENSO-Modulated Cyclogenesis over the Bay of Bengal*', Journal of Climate **26**(24), 9806–9818.
URL: *http://journals.ametsoc.org/doi/10.1175/JCLI-D-13-00134.1*

Fine, C. M., Johnson, R. H., Ciesielski, P. E. and Taft, R. K. (2016), 'The Role of Topographically Induced Vortices in Tropical Cyclone Formation over the Indian Ocean', Monthly Weather Review **144**(12), 4827–4847.
URL: *http://journals.ametsoc.org/doi/10.1175/MWR-D-16-0102.1*

Fink, A. H., Schrage, J. M. and Kotthaus, S. (2010), 'On the Potential Causes of the Nonstationary Correlations between West African Precipitation and Atlantic Hurricane Activity', Journal of Climate **23**(20), 5437–5456.
URL: *http://journals.ametsoc.org/doi/10.1175/2010JCLI3356.1*

Frank, W. M. and Ritchie, E. A. (2001), 'Effects of Vertical Wind Shear on the Intensity and Structure of Numerically Simulated Hurricanes', Monthly Weather Review **129**(9), 2249–2269.
URL: *http://journals.ametsoc.org/doi/10.1175/1520-0493(2001)129%3C2249:EOVWSO%3E2.0.CO;2*

Frank, W. M. and Young, G. S. (2007), 'The interannual variability of tropical cyclones', Monthly Weather Review **135**(10), 3587–3598.

Frappier, A. B., Sahagian, D., Carpenter, S. J., Gonzalez, L. A. and Frappier, B. R. (2007), 'Stalagmite stable isotope record of recent tropical cyclone events', Geology **35**(2), 111–114.
URL: *https://doi.org/10.1130/G23145A.1*

Freund, M. B., Brown, J. R., Henley, B. J., Karoly, D. J. and Brown, J. N. (2020), 'Warming Patterns Affect El Niño Diversity in CMIP5 and CMIP6 Models', Journal of Climate **33**(19), 8237–8260.
URL: *https://journals.ametsoc.org/doi/10.1175/JCLI-D-19-0890.1*

García-Serrano, J., Cassou, C., Douville, H., Giannini, A. and Doblas-Reyes, F. J. (2017), 'Revisiting the ENSO Teleconnection to the Tropical North Atlantic', Journal of Climate **30**(17), 6945–6957.
URL: *http://journals.ametsoc.org/doi/10.1175/JCLI-D-16-0641.1*

Gilman, D. L., Fuglister, F. J. and Jr., J. M. M. (1963), 'On the Power Spectrum of "Red Noise', Journal of the Atmospheric Sciences, **20**(2), 182–184.

Goldenberg, S. B., Landsea, C. W., Mestas-Nuñez, A. M. and Gray, W. M. (2001), 'The Recent Increase in Atlantic Hurricane Activity: Causes and Implications', Science **293**(5529), 474 LP – 479.
URL: *http://science.sciencemag.org/content/293/5529/474.abstract*

Goldenberg, S. B. and Shapiro, L. J. (1996), 'Physical mechanisms for the association of El Niño and west African rainfall with Atlantic major hurricane activity'.

Good, S. A., Martin, M. J. and Rayner, N. A. (2013), 'EN4: Quality controlled ocean temperature and salinity profiles and monthly objective analyses with uncertainty estimates', Journal of Geophysical Research: Oceans **118**(12), 6704–6716.
URL: *http://doi.wiley.com/10.1002/2013JC009067*

Goswami, B. N., Madhusoodanan, M. S., Neema, C. P. and Sengupta, D. (2006), 'A physical mechanism for North Atlantic SST influence on the Indian summer monsoon', Geophysical Research Letters **33**(2), L02706.
URL: *http://doi.wiley.com/10.1029/2005GL024803*

Gray, W. M. (1968), 'Global View of the Origin of Tropical Disturbances and Storms', Monthly Weather Review **96**(10), 669–700.

Gray, W. M. (1984), 'Atlantic Seasonal Hurricane Frequency. Part I: El Niño and 30 mb Quasi-Biennial Oscillation Influences', Monthly Weather Review **112**(9), 1649–1668.
URL: *http://journals.ametsoc.org/doi/10.1175/1520-0493(1984)112%3C1649:ASHFPI%3E2.0.CO;2*

Grinsted, A., Moore, J. C. and Jevrejeva, S. (2004), 'Application of the cross wavelet transform and wavelet coherence to geophysical time series', Nonlinear Processes in Geophysics **11**, 561–566.
URL: *https://npg.copernicus.org/articles/11/561/2004/*

Gyakum, J. R. (2011), Subtropical and Hybrid Systems Outline of discussion, in 'Seventh Int. Workshop On Tropical Cyclones', Saint-Gilles-Les-Bains, Reunion, France, World Meteorological Organisation.

Haarsma, R. J., Roberts, M. J., Vidale, P. L., Senior, C. A., Bellucci, A., Bao, Q., Chang, P., Corti, S., Fučkar, N. S., Guemas, V., von Hardenberg, J., Hazeleger, W., Kodama, C., Koenigk, T., Leung, L. R., Lu, J., Luo, J.-J., Mao, J., Mizielinski, M. S., Mizuta, R., Nobre, P., Satoh, M., Scoccimarro, E., Semmler, T., Small, J. and von Storch, J.-S. (2016), 'High Resolution Model Intercomparison Project (HighResMIP v1.0) for CMIP6', Geoscientific Model Development **9**(11), 4185–4208.
URL: *https://gmd.copernicus.org/articles/9/4185/2016/*

Haig, J., Nott, J. and Reichart, G.-J. (2014), 'Australian tropical cyclone activity lower than at any time over the past 550–1,500 years', Nature **505**(7485), 667–671.
URL: *http://dx.doi.org/10.1038/nature12882 http://www.nature.com/articles/nature12882*

Hallam, S., Guishard, M., Josey, S. A., Hyder, P. and Hirschi, J. (2021), 'Increasing tropical cyclone intensity and potential intensity in the subtropical Atlantic around Bermuda from an ocean heat content perspective 1955–2019', Environmental Research Letters **16**(3), 034052.
URL: *https://iopscience.iop.org/article/10.1088/1748-9326/abe493*

Harper, B. A., Kepert, J. D. and Ginger, J. D. (2010), Guidelines For Converting Between Various Wind Averaging Periods In Tropical Cyclone Conditions, Technical report.
URL: *papers2://publication/uuid/64FDDB1C-0E11-4C81-8978-45BA10700FB3*

Hatsushika, H., Tsutsui, J., Fiorino, M. and Onogi, K. (2006), 'Impact of Wind Profile Retrievals on the Analysis of Tropical Cyclones in the JRA-25 Reanalysis', Journal of the Meteorological Society of Japan. Ser. II **84**(5), 891–905.
URL: *http://www.jstage.jst.go.jp/article/jmsj/84/5/84_5_891/_article*

Henley, B. J. (2017), 'Pacific decadal climate variability: Indices, patterns and tropical-extratropical interactions', Global and Planetary Change **155**(June), 42–55.
URL: *https://linkinghub.elsevier.com/retrieve/pii/S0921818116304398*

Ho, C.-H., Kim, H.-S., Jeong, J.-H. and Son, S.-W. (2009), 'Influence of stratospheric quasi-biennial oscillation on tropical cyclone tracks in the western North Pacific', Geophysical Research Letters **36**(6), L06702.
URL: *http://doi.wiley.com/10.1029/2009GL037163*

Hodges, K., Cobb, A. and Vidale, P. L. (2017), 'How well are tropical cyclones represented in reanalysis datasets?', Journal of Climate **30**(14), 5243–5264.

Hodges, K. I. (1994), 'A General Method for Tracking Analysis and Its Application to Meteorological Data', Monthly Weather Review **122**(11), 2573–2586.
URL: *http://journals.ametsoc.org/doi/10.1175/1520-0493(1994)122%3C2573:AGMFTA%3E2.0.CO;2*

Hodges, K. I. (1995), 'Feature Tracking on the Unit Sphere', Monthly Weather Review **123**(12), 3458–3465.
URL: *http://journals.ametsoc.org/doi/10.1175/1520-0493(1995)123%3C3458:FTOTUS%3E2.0.CO;2*

Hodges, K. I. (1996), 'Spherical Nonparametric Estimators Applied to the UGAMP Model Integration for AMIP', Monthly Weather Review **124**(12), 2914–2932.
URL: *http://journals.ametsoc.org/doi/10.1175/1520-0493(1996)124%3C2914:SNEATT%3E2.0.CO;2*

Hodges, K. I. (1999), 'Adaptive Constraints for Feature Tracking', Monthly Weather Review **127**(6), 1362–1373.
URL: *http://journals.ametsoc.org/doi/10.1175/1520-0493(1999)127%3C1362:ACFFT%3E2.0.CO;2*

Hoffmann, L., Günther, G., Li, D., Stein, O., Wu, X., Griessbach, S., Heng, Y., Konopka, P., Müller, R., Vogel, B. and Wright, J. S. (2019), 'From ERA-Interim to ERA5: The considerable impact of ECMWF's next-generation reanalysis on Lagrangian transport simulations', Atmospheric Chemistry and Physics **19**(5), 3097–3214.

Holland, G. and Bruyère, C. L. (2014), 'Recent intense hurricane response to global climate change', Climate Dynamics **42**(3-4), 617–627.

Holland, G. J., Belanger, J. I. and Fritz, A. (2010), 'A Revised Model for Radial Profiles of Hurricane Winds', Monthly Weather Review **138**(12), 4393–4401.

Hopsch, S. B., Thorncroft, C. D. and Tyle, K. R. (2010), 'Analysis of African Easterly Wave Structures and Their Role in Influencing Tropical Cyclogenesis', Monthly Weather

Review **138**(4), 1399–1419.

URL: *http://journals.ametsoc.org/doi/10.1175/2009MWR2760.1*

Hsu, P.-C., Chu, P.-S., Murakami, H. and Zhao, X. (2014), 'An Abrupt Decrease in the Late-Season Typhoon Activity over the Western North Pacific*', Journal of Climate **27**(11), 4296–4312.

URL: *https://journals.ametsoc.org/jcli/article/27/11/4296/34735/An-Abrupt-Decrease-in-the-LateSeason-Typhoon*

Huang, N. E., Shen, Z., Long, S. R., Wu, M. C., Shih, H. H., Zheng, Q., Yen, N.-C., Tung, C. C. and Liu, H. H. (1998), 'The empirical mode decomposition and the Hilbert spectrum for nonlinear and non-stationary time series analysis', Proceedings of the Royal Society of London. Series A: Mathematical, Physical and Engineering Sciences **454**(1971), 903–995.

URL: *https://royalsocietypublishing.org/doi/10.1098/rspa.1998.0193*

IPCC (2018), 'Annex I: Glossary [Matthews, J.B.R. (ed.)]. In: Global Warming of 1.5°C. An IPCC Special Report on the impacts of global warming of 1.5°C above pre-industrial levels and related global greenhouse gas emission pathways, in the context of strengthening the '.

IPCC (2019), Summary for Policymakers. In: IPCC Special Report on the Ocean and Cryosphere in a Changing Climate [H.-O. Pörtner Roberts, D.C. Masson-Delmotte, V. Zhai, P. Tignor, M. Poloczanska, E. Mintenbeck, K. Nicolai, M. Okem, A. Petzold, J. B. Rama, N. Weyer (eds, Technical Report September.

URL: *https://www.ipcc.ch/report/srocc/*

Jagger, T., Elsner, J. B. and Niu, X. (2001), 'A Dynamic Probability Model of Hurricane Winds in Coastal Counties of the United States', Journal of Applied Meteorology **40**(5), 853–863.

URL: *http://journals.ametsoc.org/doi/10.1175/1520-0450(2001)040%3C0853:ADPMOH%3E2.0.CO;2*

Jagger, T. H. and Elsner, J. B. (2006), 'Climatology models for extreme hurricane winds near the United States', Journal of Climate **19**(13), 3220–3236.

Justus, C. G., Hargraves, W. R., Mikhail, A. and Graber, D. (1978), 'Methods for Estimating Wind Speed Frequency Distributions'.

Kim, H.-S., Vecchi, G. A., Knutson, T. R., Anderson, W. G., Delworth, T. L., Rosati, A., Zeng, F. and Zhao, M. (2014), 'Tropical Cyclone Simulation and Response to CO2 Doubling in the GFDL CM2.5 High-Resolution Coupled Climate Model', Journal of Climate **27**(21), 8034–8054.
URL: *http://journals.ametsoc.org/doi/10.1175/JCLI-D-13-00475.1*

Kim, W. and Cai, W. (2014), 'The importance of the eastward zonal current for generating extreme El Niño', Climate Dynamics **42**(11-12), 3005–3014.
URL: *http://link.springer.com/10.1007/s00382-013-1792-y*

Kishore, N., Marqués, D., Mahmud, A., Kiang, M. V., Rodriguez, I., Fuller, A., Ebner, P., Sorensen, C., Racy, F., Lemery, J., Maas, L., Leaning, J., Irizarry, R. A., Balsari, S. and Buckee, C. O. (2018), 'Mortality in Puerto Rico after Hurricane Maria.', The New England journal of medicine **379**(2), 162–170.
URL: *http://www.nejm.org/doi/10.1056/NEJMsa1803972 http://www.ncbi.nlm.nih.gov/pubmed/29809109*

Klotzbach, P. (2010), '3A.4 CARIBBEAN/CENTRAL AMERICAN HURRICANE LANDFALL PROBABILITIES'.

Klotzbach, P., Abhik, S., Hendon, H. H., Bell, M., Lucas, C., G. Marshall, A. and Oliver, E. C. J. (2019), 'On the emerging relationship between the stratospheric Quasi-Biennial oscillation and the Madden-Julian oscillation', Scientific Reports **9**(1), 2981.
URL: *http://www.nature.com/articles/s41598-019-40034-6*

Klotzbach, P. J. and Gray, W. M. (2008), 'Multidecadal Variability in North Atlantic Tropical Cyclone Activity', Journal of Climate **21**(15), 3929–3935.
URL: *https://journals.ametsoc.org/jcli/article/21/15/3929/32011/Multidecadal-Variability-in-North-Atlantic*

Knaff, J. A. (1997), 'Implications of summertime sea level pressure anomalies in the tropical Atlantic region', Journal of Climate **10**(4), 789–804.

Knaff, J. A., Brown, D. P., Courtney, J., Gallina, G. M. and Beven, J. L. (2010), 'An Evaluation of Dvorak Technique–Based Tropical Cyclone Intensity Estimates', Weather and Forecasting **25**(5), 1362–1379.
URL: *https://journals.ametsoc.org/doi/10.1175/2010WAF2222375.1*

Knapp, K. R., Diamond, H. J., Kossin, J. P., Kruk, M. C. and Schreck, C. J. (2018), 'International Best Track Archive for Climate Stewardship (IBTrACS) Project, Version 4. IBTrACS-ALL', NOAA National Centers for Environmental Information .
URL: *https://www.ncei.noaa.gov/access/metadata/landing-page/bin/iso?id=gov.noaa.ncdc:C01552*

Knapp, K. R., Levinson, D. H., Kruk, M. C., Howard, J. H. and Kossin, J. P. (2010), 'The International Best Track Archive for Climate Stewardship (IBTrACS) project: Overview of methods and Indian ocean statistics', Indian Ocean Tropical Cyclones and Climate Change pp. 215–221.

Knight, J. R. (2005), 'A signature of persistent natural thermohaline circulation cycles in observed climate', Geophysical Research Letters **32**(20), L20708.
URL: *http://doi.wiley.com/10.1029/2005GL024233*

Knutson, T. R., McBride, J. L., Chan, J., Emanuel, K., Holland, G., Landsea, C., Held, I., Kossin, J. P., Srivastava, A. K. and Sugi, M. (2010), 'Tropical cyclones and climate change', Nature Geoscience **3**(3), 157–163.
URL: *http://dx.doi.org/10.1038/NGEO779%0Ahttp://hdl.handle.net/1721.1/62558 http://www.nature.com/articles/ngeo779*

Knutson, T. R., Sirutis, J. J., Zhao, M., Tuleya, R. E., Bender, M., Vecchi, G. A., Villarini, G. and Chavas, D. (2015), 'Global projections of intense tropical cyclone activity for the late twenty-first century from dynamical downscaling of CMIP5/RCP4.5 scenarios', Journal of Climate **28**(18), 7203–7224.

Kobayashi, S., OTA, Y., HARADA, Y., EBITA, A., MORIYA, M., ONODA, H., ONOGI, K., KAMAHORI, H., KOBAYASHI, C., ENDO, H., MIYAOKA, K. and TAKAHASHI, K. (2015), 'The JRA-55 Reanalysis: General Specifications and Basic Characteristics', Journal of the Meteorological Society of Japan. Ser. II **93**(1), 5–48.
URL: *https://www.jstage.jst.go.jp/article/jmsj/93/1/93_2015-001/_article*

Kossin, J. P., Emanuel, K. A. and Camargo, S. J. (2016), 'Past and Projected Changes in Western North Pacific Tropical Cyclone Exposure', Journal of Climate **29**(16), 5725–5739.
URL: *http://journals.ametsoc.org/doi/10.1175/JCLI-D-16-0076.1*

Kossin, J. P., Emanuel, K. A. and Vecchi, G. A. (2014), 'The poleward migration of the location of tropical cyclone maximum intensity', Nature **509**(7500), 349–352.
URL: *http://dx.doi.org/10.1038/nature13278 http://www.nature.com/articles/nature13278*

Kucas, M. E., Barlow, S. J., Ballucanag, R. C. and Joint Typhoon Warning Center, Pearl Harbor, H. (2014), Subtropical CYclones: Operational Pracitces and Analysis Methods Applied at the Joint TyphoonWarning Center, in '31st Conf. on Hurricanes and Tropical Meterorology', p. 321.
URL: *https://ams.confex.com/ams/31Hurr/webprogram/Paper245159.html*

Kuhlbrodt, T., Jones, C. G., Sellar, A., Storkey, D., Blockley, E., Stringer, M., Hill, R., Graham, T., Ridley, J., Blaker, A., Calvert, D., Copsey, D., Ellis, R., Hewitt, H., Hyder, P., Ineson, S., Mulcahy, J., Siahaan, A. and Walton, J. (2018), 'The Low-Resolution Version of HadGEM3 GC3.1: Development and Evaluation for Global Climate', Journal of Advances in Modeling Earth Systems **10**(11), 2865–2888.

Land Valuation Department (2019), 'Residential property valuation methodology | Government of Bermuda'.
URL: *https://www.gov.bm/residential-property-valuation-methodology*

Lander, M. A. and Guard, C. P. (1998), 'A Look at Global Tropical Cyclone Activity during 1995: Contrasting High Atlantic Activity with Low Activity in Other Basins', Monthly Weather Review **126**(5), 1163–1173.
URL: *http://journals.ametsoc.org/doi/abs/10.1175/1520-0493%281998%29126%3C1163%3AALAGTC%3E2.0.CO%3B2*

Landsea, C. (2007), 'Counting Atlantic tropical cyclones back to 1900', Eos, Transactions American Geophysical Union **88**(18), 197–202.
URL: *http://doi.wiley.com/10.1029/2007EO180001*

Landsea, C. W. (2006), 'Can We Detect Trends in Extreme Tropical Cyclones?', Science

313(5786), 452–454.
URL: *https://www.sciencemag.org/lookup/doi/10.1126/science.1128448*

Landsea, C. W., Pielke, R. A., Mestas-Nuñez, A. M. and Knaff, J. A. (1999), 'Atlantic Basin Hurricanes: Indices of Climatic Changes', Climatic Change **42**(1), 89–129.
URL: *https://doi.org/10.1023/A:1005416332322*

Landsea, C. W., Vecchi, G. A., Bengtsson, L. and Knutson, T. R. (2010), 'Impact of Duration Thresholds on Atlantic Tropical Cyclone Counts*', Journal of Climate **23**(10), 2508–2519.
URL: *http://journals.ametsoc.org/doi/abs/10.1175/2009JCLI3034.1*

Leutbecher, M., Lock, S., Ollinaho, P., Lang, S. T. K., Balsamo, G., Bechtold, P., Bonavita, M., Christensen, H. M., Diamantakis, M., Dutra, E., English, S., Fisher, M., Forbes, R. M., Goddard, J., Haiden, T., Hogan, R. J., Juricke, S., Lawrence, H., MacLeod, D., Magnusson, L., Malardel, S., Massart, S., Sandu, I., Smolarkiewicz, P. K., Subramanian, A., Vitart, F., Wedi, N. and Weisheimer, A. (2017), 'Stochastic representations of model uncertainties at ECMWF: state of the art and future vision', Quarterly Journal of the Royal Meteorological Society **143**(707), 2315–2339.
URL: *https://onlinelibrary.wiley.com/doi/10.1002/qj.3094*

Li, T., Kwon, M., Zhao, M., Kug, J.-S., Luo, J.-J. and Yu, W. (2010), 'Global warming shifts Pacific tropical cyclone location', Geophysical Research Letters **37**(21), n/a–n/a.
URL: *http://doi.wiley.com/10.1029/2010GL045124*

Li, W., Li, L. and Deng, Y. (2015), 'Impact of the Interdecadal Pacific Oscillation on Tropical Cyclone Activity in the North Atlantic and Eastern North Pacific', Scientific Reports **5**(1), 12358.
URL: *http://www.nature.com/articles/srep12358*

Liu, F., Zhang, W., Jin, F.-F. and Hu, S. (2021), 'Decadal Modulation of the ENSO–Indian Ocean Basin Warming Relationship during the Decaying Summer by the Interdecadal Pacific Oscillation', Journal of Climate **34**(7), 2685–2699.
URL: *https://journals.ametsoc.org/view/journals/clim/34/7/JCLI-D-20-0457.1.xml*

Liu, K.-b. and Fearn, M. L. (1993), 'Lake-sediment record of late Holocene hurricane

activities from coastal Alabama', Geology **21**(9), 793–796.
URL: *https://doi.org/10.1130/0091-7613(1993)021<0793:LSROLH>2.3.CO;2*

Lough, J. M. (2007), 'Tropical river flow and rainfall reconstructions from coral luminescence: Great Barrier Reef, Australia', Paleoceanography **22**(2), 1–16.
URL: *http://doi.wiley.com/10.1029/2006PA001377*

Lübbecke, J. F. and McPhaden, M. J. (2014), 'Assessing the Twenty-First-Century Shift in ENSO Variability in Terms of the Bjerknes Stability Index*', Journal of Climate **27**(7), 2577–2587.
URL: *https://journals.ametsoc.org/jcli/article/27/7/2577/34851/Assessing-the-TwentyFirstCentury-Shift-in-ENSO*

MacLachlan, C., Arribas, A., Peterson, K. A., Maidens, A., Fereday, D., Scaife, A. A., Gordon, M., Vellinga, M., Williams, A., Comer, R. E., Camp, J., Xavier, P. and Madec, G. (2015), 'Global Seasonal forecast system version 5 (GloSea5): a high-resolution seasonal forecast system', Quarterly Journal of the Royal Meteorological Society **141**(689), 1072–1084.
URL: *http://doi.wiley.com/10.1002/qj.2396*

Madden, R. A. and Julian, P. R. (1971), 'Detection of a 40–50 Day Oscillation in the Zonal Wind in the Tropical Pacific', Journal of the Atmospheric Sciences **28**(5), 702–708.
URL: *http://journals.ametsoc.org/doi/abs/10.1175/1520-0469%281971%29028%3C0702%3ADOADOI%3E2.0.CO%3B2*
http://journals.ametsoc.org/doi/10.1175/1520-0469(1971)028%3C0702:DOADOI%3E2.0.CO;2

Madl, P. (2000), 'The El-Niño (ENSO) phenomenon', The El-Nino (ENSO) Phenomenon. Environmental Physics/Lettner .

Maloney, E. D. (2000), 'Modulation of Hurricane Activity in the Gulf of Mexico by the Madden-Julian Oscillation', Science **287**(5460), 2002–2004.
URL: *http://www.sciencemag.org/cgi/doi/10.1126/science.287.5460.2002*
https://www.sciencemag.org/lookup/doi/10.1126/science.287.5460.2002

Manganello, J. V., Hodges, K. I., Dirmeyer, B., Kinter, J. L., Cash, B. A., Marx, L., Jung, T., Achuthavarier, D., Adams, J. M., Altshuler, E. L., Huang, B., Jin, E. K., Towers,

P. and Wedi, N. (2014), 'Future changes in the western North Pacific tropical cyclone activity projected by a multidecadal simulation with a 16-km global atmospheric GCM', Journal of Climate **27**(20), 7622–7646.

Manganello, J. V., Hodges, K. I., Kinter, J. L., Cash, B. A., Marx, L., Jung, T., Achuthavarier, D., Adams, J. M., Altshuler, E. L., Huang, B., Jin, E. K., Stan, C., Towers, P. and Wedi, N. (2012), 'Tropical cyclone climatology in a 10-km global atmospheric GCM: Toward weather-resolving climate modeling', Journal of Climate **25**(11), 3867–3893.

Mann, M. E. and Emanuel, K. A. (2006), 'Atlantic hurricane trends linked to climate change', Eos, Transactions American Geophysical Union **87**(24), 233.
URL: *http://doi.wiley.com/10.1029/2006EO240001*

Mann, M. E., Steinman, B. A., Brouillette, D. J. and Miller, S. K. (2021), 'Multidecadal climate oscillations during the past millennium driven by volcanic forcing', Science **371**(6533), 1014–1019.
URL: *https://www.sciencemag.org/lookup/doi/10.1126/science.abc5810*

Mantua, N. J. and Hare, S. R. (2002), 'The pacific decadal oscillation', Journal of Oceanography **58**(Figure 23), 35–44.

Mantua, N. J., Hare, S. R., Zhang, Y., Wallace, J. M. and Francis, R. C. (1997), 'A Pacific Interdecadal Climate Oscillation with Impacts on Salmon Production', Bulletin of the American Meteorological Society **78**(6), 1069–1079.
URL: *http://journals.ametsoc.org/doi/10.1175/1520-0477(1997)078%3C1069:APICOW%3E2.0.CO;2*

MathWorks (n.d.), 'Continuous and Discrete Wavelet Transforms - MATLAB & Simulink - MathWorks United Kingdom'.
URL: *https://uk.mathworks.com/help/wavelet/gs/continuous-and-discrete-wavelet-transforms.html*

McCarthy, G. D., Haigh, I. D., Hirschi, J. J., Grist, J. P. and Smeed, D. A. (2015), 'Ocean impact on decadal Atlantic climate variability revealed by sea-level observations', Nature **521**(7553), 508–510.

Mei, W., Kamae, Y., Xie, S.-P. and Yoshida, K. (2019), 'Variability and Predictability of North Atlantic Hurricane Frequency in a Large Ensemble of High-Resolution Atmospheric Simulations', Journal of Climate **32**(11), 3153–3167.
URL: *https://journals.ametsoc.org/view/journals/clim/32/11/jcli-d-18-0554.1.xml*

Menary, M. B., Kuhlbrodt, T., Ridley, J., Andrews, M. B., Dimdore-Miles, O. B., Deshayes, J., Eade, R., Gray, L., Ineson, S., Mignot, J., Roberts, C. D., Robson, J., Wood, R. A. and Xavier, P. (2018), 'Preindustrial Control Simulations With HadGEM3-GC3.1 for CMIP6', Journal of Advances in Modeling Earth Systems **10**(12), 2018MS001495.
URL: *https://onlinelibrary.wiley.com/doi/abs/10.1029/2018MS001495*

Miller, C., Gibbons, M., Beatty, K. and Boissonnade, A. (2013), 'Topographic Speed-Up Effects and Observed Roof Damage on Bermuda following Hurricane Fabian (2003)', Weather and Forecasting **28**(1), 159–174.

Miller, D. L., Mora, C. I., Grissino-Mayer, H. D., Mock, C. J., Uhle, M. E. and Sharp, Z. (2006), 'Tree-ring isotope records of tropical cyclone activity', Proceedings of the National Academy of Sciences **103**(39), 14294–14297.
URL: *https://pnas.org/doi/full/10.1073/pnas.0606549103*

Molod, A., Takacs, L., Suarez, M. and Bacmeister, J. (2015), 'Development of the GEOS-5 atmospheric general circulation model: Evolution from MERRA to MERRA2', Geoscientific Model Development **8**(5), 1339–1356.

Muni Krishna, K. (2009), 'Intensifying tropical cyclones over the North Indian Ocean during summer monsoon—Global warming', Global and Planetary Change **65**(1-2), 12–16.
URL: *http://dx.doi.org/10.1016/j.gloplacha.2008.10.007*
https://linkinghub.elsevier.com/retrieve/pii/S0921818108001471

Murakami, H. (2014), 'Tropical cyclones in reanalysis data sets', Geophysical Research Letters **41**(6), 2133–2141.
URL: *http://doi.wiley.com/10.1002/2014GL059519*

Murakami, H., Delworth, T. L., Cooke, W. F., Zhao, M., Xiang, B. and Hsu, P.-C. (2020), 'Detected climatic change in global distribution of tropical cyclones', Proceedings of

the National Academy of Sciences **117**(20), 10706–10714.
URL: *http://www.pnas.org/lookup/doi/10.1073/pnas.1922500117*

Murakami, H., Vecchi, G. A., Underwood, S., Delworth, T. L., Wittenberg, A. T., Anderson, W. G., Chen, J. H., Gudgel, R. G., Harris, L. M., Lin, S. J. and Zeng, F. (2015), 'Simulation and prediction of category 4 and 5 hurricanes in the high-resolution GFDL HiFLOR coupled climate model', Journal of Climate **28**(23), 9058–9079.

Nakamura, J., Camargo, S. J., Sobel, A. H., Henderson, N., Emanuel, K. A., Kumar, A., LaRow, T. E., Murakami, H., Roberts, M. J., Scoccimarro, E., Vidale, P. L., Wang, H., Wehner, M. F. and Zhao, M. (2017), 'Western North Pacific Tropical Cyclone Model Tracks in Present and Future Climates', Journal of Geophysical Research: Atmospheres **122**(18), 9721–9744.

NOAA (2020a), 'Costliest U. S . Tropical Cyclones', NOAA Technical Memorandum NWS NHC-6 pp. 1–5.
URL: *https://www.nhc.noaa.gov/news/UpdatedCostliest.pdf*

NOAA (2020b), 'H*WIND-Real-time Hurricane Analysis Project'.
URL: *https://storm.aoml.noaa.gov/hwind/*

Noren, A. J., Bierman, P. R., Steig, E. J., Lini, A. and Southon, J. (2002), 'Millennial-scale storminess variability in the northeastern United States during the Holocene epoch', Nature **419**(6909), 821–824.
URL: *http://www.nature.com/articles/nature01132*

Nyberg, J., Malmgren, B. A., Winter, A., Jury, M. R., Kilbourne, K. H. and Quinn, T. M. (2007), 'Low Atlantic hurricane activity in the 1970s and 1980s compared to the past 270 years', Nature **447**(7145), 698–701.
URL: *http://www.nature.com/articles/nature05895*

Oettli, P., Morioka, Y. and Yamagata, T. (2016), 'A Regional Climate Mode Discovered in the North Atlantic: Dakar Niño/Niña', Scientific Reports **6**(1), 18782.
URL: *http://www.nature.com/articles/srep18782*

Olander, T. L. and Velden, C. S. (2007), 'The Advanced Dvorak Technique: Continued Development of an Objective Scheme to Estimate Tropical Cyclone Intensity Using

Geostationary Infrared Satellite Imagery', Weather and Forecasting **22**(2), 287–298.
URL: *https://journals.ametsoc.org/doi/10.1175/WAF975.1*

Olfateh, M., Callaghan, D. P., Nielsen, P. and Baldock, T. E. (2017), 'Tropical cyclone wind field asymmetry-Development and evaluation of a new parametric model', Journal of Geophysical Research: Oceans **122**(1), 458–469.
URL: *http://doi.wiley.com/10.1002/2016JC012237*

Oliva, F., Viau, A. E., Peros, M. C. and Bouchard, M. (2018), 'Paleotempestology database for the western North Atlantic basin', The Holocene **28**(10), 1664–1671.
URL: *http://journals.sagepub.com/doi/10.1177/0959683618782598*

Onogi, K., Tsutsui, J., Koide, H., Sakamoto, M., Kobayashi, S., Hatsushika, H., Matsumoto, T., Yamazaki, N., Kamahori, H., Takahashi, K., Kadokura, S., Wada, K., Kato, K., Oyama, R., Ose, T., Mannoji, N. and Taira, R. (2007), 'The JRA-25 Reanalysis', Journal of the Meteorological Society of Japan. Ser. II **85**(3), 369–432.
URL: *https://www.jstage.jst.go.jp/article/jmsj/85/3/85_3_369/_article*

Pahwa, A. (2007), Modeling Weather-Related Failures of Overhead Distribution Lines, in '2007 IEEE Power Engineering Society General Meeting', Vol. 21, IEEE, pp. 1–1.
URL: *http://ieeexplore.ieee.org/document/4275933/*

Palmen, E. (1948), 'On the Formation andStructure of Tropical Cyclones', Geophysica **3**, 26–38.

Palmer, T., Buizza, R., Doblas-Reyes, F., Jung, T., Leutbecher, M., Shutts, G., Steinheimer, M. and Weisheimer, A. (2009), 'Stochastic Parametrization and Model Uncertainty'.
URL: *http://www.ecmwf.int/sites/default/files/elibrary/2009/%0A11577-stochastic-parametrization-and-model-uncertainty.pdf.*

Park, D. S. R., Ho, C. H., Chan, J. C., Ha, K. J., Kim, H. S., Kim, J. and Kim, J. H. (2017), 'Asymmetric response of tropical cyclone activity to global warming over the North Atlantic and western North Pacific from CMIP5 model projections', Scientific Reports **7**(May 2016), 1–9.
URL: *http://dx.doi.org/10.1038/srep41354*

Phillips, A. S., Deser, C. and Fasullo, J. (2014), 'Evaluating Modes of Variability in Climate Models', Eos, Transactions American Geophysical Union **95**(49), 453–455.
URL: *http://doi.wiley.com/10.1002/2014EO490002*

Poli, P., Hersbach, H., Berrisford, P. and authors, O. (2015), 'ERA-20C Deterministic', ERA Report Series (20), 48.
URL: *http://www.ecmwf.int/en/elibrary/11700-era-20c-deterministic*

Poli, P., Hersbach, H., Dee, D. P., Berrisford, P., Simmons, A. J., Vitart, F., Laloyaux, P., Tan, D. G. H., Peubey, C., Thépaut, J.-N., Trémolet, Y., Hólm, E. V., Bonavita, M., Isaksen, L. and Fisher, M. (2016), 'ERA-20C: An Atmospheric Reanalysis of the Twentieth Century', Journal of Climate **29**(11), 4083–4097.
URL: *http://journals.ametsoc.org/doi/10.1175/JCLI-D-15-0556.1*

Rajeevan, M., Srinivasan, J., Niranjan Kumar, K., Gnanaseelan, C. and Ali, M. M. (2013), 'On the epochal variation of intensity of tropical cyclones in the Arabian Sea', Atmospheric Science Letters **14**(4), 249–255.
URL: *https://onlinelibrary.wiley.com/doi/10.1002/asl2.447*

Rayner, N. A., Parker, D. E., Horton, E. B., Folland, C. K., Alexander, L. V., Rowell, D. P., Kent, E. C. and Kaplan, A. (2003), 'Global analyses of sea surface temperature, sea ice, and night marine air temperature since the late nineteenth century', Journal of Geophysical Research **108**(D14), 4407.
URL: *http://doi.wiley.com/10.1029/2002JD002670*

Ren, F., Liang, J., Wu, G., Dong, W. and Yang, X. (2011), 'Reliability Analysis of Climate Change of Tropical Cyclone Activity over the Western North Pacific', Journal of Climate **24**(22), 5887–5898.
URL: *http://journals.ametsoc.org/doi/abs/10.1175/2011JCLI3996.1*

Rienecker, M. M., Suarez, M. J., Gelaro, R., Todling, R., Bacmeister, J., Liu, E., Bosilovich, M. G., Schubert, S. D., Takacs, L., Kim, G. K., Bloom, S., Chen, J., Collins, D., Conaty, A., Da Silva, A., Gu, W., Joiner, J., Koster, R. D., Lucchesi, R., Molod, A., Owens, T., Pawson, S., Pegion, P., Redder, C. R., Reichle, R., Robertson, F. R., Ruddick, A. G., Sienkiewicz, M. and Woollen, J. (2011), 'MERRA: NASA's

modern-era retrospective analysis for research and applications', Journal of Climate **24**(14), 3624–3648.

RMS (2019), 'About us'.

URL: *https://forms2.rms.com/rs/729-DJX-565/images/rms_corporate_brochure.pdf*

RMS (2020), 'Understanding catastrophe'.

URL: *https://www.rms.com/catastrophe-modeling*

Roberts, M. J., Baker, A., Blockley, E. W., Calvert, D., Coward, A., Hewitt, H. T., Jackson, L. C., Kuhlbrodt, T., Mathiot, P., Roberts, C. D., Schiemann, R., Seddon, J., Vannière, B. and Luigi Vidale, P. (2019), 'Description of the resolution hierarchy of the global coupled HadGEM3-GC3.1 model as used in CMIP6 HighResMIP experiments', Geoscientific Model Development **12**(12), 4999–5028.

Roberts, M. J., Camp, J., Seddon, J., Vidale, P. L., Hodges, K., Vanniere, B., Mecking, J., Haarsma, R., Bellucci, A., Scoccimarro, E., Caron, L.-P., Chauvin, F., Terray, L., Valcke, S., Moine, M.-P., Putrasahan, D., Roberts, C., Senan, R., Zarzycki, C. and Ullrich, P. (2020a), 'Impact of model resolution on tropical cyclone simulation using the highresmip?primavera multimodel ensemble', Journal of Climate **33**(7), 2557 – 2583.

URL: *https://journals.ametsoc.org/view/journals/clim/33/7/jcli-d-19-0639.1.xml*

Roberts, M. J., Camp, J., Seddon, J., Vidale, P. L., Hodges, K., Vannière, B., Mecking, J., Haarsma, R., Bellucci, A., Scoccimarro, E., Caron, L.-P., Chauvin, F., Terray, L., Valcke, S., Moine, M.-P., Putrasahan, D., Roberts, C. D., Senan, R., Zarzycki, C., Ullrich, P., Yamada, Y., Mizuta, R., Kodama, C., Fu, D., Zhang, Q., Danabasoglu, G., Rosenbloom, N., Wang, H. and Wu, L. (2020b), 'Projected future changes in tropical cyclones using the cmip6 highresmip multimodel ensemble', Geophysical Research Letters **47**(14), e2020GL088662. e2020GL088662 2020GL088662.

URL: *https://agupubs.onlinelibrary.wiley.com/doi/abs/10.1029/2020GL088662*

Roberts, M. J., Vidale, P. L., Mizielinski, M. S., Demory, M. E., Schiemann, R., Strachan, J., Hodges, K., Bell, R. and Camp, J. (2015), 'Tropical cyclones in the UPSCALE ensemble of high-resolution global climate models', Journal of Climate **28**(2), 574–596.

Saha, S., Moorthi, S., Pan, H. L., Wu, X., Wang, J., Nadiga, S., Tripp, P., Kistler, R., Woollen, J., Behringer, D., Liu, H., Stokes, D., Grumbine, R., Gayno, G., Wang, J., Hou, Y. T., Chuang, H. Y., Juang, H. M. H., Sela, J., Iredell, M., Treadon, R., Kleist, D., Van Delst, P., Keyser, D., Derber, J., Ek, M., Meng, J., Wei, H., Yang, R., Lord, S., Van Den Dool, H., Kumar, A., Wang, W., Long, C., Chelliah, M., Xue, Y., Huang, B., Schemm, J. K., Ebisuzaki, W., Lin, R., Xie, P., Chen, M., Zhou, S., Higgins, W., Zou, C. Z., Liu, Q., Chen, Y., Han, Y., Cucurull, L., Reynolds, R. W., Rutledge, G. and Goldberg, M. (2010), 'The NCEP climate forecast system reanalysis', Bulletin of the American Meteorological Society **91**(8), 1015–1057.

Salinger, M., Renwick, J. and Mullan, A. (2001), 'Interdecadal Pacific Oscillation and South Pacific climate', International Journal of Climatology **21**(14), 1705–1721.
URL: *https://onlinelibrary.wiley.com/doi/10.1002/joc.691*

Schenkel, B. A. and Hart, R. E. (2012), 'An examination of tropical cyclone position, intensity, and intensity life cycle within atmospheric reanalysis datasets', Journal of Climate **25**(10), 3453–3475.

Scherb, A., Garrè, L. and Straub, D. (2015), 'Probabilistic risk assessment of infrastructure networks subjected to hurricanes', 12th International Conference on Applications of Statistics and Probability in Civil Engineering, ICASP 2015 pp. 1–9.

Schlesinger, M. E. and Ramankutty, N. (1994), 'An oscillation in the global climate system of period 65–70 years', Nature **367**(6465), 723–726.
URL: *http://www.nature.com/articles/367723a0*

Schreck, C. J., Knapp, K. R. and Kossin, J. P. (2014), 'The Impact of Best Track Discrepancies on Global Tropical Cyclone Climatologies using IBTrACS', Monthly Weather Review **142**(10), 3881–3899.
URL: *http://journals.ametsoc.org/doi/10.1175/MWR-D-14-00021.1*

Sealy, K. S. and Strobl, E. (2017), 'A hurricane loss risk assessment of coastal properties in the caribbean: Evidence from the Bahamas', Ocean & Coastal Management **149**(December), 42–51.
URL: *https://linkinghub.elsevier.com/retrieve/pii/S0964569116303337*

Serra, Y. L., Kiladis, G. N. and Hodges, K. I. (2010), 'Tracking and mean structure of easterly waves over the Intra-Americas Sea', Journal of Climate **23**(18), 4823–4840.

Shao, H., Derber, J., Huang, X.-Y., Hu, M., Newman, K., Stark, D., Lueken, M., Zhou, C., Nance, L., Kuo, Y.-H. and Brown, B. (2016), 'Bridging Research to Operations Transitions: Status and Plans of Community GSI', Bulletin of the American Meteorological Society **97**(8), 1427–1440.
URL: *https://journals.ametsoc.org/doi/10.1175/BAMS-D-13-00245.1*

Shapiro, L. J. (1989), 'The Relationship of the Quasi-biennial Oscillation to Atlantic Tropical Storm Activity', Monthly Weather Review **117**(7), 1545–1552.
URL: *http://journals.ametsoc.org/doi/10.1175/1520-0493(1989)117%3C1545:TROTQB%3E2.0.CO;2*

Singh, O. P., Ali Khan, T. M. and Rahman, M. S. (2000), 'Changes in the frequency of tropical cyclones over the North Indian Ocean', Meteorology and Atmospheric Physics **75**(1-2), 11–20.
URL: *http://link.springer.com/10.1007/s007030070011*

Smith, I. (2004), 'An assessment of recent trends in Australian rainfall', Australian Meteorological Magazine **53**(3), 163–173.
URL: *http://citeseerx.ist.psu.edu/viewdoc/download?rep=rep1&type=pdf&doi=10.1.1.222.9449*

Stevens, B., Fiedler, S., Kinne, S., Peters, K., Rast, S., Müsse, J., Smith, S. J. and Mauritsen, T. (2017), 'MACv2-SP: A parameterization of anthropogenic aerosol optical properties and an associated Twomey effect for use in CMIP6', Geoscientific Model Development **10**(1), 433–452.

Stockdale, T., Balmaseda, M., Johnson, S., Ferranti, L., Molteni, F., Magnusson, L., Tietsche, S., Vitart, F., Decremer, D., Weisheimer, A., Roberts, C., Balsamo, G., Keeley, S., Mogensen, K., Zuo, H., Mayer, M. and Monge-Sanz, B. (2018), 'SEAS5 and the future evolution of the long-range forecast system'.
URL: *http://ecmwf.int/sites/default/files/elibrary/2018/18750-%0Aseas5-and-future-evolution-long-range-forecast-system.pdf.*

Strachan, J., Vidale, P. L., Hodges, K., Roberts, M. and Demory, M. E. (2013), 'Investigating global tropical cyclone activity with a hierarchy of AGCMs: The role of model resolution', Journal of Climate **26**(1), 133–152.

Sugi, M., Murakami, H. and Yoshida, K. (2017), 'Projection of future changes in the frequency of intense tropical cyclones', Climate Dynamics **49**(1-2), 619–632.
URL: *http://link.springer.com/10.1007/s00382-016-3361-7*

Terray, L. (2012), 'Evidence for multiple drivers of North Atlantic multi-decadal climate variability', Geophysical Research Letters **39**(19), n/a–n/a.
URL: *http://doi.wiley.com/10.1029/2012GL053046*

Ting, M., Kossin, J. P., Camargo, S. J. and Li, C. (2019), 'Past and Future Hurricane Intensity Change along the U.S. East Coast', Scientific Reports **9**(1), 7795.
URL: *http://www.nature.com/articles/s41598-019-44252-w*

Ting, M., Kushnir, Y., Seager, R. and Li, C. (2011), 'Robust features of Atlantic multi-decadal variability and its climate impacts', Geophysical Research Letters **38**(17), n/a–n/a.
URL: *http://doi.wiley.com/10.1029/2011GL048712*

Titchner, H. A. and Rayner, N. A. (2014), 'The Met Office Hadley Centre sea ice and sea surface temperature data set, version 2: 1. Sea ice concentrations', Journal of Geophysical Research: Atmospheres **119**(6), 2864–2889.
URL: *http://doi.wiley.com/10.1002/2013JD020316*

Tolwinski-Ward, S. E. (2015), 'Uncertainty quantification for a climatology of the frequency and spatial distribution of North Atlantic tropical cyclone landfalls', Journal of Advances in Modeling Earth Systems **7**(1), 305–319.
URL: *http://doi.wiley.com/10.1002/2014MS000407*

Toomey, M. R., Donnelly, J. P. and Woodruff, J. D. (2013), 'Reconstructing mid-late Holocene cyclone variability in the Central Pacific using sedimentary records from Tahaa, French Polynesia', Quaternary Science Reviews **77**, 181–189.
URL: *http://dx.doi.org/10.1016/j.quascirev.2013.07.019*
https://linkinghub.elsevier.com/retrieve/pii/S0277379113002849

Torrence, C. and Compo, G. P. (1998), 'A practical guide to wavelet analysis', Bulletin of the American Meteorological Society **79**(1), 61–78.

Uppala, S. M., Kallberg, P. W., Simmons, A. J., Andrae, U., Bechtold, V. D. C., Fiorino, M., Gibson, J. K., Haseler, J., Hernandez, A., Kelly, G. A., Li, X., Onogi, K., Saarinen, S., Sokka, N., Allan, R. P., Andersson, E., Arpe, K., Balmaseda, M. A., Beljaars, A. C. M., Berg, L. V. D., Bidlot, J., Bormann, N., Caires, S., Chevallier, F., Dethof, A., Dragosavac, M., Fisher, M., Fuentes, M., Hagemann, S., Hólm, E., Hoskins, B. J., Isaksen, L., Janssen, P. A. E. M., Jenne, R., Mcnally, A. P., Mahfouf, J.-F., Morcrette, J.-J., Rayner, N. A., Saunders, R. W., Simon, P., Sterl, A., Trenberth, K. E., Untch, A., Vasiljevic, D., Viterbo, P. and Woollen, J. (2005), 'The ERA-40 re-analysis', Quarterly Journal of the Royal Meteorological Society **131**(612), 2961–3012.
URL: *http://doi.wiley.com/10.1256/qj.04.176*

U.s. Bureau of Labor Statistics (n.d.), 'CPI Inflation Calculator'.
URL: *https://data.bls.gov/cgi-bin/cpicalc.pl*

U.S., E. P. A. (2021), 'Climate Change Indicators: Tropical Cyclone Activity'.
URL: *https://www.epa.gov/climate-indicators/climate-change-indicators-tropical-cyclone-activity*

van den Dool, H. M., Saha, S. and Johansson, Å. (2000), 'Empirical Orthogonal Teleconnections', Journal of Climate **13**(8), 1421–1435.
URL: *http://journals.ametsoc.org/doi/abs/10.1175/1520-0442%282000%29013%3C1421%3AEOT%3E2.0.CO%3B2*

Vecchi, G. A. and Delworth, T. L. (2017), 'Origins of Atlantic decadal swings', Nature **548**.

Vecchi, G. A. and Soden, B. J. (2007), 'Effect of remote sea surface temperature change on tropical cyclone potential intensity', Nature **450**(7172), 1066–1070.

Veiga, S. F., Giarolla, E., Nobre, P. and Nobre, C. A. (2020), 'Analyzing the influence of the North Atlantic Ocean variability on the Atlantic meridional mode on decadal time scales', Atmosphere **11**(1), 1–16.

Velden, C., Harper, B., Wells, F., Beven, J. L., Zehr, R., Olander, T., Mayfield, M., Guard, C. Lander, M., Edson, R., Avila, L., Burton, A., Turk, M., Kikuchi, A., Christian, A., Caroff, P. and McCrone, P. (2006), 'The Dvorak Tropical Cyclone Intensity Estimation Technique: A Satellite-Based Method that Has Endured for over 30 Years', Bulletin of the American Meteorological Society **87**(9), 1195–1210.
URL: *http://journals.ametsoc.org/doi/10.1175/BAMS-87-9-1195*

Verdon, D. C. and Franks, S. W. (2006), 'Long-term behaviour of ENSO: Interactions with the PDO over the past 400 years inferred from paleoclimate records', Geophysical Research Letters **33**(6), L06712.
URL: *http://doi.wiley.com/10.1029/2005GL025052*

Vidale, P. L., Hodges, K., Vannière, B., Davini, P., Roberts, M. J., Strommen, K., Weisheimer, A., Plesca, E. and Corti, S. (2021), 'Impact of Stochastic Physics and Model Resolution on the Simulation of Tropical Cyclones in Climate GCMs', Journal of Climate **34**(11), 4315–4341.
URL: *https://journals.ametsoc.org/view/journals/clim/34/11/JCLI-D-20-0507.1.xml*

Vimont, D. J. and Kossin, J. P. (2007), 'The Atlantic Meridional Mode and hurricane activity', Geophysical Research Letters **34**(7), L07709.
URL: *http://doi.wiley.com/10.1029/2007GL029683*

Walker, G. T. (1924), 'Correlation in Seasonal Variations of Weather, IX. A Further Study of World Weather', Memoirs of the India Meteorological Department **24**(9), 275–333.

Wallace, D. J., Woodruff, J. D., Anderson, J. B. and Donnelly, J. P. (2014), 'Palaeohurricane reconstructions from sedimentary archives along the Gulf of Mexico, Caribbean Sea and western North Atlantic Ocean margins', Geological Society, London, Special Publications **388**(1), 481–501.
URL: *http://sp.lyellcollection.org/lookup/doi/10.1144/SP388.12*

Walsh, K. J., Mcbride, J. L., Klotzbach, P. J., Balachandran, S., Camargo, S. J., Holland, G., Knutson, T. R., Kossin, J. P., cheung Lee, T., Sobel, A. and Sugi, M. (2016), 'Tropical cyclones and climate change', Wiley Interdisciplinary Reviews: Climate Change **7**(1), 65–89.

Walters, D., Baran, A. J., Boutle, I., Brooks, M., Earnshaw, P., Edwards, J., Furtado, K., Hill, P., Lock, A., Manners, J., Morcrette, C., Mulcahy, J., Sanchez, C., Smith, C., Stratton, R., Tennant, W., Tomassini, L., Van Weverberg, K., Vosper, S., Willett, M., Browse, J., Bushell, A., Carslaw, K., Dalvi, M., Essery, R., Gedney, N., Hardiman, S., Johnson, B., Johnson, C., Jones, A., Jones, C., Mann, G., Milton, S., Rumbold, H., Sellar, A., Ujiie, M., Whitall, M., Williams, K. and Zerroukat, M. (2019), 'The Met Office Unified Model Global Atmosphere 7.0/7.1 and JULES Global Land 7.0 configurations', Geoscientific Model Development **12**(5), 1909–1963.
URL: *https://gmd.copernicus.org/articles/12/1909/2019/*

Wang, B. and Chan, J. C. (2002), 'How strong ENSO events affect tropical storm activity over the western North Pacific', Journal of Climate **15**(13), 1643–1658.

Webster, P. J., Holland, G. J., Curry, J. A. and Chang, H.-R. (2005), 'Changes in Tropical Cyclone Number, Duration, and Intensity in a Warming Environment', Science **309**(5742), 1844–1846.
URL: *http://www.sciencemag.org/cgi/doi/10.1126/science.1116448*

Wehner, M., Prabhat, Reed, K. A., Stone, D., Collins, W. D. and Bacmeister, J. (2015), 'Resolution Dependence of Future Tropical Cyclone Projections of CAM5.1 in the U.S. CLIVAR Hurricane Working Group Idealized Configurations', Journal of Climate **28**(10), 3905–3925.

Weinkle, J., Maue, R. and Pielke, R. (2012), 'Historical global tropical cyclone landfalls', Journal of Climate **25**(13), 4729–4735.

Williams, K. D., Copsey, D., Blockley, E. W., Bodas-Salcedo, A., Calvert, D., Comer, R., Davis, P., Graham, T., Hewitt, H. T., Hill, R., Hyder, P., Ineson, S., Johns, T. C., Keen, A. B., Lee, R. W., Megann, A., Milton, S. F., Rae, J. G., Roberts, M. J., Scaife, A. A., Schiemann, R., Storkey, D., Thorpe, L., Watterson, I. G., Walters, D. N., West, A., Wood, R. A., Woollings, T. and Xavier, P. K. (2018), 'The Met Office Global Coupled Model 3.0 and 3.1 (GC3.0 and GC3.1) Configurations', Journal of Advances in Modeling Earth Systems **10**(2), 357–380.

WMO (2015), 'Typhoon Committee Operational Manual, Meteorological Component,

2015 Edition', (196), 169.
URL: *library.wmo.int/doc_num.php?explnum_id=7633*

Wu, L. and Tao, L. (2011), 'A mechanism for long-term changes of Atlantic tropical cyclone intensity', Climate Dynamics **36**(9-10), 1851–1864.
URL: *http://link.springer.com/10.1007/s00382-010-0768-4*

Yamada, Y., Satoh, M., Sugi, M., Kodama, C., Noda, A. T., Nakano, M. and Nasuno, T. (2017), 'Response of tropical cyclone activity and structure to global warming in a high-resolution global nonhydrostatic model', Journal of Climate **30**(23), 9703–9724.

Yan, X., Zhang, R. and Knutson, T. R. (2017), 'The role of Atlantic overturning circulation in the recent decline of Atlantic major hurricane frequency', Nature Communications **8**(1), 1695.
URL: *http://dx.doi.org/10.1038/s41467-017-01377-8*
http://www.nature.com/articles/s41467-017-01377-8

Yoshida, K., Sugi, M., Mizuta, R., Murakami, H. and Ishii, M. (2017), 'Future Changes in Tropical Cyclone Activity in High-Resolution Large-Ensemble Simulations', Geophysical Research Letters **44**(19), 9910–9917.

Zehr, R. M., Beven, J. L. and DeMaria, M. (2010), 'Analysis of high resolution infrared images of hurricanes from polar satellites as a proxy for goes-r.'.

Zhang, C. (2005), 'Madden-Julian Oscillation', Reviews of Geophysics **43**(2), RG2003.
URL: *http://doi.wiley.com/10.1029/2004RG000158*

Zhang, L., Karnauskas, K. B., Donnelly, J. P. and Emanuel, K. (2017), 'Response of the North Pacific Tropical Cyclone Climatology to Global Warming: Application of Dynamical Downscaling to CMIP5 Models', Journal of Climate **30**(4), 1233–1243.
URL: *http://journals.ametsoc.org/doi/10.1175/JCLI-D-16-0496.1*

Zhang, R. and Delworth, T. L. (2006), 'Impact of Atlantic multidecadal oscillations on India/Sahel rainfall and Atlantic hurricanes', Geophysical Research Letters **33**(17), L17712.
URL: *http://doi.wiley.com/10.1029/2006GL026267*

Zhang, R., Delworth, T. L., Dixon, K. W., Held, I. M., Ming, Y., Msadek, R., Rosati, A. J., Vecchi, G. A., Sutton, R., Hodson, D. L. R., Robson, J., Kushnir, Y., Ting, M. and Marshall, J. (2013), 'Have aerosols caused the observed atlantic multidecadal variability?', Journal of the Atmospheric Sciences **70**(4), 1135–1144.

Zhao, M., Held, I. M., Lin, S.-J. and Vecchi, G. A. (2009), 'Simulations of Global Hurricane Climatology, Interannual Variability, and Response to Global Warming Using a 50-km Resolution GCM', Journal of Climate **22**(24), 6653–6678.
URL: *http://journals.ametsoc.org/doi/10.1175/2009JCLI3049.1*

Zhao, X. and Chu, P.-S. (2006), 'Bayesian Multiple Changepoint Analysis of Hurricane Activity in the Eastern North Pacific: A Markov Chain Monte Carlo Approach', Journal of Climate **19**(4), 564–578.
URL: *http://journals.ametsoc.org/doi/abs/10.1175/JCLI3628.1*